

AN ABSTRACT OF THE DISSERTATION OF

Mohammad Ghazvini for the degree of Doctor of Philosophy in Mechanical Engineering
presented on September 23, 2013.

Title: Compact Integrated Microchannel Combustor Recuperator and Heat Exchanger For
Hydrogen Storage Applications

Abstract approved:

Vinod Narayanan

A novel microscale combustor-heat exchanger (μ CHX) for hydrogen storage applications is presented in this dissertation. The design of the μ CHX is motivated by its application to two particular systems for automotive use- those that utilize metal hydrides (MH) and cryo-adsorbents (CA) to store hydrogen. Thermal energy needs to be supplied to the MH bed to raise its temperature to 170 °C in order to desorb hydrogen for use in a fuel cell. On the other hand, in a CA system, hydrogen gas that exits the storage tank needs to be heated to a minimum temperature of -40 °C prior to entering the fuel cell. During cold start conditions, heat exchange with ambient air or with the fuel cell coolant is insufficient to provide this minimum temperature, thereby requiring an additional source of thermal energy. For both storage systems, the required thermal energy can be provided by oxidizing a small amount of hydrogen and transferring the heat from combustion to the working fluid, which is an oil in a MH system and hydrogen in a CA system.

The μ CHX presented herein is a compact and highly efficient way of providing the required thermal energy rate.

The μ CHX is comprised of repeating unit cells that each perform identical unit operations, namely (a) catalytic combustion of a hydrogen-air mixture, (b) transfer of produced thermal energy rate to a heat transfer fluid, and (c) recuperation between the exhaust gas stream and incoming reactant gases. Heterogeneous catalytic combustion occurs on the walls of microchannels in the presence of a platinum catalyst. A multi-kilowatt μ CHX device can be achieved by having multiple unit cells with appropriate fluidic distribution headers. The μ CHX design is common for both hydrogen storage systems with minor changes. The design of the μ CHX is performed using computational fluid dynamics simulations (CFD) at the unit cell and device level.

At the unit cell level, the performance is documented using validated CFD simulations for variations in geometric and fluidic parameters. Varied geometric parameters include the length and location of the catalyst bed, length of the device, and the height of the combustion channel. Varied fluidic parameters include the working fluid inlet temperature, flow rates of the working fluid and reactants, and the equivalence ratio of the reactants. Performance is characterized using a global efficiency, heat transfer effectiveness and hydrogen conversion. The parametric variations are captured non-dimensionally as variations in Damkohler and Peclet numbers, which are in turn used to describe the changes in hydrogen conversion and efficiency. Performance maps for hydrogen conversion and pressure drop in the combustion channel are presented based on values of the Damkohler and Peclet numbers and regions of desired operability of the combustor are identified. For the CA μ CHX, it is shown that with the help of a novel distributed catalyst arrangement, extinction of the reaction due to the cold gas stream is prevented and hydrogen

conversion in excess of 95 percent is achieved for a range of operating conditions. Comparisons between simulations and experiments are not performed since, in the simulations, (a) ideal catalyst activity and surface distribution are assumed, and (b) the effect of substrate conduction is not considered.

At the device level, three dimensional simulations of fluid flow are performed to ensure uniformity in flow distribution while maintaining low pressure drop through the device. Fabrication constraints are also incorporated into the device level design and simulations.

A multi-watt CA μ CHX consisting of 16 unit cells is experimental characterized using nitrogen as a surrogate heat exchange fluid. In experiments, a total catalyst length of 22.5 mm is used instead of 12.5 mm (which was used for the simulations) to account for reduced catalyst activity from the simulated ideal case. Experimental results show that hydrogen residence time and body temperature have significant effects on the overall efficiency of the device. Conversions as high as 94.1% and efficiencies as high as 88.3% are achieved. Highest hydrogen conversion is recorded at an equivalence ratio of 0.6.

© Copyright by Mohammad Ghazvini
September 23, 2013
All Rights Reserved

Compact Integrated Microchannel Combustor Recuperator and Heat Exchanger For
Hydrogen Storage Applications

by
Mohammad Ghazvini

A DISSERTATION
submitted to
Oregon State University

in partial fulfillment of
the requirements for the
degree of

Doctor of Philosophy

Presented September 23, 2013
Commencement June 2014

Doctor of Philosophy dissertation of Mohammad Ghazvini presented on September 23, 2013.

APPROVED:

Major Professor, representing Mechanical Engineering

Head of the School of Mechanical, Industrial and Manufacturing Engineering

Dean of the Graduate School

I understand that my dissertation will become part of the permanent collection of Oregon State University libraries. My signature below authorizes release of my dissertation to any reader upon request.

Mohammad Ghazvini, Author

ACKNOWLEDGEMENTS

I wish to express my appreciation and gratitude to everyone who have been directly or indirectly involved and helped me with this research. I want to thank my advisor Dr. Vinod Narayanan for his help, support and guidance throughout this work. I'm always impressed by his knowledge and hard work.

I want to thank my graduate committee members, Dr. Deborah Pence, Dr Sourabh Apte, Dr. Murthy Kanury and my GCR Dr. Abi Farsoni for accepting to be on my committee and for their helpful comments. I also want to acknowledge people in the OSU Hydrogen Storage Group, the leadership of Dr. Kevin Drost and all of the guidance and collaboration I received from Dr. Brian paul and Dr. Goran Jovanovic. I would like to extend my gratitude to my lab mates who helped me a lot, David Haley, Ruander Cardenas, Preeti Mani, specially Mohammad Hadi Tabatabaee. I also want to thank my old friend Erfan Rasouli for his help. I am grateful for all my friends here in Corvallis that made the past 4 years enjoyable.

I would like to thank my fiancé Somaye, for being a continuous source of love and support especially during the long nights of studying and testing. I am eternally grateful to have her by my side throughout this journey.

Finally, I want to express my appreciation and gratitude to my parents and my brother Hamed and my sister Maryam for all their support and encouragement throughout these years. Nothing would have been possible without their love and guidance that have shaped me into the person that I am today. This dissertation is dedicated to my parents.

TABLE OF CONTENTS

	<u>Page</u>
1- INTRODUCTION	1
2- LITERATURE REVIEW	11
2-1 Catalytic Reactions	11
2-2 Reaction in Microchannels	14
2-2-1 The effect of inlet velocity (residence time effects)	17
2-2-2 The effect of wall conductivity	19
2-2-3 The effect of operating pressure	20
2-2-4 Effect of reactant mixture temperature	21
2-2-5 Catalyst segmentation	21
2-2-6 Recuperation	22
2-2-7 Integrated combustor and heat exchanger	24
2-3 Stacked up Microchannels	25
3- OBJECTIVES	28
4- UNIT CELL DESIGN AND SIMULATIONS	31
4-1 Method and Model Development	31
4-1-1 MH μ CHX design	31
4-1-2 Simulation method	34
4-2 Governing Equations	34
4-2-1 Dimensionless equations	40
4-2-2 Time scales	44
4-3 Simulation Method and Model Validation	50
4-3-1 Grid independence study	50
4-3-2 Model validation	53
4-4 Sensitivity Analysis	55
4-5 Effect of Catalyst Active Area	57
4-6 Parametric Study of the MH μ CHX	59
4-6-1 Performance indices	60
4-6-2 Catalyst bed length	63

TABLE OF CONTENTS (Continued)

	<u>Page</u>
4-6-3 Channel length.....	66
4-6-4 Channel height.....	66
4-6-5 Inlet gas velocity	69
4-6-6 Equivalence ratio.....	71
4-6-7 Oil inlet temperature.....	72
4-6-8 Oil inlet velocity.....	74
4-7 Performance Map	75
4-8 Design and Simulations of a CA μ CHX Unit Cell.....	81
4-8-1 Design	81
4-8-2 Numerical simulation procedure	86
4-8-3 Parametric variations.....	88
5- DEVICE LEVEL DESIGN AND FABRICATION OF A MULTI-WATT μ CHX.....	92
5-1 Fabrication Steps	92
5-1-1 Microlamination.....	93
5-1-2 Chemical etching.....	93
5-1-3 Diffusion bonding	94
5-2 Device level Design and Fabrication.....	96
5-2-1 Layer design	96
5-2-2 Design of the headers	101
5-2-3 Fabricated parts	107
6- EXPERIMENTAL FACILITY AND METHODS	112
6-1 Design Requirements.....	112
6-2 Catalyst Preparation.....	114
6-2-1 Catalyst deposition	114
6-2-2 Catalyst activation.....	120
6-2-3 Catalyst performance at high temperatures	123
6-3 Experimental Test Section.....	130
6-4 CA μ CHX Test Facility.....	134

TABLE OF CONTENTS (Continued)

	<u>Page</u>
6-5 Experimental Procedures	140
6-5-1 Start up procedure	140
6-5-2 Continuous operation	143
6-5-3 Shutdown procedure.....	144
6-5-4 Emergency shutdown process	146
6-5-5 Hydrogen cabinet operation	146
6-6 Safety Considerations	146
7- DATA ANALYSIS AND CALIBRATION.....	154
7-1 Calibration	154
7-1-1 Thermocouple calibration	154
7-1-2 Pressure transducers calibration	156
7-1-3 Gas Chromatograph Calibration.....	158
7-2 Uncertainty Analysis	159
7-3 Leak Test	161
7-4 Heat Loss Calculations	163
8- EXPERIMENTAL RESULTS AND DISCUSSION	166
8-1 Experimental Matrix.....	166
8-2 Repeatability of the Experiments.....	168
8-3 Experimental Results	169
8-3-1 Effect of residence time.....	171
8-3-2 Effect of body temperature.....	174
8-3-3 Effect of equivalence ratio	178
8-3-4 Effect of N ₂ inlet temperatures	180
8-3-5 Pressure drops	182
8-3-6 Performance map.....	182
9- CONCLUSION AND FINAL REMARKS.....	185
9-1 Conclusions	185
9-2 Recommendation for Future Study.....	188

TABLE OF CONTENTS (Continued)

	<u>Page</u>
BIBLIOGRAPHY	190
APPENDICES	196
APPENDIX A. PARATHERM MR PROPERTIES.....	197
APPENDIX B. MH μ CHX LAYERS	198
APPENDIX C: SAMPLE UNCERTAINTY CALCULATIONS	199
APPENDIX D: CHEMKIN REACTION MECHANISM CODE.....	201

LIST OF FIGURES

<u>Figure</u>	<u>Page</u>
Figure 1. Gravimetric energy density of different storage methods and materials (Data from [3])	2
Figure 2: Volumetric energy density of hydrogen compared to different fuels (Data from [6])	3
Figure 3. Volumetric versus gravimetric capacities of different storage methods (Data from [4])	3
Figure 4: Schematic view of the μ CHX in a metal hydride storage system	5
Figure 5: Schematic view of option 1 combustor-heat exchanger in the CA system	6
Figure 6: Schematic view of option 2 combustor-heat exchanger in the CA system	7
Figure 7: Schematic view of option 3 heat exchanger in the CA system	8
Figure 8: Schematic view of μ CHX in a cryo-adsorbent system	9
Figure 9: Inlet preheat temperatures required for different inlet velocities (adapted from [22])	17
Figure 10: (a) Temperature distribution along the channel for different inlet velocities, and (b) Homogeneous and heterogeneous reaction in three different regions [23]	18
Figure 11: Bulk temperature as a function of axial distance for (a) $k=2$ W/m-K, (b) $k=200$ W/m-K [24]	19
Figure 12: a) Schematic view of the Swiss roll combustor [34] b) Reaction rate along the channel center for $Re=500$ and different fuel concentration [35]	24
Figure 13: A multi-Watt μ CHX consisting of several internal units	29
Figure 14: Schematic of a simple combustor and heat exchanger	32
Figure 15: Schematics of the two different geometry configurations	33
Figure 16: Schematic of the microscale integrated combustor recuperator heat exchanger	33

LIST OF FIGURES (Continued)

<u>Figure</u>	<u>Page</u>
Figure 17: Axial variation along the length of the combustion channel of (a) temperature and hydrogen mass fraction, (b) local time scales	48
Figure 18: (a) Comparison channel non-uniform grids, (b) Combustion channel grids after adaption.....	51
Figure 19: Grid independence study comparing the global results of conversion and efficiency as a function of the number of grids.....	52
Figure 20: Local values of H ₂ mass fraction and temperature as a function of y (height of the channel) at three different locations. (a) x = 5 mm, (b) x = 10 mm, and (c) x = 20 mm..	53
Figure 21: A schematic view of the geometry of Appel et al. [48].....	54
Figure 22: Comparison of the results from current model simulations with experimental and numerical data from Appel et al. [48]. Profiles of H ₂ and temperature are shown at four Streamwise locations: (a) x = 25 mm, (b) x = 85 mm, (c) x = 105 mm, (d) x = 165 mm.....	55
Figure 23: Sensitivity analysis on the elementary schemes of Deutschmann et al. [13] listed in Table 6	56
Figure 24: Change in H ₂ conversion by variation of factor <i>B</i> in percentage	58
Figure 25: a) Temperature contours (K), b) H ₂ mass fraction contours, and c) H ₂ O mass fraction contours. The heavy lines indicate the location of the catalyst bed.	59
Figure 26: Variation of oil and exhaust temperature difference (ΔT_{ave}) and exhaust exit temperature ($T_{exhaust,ave}$) with effectiveness as defined in Eq.(45).	62
Figure 27: Variation of performance indices with catalyst length.....	64
Figure 28: Variation of Damkohler and Peclet numbers with catalyst bed lengths.....	65
Figure 29: Variation of performance indices with combustion channel height	68
Figure 30: Variation of Damkohler and Peclet numbers with channel heights	68

LIST OF FIGURES (Continued)

<u>Figure</u>	<u>Page</u>
Figure 31: Variation of performance indices with inlet residence time.....	70
Figure 32: Variation of Damkohler and Peclet numbers with residence times.....	70
Figure 33: Variation of performance indices and pressure drop with equivalence ratio	71
Figure 34: Performance indices as functions of inlet oil temperature	73
Figure 35: Parity of conversions estimated from simulations and conversions predicted by Eq. (46).....	76
Figure 36: Contours of H ₂ conversion based on numerical data from this study.....	77
Figure 37: Contours of pressure drop (in Pa) in the combustor channel	78
Figure 38: Performance map indicating different regions of operability based on H ₂ conversion and ΔP - The regions are described in Table 11.	79
Figure 39: A schematic of a unit cell of the CA μ CHX with the catalyst beds shown as gray lines	82
Figure 40: Temperature contours for the CA μ CHX unit cell (K), catalyst located in the combustion channel	83
Figure 41: Hydrogen mass fraction along the length of the combustion channel.....	84
Figure 42: A schematic of a unit cell of the μ CHX for cryo-adsorbent systems with distributed catalyst with the catalyst beds shown as gray lines	85
Figure 43: Temperature contours for the cryo-adsorbent μ CHX unit cell (K), segmented catalyst	85
Figure 44: Hydrogen mass fraction along the length of the combustor and exhaust channels.....	86
Figure 45: Designed channel versus etched channel	94

LIST OF FIGURES (Continued)

<u>Figure</u>	<u>Page</u>
Figure 46: Schematic describing the diffusion bonding limitation.....	95
Figure 47: A set of 8 unit cells consisting 5 different layers	98
Figure 48: Combustor channel shim consisting of 8 channels.....	98
Figure 49: Dimensions of the combustion layer (numbers are in millimeters).....	99
Figure 50: Streamwise velocity magnitude contours (m/s) for one half of the microchannels within the combustor layer shown in Figure 48.....	100
Figure 51: Streamwise velocity magnitude contours (m/s) for one half of the microchannels within the nitrogen layer shown in Figure 47	101
Figure 52: Schematic of the locations of the inlets and outlets.....	102
Figure 53: The top layers of H ₂ /air and nitrogen headers showing the transition from circular tubing to the respective plena	103
Figure 54: The bottom layers of the exhaust headers	104
Figure 55: Pressure contours (Pa) of the combustible gases flow through the headers and layers	104
Figure 56: N ₂ recirculation showed by velocity vectors in the first plenum (m/s)	105
Figure 57: N ₂ inlet headering system (a) First and second plenums, (b) First plenum and the location of the passages	106
Figure 58: Pressure contours (Pa) of the nitrogen flow through the headers and layers.....	107
Figure 59: Sample fabricated layers for the CA μ CHX.....	108
Figure 60: ZeScope analysis of a combustion layer with defects	109
Figure 61: One quarter of the combustor layer	110

LIST OF FIGURES (Continued)

<u>Figure</u>	<u>Page</u>
Figure 62: The entrance region (first and second plenum) of nitrogen on the combustor layer ..	111
Figure 63: SEM pictures of deposited chloroplatinic acid at two different locations with the same magnification	115
Figure 64: Top view of a combustor layer.....	116
Figure 65: The back of a combustor shim covered with mask for etching.....	117
Figure 66: Etched channels on the back side of a channel.....	117
Figure 67: a) Profile of a section of the channels, b) Plot of the height of the area shown with a dark line	118
Figure 68: Syringes used for catalyst deposition	119
Figure 69: Catalyst deposited on back side of a shim.....	119
Figure 70: Use of mask and RTV to confine the catalyst area.....	119
Figure 71: SEM pictures of a catalyst surface after activation processes , (a) 500 x magnification, (b) 3000 magnification, (c) and (d) 30000 magnification at two different locations.....	121
Figure 72: Final assembly of the device for activation process	122
Figure 73: (a) Bottom aluminum block, the mica gasket and catalyst layers on the top (b) Detailed picture of the assembly	122
Figure 74: (a) Stainless steel shim coated by catalyst, (b) Test section for the catalyst activity comparison.....	124
Figure 75: SEM pictures of a catalyst surface after diffusion bonding process , (a) under 850 °C, 500 x magnification, (b) under 1000 °C, 500 x magnification, (c) under 850 °C, 5000 x magnification, (d) under 1000 °C, 5000 x magnification, (e) under 850 °C, 15000 x magnification, (f) under 1000 °C, 15000 x magnification	125

LIST OF FIGURES (Continued)

<u>Figure</u>	<u>Page</u>
Figure 76: EDX analysis of a catalyst surface after going through a 1000 °C process.....	126
Figure 77: EDX elemental mapping for a 1000 °C catalyst surface (6400 x).....	128
Figure 78: Elemental mapping of iron (blue), platinum (green) and oxygen (red) combined (Nickel and chromium are not shown in this map.).....	128
Figure 79: Temperature of the catalyst surface versus time for different processes catalysts (experimental results).....	130
Figure 80: Assembly view of the test section without diffusion bonding to be bolted together..	131
Figure 81: μ CHX layers after activation.....	131
Figure 82: Top view of the top PEEK cap (left), bottom view of the top PEEK cap (middle), and assembly view of the test section (right).....	132
Figure 83: Detailed picture of the test section assembly.....	132
Figure 84: Final assembly of the test section.....	133
Figure 85: Test facility schematic.....	136
Figure 86: Nitrogen temperature and flow control system	137
Figure 87: Data acquisition system used for the experiments.....	139
Figure 88: Test facility start up procedure.....	142
Figure 89: Continuous Operation Procedure	144
Figure 90: Shutdown Procedure.....	145
Figure 91: Emergency Shutdown Procedure	147
Figure 92: Chiller used to calibrate the thermocouples	156

LIST OF FIGURES (Continued)

<u>Figure</u>	<u>Page</u>
Figure 93: temperature calibration curves for thermocouple #1, (a) Below 0 °C, (b) above 0 °C K	156
Figure 94: Differential pressure calibration for nitrogen side pressure transducer.....	157
Figure 95: Micro GC composition analysis for a calibration gas mixture.....	158
Figure 96: Pressure decay versus time and the rate at 1.5 bar.....	162
Figure 97: The test section covered by insulation.....	164
Figure 98: Temperature decay by time.....	165
Figure 99: Experimental operating condition and the performance map.....	167
Figure 100: Cross section of a combustion channel.....	172
Figure 101: Variation of H ₂ conversion, efficiency and heat loss ratio by residence time.....	174
Figure 102: Variation of H ₂ conversion, efficiency and heat loss ratio by body temperature.....	175
Figure 103: Variation of the performance indices at low body temperatures.....	176
Figure 104: Location of thermocouples measuring the body temperatures.....	178
Figure 105: The effect of equivalence ratio on efficiency.....	179
Figure 106: The effect on inlet nitrogen temperature on performance indices.....	181
Figure 107: Heat pathways and location of thermocouples.....	182
Figure 108: Comparison between the experimental and correlation values for hydrogen conversions.....	183
Figure 109: Comparison between the experimental and modified correlation (Eq. 61) values for hydrogen conversions.....	184

LIST OF TABLES

<u>Table</u>	<u>Page</u>
Table 1: Option 1 heat exchanger operating conditions	6
Table 2: Option 2 heat exchanger operating conditions	7
Table 3: Option 3 heat exchanger placement and operating conditions	8
Table 4: Option 4 heat exchanger placement and operating conditions	9
Table 5: Desired operating conditions for the μ CHX in a cryo-adsorbent storage system.....	9
Table 6: Heterogeneous chemical reaction mechanisms of hydrogen on platinum [13]	13
Table 7: Geometrical and fluidic conditions for the base case	47
Table 8: Summary of geometrical and thermo-fluidic parameters for the MH μ CHX ^a	62
Table 9: Comparison of different channel lengths at the same catalyst length.....	66
Table 10: The effect of changing oil inlet velocity on the performance indices.....	74
Table 11: Different regions (Figure 38) and their performance ranges	80
Table 12: Simulation results for the desired pressure and hydrogen mass flow rate ranges shown in Table 5	88
Table 13: Simulation results for nitrogen as the working fluid for the cryo-adsorbent μ CHX	90
Table 14: Average velocity within each of the channels within a single layer.....	101
Table 15: Average velocity magnitude in combustor layers.....	105
Table 16: Average velocity magnitude in nitrogen layers	107
Table 17: Elements and their weight and mass percentages	127
Table 18: List of instrumentation and equipment for the facility shown in Fig. 13.....	135
Table 19: Design Flow Rates for μ CHX ($\phi=1$, max H ₂ flow)	138

LIST OF TABLES (Continued)

<u>Table</u>	<u>Page</u>
Table 20: Operating Parameters for μ CHX	138
Table 21: Data acquisition system components	140
Table 22: Failure Modes and Effects Analysis	149
Table 23: Failure Modes and Effects Analysis Legend	150
Table 24: Uncertainty of measured parameters for a sample experiment.....	160
Table 25: calculated parameters and indices and their equations	160
Table 26: Uncertainty of calculated parameters for a sample experiment.....	161
Table 27: Experimental matrix of the μ CHX experiments	166
Table 28: Operating conditions and date of the experiments.....	168
Table 29: Result comparison among three cases of the repeatability study.....	169
Table 30: Test conditions related to Figure 101	172
Table 31: Size and weight of a 1kW device for different equivalence ratios	179

Compact Integrated Microchannel Combustor, Recuperator and Heat
Exchanger For Hydrogen Storage Applications

NOMENCLATURE

A	Pre-exponential factor (Arrhenius equation) (mol-cm-K-s)
B	Ratio of active catalyst area to the geometrical catalyst area
C_p	Specific heat at constant pressure (J/kg.K)
C_g	Gas species molar concentration (mol/cm ³)
C_m	Surface species molar concentration (mol/cm ²)
d	Diffusion distance (m)
D	Species diffusion coefficient (m ² /s)
Da	Damkohler number
D_m	Mixture-average species diffusion coefficient
D^T	Species thermal diffusion coefficient (m ² /s)
E_a	Activation energy (Arrhenius equation) (kJ/mol)
F	Multiplication/division factor
h	Enthalpy (J/kg)
H^*	Channel height ratio
H_b	Channel height of base case (m)
H_c	Combustion channel height (m)
H_o	Oil channel height (m)
H_E	Exhaust channel height (m)
K	Reaction coefficient (mol-cm-K-s)
k	Thermal conductivity (W/m.K)

L	Length of the catalyst bed (m)
L_{CH}	Length of the channel
Le	Lewis number
M	Molar mass (kg/kmol)
\bar{M}	Mixture average molecular weight (kg/kmol)
N_g	Total number of gaseous species
N_r	Total number of reaction steps
N_s	Total number of surface species
\dot{m}	Mass flow rate (kg/s)
P	Pressure (Pa)
Pe	Peclet number
R	Gas constant (8.3145×10^{-3} kJ/mol-K)
S	sticking coefficients
\dot{s}	Molar production rate
T	Temperature (K)
t_r	Residence time (s)
t_d	Diffusion time (s)
t_c	Chemical time (s)
u	Velocity in x direction (m/s)
v	Velocity in y direction (m/s)
\bar{V}	Cross sectionally averaged velocity (m/s)
X_g	Mole fraction of g^{th} gaseous species
Y_g	Mass fraction of g^{th} gaseous species

x	Streamwise coordinate
y	Transverse coordinate

GREEK SYMBOLS

β	Temperature exponent (Arrhenius equation)
ε	Effectiveness
ϕ	Species equivalence ratio in a reaction
Γ	Surface site density (mol/cm ²)
η	Efficiency index
κ_T	Thermal diffusion ratio
μ	Viscosity (kg/m.s)
ρ	Density (kg/m ³)
τ	Sum of surface reactants' stoichiometric coefficients
ν	Species stoichiometric coefficient
ν'	Species stoichiometric coefficient of a reactant
σ_m	m^{th} surface species site occupancy (mol/cm ²)

SUBSCRIPTS

0	Value at the inlet
C	Combustion channel
E	Exhaust channel
HX	Heat exchanger
<i>in</i>	Inlet
<i>g,m</i>	Indices for gas-phase and surface species

<i>O</i>	Oil Channel
<i>oil</i>	Oil
<i>out</i>	Outlet
<i>r</i>	Index for reaction step
<i>s</i>	Surface of the catalyst
<i>W</i>	Wall
<i>x</i>	Streamwise coordinate
<i>y</i>	Transverse coordinate

1- INTRODUCTION

The world's energy consumption continues to grow as its population increases. Fossil fuels like coal, natural gas and gasoline account for approximately 81% of the total energy used and 98% of energy used in the transportation sector in the world [1]. Limited supplies of fossil fuels as well as their environmental effects are among issues that make alternative energy sources a necessity.

Over the last three decades CO₂ emissions has increased by 50% as a result of using hydrocarbon fuels [2]. Therefore it is imperative that fossil fuels not be energy sources of the future. There has been a lot of research to obtain energy from renewable and sustainable sources like solar and wind. One of the challenges of renewable energies like solar and wind is energy storage. Several storage options have been considered and tested. One method of storage is to convert renewable energy to electricity and then store electricity in batteries. Another method is to use the renewable energies and transform it to a chemical energy source (such as hydrogen) for storage. Desired characteristic of an energy storage method is that the energy storage density be large. This would permit a compact scheme. Figure 1 compares the gravimetric energy density, defined as the amount of energy stored in unit weight of the material, of different materials and technologies. Please note that the y-axis is on a log scale and the differences in energy per kilogram of these materials are significant. The figure shows that, on a weight basis, if hydrogen is reacted and the heat is used to produce electricity with the overall efficiency of even one percent, the resulting electric power will be more than that stored in most of the batteries available today. On a volumetric basis, on the other hand, hydrogen does not compare well with other methods; therefore storing hydrogen in a volumetrically efficient system is important. Figure 2 compares the volumetric energy density of hydrogen with other fuels. It shows that hydrogen in its natural

form has very low volumetric energy density, however, as the storage pressure is increased, hydrogen volumetric density increases. Liquid hydrogen has higher energy density than pressurized hydrogen however; room temperature liquid hydrogen is stored in tanks under very high pressures. Therefore different methods of storing hydrogen effectively are being investigated by several institutes. Ni metal hydrides, for example, have similar volumetric energy density as liquid hydrogen and do not require high pressures (Figure 2). However their gravimetric density is extremely low as seen in Figure 1.

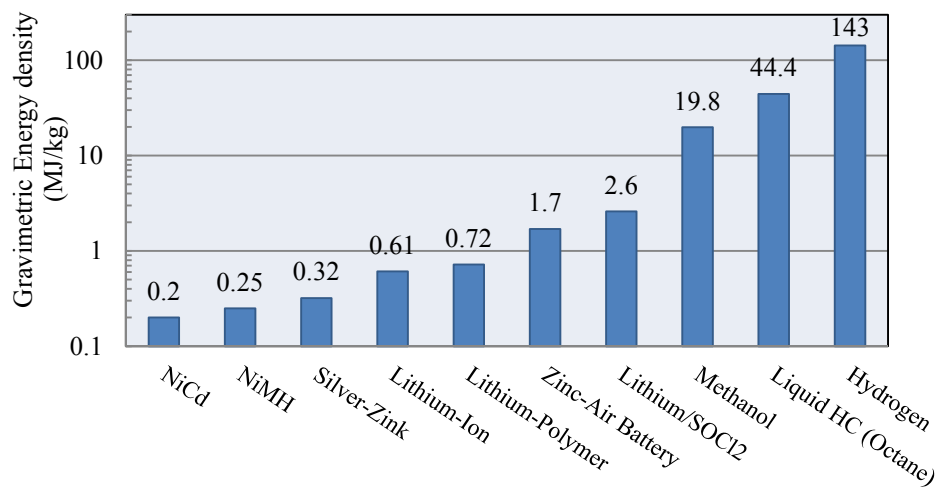


Figure 1. Gravimetric energy density of different storage methods and materials (Data from [3])

There are three classes of systems that utilize materials for hydrogen storage namely metal hydrides (ex. NaAlH_4), chemical hydrides (ex. AB) and adsorbents (ex. AX-21, MOF). Figure 3 shows different hydrogen storage methods and their volumetric and gravimetric capacities. It also shows the targets of United States Department of Energy (DOE) for 2010 and 2015 [4]. The 2015 targets are 5.5 % H_2 by weight and 40 g of H_2 per liter with ultimate targets of 7.5% H_2 by weight and 70 H_2 per liter. With these targets in mind, DOE has instituted parallel research tracks with a focus on on-board reversible storage systems [5]. In an on-board reversible storage system,

hydrogen is directly added into the storage tank at the refueling station, this addition may be facilitated by some thermal conditioning.

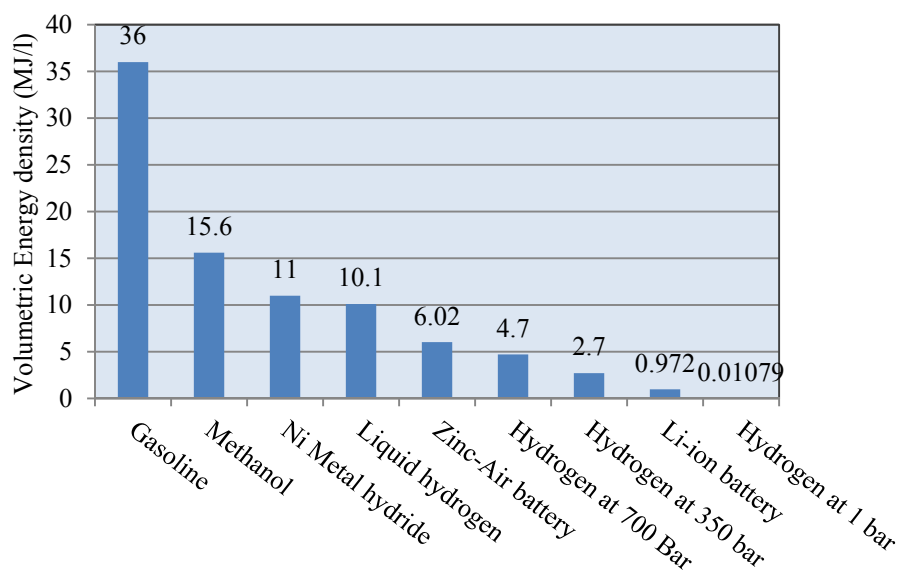


Figure 2: Volumetric energy density of hydrogen compared to different fuels (Data from [6])

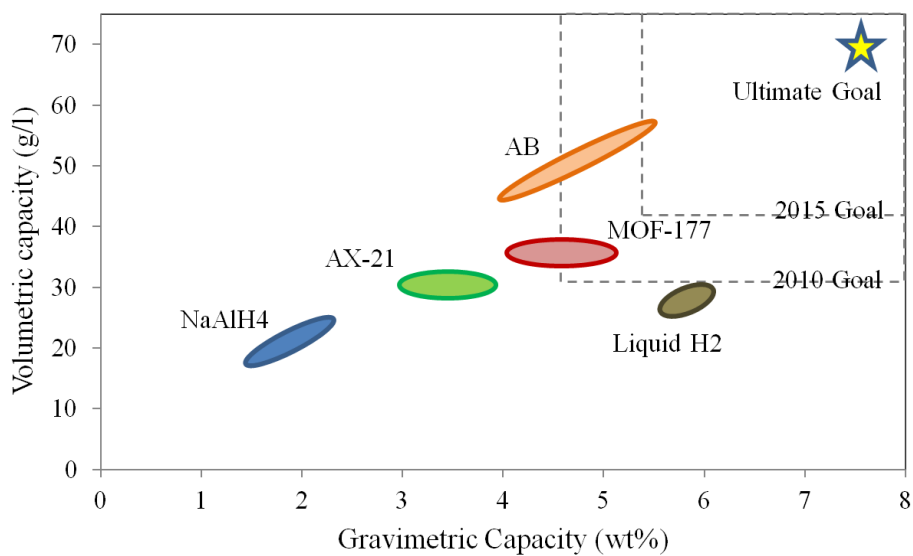


Figure 3. Volumetric versus gravimetric capacities of different storage methods (Data from [4])

Metal hydrides form strong chemical bonds with hydrogen ions within the host metal lattice during adsorption [7]. Desorption of hydrogen from metal hydrides is an exothermic process, therefore there is need for a large amount of heat, as dictated by heat of reaction (84 kJ/mol) [8], to the system while desorption. The heat can be provided using electric resistance or gas heaters.

There has been a lot of research on the development of high surface area adsorbents. Although there are several different materials that have the ability to store hydrogen, activated carbon and metal organic frameworks (MOF) have gained a lot of attention. Unlike metal hydrides, activated carbons physically store hydrogen on the material surface by physisorption caused by Van der Waals forces [9]. Because of the weakness of physisorption, large quantities of hydrogen storage can only be achieved at very low temperatures (-196 °C) and moderate pressures (~60-100 bars H₂). Adsorbents generate much less heat during storage (heat of adsorption <10 kJ/mol) and need similar amount of heat for desorption [5].

In both storage systems, i.e. metal hydrides and adsorbents, there is a need for a heat source for desorption. This heat could be provided by oxidizing a portion of the hydrogen stored in the tank in a burner and provide the heat of reaction to desorb the rest of the hydrogen in the tank. In order to meet the DOE gravimetric and volumetric goal, the size and weight of the system should be minimized. Concurrently DOE has an onboard efficiency goal, which requires a high efficiency burner. It is in this context that a compact microscale combustor and heat exchanger (μ CHX) is explored in this thesis.

A compact, high efficiency burner is an important balance of plant component in a metal hydride storage system since the heat of desorption needs to be provided at between 160 – 180 °C. Figure

4 illustrates the microscale combustor- heat exchanger (μ CHX) location in a metal hydride hydrogen storage system. In cryo-adsorbent storage, hydrogen that leaves the bed is very cold (as low as $-240\text{ }^{\circ}\text{C}$) and needs to be heated to at least $-40\text{ }^{\circ}\text{C}$ before entering a fuel cell. Hydrogen is stored in the adsorbent bed at high pressures (10-240 bar) and when hydrogen is released, a pressure reduction valve is used to reduce the pressure to between 5 and 20 bar. A heat exchanger is positioned after the pressure reduction valve to heat the hydrogen stream. For this project, JPL (Jet Propulsion Laboratory, Pasadena, California) was assigned to design such a heat exchanger. Fuel cell oil was to be used as the hot fluid. For desorption of hydrogen from the bed, significant amount of heat is not needed to desorb hydrogen and the needed power can be provided largely by the fuel cell coolant, exchange of heat with ambient air, or electrical heating. However, there were four conditions/scenarios, as identified by Savannah River national lab, under which a burner might be needed. These four options are briefly discussed below.

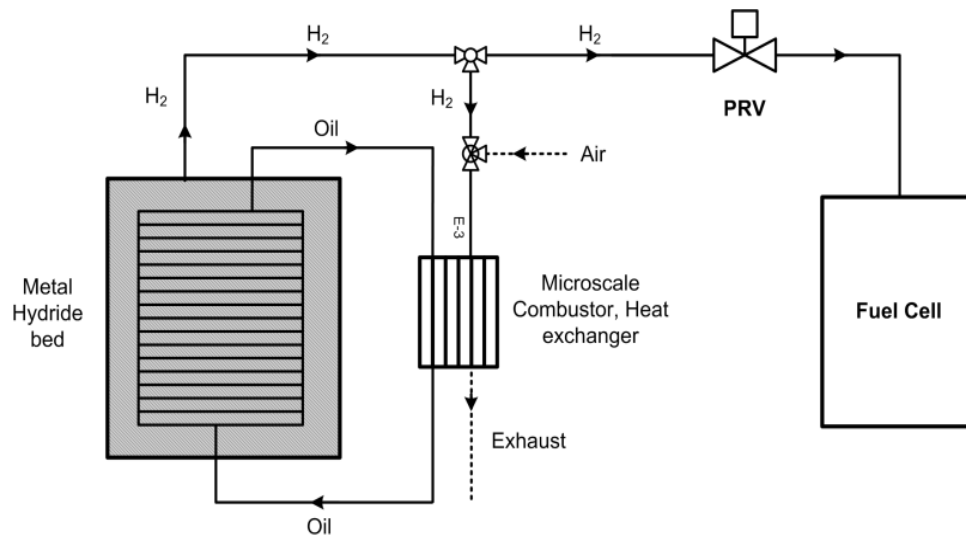


Figure 4: Schematic view of the μ CHX in a metal hydride storage system

Option 1) Pre-conditioning: The combustor is to be located directly downstream of the cryo-adsorbent tank and prior to the pressure reduction valve to preheat the H₂ stream and prevent condensation within the pressure reduction valve. Figure 5 and Table 1 provides details on the operating conditions of the pre-conditioning μ CHX.

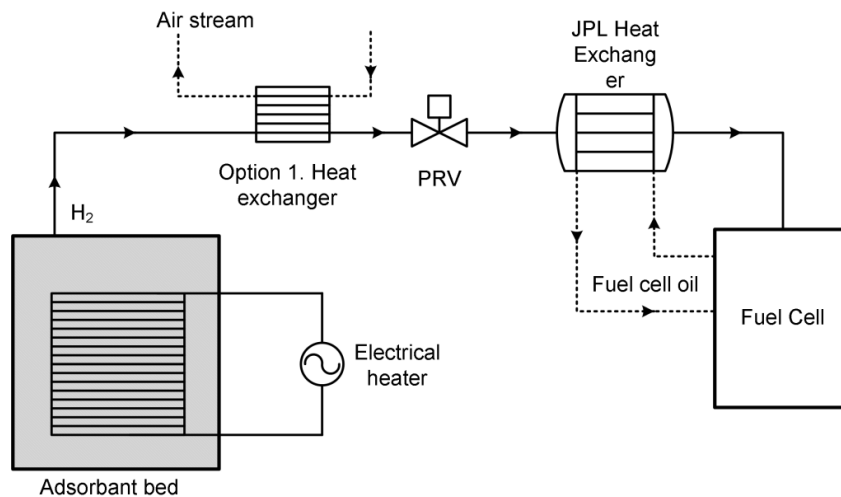


Figure 5: Schematic view of option 1 combustor-heat exchanger in the CA system

Table 1: Option 1 heat exchanger operating conditions

Pressure range	Inlet pressure of 10 bar to 240 bar; outlet pressure greater than or equal to 5 bar
Temperature range	Inlet temperature of -233 °C (40 K) to -133 °C (140 K)
Target Heating	increase temperature by a minimum of 40 degrees
Fluid flow rate	maximum 2 g/s

Upon a preliminary energy balance estimate, a burner was found to be unnecessary for this application because ambient air (even at its lowest temperature of -40 °C (233 K)) can provide enough heat to increase hydrogen temperature by the needed 40 °C.

Option 2) H_2 conditioning: For this option the combustor in combination with a fuel cell heat exchanger is to be located directly downstream of the pressure reduction valve to heat the H_2 stream to the acceptable fuel cell temperature ranges. Figure 6 and Table 4 provides details about option 2 heat exchanger placement and operating conditions.

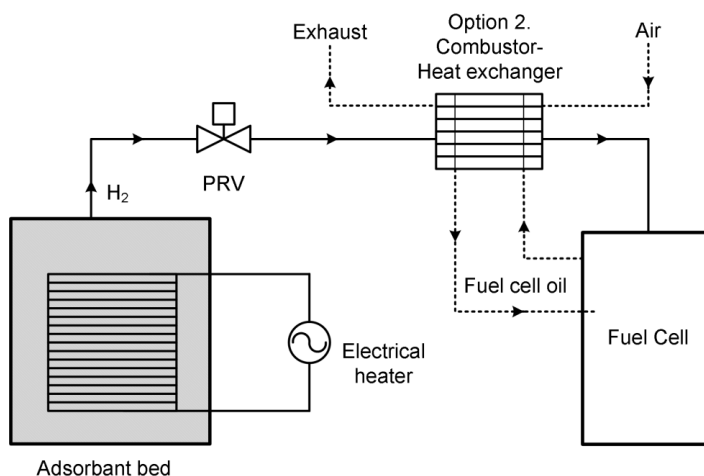


Figure 6: Schematic view of option 2 combustor-heat exchanger in the CA system

Table 2: Option 2 heat exchanger operating conditions

Pressure range	inlet pressure of 5 to 20 bar; outlet pressure greater than or equal to 5 bar
Temperature range	Inlet temperature of 35 K to 140 K
Target Heating	increase temperature to a minimum of -40 °C
Fluid flow rate	maximum 2 g/s

Option 3) In-tank heating system: For the in-tank heating system, the combustor is to be used to burn a fraction of the hydrogen from the tank in order to desorb the rest of the hydrogen from the cryo-adsorbent. The device would be located upstream of the pressure reducing valve and would utilize the fuel cell coolant heat in addition to burning hydrogen (Figure 7). Table 3 and Figure 7 provide details about option 3 heat exchanger placement and operating conditions.

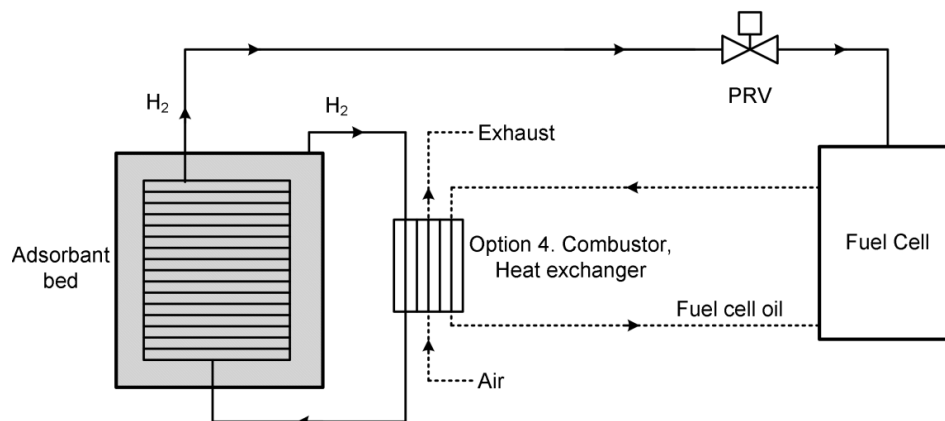


Figure 7: Schematic view of option 3 heat exchanger in the CA system

Table 3: Option 3 heat exchanger placement and operating conditions

Pressure range	Inlet pressure of 10 to 240 bar; outlet pressure greater than or equal to 5 bar
Temperature range	Inlet temperature of 35 K to 140 K
Target Heating	Provide up to 500 Watts of heat within the tank
Fluid flow rate	Maximum 2 g/s

Option 4) Secondary H_2 conditioning position for "cold-start": Under normal operating conditions, sufficient heat can be provided by the fuel cell oil to condition hydrogen from the cryo-adsorbent tank to a temperature greater than $-40\text{ }^\circ\text{C}$ (233 K). However, under the scenario of cold start condition (for example, on a cold winter day), a burner would be needed to provide additional heat to the hydrogen stream prior to the fuel cell. This burner would be located in between the heat exchanger and the fuel cell as shown in Figure 8. Table 4 provides details about option 4 combustor-heat exchanger placement and operating conditions.

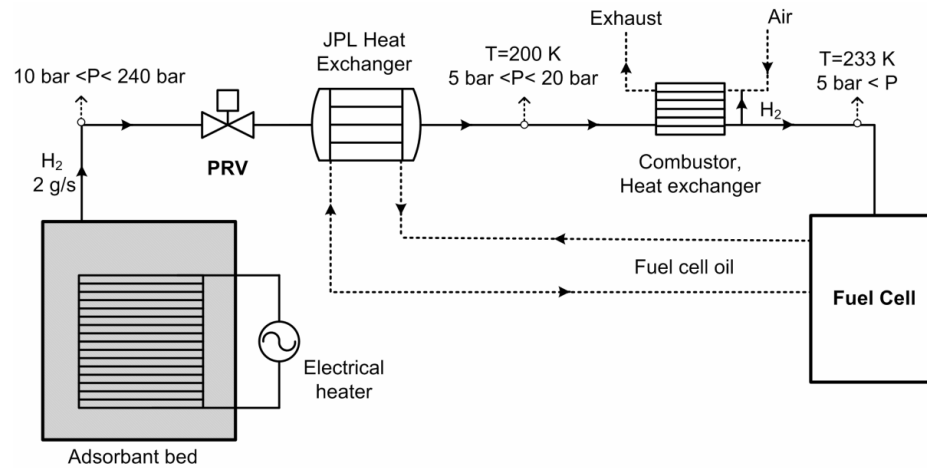


Figure 8: Schematic view of μ CHX in a cryo-adsorbent system

Table 4: Option 4 heat exchanger placement and operating conditions

Pressure range	Inlet pressure of 5 to 20 bar; outlet pressure greater than or equal to 5 bar
Temperature range	Inlet temperature of ~ 200 K
Target Heating	Increase temperature to a minimum of -40 °C
Fluid flow rate	Maximum 2 g/s

After investigating each of the above options, it was decided to design and characterize a μ CHX for option 4. Table 5 summarizes the desired operating conditions of a heating device for a metal hydride and a cryo-adsorbent hydrogen storage systems.

Table 5: Desired operating conditions for the μ CHX in a cryo-adsorbent storage system

Storage system	Heat Exchange fluid	$T_{HX,in}$ (°C)	$T_{HX,out}$ (°C)	$P_{H2,in}$ (bar)	\dot{m} (g/s)	$T_{c,in}$ (°C)	$P_{c,in}$ (bar)
Metal hydrides	Oil	160	180	2 - 3	1500	27	1
Cryo-adsorbent	Hydrogen	-73	-40	5 - 20	0.5 - 2	-40	1

Design, simulation and characterization of a compact and high efficiency combustor, recuperator and heat exchanger for metal hydride and cryo-adsorbent storage systems are presented in this dissertation.

2- LITERATURE REVIEW

This chapter provides a review of literature in two areas related to the work performed, catalytic combustion and microscale combustor and heat exchanger. To limit the scope of the literature review, the focus is on catalytic combustion of hydrogen.

2-1 Catalytic Reactions

The rate of a reaction like $A+B \rightarrow C+D$ is given by

$$rate = -\frac{dC_A}{dt} = -\frac{dC_B}{dt} = \frac{dC_C}{dt} = \frac{dC_D}{dt} = KC_A C_B \quad (1)$$

where C is the species concentration and K is reaction rate constant. Arrhenius equation is used to determine rate coefficient (K in Eq. (1)).

$$K = AT^\beta e^{-E_a/RT} \quad (2)$$

where A is pre-exponential factor, β is temperature exponent and E_a is activation energy. A , β and E_a are empirical numbers and several sets of data are available in the literature for different reactions. Reaction data in the literature are available for both homogeneous and heterogeneous reactions [10], [11]. Each global reaction usually consists of several steps and each step should be considered for calculating the rate of the global reaction.

In a heterogeneous reaction, a catalyst facilitates the reaction by decreasing the activation energy needed for reaction. In the reaction mechanisms of a heterogeneous reaction, surface sites and species are also included. A catalytic reaction happens in three stages. Adsorption, surface reaction and desorption. Molecules of fuel and oxidizer collide with the surface of the catalyst because of their Brownian motion. If the energy of this collision is sufficient, the bond between molecules split and atoms get adsorbed. Once different atoms from the molecules get adsorbed on the surface, they fuel and oxidizer atoms recombine and release energy. The new molecules or radicals get desorbed using a little of the generated thermal energy.

Noble metals are good choices for catalysts. Aryafar and Zaera [12] studied catalytic oxidation of five different alkanes (methane, ethane, propane, *n*-butane and isobutene) over nickel, palladium and platinum foils and showed that for all cases considered, oxidation occurs at temperatures lower than in homogeneous combustion. They also found that platinum was the most effective catalyst for oxidation of all fuels studied, with the exception of methane. One of the most approved reaction data for hydrogen oxidation on platinum is provided by Deutschmann et al. [13] and is presented in Table 6. When a mixture of hydrogen and air is considered for reaction, the same reaction scheme can be used since nitrogen does not participate in the catalytic reaction of hydrogen and oxygen, and nitrogen is treated as an inert gas in the scheme.

Although there are several mechanisms available in the literature, care should be taken while using a specific mechanisms in numerical studies. Reaction steps and reaction coefficients might be different in different studies. For example, Hellsing et al. [14] studied the kinetics of H_2-O_2 reaction on platinum numerically and experimentally. In their model, they considered two alternative routes for water formation and each of these routes had different activation energies.

Warnatz et al. [15] reported that hydrogen-oxygen combustion on platinum surfaces depends largely on literature values of surface reaction rates. They numerically studied catalytic combustion of lean hydrogen-oxygen mixtures in a stagnation flow over a platinum surface.

Table 6: Heterogeneous chemical reaction mechanisms of hydrogen on platinum [13]

Reaction	A	β	E_a (kJ/mol)	Sticking coefficient
1. $H_2 + 2Pt(s) \rightarrow 2H(s)$	-	0.0	0	0.046 /Pt(s) 1/
2. $2H(s) \rightarrow H_2 + 2Pt(s)$	3.7E+21	0.0	67.4-6.0H(s)	-
3. $O_2 + 2Pt(s) \rightarrow 2O(s)$	-	-1.0	0	21
4. $2O(s) \rightarrow O_2 + 2Pt(s)$	3.7E+21	0.0	213.2-60O(s)	-
5. $H + Pt(s) \rightarrow H(s)$	-	0.0	0	1
6. $O + Pt(s) \rightarrow O(s)$	-	0.0	0	1
7. $OH + Pt(s) \rightarrow OH(s)$	-	0.0	0	1
8. $H_2O + Pt(s) \rightarrow H_2O(s)$	-	0.0	0	0.75
9. $H(s) + O(s) \leftrightarrow OH(s) + Pt(s)$	3.7E+21	0.0	11.5	-
10. $H(s) + OH(s) \leftrightarrow H_2O(s) + Pt(s)$	3.7E+21	0.0	17.4	-
11. $H_2O(s) + O(s) \leftrightarrow OH(s) + OH(s)$	3.7E+21	0.0	48.2	-
12. $OH(s) \rightarrow OH + Pt(s)$	1.0E+13	0.0	192.8	-
13. $H_2O(s) \rightarrow H_2O + Pt(s)$	1.0E+13	0.0	40.3	-

For the adsorption of gaseous species sticking coefficients are specified. The sticking coefficient is the probability that adsorption takes place when a collision occurs. In order to convert a sticking coefficient (S) to the reaction rate coefficient, the following equation can be used [16].

$$K_{ads} = \frac{S}{1 - S/2} \frac{1}{\Gamma^\tau} \sqrt{\frac{RT}{2\pi M}} \quad (3)$$

where Γ is total surface site concentration (mol/cm²), τ is sum of surface reactants' stoichiometric coefficients, T is gas temperature (K), and M is molecular mass of the colliding molecule (kg/mol).

Both sticking coefficients and activation energy may be a function of surface coverage or species concentrations. Fridell et al. [17] studied OH desorption from platinum in H₂O-O₂/H₂ mixtures and determined that sticking coefficients of H₂O, oxygen and hydrogen depend on their concentrations. However, the dependency for water could be neglected. Reactions number 2 and 4 in Table 6 are examples of reactions with surface coverage dependency on rate coefficients. The modified version of Arrhenius correlation that considers the concentration of species and gives the reaction rate constant of the ith reaction is as follows [18].

$$K_i = A_i T^{\beta_i} \exp\left(\frac{-E_{ai}}{RT}\right) \prod_{m=1}^{N_s} 10^{\eta_{mi}[Z_m(n)]} [Z_m(n)]^{\mu_{mi}} \exp\left(\frac{-\varepsilon_{mi}[Z_m(n)]}{RT}\right) \quad (4)$$

where η , μ and ε are empirical values and are presented in the literature. $Z_m(n)$ is the surface coverage of mth species on nth site (in case of only one catalyst site, n=1). To show the surface coverage dependency, the activation energy in Eq. (4) can be written as

$$E_a = E_{ai} + \sum_{m=1}^{N_s} \varepsilon_{mi} [Z_m(n)] \quad (5)$$

2-2 Reaction in Microchannels

Advances in microfabrication techniques have opened doors to innovations and design of microscale devices. Although there are some limitations, these devices have significant abilities and advantages compared to their macroscale counterparts. The microfabrication techniques and

advancements in combustion mechanisms have provided new opportunities for scientists in the field of meso and microscale combustion and power generation.

A possible use for micro power generation based on combustion is as a portable power source for electronic devices or devices that require heat for part of their operation. There are also several applications for microscale heat production, such as in Stirling engines and hydrogen storage technologies. In the present research, combustion of hydrogen in microchannels was investigated to provide the required heat for the hydrogen storage systems describe before. Although the continuum governing equations for heat and fluid flow are applicable in microscale devices with channel dimensions in the hundreds of micrometers, the reduced size results in some differences. For example, as the characteristic length of the device is decreased the Reynolds number will decrease, resulting in negligible turbulent effects in most cases.

Although the concepts of combustion in micro and macroscale are the same, there are differences caused by sizing effects that distinguish the combustion at the microscale. A certain amount of time is required for completion of a reaction; this is called chemical (reaction) time. If the time period that the fuel mixture is in the combustion chamber (residence time) is less than the chemical time, complete combustion will not take place. The residence time is determined by the velocity of the fuel mixture and the length of the chamber. In a catalytic combustion, when the cross-sectional area of combustion channels decreases, the time that a molecule requires to reach the catalytic surface via lateral diffusion (diffusion time) reduces significantly. These time scales and their interplay in reacting microchannel flows are described in more detail in section 4-2.

Another size effect is quenching, which can happen in very small combustion chambers. Heat loss through the walls, high velocities (advection heat losses) and radical quenching can cause flame extinction [19]. Ronney [20] used a dimensionless mass flux parameter, $\Pi = \dot{m} C_p / hL$ and compared flame extinction in different conditions based on this number. He investigated the extinction limits on a homogeneous heat recirculating burner with a length L and heat transfer coefficient, h . He found that extinction is possible for both high and low Π values. Extinction in higher Π is because of the shorter residence times whereas in low Π , high heat transfer coefficient causes higher heat losses and thus thermal quenching.

Boyarko et al. [21] characterized hydrogen-oxygen mixture combustion in a platinum microtube and found that the 400 μm and 800 μm tubes used in their experiments were below quenching size under most atmospheric pressure test conditions. In both numerical simulations as well as experiments, they observed that there was a minimum threshold heat flux necessary for ignition. When the ignition heat flux was increased further, the gas temperature got so high that a choked flow resulted inside the tube.

Generally speaking, most of the numerical and experimental studies available in the literature have focused on the steady state combustion in microcombustors while a few studies investigated the transient behavior and ignition process. The ignition temperature for the heterogeneous reaction is much lower than that for homogeneous reactions because the catalyst reduces the activation energy. In the following sections, some of the studies that investigated the effects of different parameters on catalytic combustion are reviewed.

2-2-1 The effect of inlet velocity (residence time effects)

Stefanidis et al. [22] investigated several issues related to catalytic ignition of lean propane-air mixtures flowing over platinum coated walls inside a 300 μm channel. They considered two modes for ignition: inlet preheating and resistive heating (electrical heaters). Chemkin subroutines were used for thermodynamic and transport properties in their 2D numerical model. The ignition point was defined as the point where temperature of the combustion channel increased dramatically. Figure 9 shows their results for adiabatic wall and different inlet velocities. It shows that increasing the inlet velocity requires a higher inlet temperature in order to ignite the mixture.

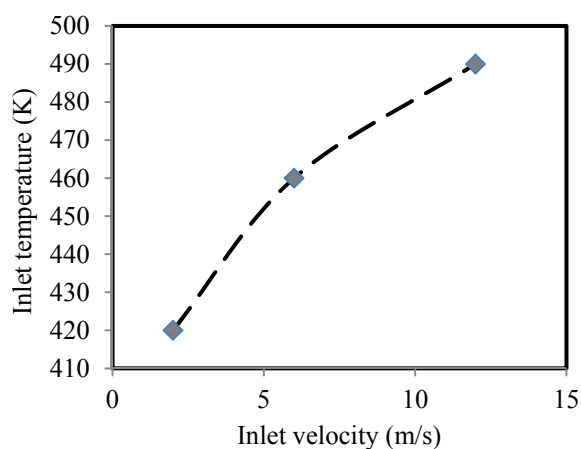


Figure 9: Inlet preheat temperatures required for different inlet velocities (adapted from [22])

Chen et al. [23] used a commercial code, CFD-ACE coupled with Chemkin, to model reaction of hydrogen and air on a simple 1 mm diameter tube with platinum covered walls. Heat loss to the environment was considered by both convection and radiation. The channel wall was assumed to be thermally thin. The authors compared three different reaction modes for hydrogen: both

homogeneous and heterogeneous, homogeneous-alone and heterogeneous-alone mechanisms. They tried to capture the effects of different reaction modes on each other while investigating parameters like inlet velocity, tube diameter and wall conductivity. Figure 10 (a) shows the effect of inlet velocity on temperature distribution along the channel. Combustion started heterogeneously and when the bulk temperature was sufficiently high, homogeneous reaction occurred. The slope of temperature graph is greater for homogeneous reaction due to the higher rate of reaction. It was seen that increasing the inlet velocity (reducing the residence time) shifted the onset of the homogeneous reaction downstream and for the case of 12 m/s no homogeneous reaction occurred. Moreover, based on their simulations for different tube diameters and inlet velocities, the authors divided the interaction between heterogeneous and homogeneous reaction into three types. As can be seen from Figure 10 (b), in type I with low inlet velocity and higher tube diameters, homogeneous reaction is the dominant reaction mode. However, when the inlet velocity is increased, heterogeneous combustion dominated (type II and III).

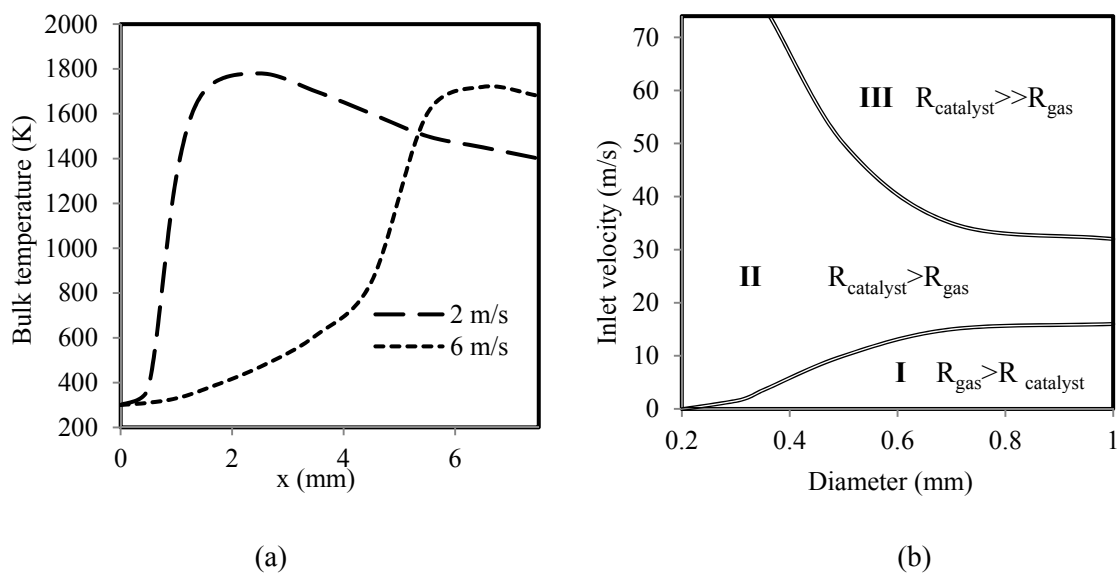


Figure 10: (a) Temperature distribution along the channel for different inlet velocities, and (b) Homogeneous and heterogeneous reaction in three different regions [23]

2-2-2 The effect of wall conductivity

Kaisare et al. [24] performed a transient numerical study for different wall thermal conductivities for catalytic reaction of propane. The thickness of the walls was 1 mm with the channel height of 300 μm . They found that higher wall thermal conductivities required higher inlet temperatures for ignition, with the reason being that higher thermal conductivities had greater heat loss to the environment. They showed that ignition time increased with an increase in the wall conductivity. Temperature profiles are shown in Figure 11 for different wall conductivities. In Reaction started (Figure 11 (a)), at 280 seconds at the end of the channel and crept upstream and stopped near the front-end of the channel. It should be noted that after reaction was started, inlet preheating was turned off. When the wall conductivity was 200 W/m-K, the reaction started much later and at 940 seconds. Higher heat loss was described by the authors as the reason for the delay in ignition.

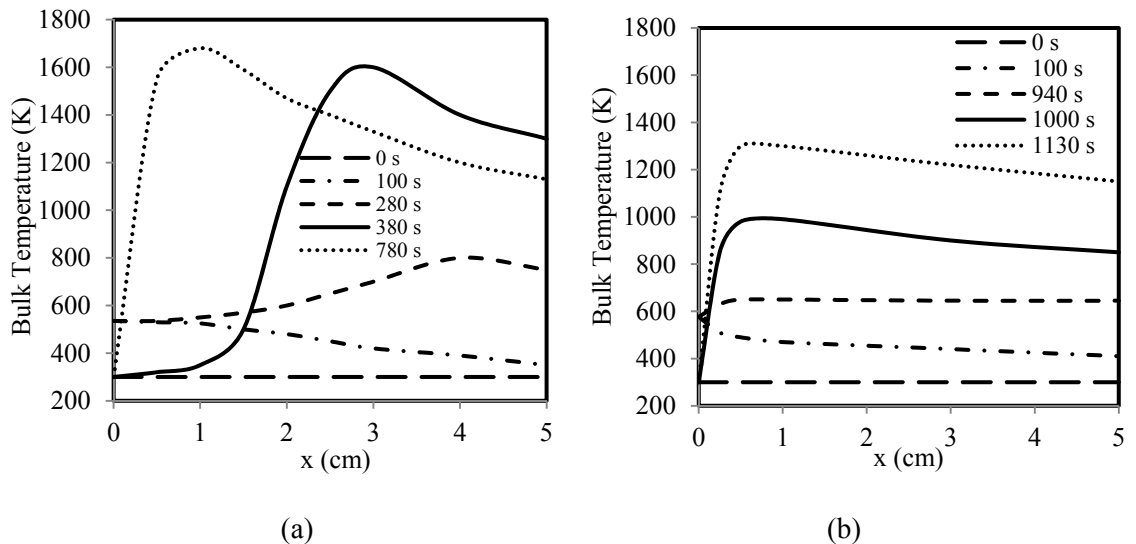


Figure 11: Bulk temperature as a function of axial distance for (a) $k=2$ W/m-K, (b) $k=200$ W/m-K [24]

Zhou et al. [25] modeled conjugate heat transfer within a 500 μm channel made of different wall materials (quartz glass, alumina ceramic, copper) to investigate the effect of wall thermal conductivity on homogeneous/heterogeneous combustion of hydrogen-air mixture. They observed that heterogeneous reaction became dominant as thermal conductivity of the material was increased. Chen et al. [23], who simulated combustion in a 1-mm channel with different wall materials, reached a similar conclusion. They found that heterogeneous reaction was dominant in the beginning of the tube, followed by homogeneous reaction downstream of the tube. Lower wall conductivity was observed to lead to a larger temperature gradient on the surface causing homogeneous combustion to shift upstream. At the highest studied velocity (20 m/s), no homogeneous reaction was observed in channel heights lower than 200 μm in diameter.

2-2-3 The effect of operating pressure

Another important parameter in the study of combustion is the pressure under which the reactions occur. Usually pressures up to about 5 bar are appropriate for portable power generation, however small gas turbines operate at higher pressures [26]. Several authors have investigated combustion at different pressures. Mantzaras et al. [26] investigated the effect of pressure on heterogeneous and homogeneous combustion of hydrogen over platinum both experimentally and numerically. They studied two different equivalence ratios of 0.28 and 0.32 at two Reynolds numbers (Re) in the laminar region (Re=1000 and 2000). The authors showed that the conversion rate is lower at higher pressures and thus increasing the pressure has a negative impact on the combustion. They attributed the reason to the competition of the chain branching step $\text{H} + \text{O}_2 \rightarrow \text{O} + \text{OH}$ and the chain terminating step $\text{H} + \text{O}_2 + \text{M} \rightarrow \text{HO}_2 + \text{M}$, where M is a third body (other molecules, surface of the wall). Based on their rate computations, they indicated that for pressures above 2 bars, the

terminating step overtakes the branching step. In addition, they mentioned that homogeneous combustion was largely suppressed at pressures higher than 4 bar. On the other hand, Karagiannidis and Mantzaras [27] used a 2D model to simulate transient hetero-homogeneous combustion of methane over platinum catalyst within a 1 mm channel. They found higher pressure increased the reaction rate and reduced the ignition time, for the pressures in the range of 1 bar – 5 bar.

2-2-4 Effect of reactant mixture temperature

Zhang et al. [28] synthesized a Pt-based catalyst, and investigated the behavior of hydrogen catalytic combustion at low temperatures of the hydrogen/dry air mixture. They found that for low temperature catalytic combustion of hydrogen, the initial reaction temperature, H₂ concentration, and flow rates were very important parameters. They tried hydrogen combustion at mixture temperatures of 298 K and 263 K and their results show that higher H₂ concentration was helpful in initiating and sustaining catalytic combustion. For the 263 K combustion, the authors could not achieve conversions higher than 40% for low hydrogen concentrations and although they could start the catalytic combustion, they described the largest challenge to be avoiding product water from freezing.

2-2-5 Catalyst segmentation

Bendetto et al. [29] tried to reach higher conversion ratios by dividing the combustion channel into two parts. They used Fluent to model a 2D geometry with simplified heterogeneous and

homogeneous reaction models for propane flowing inside a 600 μm . The first 1 cm of the channel walls were covered by platinum and the reaction starts heterogeneously. The heat provided by the surface reaction caused homogeneous reaction to occur. The heat produced in the first part was transferred by the wall conduction and axial convection. In addition, the authors mentioned that walls with higher thermal conductivity provide better heat transfer along the length of the channel, resulting in less limitation for inlet velocity.

Chen et al. [30] addressed the combustion characteristics of multi-segment catalysts. In their study, multi-segment catalyst was compared to one segment catalyst with the same total length and was shown that the former arrangement exhibited better conversion. They mentioned that the space between catalyst segments enhances homogeneous reaction by keeping the wall temperature at a high level for a longer distance.

2-2-6 Recuperation

The concept of using recuperation in order to preheat the combustion gas mixture has been studied by several groups [31]. Recuperation is using some of the excess heat that usually exists in the exhaust gases to preheat the reactant stream and which can be performed using counter flow channels. Ronney [20] investigated heat-recirculating “excess enthalpy” microscale burners. His model consisted of two parallel reactant and product channels (counter flow heat exchanger) with a well-stirred reactor at the end of the reactants channel. The products of the reaction in the reactor then flows in the product channel counter to the reactants. He solved simplified transport and chemistry models analytically and showed that wall conduction and heat losses can have significant effects on quenching and temperature profiles. Lloyd and Weinberg [32] fabricated a

spiral counterflow combustor, often referred to as a “Swiss roll” type combustor to improve the efficiency of combustion processes. Peterson et al. [33] developed a microscale hydrogen combustor with counterflow heat recuperator. They observed that preheating provided by recuperation helped to sustain homogeneous reaction.

Ahn et al. [34] performed experiments on spiral counterflow “Swiss roll” combustors with propane as the fuel and platinum as the catalyst. A schematic view of their design is shown in Figure 12 (a). The channel width and length were 3.5 mm and 70 mm, respectively. They studied extinction limits as functions of equivalence ratio and Reynolds number and developed a map based on these two numbers. They concluded that Re effects dominate combustor performance in a way that for sufficiently low Re numbers neither homogeneous nor heterogeneous reactions occurred. Furthermore, at higher Re numbers the homogeneous reaction dominated because of the limited surface area available for catalyst. Moreover, the authors observed some instabilities and flame propagation toward the inlet at conditions under which the combustion was self-sustaining. Figure 12 (b) shows the reaction rate along the channel center for different lean mixtures which were presented by Kuo and Ronney [35]. This figure illustrates how combustion shifts to the inlet. They performed a 2D numerical simulation for the geometry and conditions of Ahn et al. [34] and compared their results.

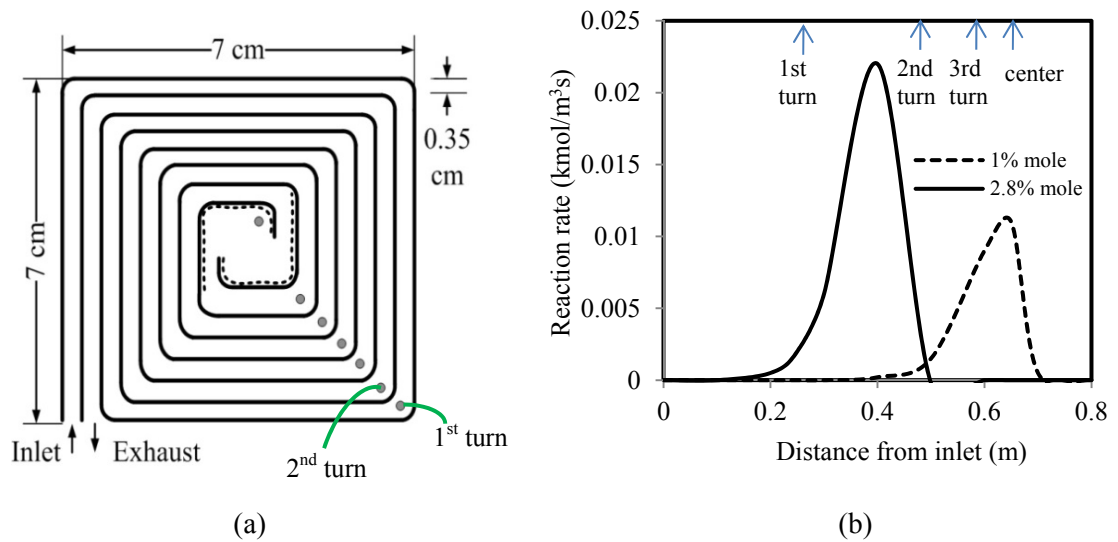


Figure 12: a) Schematic view of the Swiss roll combustor [34] b) Reaction rate along the channel center for $Re=500$ and different fuel concentration [35]

2-2-7 Integrated combustor and heat exchanger

The heat transfer from the combustion process to the working fluid will alter the wall temperature distribution, which will in turn affect the combustion process [25]. Janicke et al. [36] used hydrogen combustion over a platinum covered surface to heat a nitrogen stream in cross-flow to the combustion gas flow in a microscale heat exchanger. The combustor channel dimensions were $140\ \mu\text{m}$ to $200\ \mu\text{m}$. Their goal was to show a 2 to 1 volumetric ratio of air and hydrogen can be reacted safely and without an explosion when enough heat is removed from the combustor. They also studied the transient temperature of the combustor/heat exchanger at different flow conditions. For a similar application, Ryi et al. [37] were able to achieve almost 100% hydrogen conversion while using hydrogen-air reaction in the presence of a catalyst to provide heat to a microscale steam methane reforming system.

Johnson and Kanouff [38] designed and tested a 30 kilowatt hydrogen combustor/heat exchanger to heat oil in the context of providing energy for desorption of hydrogen from a metal hydride bed. Their design consisted of two coupled finned plate heat exchangers. The first plate heat exchanger housed the catalytic reactor and oil heat exchange channels. Heat from catalytic combustion was transferred directly to the oil. In the second plate heat exchanger, the exhaust combustion gases from the reactor transferred heat to the incoming combustion gases, thereby recuperating waste heat. Large gas channel dimensions (of 4.8 mm sides) and low hydrogen inlet concentration (10%) were chosen to avoid high temperatures within the reactor and oil channels. They were able to achieve total efficiencies and hydrogen conversions of about 75% and 98%, respectively.

2-3 Stacked up Microchannels

Several microchannels can be numbered up in parallel in order to meet the thermal power requirement of the desired application. These parallel microchannels are linked together by inlet and outlet headers that distribute the flow uniformly amongst the microchannels. When only one working fluid is involved, a single layer (sheet) of parallel microchannels could be sufficient, as in the case of a heat sink or simple chemical reactors. However, for heat or mass exchangers and more complex chemical reactors, a stacked up, multi-layer parallel microchannel architecture is needed. In the design of such microchannel devices, it is sufficient to characterize the performance of a single microchannel “unit cell” (for example, two microchannels separated by a non-permeable wall if the device is a heat exchanger) and to ensure that the flow distribution between the microchannel unit cells and between the stacked layers is uniform. Typically, the unit cells and headers are also designed with pressure drop constraints in mind.

There have been several studies involving stacked microchannel arrays for various applications. The review articles by Fan and Luo [39] and Khan and Fartaj [40] provide some of the recent examples of stacked microchannel devices including heat exchangers and chemical reactors. In stacked microscale reactors, one layer could have several parallel microchannels wherein a reaction occurs while exchanging heat with a working fluid that flows in an adjacent layer. Such an arrangement has been used for methane steam reforming where a fuel combusts in the combustor layers and transfers the produced heat to the reformer sheets [37], [41], [42], [43], [44]. Ryi et al. [37] tested methane steam reforming with hydrogen catalytic combustion in an integrated microchannel reactor. The designed device consisted of cover plate, a base plate and 50 plates (25 alternating combustor and reformer plates) with microchannels. Inconel plates were used to fabricate the microchannel sheets and stainless steel sheets were used for the cover and base plates. Each sheet had 22 microchannels in parallel with 500 μm in diameter, 250 μm in depth and 17mm in length. Pt–Sn/Al₂O₃ and Rh–Mg/Al₂O₃ were impregnated by wash-coating in the combustor and reformer for catalytic reactions respectively. Hwang et al. [41] developed a similar combined combustor and methane reformer device and were able to achieve 95% conversions and hydrogen production rate of 0.78 mol/h in the reformer. Their device consisted of a variety of chemically etched metal plates, such as half-etched straight channel plates (10 sheets), fully etched 3D mixing channel plates (2 sheets), and cover/holder/separator plates (5 sheets). Hydrogen and/or methane were used as the fuel in the combustor sheets to provide heat for methane reformation. A Pt-coated mesh catalyst was used as an igniter at the inlet of the combustor until a flame was generated.

Mettler et al. [42] used CFD simulations to model stacks of different sizes and characterize the effects of scaling up of microchemical systems. They studied syngas production from methane using a parallel-plate reactor with alternating combustion and steam reforming channels. The author compared stacks of 3 units to 15 units, each comprised of a combustor channel and reformer channel. They found that heat losses caused extinction of combustion in the outer channels and consequently reduced the efficiency of the smaller stack. Whereas extinction of combustion occurred in the outer channels even for the larger stack, the interior channels sustained combustion, resulting in a higher efficiency. They also recommended stack materials with thermal conductivities higher than 100 W/m-K for a more stable device.

3- OBJECTIVES

In order to meet the Department of Energy's gravimetric and volumetric targets for automotive hydrogen storage [45], it is necessary to have a high efficiency and compact (low weight and volume) combustor. It is in this context that this thesis presents the design and performance of a novel μ CHX design. The development of this μ CHX is motivated by application to metal hydrides (MH) and cryo-adsorbent (CA) storage systems. A hydrogen-air mixture is reacted heterogeneously and the heat is transferred to a working fluid. The objective is to design and characterize the performance of the MH and CA μ CHX.

The working fluid in the heat exchange channels for the metal hydride μ CHX (MH μ CHX) is an oil (Paratherm $\text{\textcircled{R}}$ MG) at $T_{in} = 160 \text{ }^\circ\text{C}$ while the working fluid for the cryo-adsorbent μ CHX (CA μ CHX) is cold hydrogen at $T_{in} = -73 \text{ }^\circ\text{C}$ (200K). Table 5 in chapter 1 summarizes the desired operating conditions of the μ CHX for the both storage systems. However the parameter space was varied over a larger range to obtain trends in both simulations and experiments.

A μ CHX for either metal hydrides or cryo-adsorbent applications would consist of several repeating unit cells. Each unit cell would generate and transfer a certain amount of heat to the working fluid. By having multiple of these unit cells in parallel, the desired total heating power can be achieved. For example, a μ CHX shown in Figure 13 is a 200 W device that consists of several internal units. The smallest unit that performs the desired operation of combustion, recuperation and heat exchange is called a unit cell. A cross section of the device is shown in Figure 13 for better understanding the concept.

The design process consisted of characterizing the performance of each unit cell for both the MH μ CHX and CA μ CHX. Computational fluid dynamics (CFD) simulations were performed using Fluent with multiple step reaction by coupling with Chemkin.

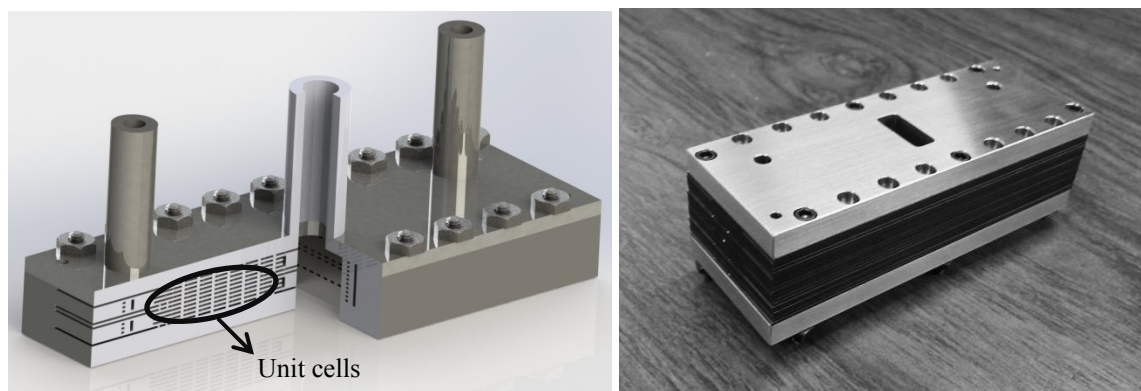


Figure 13: A multi-Watt μ CHX consisting of several internal units

At the unit cell level, effects of variation of different geometrical and thermo-fluidic parameters are investigated. The varied geometrical parameters include location and length of the catalyst, and the combustion channel length and height. Varied thermo-fluidic parameters include heat exchanger fluid's inlet velocity and temperature, equivalence ratio, and flow rate of the reactants. The parametric study is then used to find operating conditions with the highest efficiency, given realistic constraints. A constraint was placed on the exhaust exit temperature to be greater than 373 K in order to avoid condensation within the exhaust channels. Also, for the MH μ CHX, the oil temperature was constrained remain below the maximum film temperature of 590 K. The varied parameters are presented in the context of different time scales and dimensionless numbers to provide for a better understanding of reaction and heat transfer mechanisms, and to identify the parameter space for high efficiency and low pressure drop (in combustion channel) operation of

the μ CHX. The same design concept as MH μ CHX is used to simulate for different flow rates and pressures (5 bar to 20 bar) for the CA μ CHX.

The device level design is then undertaken to ensure uniform flow distribution through each unit cell. Experiments are performed only on the CA μ CHX. A 100 W multiple unit cell μ CHX is fabricated and tested. Nitrogen is used as the heat exchange fluid for the experiments for safety issues.

4- UNIT CELL DESIGN AND SIMULATIONS

As mentioned in the objectives section, the purpose of the μ CHX discussed in this work is to provide thermal energy to either an oil for desorption of hydrogen from a metal hydride storage system or a hydrogen stream prior to a fuel cell in a cryo-adsorbent bed storage system. This purpose can be achieved by multiple unit cells connected in parallel with appropriate headers. Each unit cell would perform the task of producing and transferring heat from reacted gases to the working fluid. Since the design concepts are the same for the two applications of the μ CHX, in order to avoid repetition, the rest of this section only considers oil as the working fluid. First, the MH μ CHX design for unit cell is provided in section 4-1 along with details of the simulation method. Governing equations and model validation are also presented. Sections 4-1 to 4-4 are common for both MH μ CHX and CA μ CHX. In Section 4-5, the parametric study of the MH μ CHX is presented while in section 4-6, the CA μ CHX design and simulation results are presented.

4-1 Method and Model Development

4-1-1 MH μ CHX design

The thermal energy rate from each unit cell would add up depending on the number of unit cells to meet the several kilowatt range needed for the application. One unit cell geometry that would perform the task of reaction and heat exchange could consist of a rectangular combustor channel that is surrounded by oil channels (Figure 14). However, simulations of such geometry showed that the oil temperature significantly exceeds its maximum operating temperature. Therefore, there was need for a thermal buffer between the combustion and oil channels.

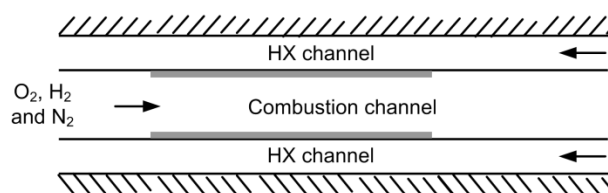


Figure 14: Schematic of a simple combustor and heat exchanger

One method of providing this buffer could be having larger combustion channels that spread the heat over a larger area. That will not be a good solution in this study because homogeneous combustion is more probable in channels with larger cross sectional area (which is not desired), and also higher channel dimensions would increase the diffusion time and hence decrease the conversion ratio for the same velocity and inlet mixture composition. An innovative arrangement would be to have the exhaust channels integrated within a single unit cell. The exhaust gas channel could then act as a thermal buffer between the combustion and oil channels, as shown schematically by Geometry (a) in Fig. 15. Oil and exhaust exit temperatures from simulations performed on such geometry are shown in Fig. 15 and indicate that the exhaust gas exit temperature is significantly high, which translates to wasted sensible thermal energy. A recent study by Johnson and Kanouff [38] with such a configuration of combustion and heat exchanger showed that a significant portion of the produced heat (19%) is lost to the exhaust gases. In order to recover that energy, they designed a separate recuperator heat exchanger. A possible modification to this design presented in Figure 15 (a) would be to extend the length of the exhaust gas and combustor channels so that thermal recuperation can occur between the exhaust gases and incoming reactant gases. Such geometry is shown as geometry (b) in Fig. 15 and simulations indicate that the exhaust gas temperature is lowered by 168 K compared with geometry (a). In addition to a reduction in lost sensible thermal energy, recuperation increases reactant gas temperature entering the catalyst bed, which results in higher rates of reactions thereby leading to

larger hydrogen conversion for a given length of catalyst bed. Consequently, geometry (b) was chosen as the design for the MH μ CHX.

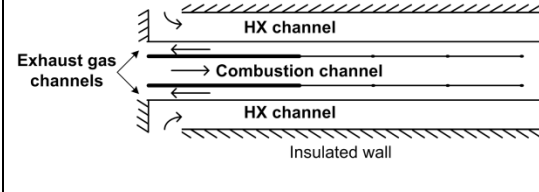
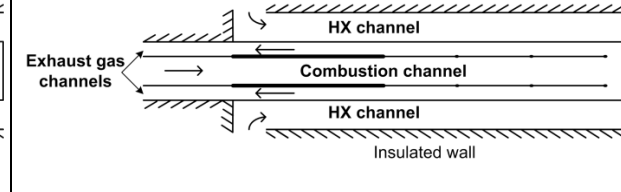
Geometry (a)		Geometry (b)	
			
Parameters		Parameters	
$T_{out, oil}$ (K)	$T_{out, exhaust}$ (K)	$T_{out, oil}$ (K)	$T_{out, exhaust}$ (K)
513.8	556.1	529.6	387.7

Figure 15: Schematics of the two different geometry configurations

Figure 16 shows a schematic view of the MH μ CHX unit cell geometry for CFD simulations. The modeled device geometry consists of a central combustor channel surrounded by two exhaust and two oil channels. All outer walls are insulated and the inside walls of the combustor are partially covered with platinum catalyst to varying lengths. The fixed geometrical parameters are H_O at 300 μm and H_R at 150 μm . The combustor channel height is varied between 300 μm and 700 μm .

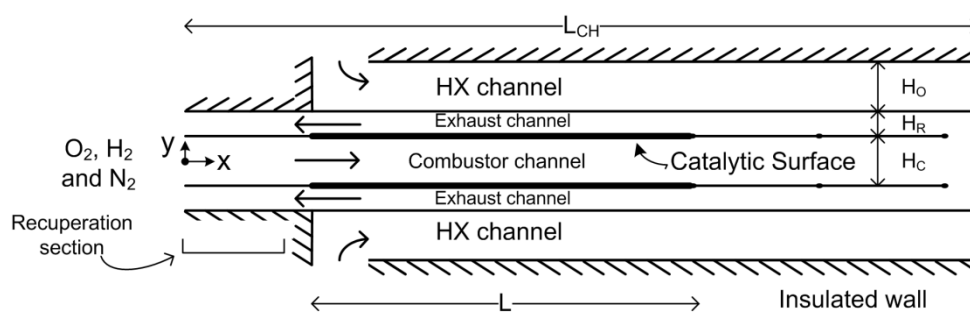


Figure 16: Schematic of the microscale integrated combustor recuperator heat exchanger

Simulations with four different locations of catalyst along the length of the combustion channel showed that the exhaust temperature is higher than 373 K only when the catalyst is located close to the beginning of the channel. Therefore, although systems with catalyst located close to the end of the channel produce higher efficiencies, the catalyst bed location was chosen to be at 5 mm downstream of the inlet for the results presented in this thesis.

4-1-2 Simulation method

In this work, FLUENT V12 and V14 were used in conjunction with Chemkin-CFD for reaction mechanism calculations. The mechanism files were imported into the two dimensional CFD code. A non-uniform mesh was used to refine the near-wall regions. The total number of grids was 30700 for the whole model domain. An orthogonal staggered non-uniform grid of 606×20 grid points (in x and y, combustion channel) was sufficient to produce a grid independent solution. Adaptive Mesh Refinement (AMR) was also applied in several locations on the gradients of mass imbalance for better convergence. The simulation convergence was decided when the residuals approaches steady values asymptotically and when the relative residuals were smaller than 10^{-3} in all cases and less than 10^{-7} for continuity, momentum, energy and major species.

4-2 Governing Equations

Two-dimensional, steady-state simulations were carried out on the mass, momentum and energy balance equations as well as the species balance equations for each of the gas-phase and surface species using ANSYS FLUENT. A flat profile was assumed for the heat exchanger fluid (HX) and gas inlet velocities and the inlet gases are regarded as well mixed. No slip boundary

conditions at all channel walls were assumed. The combustor exit was assumed to be at atmospheric pressure. The governing equations described in this section are common for both MH μ CHX and CA μ CHX.

Because of the large temperature variation within the device, all property estimates are temperature dependent and gas mixture properties were found by a mass fraction weighted average of species properties. Paratherm MR, a synthetic organic-based oil, was considered for the MH μ CHX because of the appropriate working temperature range for the desorption application in a metal hydride system. Details of different physical properties of the oil are available from the manufacturer [46] and are presented in Appendix A. Hydrogen was used as the working fluid for the CA μ CHX.

The overall mass conservation equation for HX and combustor channels, assuming steady state, two-dimensional flow is given as

$$\frac{\partial(\rho u)}{\partial x} + \frac{\partial(\rho v)}{\partial y} = 0 \quad (6)$$

The momentum equation for combustor and oil channel flows, assuming Newtonian fluids and negligible body forces is given as

$$\frac{\partial(\rho uu)}{\partial x} + \frac{\partial(\rho uv)}{\partial y} + \frac{\partial P}{\partial x} - \frac{\partial}{\partial y} \left[\mu \left(\frac{\partial u}{\partial y} + \frac{\partial v}{\partial x} \right) \right] - \frac{\partial}{\partial x} \left[2\mu \frac{\partial u}{\partial x} - \frac{2}{3} \mu \left(\frac{\partial u}{\partial x} + \frac{\partial v}{\partial y} \right) \right] = 0 \quad (7)$$

$$\frac{\partial(\rho w)}{\partial x} + \frac{\partial(\rho v)}{\partial y} + \frac{\partial P}{\partial y} - \frac{\partial}{\partial x} \left[\mu \left(\frac{\partial u}{\partial y} + \frac{\partial v}{\partial x} \right) \right] - \frac{\partial}{\partial y} \left[2\mu \frac{\partial v}{\partial y} - \frac{2}{3} \mu \left(\frac{\partial u}{\partial x} + \frac{\partial v}{\partial y} \right) \right] = 0 \quad (8)$$

Species balance equations are used for each gas phase reactant and product,

$$\frac{\partial(\rho u Y_g)}{\partial x} + \frac{\partial(\rho v Y_g)}{\partial y} + \frac{\partial}{\partial x} (\rho Y_g V_{g,x}) + \frac{\partial}{\partial y} (\rho Y_g V_{g,y}) - \dot{\omega}_g M_g = 0, \quad g = 1, \dots, N_g \quad (9)$$

where \bar{V}_g is the diffusion velocity of species g that accounts for both ordinary and thermal diffusion,

$$\bar{V}_g = -D_{gm} \nabla \left[\ln \left(\frac{Y_g \bar{M}}{M_g} \right) \right] + \left[\frac{D_g^T M_g}{\rho Y_g \bar{M}} \right] \nabla (\ln T) \quad (10)$$

where D_g^T thermal diffusion of g species into the mixture and D_{gm} is the mixture average species diffusion coefficient and is calculated using the binary diffusion of gas species.

$$D_{gm} = \frac{1 - Y_g}{\sum_{j=1, \neq g}^{N_g} X_j / D_{jg}} \quad (11)$$

Where D_{jg} is the binary diffusion of j in species g . The source term for species production or disappearance from homogeneous reactions, $\dot{\omega}_g$, was set to zero to model heterogeneous

combustion alone. For the range of combustor heights considered, Norton et al [47] have reported only heterogeneous combustion. Furthermore, experiments carried out by Haley and Narayanan [48] have also confirmed that only heterogeneous combustion occurs for H_C of 250 micrometers. The surface species coverage equation is given as

$$\sigma_m \frac{\dot{S}_m}{\Gamma} = 0, \quad m = 1, \dots, N_s \quad (12)$$

where \dot{S}_m represents the molar production rate of the m^{th} species. σ_m is the m^{th} surface species site occupancy and Γ is the surface site density. The energy equation used for the combustion and exhaust channel flows is provided below

$$\frac{\partial(\rho u h)}{\partial x} + \frac{\partial(\rho v h)}{\partial y} + \frac{\partial}{\partial x} \left(\rho \sum_{g=1}^{N_g} Y_g h_g V_{g,x} - k \frac{\partial T}{\partial x} \right) + \frac{\partial}{\partial y} \left(\rho \sum_{g=1}^{N_g} Y_g h_g V_{g,y} - k \frac{\partial T}{\partial y} \right) = 0 \quad (13)$$

The first terms in the terms within parentheses in Eq. (13) represent the species inter-diffusion contributions to energy transport. The enthalpy of each species, h_g , is based on the enthalpy of formation, h_g^o and calculated as

$$h_g = h_g^o(T_0) + \int_{T_0}^T C_{p_g} dT \quad (14)$$

The boundary condition for the species balance equation (Eq. (9)) at the catalytic wall is given as

$$\left(\rho Y_g V_g\right)_{wall} + \dot{s}_g M_g = 0 \quad (15)$$

A 1D energy balance gives the following boundary condition at the wall between combustor and exhaust channels which is covered with catalyst

$$-k_C \frac{\partial T}{\partial y} \Big|_{y=H_C/2} + \sum_{g=1}^{N_g} \left(\dot{s}_g h_g M_g \right) = -k_E \frac{\partial T}{\partial y} \Big|_{y=H_C/2} \quad (16)$$

For the regions in the absence of the catalyst, the boundary condition for energy equation simplifies to

$$-k_C \frac{\partial T}{\partial y} \Big|_{y=H_C/2} = -k_E \frac{\partial T}{\partial y} \Big|_{y=H_C/2} \quad (17)$$

The energy equation for the HX channels is simplified form of Eq. (13) for a single species. A similar boundary condition as in Eq. (17) can be written for exhaust-HX channel wall

$$-k_E \frac{\partial T}{\partial y} \Big|_{y=H_E+H_C/2} = -k_{HX} \frac{\partial T}{\partial y} \Big|_{y=H_E+H_C/2} \quad (18)$$

To calculate the molar production rate of each species, the following relation was used

$$\dot{s}_i = \sum_{r=1}^{N_r} \left(\nu_{i,r} K_r \prod_{i=1}^{N_g+N_s} [C_i]^{v_{i,r}} \right) \quad (19)$$

where i is an index for either gas or surface species and r is a reaction step in a multiple step reaction mechanism. To calculate the reaction coefficient, K , Arrhenius equation was used,

$$K = AT^\beta e^{-E_a/RT} \quad (20)$$

where A is pre-exponential factor, β is temperature exponent and E_a is activation energy. These are empirical numbers and are presented in Table 6.

For the adsorption of gaseous species sticking coefficients are given. The sticking coefficient is the probability that adsorption takes place when a collision occurs. In order to convert a sticking coefficient to the reaction rate coefficient, the following correlation can be used [27].

$$K_{ads} = \frac{S}{1-S/2} \frac{1}{\Gamma^\tau} \sqrt{\frac{RT}{2\pi M}} \quad (21)$$

where Γ is the total surface site concentration, τ is the sum of surface reactants' stoichiometric coefficients, T is gas temperature, and M is molecular mass. Both sticking coefficients and activation energy may be a function of surface coverage or species concentrations.

The reactant gases entering the channel were modeled as comprised of a hydrogen and dry air (approximated as a 21 percent by volume oxygen and 79 percent by volume nitrogen mixture)

mixture. The mass fraction of species at the inlet is defined by the equivalence ratio, ϕ , which is the ratio of the molar fuel-to-air ratio at the desired test conditions to that at stoichiometric conditions. Thus, a ϕ value of less than unity denotes a lean mixture while a value greater than unity denotes a rich mixture.

4-2-1 Dimensionless equations

Governing equations are non-dimensionalized in this section to provide better understanding of the problem in terms of dimensionless numbers. Utilizing the dimensionless numbers to present the results increases the range of applicability of the solutions for similar problems.

The properties were normalized by their value at the inlet of the combustion channel ($T = 300 \text{ K}$),

$$\rho^* = \rho / \rho_0, \mu^* = \mu / \mu_0, k^* = k / k_0, Cp_g^* = Cp_g / Cp_0 \quad (22)$$

where the superscript (*) denotes normalized parameters. The axial location, x , was normalized by the length of the catalyst bed (L) and the spanwise location, y , was normalized by one half the height of the combustion channel ($H_c/2$).

The overall mass conservation equation for the oil and combustor channels is given as

$$\frac{H_c}{2L} \frac{\partial(\rho^* u^*)}{\partial x^*} + \frac{\partial(\rho^* v^*)}{\partial y^*} = 0 \quad (23)$$

where $u^* = u/u_0$, and $v^* = v/u_0$.

The dimensionless momentum equations in the x and y directions for combustor and oil channel flows, assuming Newtonian fluids and negligible body forces are given as

$$\begin{aligned} & \frac{H_C}{2L} \frac{\partial(\rho^* u^* u^*)}{\partial x^*} + \frac{\partial(\rho^* u^* v^*)}{\partial y^*} + \frac{H_C}{2L} \frac{\partial P^*}{\partial x^*} - \frac{4}{\text{Re}_0} \frac{\partial}{\partial y^*} \left[\mu^* \left(\frac{\partial u^*}{\partial y^*} + \frac{H_C}{2L} \frac{\partial v^*}{\partial x^*} \right) \right] \\ & - \frac{4}{3\text{Re}_0} \frac{\partial}{\partial x^*} \left[\mu^* \left(\frac{H_C^2}{L^2} \frac{\partial u^*}{\partial x^*} - \frac{H_C}{L} \frac{\partial v^*}{\partial y^*} \right) \right] = 0 \end{aligned} \quad (24)$$

$$\begin{aligned} & \frac{H_C}{2L} \frac{\partial(\rho^* u^* v^*)}{\partial x^*} + \frac{\partial(\rho^* v^* v^*)}{\partial y^*} + \frac{\partial P^*}{\partial y^*} - \frac{2}{\text{Re}_0} \frac{\partial}{\partial x^*} \left[\mu^* \left(\frac{H_C}{L} \frac{\partial u^*}{\partial y^*} + \frac{H_C^2}{2L^2} \frac{\partial v^*}{\partial x^*} \right) \right] \\ & - \frac{4}{3\text{Re}_0} \frac{\partial}{\partial y^*} \left[\mu^* \left(2 \frac{\partial v^*}{\partial y^*} - \frac{H_C}{L} \frac{\partial u^*}{\partial x^*} \right) \right] = 0 \end{aligned} \quad (25)$$

where pressure is made non-dimensionalized by using the dynamic pressure as $P^* = P/(\rho_0 u_0^2)$,

and Re_0 is the Reynolds number based on the inlet mixture properties and inlet velocity,

$$\text{Re}_0 = \frac{\rho_0 u_0 (2H_C)}{\mu_0} \quad (26)$$

Species balance equations for each of the gas phase reactants and products is given as follows

$$\begin{aligned} & \text{Pe}_{g,0} \frac{\partial(\rho^* u^* Y_g)}{\partial x^*} + 2\text{Pe}_{g,0} \frac{L}{H_C} \frac{\partial(\rho^* v^* Y_g)}{\partial y^*} - \frac{H_C^2}{4L^2} \frac{\partial}{\partial x^*} \left[D_g^* \rho^* \left(\frac{\partial Y_g}{\partial x^*} - \frac{\kappa_{T,g}(T_s - T_0)}{T^*(T_s - T_0) + T_0} \frac{\partial T^*}{\partial x^*} \right) \right] \\ & - \frac{\partial}{\partial y^*} \left[D_g^* \rho^* \left(\frac{\partial Y_g}{\partial y^*} - \frac{\kappa_{T,g}(T_s - T_0)}{T^*(T_s - T_0) + T_0} \frac{\partial T^*}{\partial y^*} \right) \right] = 0, \quad g = 1, \dots, N_g \end{aligned} \quad (27)$$

where g is gas phase species index, $T^* = (T - T_0)/(T_s - T_0)$, $D_g^* = D_g / D_{g,0}$. The thermal diffusion ratio for species g , $\kappa_{T,g}$, is defined as $\kappa_{T,g} = D_g^T / D_g$. The third and fifth terms in Eq. (27) are ordinary species diffusion while the fourth and sixth terms are species diffusion due to a temperature gradient (Soret effect). In Eq. (27), $Pe_{g,0}$ is the mass transfer Peclet number of species g and is defined as

$$Pe_{g,0} = \frac{u_0 (H_C^2 / 4L)}{D_{g,0}} \quad (28)$$

The rationale behind using $H_C^2 / 4L$ as a length scale for $Pe_{g,0}$ stems from definition of $Pe_{g,0}$ in terms of relevant time scales and is described further in section 4-2.

The normalized energy equation used for the combustion and exhaust channel flows is provided below

$$\begin{aligned} & Re_0 \frac{H_C}{2L} \frac{\partial(\rho^* u^* Cp^* T^*)}{\partial x^*} + Re_0 \frac{\partial(\rho^* v^* Cp^* T^*)}{\partial y^*} \\ & - \frac{1}{Pr_0} \frac{H_C^2}{L^2} \frac{\partial}{\partial x^*} \left[\sum_{g=1}^{N_g} \frac{1}{Le_{g,0}} \frac{k_{g,0}}{Y_{g,0} k_0} D_g^* \rho^* Cp_g^* \left(\frac{T^* (T_s - T_0) + T_0}{T_s - T_0} \frac{\partial Y_g}{\partial x^*} + \kappa_T \frac{\partial T^*}{\partial x^*} \right) + k^* \frac{\partial T^*}{\partial x^*} \right] \\ & - \frac{4}{Pr_0} \frac{\partial}{\partial y^*} \left[\sum_{g=1}^{N_g} \frac{1}{Le_{g,0}} \frac{k_{g,0}}{Y_{g,0} k_0} D_g^* \rho^* Cp_g^* \left(\frac{T^* (T_s - T_0) + T_0}{T_s - T_0} \frac{\partial Y_g}{\partial y^*} + \kappa_T \frac{\partial T^*}{\partial y^*} \right) + k^* \frac{\partial T^*}{\partial y^*} \right] = 0 \end{aligned} \quad (29)$$

where Pr_0 is the mixture Prantdl number at the inlet: $Pr_0 = \mu_0 Cp_0 / k_0$ and $Le_{g,0}$ is the g^{th} species Lewis number at the inlet: $Le_{g,0} = k_{g,0} / (\rho_{g,0} Cp_{g,0} D_{g,0})$. $k_{g,0}$ and $Y_{g,0}$ are the g^{th} species thermal conductivity and mass fraction at the inlet, respectively while k_0 is the mixture thermal conductivity at the inlet.

The boundary condition for the species balance equations (Eq.(27)) at the catalytic wall was given as

$$\rho_g^* D_g^* \frac{\partial Y_g}{\partial y^*} \Big|_{y^*=0.5} - \frac{\rho_g^* \kappa_T D_g^* (T_s - T_0)}{T^* (T_s - T_0) + T_0} \frac{\partial T^*}{\partial y^*} \Big|_{y^*=0.5} + 2Da_{g,0} Pe_{g,0} \dot{s}_g^* = 0 \quad (30)$$

In Eq. (30), the density of each species is normalized by the inlet density of that species,

$\rho_g^* = \rho / \rho_{g,0}$, and the source term is normalized using $\dot{s}_{g,0}$, the rate of

production/consumption of g^{th} species calculated based on the inlet values. Damkohler number of g^{th} species, $Da_{g,0}$, is defined as the ratio of chemical rate over physical rate

$$Da_{g,0} = \frac{(\dot{s}_{g,0} M_g / \rho_{g,0} H_C)}{u_0 / L} \quad (31)$$

A 1-D energy balance gives the following boundary condition at the wall covered with catalyst between combustion and exhaust channels:

$$-k_C^* \frac{\partial T^*}{\partial y^*} \Big|_{y^*=0.5} + \frac{H_C \bar{M}}{2k_0} \sum_{g=1}^{N_g} \left(\dot{s}_{g,0} C p_{g,0} \dot{s}_g^* C p_g^* M_g^* \frac{T^*(T_s - T_0) + T_0}{T_s - T_0} \right) = -k_E^* \frac{\partial T^*}{\partial y^*} \Big|_{y^*=0.5} \quad (32)$$

where \bar{M} is the mixture molar mass, and subscripts C and E refer to the gases in the combustion and exhaust channels, k_C^* and k_E^* are the mixture averaged thermal conductivities in the combustor and exhaust channels, respectively, normalized by the inlet mixture conductivity. In the regions without the catalyst, the second term on the left side of Eq. (32) goes to zero.

4-2-2 Time scales

Variation of geometric and fluidic parameters in the combustion channel impact several co-mingled physical phenomena in the μ CHX unit cell that result from a competition of different time scales. For example, variation of the inlet reactant gas velocity or catalyst length affect the residence time for combustion and hence the conversion of hydrogen. However, one can reach the same residence times by either having long catalyst bed length and high inlet velocity or short catalyst bed length and low inlet velocity. Although both scenarios have identical residence times, hydrogen conversion and efficiency will not be the same. This is because in the former scenario, the reactant gases have a larger chemical power and consequently, the average temperature in the reaction zone is larger, which in turn affects the reaction rate and heat transfer rate to the oil channels. Different temperatures in both scenarios will cause local velocity and diffusion to be different. Hence, it is important to characterize the performance of the combustor in more universal terms by considering all relevant time scales and dimensionless numbers that are altered by variations in the geometrical and fluidic parameters. The time scales that are of are

importance for catalytic combustion are residence time, diffusion time, and chemical time. These can be defined at the inlet, wherein the time scales are fixed for a given operating condition and geometry, or on a *local* basis, wherein the time scales vary depending on the local velocity, temperature and length scales.

Residence time refers to the flow time over the desired section (in this case the catalytic surface), and is defined as a ratio of a length scale, L , to a velocity scale, V , of importance in the problem

$$t_r = L/\bar{V} \quad (33)$$

A *local* residence time can be defined such that L represents the remaining length of the catalyst downstream of the location under consideration and \bar{V} is the local velocity that is averaged over the cross section. This velocity is calculated at each axial position along the combustor and provides local estimate for the residence time. Gas mixture velocity and the catalyst length are two parameters that have direct influence on the local residence time. However, other parameters like equivalence ratio affect the residence time by changing the gas temperature along the catalyst bed. In the definition of the residence time, L in Eq. 16 refers to the total catalyst length, while \bar{V} refers to the inlet fluid velocity, u_0 ,

$$t_{r,0} = L/u_0 \quad (34)$$

A second time scale consequential for heterogeneous surface reactions pertains to the time required for species to diffuse laterally and reach the desired location (in this case the catalytic

surface). When the channel size decreases, for a fixed inlet mass flow rate, the Reynolds number and residence time also decrease. In such microchannel flows with low Reynolds numbers (laminar flows), species mixing occurs mostly by molecular diffusion. Hence, the diffusion time for species g is defined as

$$t_{d,g} = (H_c/2)^2 / D_g \quad (35)$$

where $H_c/2$ is the largest diffusion distance within the combustor channel for a species, and D_g is the molecular diffusivity of g^{th} species. The diffusion time is defined by estimating the species diffusivity at the inlet temperature while the *local* diffusion time is determined by estimating the diffusivity at the local temperature within the channel. Since each species has a different diffusivity, the diffusion time of each species would be different. In the current study, diffusion of hydrogen and oxygen is of importance therefore the diffusion time scales for these two species are calculated and compared against the other time scales.

The third time scale, known as chemical time or reaction time, refers to the time needed to complete a reaction. It is defined as the ratio of the amount of the fuel available to the rate of fuel consumption. In order to find the local values of chemical time, local mass fraction, local velocity and local axial gradient in each species mass fraction can be used,

$$t_c = \frac{Y_{H_2}}{V \cdot \frac{dY_{H_2}}{dx}} \quad (36)$$

Local values of chemical time can be calculated when the change in hydrogen mass fraction along the length of the channel is known and hence this definition is useful only for analysis of the results. However, for design purposes, dY_{H_2}/dx is unknown and hence a chemical time needs to be defined based on the initial hydrogen mass fraction and reaction rate. Since catalytic combustion of hydrogen is a multistep reaction, reaction rate of the limiting step was considered. Based on the sensitivity analysis presented in section 4-4, adsorption of oxygen (Reaction 3 in Table 6) was found to be the rate-limiting reaction step. Therefore oxygen adsorption rate based on inlet concentration of O_2 was considered for calculation of chemical time,

$$t_{c,0} = \frac{C_{O_2,0}}{\dot{s}_{O_2,0}} \quad (37)$$

In order to illustrate how the local species concentration and temperature affect local residence times, consider a base condition of a MH μ CHX unit cell wherein the inlet gas mixture has a velocity of 4 m/s. The catalyst is located on the wall over a 10 mm length from $x = 5$ mm to $x = 15$ mm. The fluidic and geometric conditions of this base case are summarized in Table 7.

Table 7: Geometrical and fluidic conditions for the base case

Parameter	L (mm)	L_{CH} (mm)	H_C (μ m)	Gas inlet velocity (m/s)	Equivalence ratio (ϕ)	Oil inlet velocity (m/s)	Oil inlet temperature (K)
Value	10	30	300	4	1	0.01	300

Figure 17 (a) shows the temperature and hydrogen mass fraction distribution along the channel centerline while Figure 17 (b) shows the variation of the local residence, diffusion and chemical

time scales, as defined in this section. Diffusion time scales are shown for both hydrogen and oxygen. Upon the start of the catalyst region at $x = 5$ mm, the hydrogen mass fraction decreases rapidly resulting in a rise in temperature due to catalytic combustion. This rise in temperature causes an increase in area-averaged velocity as a result of reduced density, and hence a sharp decrease in residence time (Figure 17 (b)). An increase in temperature also increases the reaction rate and therefore decreases the chemical time. The diffusivities increase with an increase in temperature resulting in a decrease of diffusion time with temperature. Both the diffusion times and chemical times reach their minima around the middle of the catalyst section where the fluid temperature is the largest.

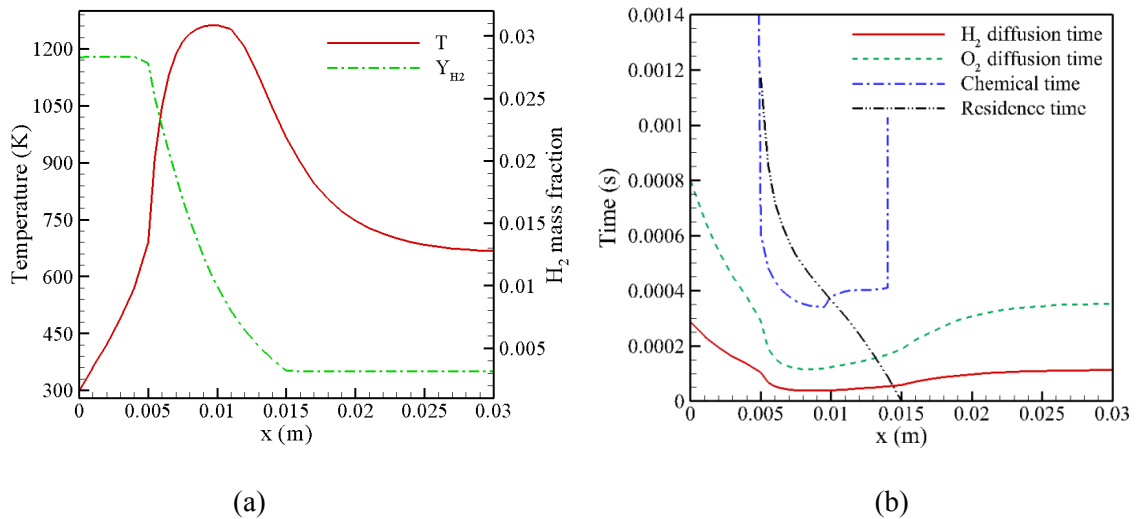


Figure 17: Axial variation along the length of the combustion channel of (a) temperature and hydrogen mass fraction, (b) local time scales

A comparison of the three time scales indicates that the local diffusion time is usually much smaller than the reaction and residence times owing to the small channel dimensions. All along the length of the combustion channel H_2 diffusion time is lower than that of O_2 and henceforth only O_2 diffusion is considered in the following sections in estimating the diffusion time. The

mixture average diffusion coefficient of oxygen and hydrogen at the inlet are

$D_{O_2,m} = 2.8 \times 10^{-5} \text{ (m}^2/\text{s)}$ and $D_{H_2,m} = 7.8 \times 10^{-5} \text{ (m}^2/\text{s)}$. The diffusion time is defined as

$$t_{d,0} = (H_c/2)^2 / D_{O_2,0} \quad (38)$$

where $D_{O_2,0}$ is mixture average diffusion coefficient of oxygen based on the inlet temperature. In order to have high completion of a reaction, t_c should be smaller than both t_d and t_r . In addition, t_d should be less than t_r to ensure that the fuel molecules can reach the catalyst surface before they are convected downstream from the catalyst section. To make the comparisons between the three time scales simpler and easier to understand, two commonly used dimensionless numbers in combustion are adopted, namely Da and Pe where

$$Da = \frac{t_r}{t_c} \text{ and } Pe = \frac{t_d}{t_r} \quad (39)$$

Damkohler number is the ratio of residence time over the chemical time while mass transfer

Peclet number is the ratio of the diffusion time over the residence time. A $Da > 1$ implies that for the specific geometry and flow characteristics, the chemical time is sufficiently small compared with flow time for the reaction to proceed to completion. On the other hand, in catalytic reactions, $Pe < 1$ is needed to ensure higher completion. Peclet numbers higher than unity imply that the fuel and oxidizer molecules are convected out of the catalyst region prior to diffusing laterally to the wall where the catalyst exists.

In section 4-2-1 , the $Da_{g,0}$ and $Pe_{g,0}$ are defined based on the time scales of each species.

However, as mentioned before, oxygen diffusion and reaction rates are the limiting factors in the conversion efficiency of the system, therefore *inlet* time scales (which are based on oxygen diffusion and reaction rates) are preferred henceforth. These dimensionless numbers are defined as

$$Da_{O_2,0} = \frac{t_{r,0}}{t_{c,0}}, Pe_{O_2,0} = \frac{t_{d,0}}{t_{r,0}} \quad (40)$$

4-3 Simulation Method and Model Validation

4-3-1 Grid independence study

Non-uniform rectangular grids with progressively smaller grids close to the walls (Figure 18 (a)) were used to give higher resolution in regions of large gradients in velocity, temperature and species while minimizing the overall number of grids to reduce computation time. Significant changes in mass fraction of the species and temperature occurred at regions very close to the walls with the catalyst. The grids were refined further using adaption for gradient of mass fraction of hydrogen with a criterion of 0.003 (10% change in H₂ mass fraction). Another grid refinement step was performed at locations with significant mass imbalances. Figure 18 (b) shows the grids near the catalytic walls upon completion of both refinement steps. The catalyst locations are shown by bold lines. The size of the smallest grid was 1.44 μm × 12.5 μm. With H_C = 300 μm and L_{CH} = 30 mm the relative size can be calculated as Δy/H_C = 4.8 × 10⁻³ and Δx/ L_{CH} = 4.2 × 10⁻⁴. The size of the largest grid was 30 μm × 50 μm (Δy/H_C = 0.1 and Δx/ L_{CH} = 1.6 × 10⁻³). The maximum aspect ratio of the grid was 8.71.

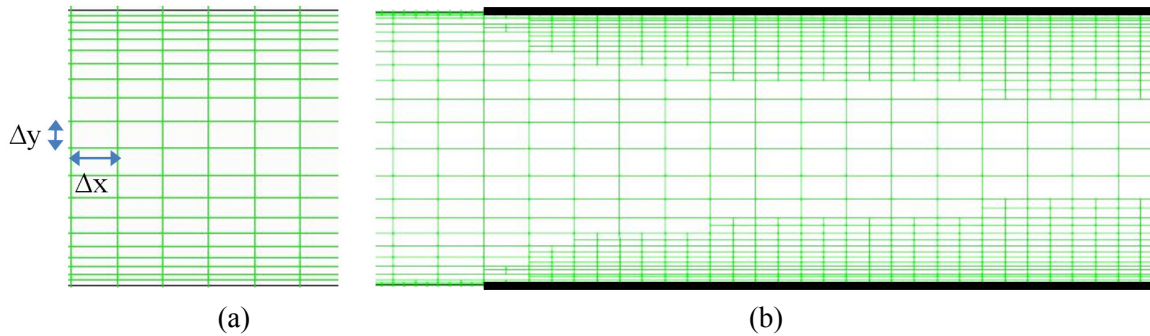


Figure 18: (a) Comparison channel non-uniform grids, (b) Combustion channel grids after adaption, The size of the smallest grid was $1.44 \mu\text{m} \times 12.5 \mu\text{m}$ ($\Delta y/H_C = 4.8 \times 10^{-3}$ and $\Delta x/L_{CH} = 4.2 \times 10^{-4}$). The size of the largest grid was $30 \mu\text{m} \times 50 \mu\text{m}$ ($\Delta y/H_C = 0.1$ and $\Delta x/L_{CH} = 1.6 \times 10^{-3}$)

It should be verified that the solution of a CFD simulation is independent of the grid resolution. An initial solution was performed with a coarse mesh with a total number of 15,200 grids. The number of grids was increased to 30,700, 122,800, 491,200, and 1,964,800 in the refinement study. It should be noted that the number of grids take the aforementioned refinement steps into account. For each case the residuals were ensured to be less than 10^{-3} for some species equations and less than 10^{-7} for all other equations and the results were compared. Figure 19 shows the change in efficiency and H_2 conversion by increasing the number of grids. Results changed less than 2% with increasing the number of grids after 30,700 while the computation time increased significantly (from hours to days). Therefore 30,700 grids were used for all the followed simulations. It should also be mentioned that the model with number of grids less than 15,000 did not result a solution and diverged.

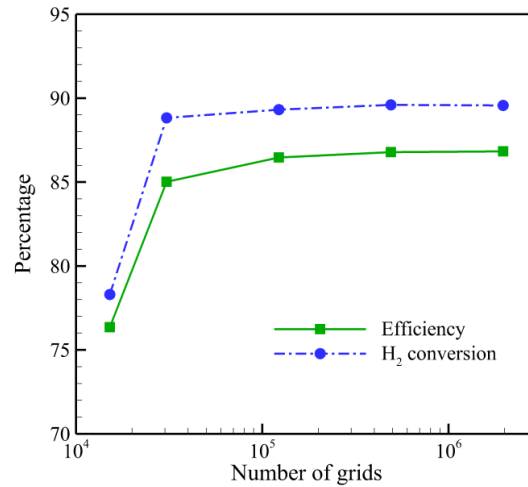


Figure 19: Grid independence study comparing the global results of conversion and efficiency as a function of the number of grids.

In order to investigate the effect of grid resolution on the local solution, local values of H₂ mass fraction and temperature are shown in three different longitudinal locations, i.e. $x = 5$ mm, $x = 10$ mm and $x = 20$ mm along the microchannel combustor. Figure 20 shows these parameters versus y (height of the channel). These parameters are shown for three different numbers of grids: 15,200 and 30,700 and 122,800. The values of the case with 15,200 grids are shown by symbols for clarity. Dashed lines and solid lines show the parameters values for the cases with 30,700 and 122,800 grids. Green lines and green rectangular symbols correspond to H₂ mass fractions and blue lines and blue triangular symbols correspond to temperature values. It can be seen that the dashed lines and solid lines have a good agreement while symbols do not show the values accurately. Therefore, as recommended by Fig. 18, increasing the number of grids from 30,700 to 122,800 did not provide more accuracy and a solution based on a case with 30,700 grids was deemed grid independent.

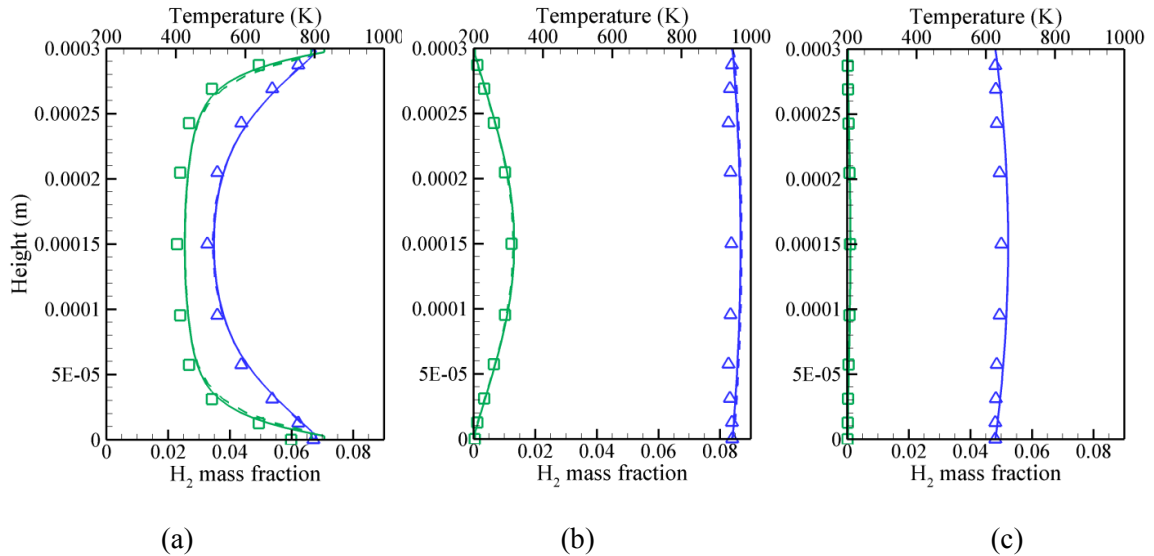


Figure 20: Local values of H₂ mass fraction and temperature as a function of y (height of the channel) at three different locations. (a) $x = 5$ mm, (b) $x = 10$ mm, and (c) $x = 20$ mm. The values of the case with 15200 grids are shown by symbols. Dashed lines and solid lines show the parameters values for the cases with 30,700 and 122,800 grids. Green lines and green rectangular symbols correspond to H₂ mass fractions and blue lines and blue triangular symbols correspond to temperature values.

The 3D simulation results presented in section 5-2 were carried out in steady state and laminar flow. Only momentum equations were solved to study the flow distribution. Number of grids was different for different 3D geometries. When the simulation result of a case with a specific number of grids was within 2% of the simulation result of the same case with four times higher number of grids, the result was deemed to be grid independent.

4-3-2 Model validation

The available experimental and numerical studies in literature on hydrogen combustion are either for a single combustor channel or a combustor with recuperator channels. For the latter, local data of boundary conditions were not available for validation. To validate the current method, a

combined experimental and numerical study by Appel et al. [49] was chosen. They studied hetero-/homogeneous combustion of hydrogen/air mixtures over platinum in a single channel. Although the geometry is different from that of the current study, the similarity in the gas mixtures and combustion scheme helped to validate the current model. The heterogeneous reaction scheme of Deutchmenn et al. [13] was used for surface reactions and for gaseous reactions; the scheme of Warnatz et al. [50] was used. These same schemes were used by Appel et al. in their numerical study. A 2D rectangular channel was modeled with specified temperature profiles at the walls, identical to that of Appel et al. [20]. H_2 /air mixture with the equivalence ratio of 0.28 flowed in a 300 mm long \times 7 mm high channel, the Reynolds number is 1105 and the operating pressure was 1 bar (Figure 21).

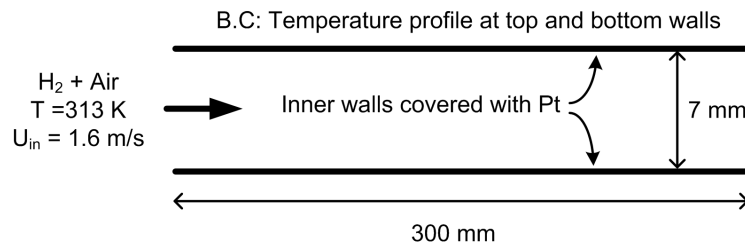


Figure 21: A schematic view of the geometry of Appel et al. [48]

Results of the H_2 mole fraction and temperature at different streamwise locations are compared in Figure 22. The figure shows that current simulation predicts the trends in the experimental data and model of Appel et al. [49] reasonably well. Based on the reasonable agreement of the present simulations with literature, the scheme was used to further investigate the performance of the μCHX .

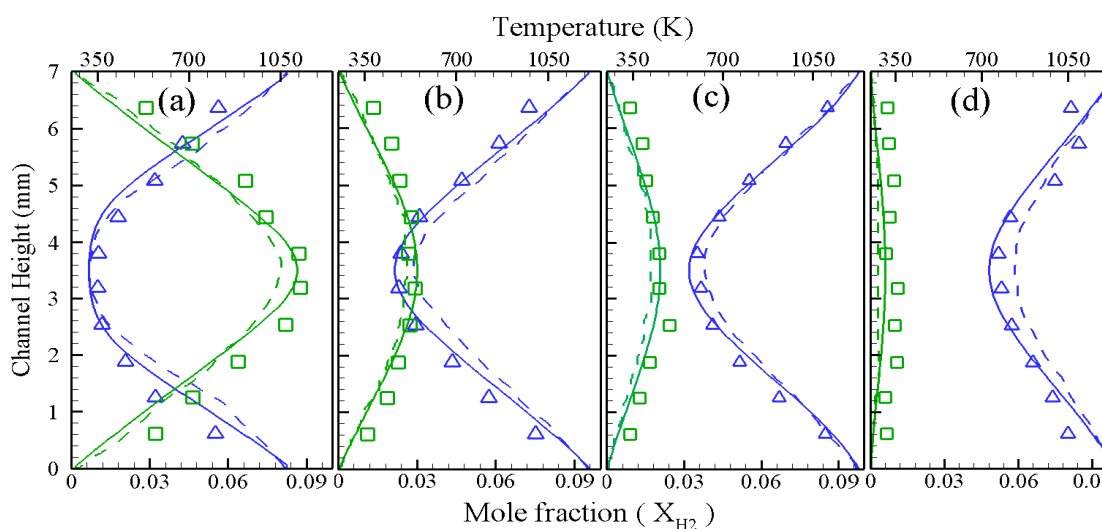


Figure 22: Comparison of the results from current model simulations with experimental and numerical data from Appel et al. [48]. Profiles of H_2 and temperature are shown at four Streamwise locations: (a) $x = 25$ mm, (b) $x = 85$ mm, (c) $x = 105$ mm, (d) $x = 165$ mm. Solid lines are the results from the current study, dashed lines and symbols are numerical and experimental results provided by Appel et al. [48]. Squares and triangles represent H_2 mole fraction and temperature, respectively.

4-4 Sensitivity Analysis

To better understand the major reaction steps and identify a limiting reaction step for use in the chemical time estimate, a sensitivity analysis was performed on all elementary reactions in the mechanism of Deutschmann et al. [13] (Table 6). Sensitivity analysis is often used as a tool to obtain reduced reaction mechanisms [51] and to identify the rate-limiting reaction steps [50]. The base case geometry and flow conditions indicated in Table 7 were chosen for the sensitivity study. In the sensitivity analysis, the pre-exponential constant of a particular reaction step was perturbed by multiplying or dividing it by a factor (F) while keeping all other pre-exponential constants at their original values shown in Table 6. The hydrogen mass fraction at the exit was computed and compared against the hydrogen mass fraction of the unperturbed case. A large

deviation in hydrogen exit mass fraction was an indication that the perturbed reaction step was important to the overall completion of the multi-step reaction.

Multiplication and division of the pre-exponential constant by F of 1.1 and 1.5 produced the same set of significant reactions. Figure 23 shows the significant results from the sensitivity analysis wherein the percentage change in hydrogen mass fraction at the outlet is shown for the three reaction steps that have the most effect on hydrogen conversion. The solid bars indicate results when the reaction pre-exponential constant is multiplied by F and the empty bars show results for division by F. Among these three reaction steps, oxygen adsorption is seen to be the most important in determining the total rate of the catalytic hydrogen combustion reaction. Hence, this rate is used in defining the chemical time scale based on the inlet parameters as discussed in the previous section.

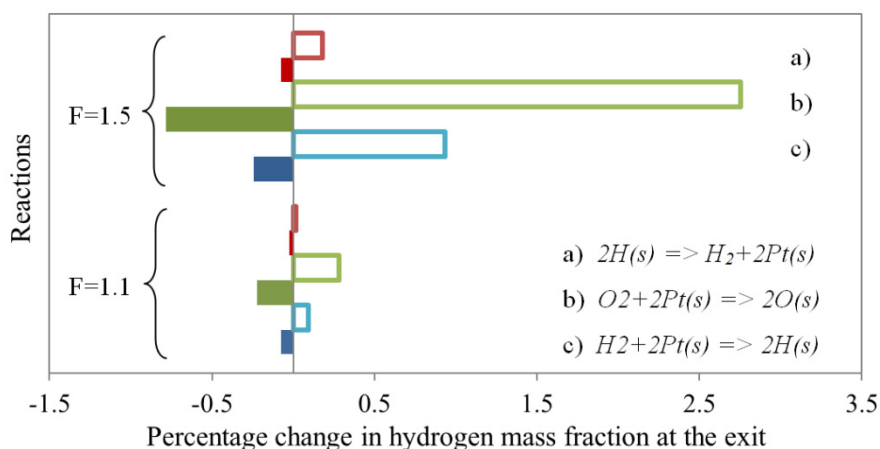


Figure 23: Sensitivity analysis on the elementary schemes of Deutschmann et al. [13] listed in Table 6

4-5 Effect of Catalyst Active Area

The goal of the numerical simulations presented herein is to assist with the design of the μ CHX. However, it would be of value to compare results from the simulations with that of the experiments in future work. With this longer term goal in perspective, sensitivity analysis on the catalyst surface area is presented in this section.

When comparing the results from experiments to simulation results, it is important to quantify the active catalyst area in the experiments. The active catalyst area can vary for different experiments depending on the method used to deposit the catalyst and the activation process performed.

Active catalyst area can be determined by chemisorption tests which reveal the active area per weight of the catalyst. With knowing the weight of the deposited catalyst and the deposited area, the ratio of the active area over the geometric area can be calculated [52] [53] [54]. This factor (B) represents the ratio of the active area in the experiments over the geometrical area in the simulations. To understand the effect of catalyst dispersion or to take the uneven distribution of catalyst and un-activated catalyst area into account, a parametric study was carried out by varying the factor B . The boundary condition for the species balance equation at the catalytic wall (Eq. 14) was rewritten as

$$\left(\rho Y_g V_g\right)_{wall} + B \dot{s}_g M_g = 0 \quad (41)$$

The boundary condition at the wall between combustor and exhaust channels which is covered with catalyst (Eq. 15)

$$-k_C \frac{\partial T}{\partial y} \Big|_{y=H_C/2} + \sum_{g=1}^{N_g} (B \dot{s}_g h_g M_g) = -k_E \frac{\partial T}{\partial y} \Big|_{y=H_C/2} \quad (42)$$

The surface site density of the catalyst (Γ) was chosen to be 2.7×10^{-9} representing crystalline platinum and was input to the software through the Chemkin mechanism file. It should be noted that to study the effect of variation of the active catalyst area on the overall rate of the reaction, Γ should not be changed since it is a physiochemical property of platinum.

All the conditions were kept at the base case discussed in Table 7 and B was varied. The results showed that at B values close to and higher than one, small variations of the factor B do not have a significant effect on overall rate of the catalytic reaction of hydrogen and oxygen. Figure 24 shows the percent change in H_2 conversion from the ideal case of $B=1$ with changing the factor B from 1 to 0.07. Further reduction of the factor did not result in a reaction and the hydrogen quantity left the channels unreacted. As can be seen, H_2 conversion decreases with factor B , which means less active catalyst sites are available over the same geometrical area for reaction.

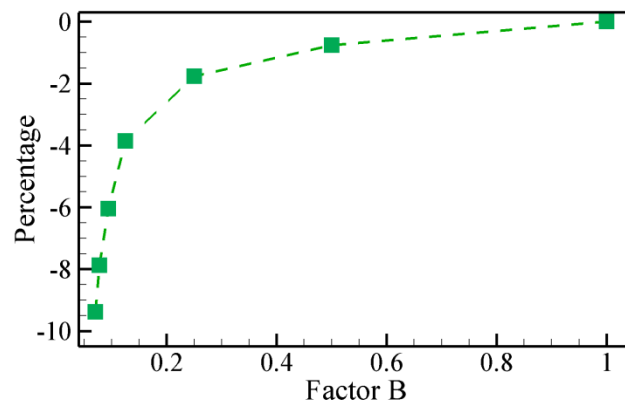


Figure 24: Change in H_2 conversion by variation of factor B in percentage

4-6 Parametric Study of the MH μ CHX

Temperature, H_2 and H_2O mass fraction contours for the base case indicated in Table 7 are shown in Figure 22. The inlet temperatures for both the oil and inlet gas mixture are at 300 K. The catalytic surface is 10 mm in length and is located 5 mm downstream from the inlet on the walls of the combustion channel which has the total length of 30 mm. The gas temperature contours in Figure 25 (a) indicate that because of heterogeneous combustion, the temperature increases near the wall. Temperature reaches its highest value of 993 K at about 7 mm from the inlet and decreases downstream due to the transfer of heat to the recuperator and oil channels. For this condition, outlet oil and exhaust gas temperatures are 529.6 K and 387.7 K, respectively.

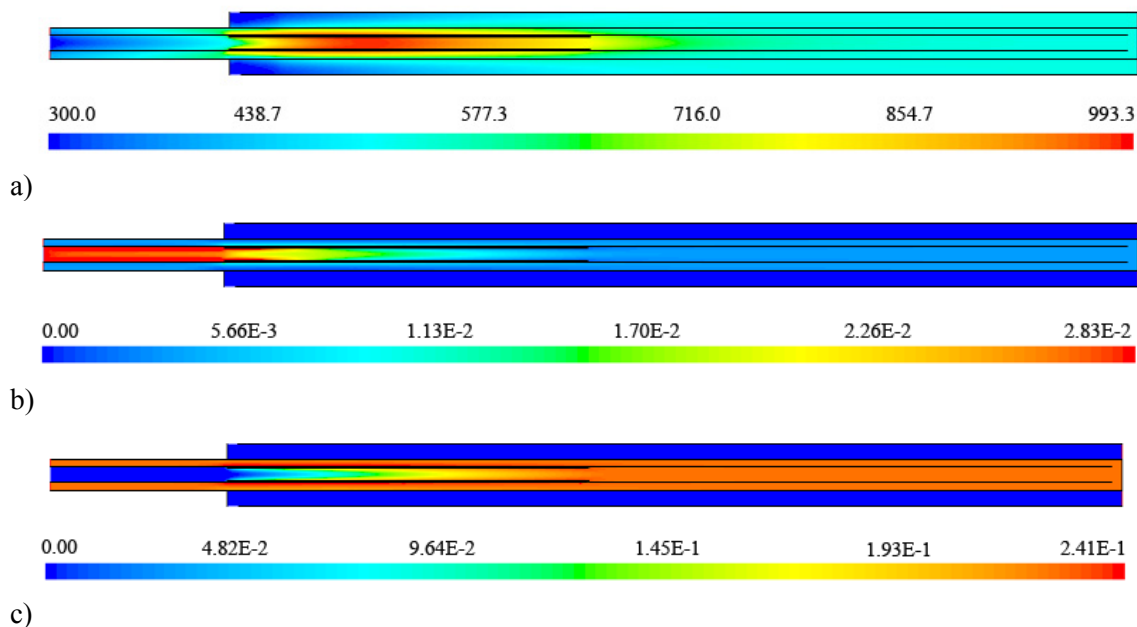


Figure 25: a) Temperature contours (K), b) H_2 mass fraction contours, and c) H_2O mass fraction contours. The heavy lines indicate the location of the catalytic bed.

Figure 25 (b) depicts the hydrogen mass fraction along the channel and indicates that about 90 percent of the hydrogen is consumed within the 10 mm length of the catalyst surface. Production of H₂O, depicted in Figure 22 (c), indicates that water vapor mass fraction increases from zero to values in excess of 20 percent by the end of the catalyst section.

4-6-1 Performance indices

The performance of the μ CHX unit cell is characterized over a range of geometric and thermo-fluidic parameters. The varied geometric parameters include the catalyst bed location and length, and the channel length and height. Varied fluidic parameters include the equivalence ratio, gas inlet velocity, and the oil inlet temperature and velocity. In order to quantify the μ CHX unit cell performance for these parametric variations, three different measures, namely the efficiency index, effectiveness and hydrogen conversion, are used.

Efficiency index is used to identify the overall performance of the μ CHX unit cell, and is defined as the ratio of the amount of heat transferred to oil to the chemical energy of input hydrogen,

$$\eta = \frac{\dot{m}_{oil} (h_{out} - h_{in})_{oil}}{\dot{m}_{H_2} \Delta \bar{h}_{reaction} / M_{H_2}} \quad (43)$$

where M_{H_2} is the molar mass of hydrogen, $\Delta \bar{h}_{reaction}$ is the molar enthalpy of reaction, and \dot{m}_{H_2} is the inlet hydrogen mass flow rate. Enthalpy of reaction was calculated at the volumetrically-averaged temperature in the catalyst section of the combustor.

Hydrogen conversion is defined as the ratio of the amount of hydrogen reacted to that of input hydrogen,

$$H_2 \text{ Conversion} = \frac{Y_{H_2,in} - Y_{H_2,out}}{Y_{H_2,in}} \quad (44)$$

Effectiveness is used as a criterion to characterize the heat transfer performance of the μ CHX and is defined as the ratio of the heat transfer rate to oil compared to the amount of heat produced by combustion

$$\varepsilon = \frac{\dot{m}_{oil} (h_{out} - h_{in})_{oil}}{(\dot{m}_{H_2,in} - \dot{m}_{H_2,out}) \Delta h_{reaction} / M_{H_2}} \quad (45)$$

Given the constant overall heat transfer coefficient under laminar flow conditions for a fixed geometry, a higher effectiveness translates to higher heat transfer rate to the oil caused by a larger temperature difference between oil and exhaust channels. Figure 26 shows the positive correlation between ε and average driving temperature difference, ΔT_{ave} , for parametric variation of combustor channel heights. In this plot, the horizontal axis shows ε evaluated at different channel heights. The driving temperature difference was calculated using the cross sectional averaged temperatures of oil and exhaust channels along the length of the combustor. It can be seen that an increased ε corresponds to conditions of increased temperature difference (ΔT) and decreased exhaust exit cross sectional averaged temperature, $T_{exhaust,ave}$. Henceforth, ε will be used as a criterion for the performance of the heat exchanger.

Table 8 shows a summary of the geometric and fluidic parameters and their range studied in this work. The ranges for the parameters were chosen to ensure that the outlet oil and exhaust temperatures are within the limiting values mentioned before. However, since the range is narrow for some parameters due to the operating constraints, a larger range is provided to place the results in a broader context; these results are clearly identified in the discussion of the results.

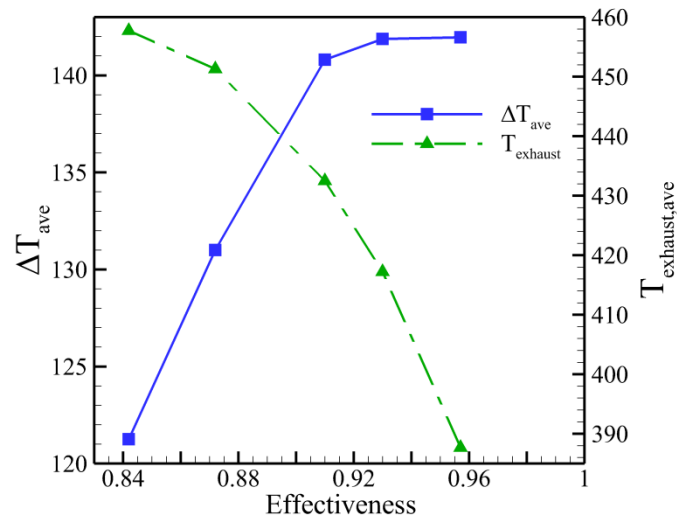


Figure 26: Variation of oil and exhaust temperature difference (ΔT_{ave}) and exhaust exit temperature ($T_{exhaust,ave}$) with effectiveness as defined in Eq.(45).

Table 8: Summary of geometrical and thermo-fluidic parameters for the MH μ CHX ^a

Parameter		Range	Effect of parameter variation on non-dimensional numbers	
			$Da_{O_2,0}$	$Pe_{O_2,0}$
Geometrical	L_{CH} (mm)	15-60	-	-
	H_C (μ m)	300-700	2.10	0.32-1.73
	L (mm)	5-25	1.05-5.24	0.13-0.64
Fluidic	Gas mixture inlet velocity (m/s)	3-7	1.20-2.80	0.24-0.56
	Equivalence ratio (ϕ)	0.3-1	2.10	0.32-0.40
	Oil inlet velocity (m/s)	0.01-0.03	-	-
	Oil inlet temperature (K)	300-370	-	-

^a Dashes mean there is no significant effect

The effects of each of the parameters on the dimensionless numbers are also shown in Table 8. Catalyst bed length, gas velocity and equivalence ratio change $Da_{O_2,0}$ significantly while channel height, catalyst bed length and equivalence ratio influence $Pe_{O_2,0}$.

Simulations with four different locations of catalyst along the length of the combustion channel showed that the exhaust temperature is higher than 373 K only when the catalyst is located close to the beginning of the channel. Therefore, although systems with catalyst located close to the end of the channel produce higher efficiencies, catalyst bed was chosen to be at a fixed location 5 mm downstream of the inlet. The height of the combustor channel (H_C) is restricted to be less than 1000 μm . The fixed geometries are H_O at 300 μm and H_R at 150 μm . The combustor channel height is varied between 300 μm and 700 μm .

In the following sections the effects of different parameters on the performances indices of the unit cell are presented. The results for the dimensionless numbers ($Da_{O_2,0}$ and $Pe_{O_2,0}$) are also shown and discussed. Variation of each parameter is analyzed while maintaining the rest of the parameters at a constant value represented by the base case shown in Table 7.

4-6-2 Catalyst bed length

In order to minimize the weight, volume and cost of the μCHX , it is important to have just the requisite amount of catalyst to have near complete conversion. Simulations of five different catalyst lengths of 5, 10, 15, 20 and 25 mm were performed while holding other parameters at

constant values summarized in Table 7. All catalyst beds in this study begin at a distance of 5 mm from the combustor inlet.

Figure 27 shows the variation of performance indices as a function of catalyst bed length. A significant increase in hydrogen conversion is observed with increasing catalyst length from L of 5 mm to 15 mm, with little further increase in conversion from L of 15 mm to 25 mm. However, the effectiveness shows little to no dependence on catalyst length. The η of μ CHX unit cell follows the same trend as the hydrogen conversion. It should be noted that although the channel length and the inlet velocity are identical for all five catalyst bed lengths, the pressure drop increases with catalyst length significantly from L of 5 to 15 mm due to the higher gas temperatures that accompany increased conversion. Consequently, the pressure drop also does not change appreciably between L of 15 and 25 mm.

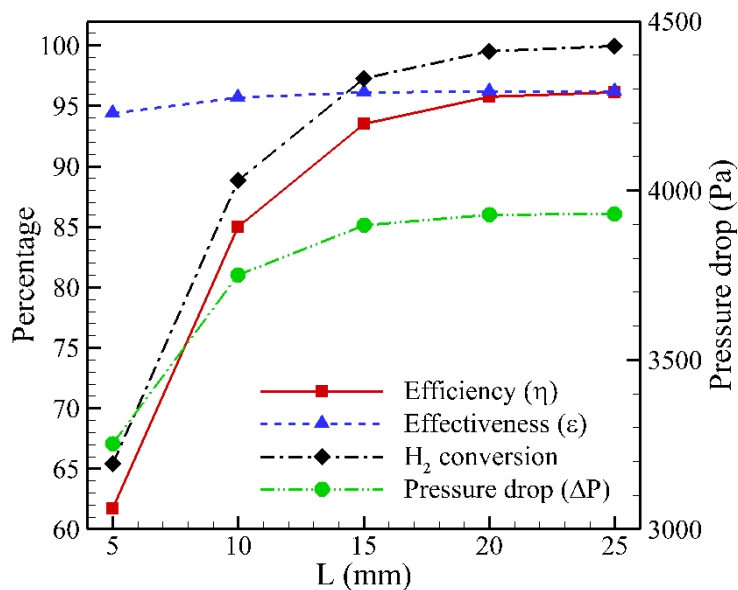


Figure 27: Variation of performance indices with catalyst length

The trends of Damkohler and Peclet numbers for different catalyst lengths are shown in Figure 28. It is seen that both numbers change appreciably with L due to an increase in residence time with catalyst length. Even for the shortest catalyst length, $Pe_{O_2,0}$ is lower than unity, indicating that diffusion is not a limiting time scale in microchannel combustors of the scale considered herein. On the other hand, $Da_{O_2,0}$ increases to values higher than unity with increase in catalyst length. As mentioned before, a higher value of $Da_{O_2,0}$ implies better conversion since the residence time is higher for longer catalyst beds, leading to higher conversion of reactants.

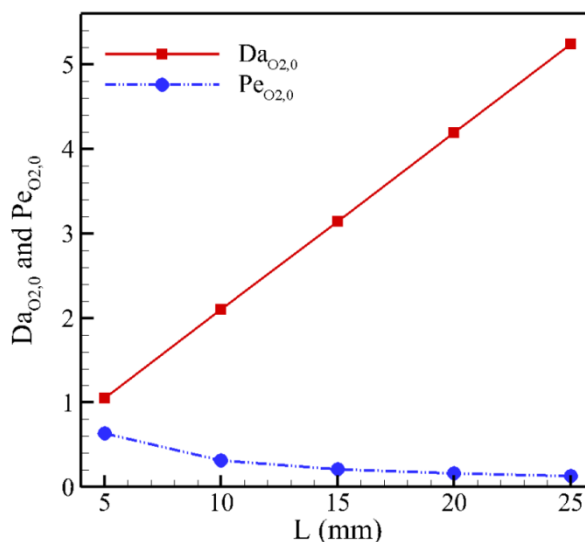


Figure 28: Variation of Damkohler and Peclet numbers with catalyst bed lengths

With a goal of minimizing the quantity of noble metal catalyst used, it can be concluded from Figure 27 and Figure 28 that a catalyst bed length of 15 mm would be a good compromise between cost and efficiency. However, for the rest of the parametric studies, a 10-mm catalyst bed length is used in order to capture distinct variations in performance indices with parameters.

4-6-3 Channel length

With a constant catalyst length of $L=10$ mm, the effect of changing the length of the μ CHX unit cell is investigated. In Table 9, the performance indices of three different channel lengths are compared. The fixed values of other parameters are provided in Table 7. Changing the channel length has almost no effect on hydrogen conversion because the catalyst length, and as a result, the residence time is the identical for all three lengths. The overall efficiency increases by 3.2 percent because of an increase in ε of 3.3 percent. The longer is the length of the channel (and consequently the heat exchange area between the exhaust gases and oil); the better is the heat transfer from the exhaust channels to the oil channels due to the increased heat exchange area. Although the efficiency increases marginally with increase in channel length; the pressure drop almost triples as the length increases from 15 mm to 60 mm, indicating that for this particular set of fixed parameters, an increase in catalyst length beyond 15 mm does not provide appreciable benefits.

Table 9: Comparison of different channel lengths at the same catalyst length

L_{CH} (mm)	L (mm)	ΔP (Pa)	ε	H ₂ conversion	η
15	10	2335.4	0.940	0.889	0.835
30	10	3749.7	0.957	0.888	0.850
60	10	6542.9	0.971	0.888	0.862

4-6-4 Channel height

In order to identify the effects of different diffusion times on hydrogen conversion and efficiency of the μ CHX, combustion channel heights were varied from 300 μ m to 700 μ m while $t_{r, inlet}$ is kept

fixed. The fixed values of the other parameters are shown in Table 7. Larger channel heights translate to higher diffusion times (Eq. (34)) hence Peclet number would become important in determining conversion at these larger channel heights. It should be noted here that in all simulations presented in this paper, only heterogeneous reactions are modeled. Therefore, although homogeneous reaction is likely to happen in a 700 μm channel, the results for the larger channel heights are shown for better understanding of the effect of diffusion time.

From Figure 29, it can be seen that hydrogen conversion decrease significantly with an increase in H_C . In addition, the effectiveness also decreases with an increase in channel height. A reduction in both these indices causes a decrease in the unit cell efficiency. The reason behind the decrease in hydrogen conversion is clarified by considering $Da_{O_2,0}$ and $Pe_{O_2,0}$ numbers as a function of channel height shown in Figure 30. $Da_{O_2,0}$ does not change with channel height since the inlet residence and chemical times are unaffected by changes in channel height for a given inlet velocity. However with an increase in the height of the combustion channel, the time needed for a hydrogen (or oxygen) molecule to reach the walls, where the catalyst is deposited, increases. This time scale should be smaller than both residence and chemical times in order to obtain high conversion. As seen in Figure 30, $Pe_{O_2,0}$ increases with an increase in channel height and exceeds unity past a channel height of 500 μm , beyond which height diffusion becomes a limiting factor in hydrogen conversion. The combined effect of an unchanging $Da_{O_2,0}$ (albeit greater than one) and increased $Pe_{O_2,0}$ causes incomplete conversion for higher channel heights, leading to a decrease in effectiveness (lower driving temperature differential) and decreased unit cell efficiency.

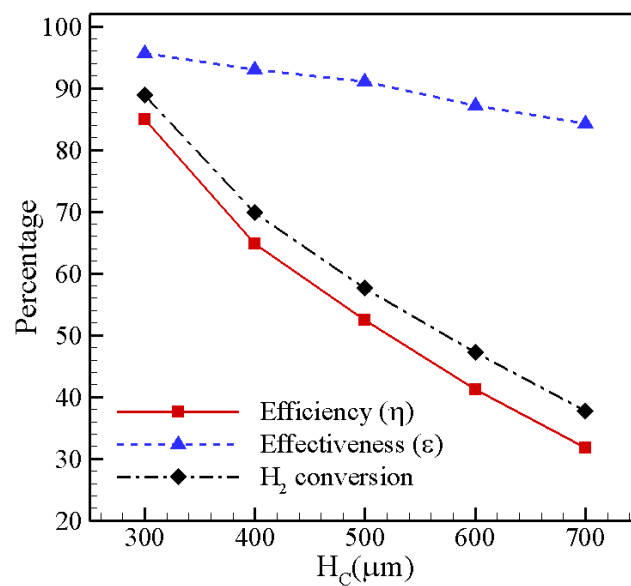


Figure 29: Variation of performance indices with combustion channel height

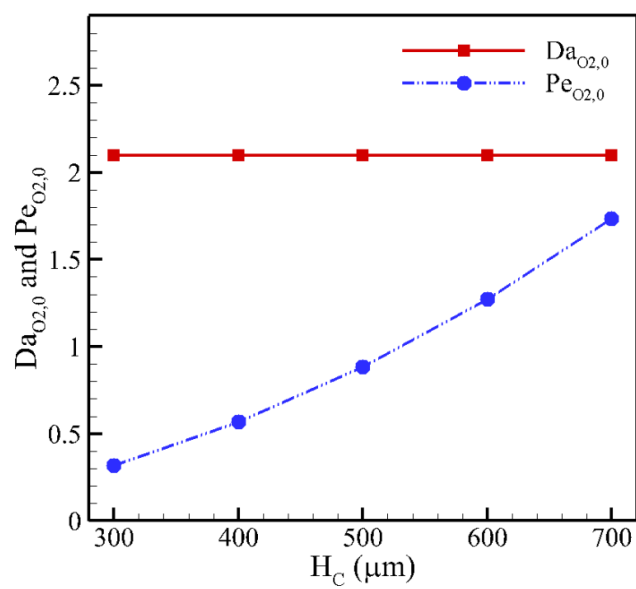


Figure 30: Variation of Damkohler and Peclet numbers with channel heights

4-6-5 Inlet gas velocity

Increase in the inlet gas mixture velocity, while keeping the equivalence ratio constant, causes an increase in the amount of input chemical energy rate as a consequence of the larger mass flow rate of hydrogen. The effect of increasing inlet velocity on η depends on the length of the catalyst and can be significant for small catalyst lengths. If the length of the catalyst bed is fixed, increasing gas inlet velocity decreases the residence time of gas molecules in the catalyst region. This reduction in residence time can have significant effect on fuel conversion and hence η if the reaction is not sufficiently fast. The values of parameters held constant in this parametric study are summarized in Table 7. Figure 31 shows the performance indices along with pressure drop as a function of inlet residence time. The x -axis of the plot is in logarithmic scale to show the values at lower residence times more clearly. Dotted lines and open symbols represent data that do not satisfy the constraints of exhaust or oil outlet temperatures; however, they are shown in the plot for a description of the effect of the parameter over a wider range of values. Efficiency and hydrogen conversion are seen to increase significantly with $t_{r, inlet}$ (decreasing inlet velocity) between 1.4 and 3.3 ms. The effectiveness variation from 90 percent at the low $t_{r, inlet}$, to 98 percent at larger $t_{r, inlet}$, is much less pronounced. The effectiveness and conversion trends indicate that the trends in the efficiency index are due to chemical time limitation being reached at low $t_{r, inlet}$ (higher inlet velocity). Increase in hydrogen conversion at higher residence times corresponds to higher $Da_{O_2,0}$. At higher $t_{r, inlet}$ pressure drop is lower since higher $t_{r, inlet}$ corresponds to lower inlet velocities. The effect decreasing inlet velocity on $Da_{O_2,0}$ and $Pe_{O_2,0}$ is similar to that obtained when increasing the catalyst bed length, and is represented in Figure 32. It is seen that $Da_{O_2,0}$ increases as a result of increasing $t_{r, inlet}$, while the value of $Pe_{O_2,0}$ decreases with an increase in $t_{r, inlet}$ and its value remains to be under one.

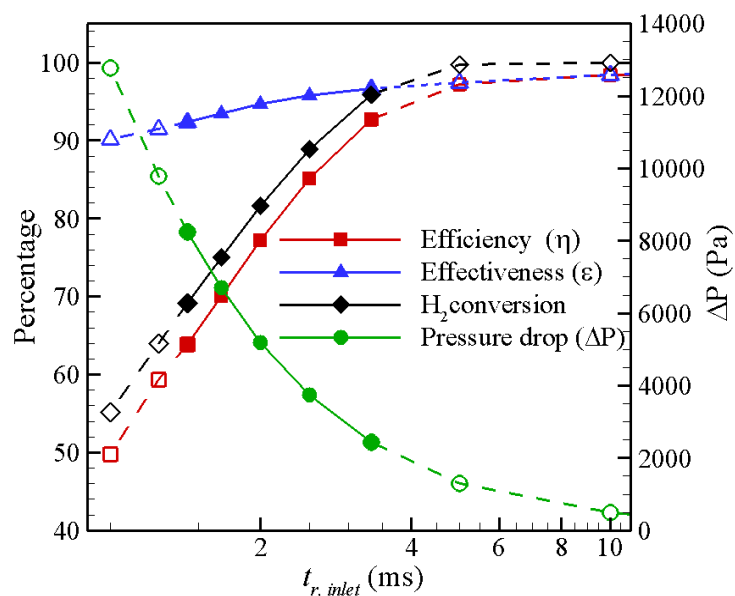


Figure 31: Variation of performance indices with inlet residence time, dotted lines and open symbols represent data that do not satisfy the constraints of exhaust or oil outlet temperatures; however, they are shown in the plot for a description of the effect of the parameter over a wider range of values.

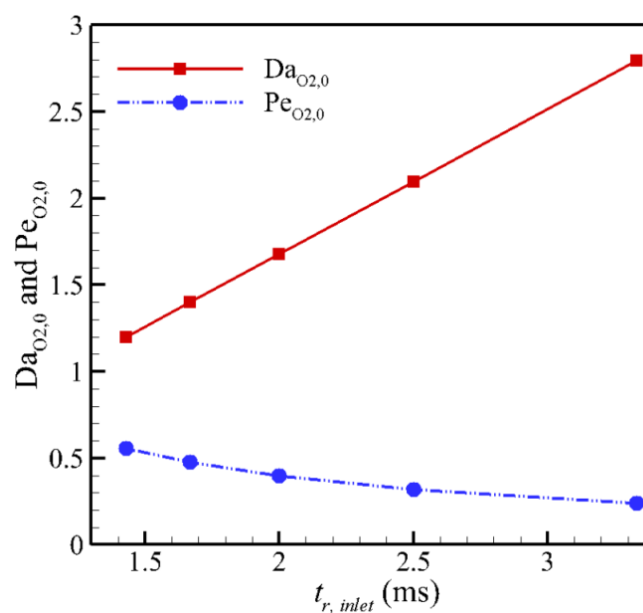


Figure 32: Variation of Damkohler and Peclet numbers with residence times

4-6-6 Equivalence ratio

As mentioned before, the equivalence ratio, ϕ , is defined as the ratio of the molar fuel-to-air ratio at the test conditions to that at stoichiometric conditions. Other parameters are kept fixed at values indicated in Table 7 and equivalence ratio is varied from 0.1 (fuel-lean mixture) to 1 (stoichiometric). Figure 33 shows how the performance indices and pressure drop change relative to the equivalence ratio. Although η does not change much by varying the equivalence ratio, there is a maximum at $\phi=0.6$. In the case of this parameter variation, η is affected by both ε and hydrogen conversion, which exhibit contrasting trends with equivalence ratio. Pressure drop increases with an increase in ϕ since streams with higher equivalence ratios have higher chemical power and produce more heat when reacted. Higher amount of reacted hydrogen increases the gas stream temperature and viscosity and hence the pressure drop.

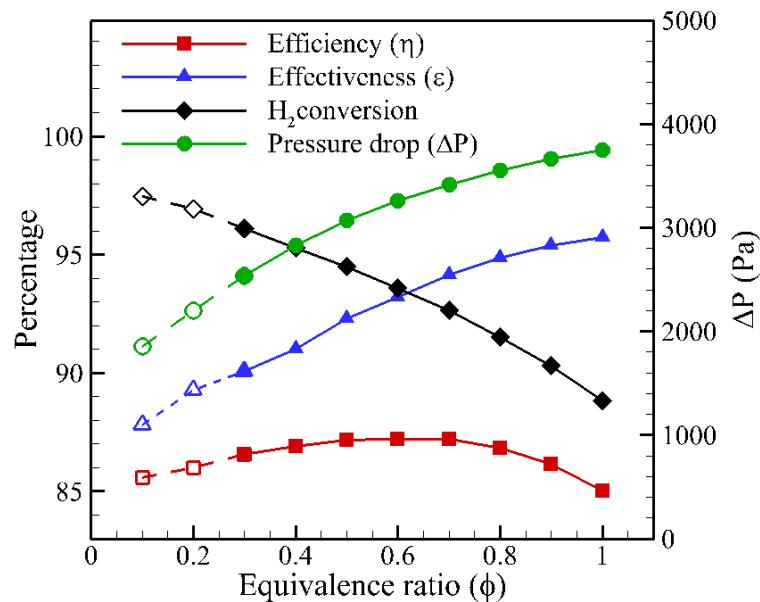


Figure 33: Variation of performance indices and pressure drop with equivalence ratio, dotted lines and open symbols represent data that do not satisfy the constraints of exhaust or oil outlet temperatures; however, they are shown in the plot for a description of the effect of the parameter over a wider range of values.

For a given fixed inlet velocity, a higher equivalence ratio results in more chemical energy rate at the combustor channel, resulting in larger heat generation. This larger heat release increases the local and average temperature within the combustor, which in turn increases the local velocity. Thus the local residence time is lower at higher equivalence ratios, resulting in a decrease in H₂ conversion. However, an increase in heat release at higher equivalence ratio causes a larger average temperature difference between the exhaust and oil channels thereby increasing the driving potential for heat transfer to oil. Hence, the effectiveness increases with equivalence ratio. Since η is influenced by both H₂ conversion and ε , which have contrasting trends with equivalence ratio, only a slight variation in this index is observed with a peak at $\phi=0.6$.

4-6-7 Oil inlet temperature

Variation of the oil flow rate or inlet temperature changes the boundary condition of the combustor microchannel and hence could affect hydrogen conversion and unit cell efficiency. Higher inlet oil temperature or lower mass flow rate would result in higher combustion channel wall temperatures. This increased temperature would cause a decrease in chemical time due to the strong influence of temperature on the reaction rate constant. At the same time, an increased combustor wall temperature increases the gas temperature within the combustion channel, thereby decreasing the residence time. The decrease in residence time and chemical time therefore compete against each other with respect to hydrogen conversion and provide the trends seen by variations in oil parameters shown below.

Figure 34 illustrates the variation of η with varying oil inlet temperature. Parameters held constant for this study are summarized in Table 7. Corresponding to the variation in inlet oil

temperature at a fixed mass flow rate, the oil outlet temperature varied from 540 K (for $T_{in, oil} = 300$ K) to 589 K (for $T_{in, oil} = 370$ K). Note that the film temperature of oil places a restriction on the higher value of oil temperatures; however, the extrapolated trends for higher oil temperatures are shown by the dotted lines up to an inlet temperature of 450 K. The figure shows that there is a slight reduction in η with increase in oil inlet temperature for the fixed parameters of this study. The conversion is seen to play a more important role in dictating the efficiency for this parameter variation. The trend in conversion indicates that the reduction in residence time has a stronger influence compared with the decrease in chemical time with an increase in oil inlet temperature.

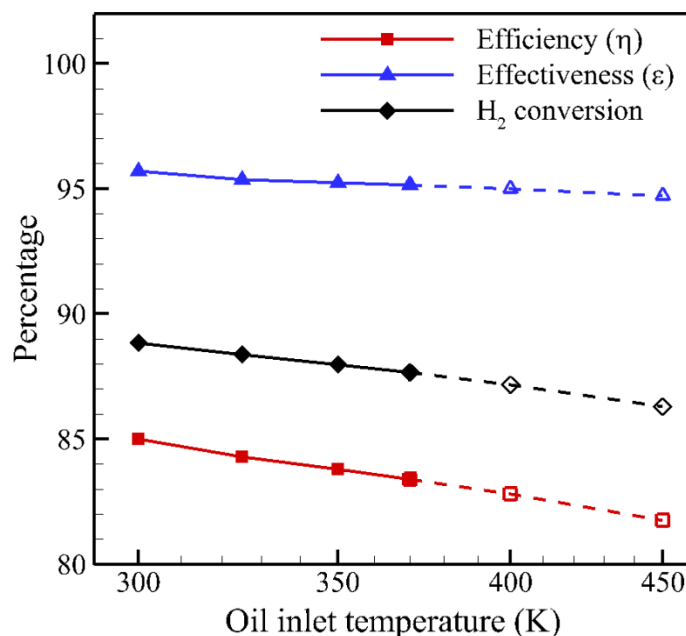


Figure 34: Performance indices as functions of inlet oil temperature, dotted lines and open symbols represent data that do not satisfy the constraints of exhaust or oil outlet temperatures; however, they are shown in the plot for a description of the effect of the parameter over a wider range of values.

Inlet and outlet oil temperatures from the combustor are parameters of relevance for the automotive hydrogen storage application. For the particular application of sodium alanate

hydrogen storage, desorption occurs in a narrow temperature range of approximately 433 K (160 °C) to 453 K (180 °C). Simulation results showed that with the inlet oil temperature of 433 K and outlet oil temperature of 453 K with oil inlet velocity of 0.105 m/s, a 15 mm catalyst bed gives 99 percent conversion with an efficiency of 96 percent.

4-6-8 Oil inlet velocity

The mass flow rate of oil within each unit cell determines the number of unit cells, such as those shown in Figure 16, which would be required for a multi-kilowatt heating application. The exit oil temperature would typically be specified by the application and hence it is important that the μ CHX be able to operate at high efficiencies for a variety of exit temperatures, and consequently, mass flow rates. Combustion channel height, inlet gas mixture velocity and oil inlet temperature are kept constant as indicated in Table 7. The results of this parametric study, summarized in Table 10, shows that increasing oil velocity by three fold varies the oil exit temperature from 382.4 K to 529.6 K. However, there is little variation in the hydrogen conversion and effectiveness and consequently the unit cell efficiency. For the range of flow rates studied herein, this trend in conversion indicates that the variation in residence time and chemical time balance each other.

Table 10: The effect of changing oil inlet velocity on the performance indices

V_{Oil}	η	ε	H ₂ conversion	Exit oil temperature (K)
0.01	0.85	0.96	0.89	529.6
0.02	0.86	0.96	0.90	421.1
0.03	0.87	0.96	0.90	382.4

4-7 Performance Map

From a practical standpoint, it is of interest to identify regions in the parameter space where the μ CHX can operate with high efficiency. Another important consideration is to find regions of operation where the pressure drop in the gas side is not so significant that the use of a compressor, as opposed to a fan or a blower, is warranted. For the geometry studied in this paper, the overall efficiency of the system is very much dependent on the hydrogen conversion; this section presents a correlation and a performance map for hydrogen conversion in terms of dimensionless numbers.

Based on the estimates of conversion from simulations, a predictive correlation for hydrogen conversion was developed,

$$\text{Con}_{H_2} = 1 - 0.45 \sqrt{\frac{\phi H^* \text{Pe}_{O_2,0}}{\text{Da}_{O_2,0}}} \quad (46)$$

where H^* is the height ratio, $H^* = H_C/H_b$ ($H_b = 3 \times 10^{-4}$ m) and all the dimensionless numbers are found at the inlet of the channel. Equation (46) was developed by identifying the important dimensionless numbers and curve fitting the numerical results.

The correlation is valid for the μ CHX unit cell geometry shown in Figure 16 for 25 different simulation conditions. These conditions consist of the range of parameters summarized in Table 8, as well as 4 fluidic conditions for the channel height of 700 μm and 4 other fluidic conditions for the channel height of 500 μm . These 8 data points are added to cover a larger span of

hydrogen conversions and to increase the precision of the estimate. Figure 35 compares predicted hydrogen conversions to the conversions determined from the simulations and indicates that Eq. (46) can predict all numerical results within $\pm 10\%$ error.

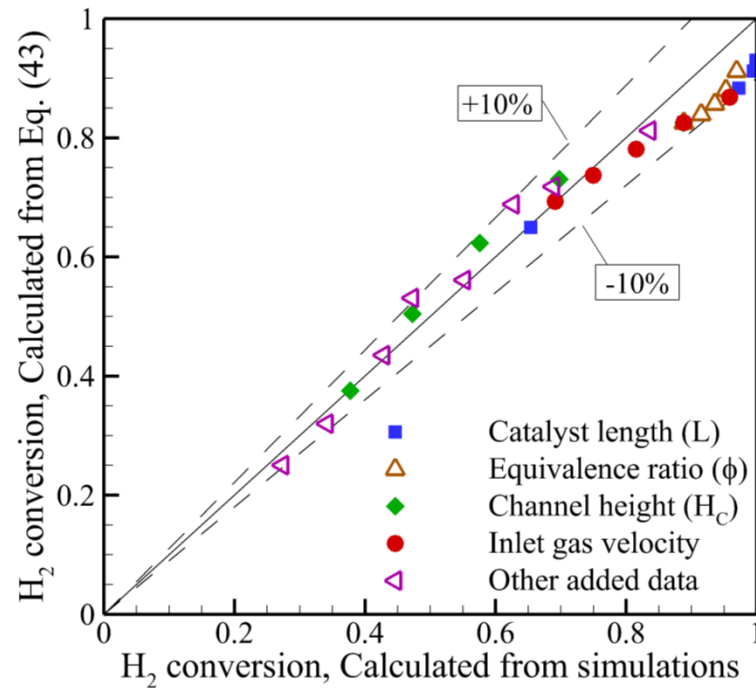


Figure 35: Parity of conversions estimated from simulations and conversions predicted by Eq. (46)

As suggested by Eq. (46), a high hydrogen conversion can be achieved by increasing $Da_{O_2,0}$ and decreasing $Pe_{O_2,0}$. Other than these two numbers, channel height ratio (H^*) and equivalence ratio (ϕ) are also of significance. An increase in both these parameters has a negative effect on hydrogen conversion. A more visual indication of the regions of high efficiency is provided by a contour map of hydrogen conversion in Figure 36. For this plot, the dimensionless numbers appearing in Eq. (46) are divided in two parts. The term $\sqrt{H^* \cdot Pe_{O_2,0}}$ has the physical terms in it

while $\sqrt{\phi/Da_{O_2,0}}$ has more chemical meaning. The small circles in the plot show the data points that were used to generate the plot.

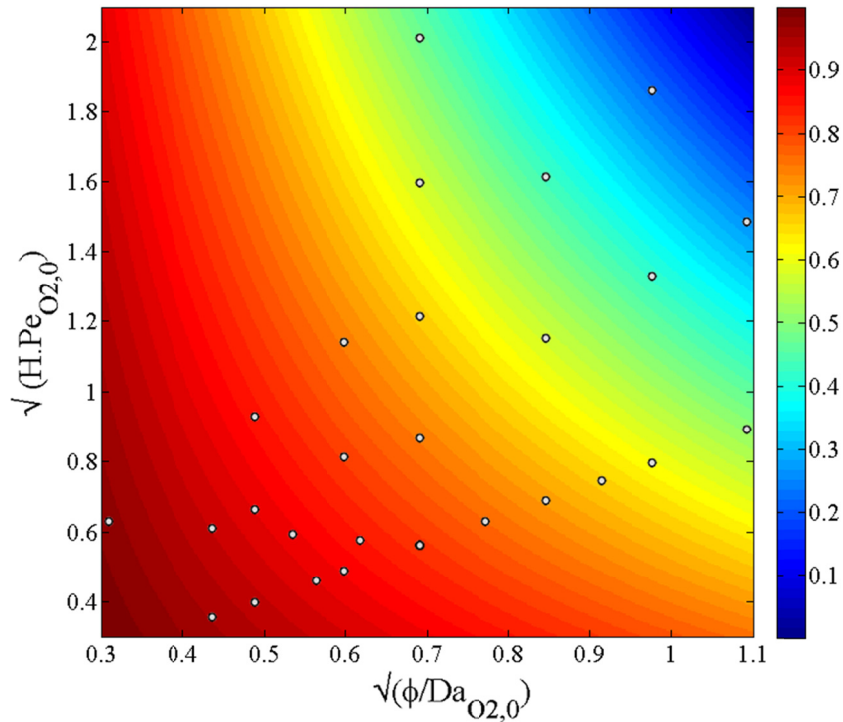


Figure 36: Contours of H₂ conversion based on numerical data from this study

It can be seen from Figure 36 that hydrogen conversion is affected by both physics and chemistry of the problem and for high conversion, one should try to operate the combustor in the lower left side of the plot, i.e. lower values of $\sqrt{H^*.Pe_{O_2,0}}$ and $\sqrt{\phi/Da_{O_2,0}}$.

Pressure drop is also important when designing a combustor and should be considered along with hydrogen conversion. A contour map of pressure drop of the simulated cases is plotted against the same parameters in Figure 37. It should be noted that this plot shows the pressure drop in the

combustor channel and not in the entire combustor-heat exchanger. It can be seen that lower

$\sqrt{\phi/Da_{O_2,0}}$ and higher $\sqrt{H^*.Pe_{O_2,0}}$ has lower pressure drop.

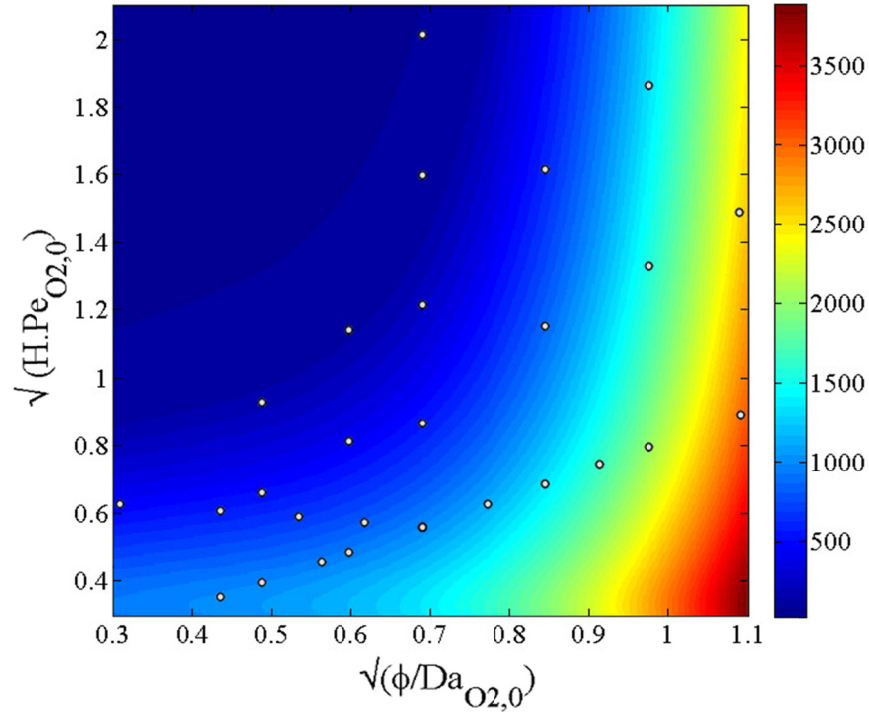


Figure 37: Contours of pressure drop (in Pa) in the combustor channel

Lower inlet velocities causes higher residence times therefore higher Da_0 and lower $\sqrt{\phi/Da_{O_2,0}}$, so the lower is $\sqrt{\phi/Da_{O_2,0}}$, the lower is pressure drop. Higher channel heights reduces pressure drop as well. On the other hand, the higher is the equivalence ratio, the more heat is generated inside the channel and the higher is the average temperature, that causes higher velocities and viscosities and as a results higher pressure drop.

Based on the conversion map, it can be concluded that lower channel heights (lower $\sqrt{H^* . Pe_{O_2,0}}$), lower inlet velocities and longer catalyst beds (lower $\sqrt{\phi / Da_{O_2,0}}$) lead to higher conversions; however, depending on the systems application and limitations, pressure drop may place a constraint on the operating space. Considering both contours of hydrogen conversion and pressure drop, the parametric space for the μ CHX operation can be divided into four regions as shown in Figure 38.

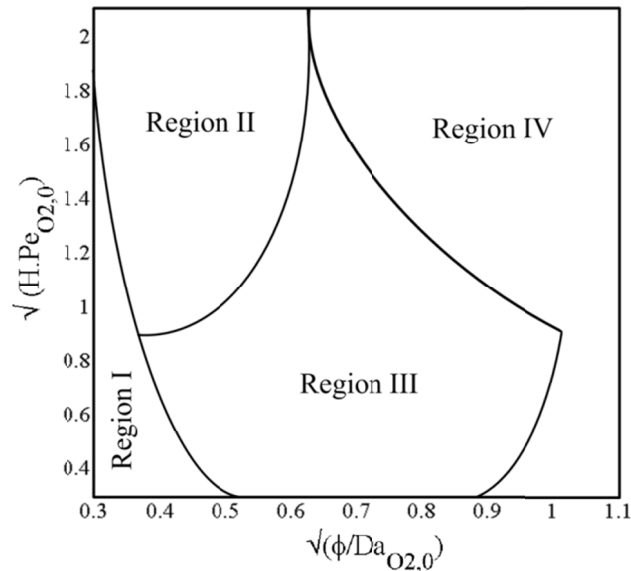


Figure 38: Performance map indicating different regions of operability based on H₂ conversion and ΔP - The regions are described in Table 11.

Error! Not a valid bookmark self-reference. summarizes the description of these regions and gives examples of physical parameters that one can use to attain the performance characteristics indicated by that region.

In cases where very high efficiencies are necessary and pressure drop is of secondary importance, region I is the best choice. If both high efficiencies and lower pressure drop is considered, region II satisfies the needs. Region III has moderate efficiencies and pressure drop and Region IV has either poor efficiencies or high pressure drops, and one should avoid using the μ CHX in this region. As an example of the scale of a multiple unit cell device, consider a device operating point within region I. Assuming a 10 mm width of the unit cell, 30 μ CHX unit cells of the dimensions as shown in Figure 16 would be required for a 1 kW device. The total mass flow rates of H_2 /air mixture and oil in this device would be 0.29 g/s and 1.4 g/s, respectively. The pressure drop in the combustion channels, as estimated using two-dimensional simulations, would be 1 kPa and the efficiency of the device would be 95.7 %. In such a multiple unit cell device, in addition to the performance of the unit cell as discussed in this section, fluid headering schemes that ensure compactness while providing for uniform flow distribution amongst unit cells is also an important consideration. These considerations are discussed in Chapter 5.

Table 11: Different regions (Figure 38) and their performance ranges

Region	H_2 conversion	ΔP (Pa)	Example of physical variable combinations
I	H_2 conversion > 90%	$\Delta P < 1000$	$H^* < 1, \phi < 0.5, L > 20$ mm, Low velocities
II	$60\% < H_2$ conversion < 90%	$\Delta P < 500$	$H^* > 1.67, L < 20$, Low velocities
III	$60\% < H_2$ conversion < 90%	$500 < \Delta P < 2500$	$H^* < 1.67, \phi > 0.5$, High velocities
IV	H_2 conversion < 60%	$\Delta P > 2500$	

4-8 Design and Simulations of a CA μ CHX Unit Cell

As mentioned in chapter 1, the purpose of the developed CA μ CHX is to add more heat to the H₂ stream to increase its temperature from -73 oC (200 K) to -40 oC (233 K) prior to entering the fuel cell under cold start conditions. The desired operating conditions for the device are shown in Table 5 of chapter 1. A fraction of the incoming cold hydrogen gas would be premixed with air and reacted in the combustion channels to provide the thermal energy rate needed to increase the temperature of the rest of the hydrogen flow from 200 K to 233 K flowing in the HX channels. The hydrogen flow rate to the fuel cell could vary between 0.5 g/s to 2 g/s and the working pressure could vary between 5 to 20 bars. For the cold start condition, the environment, from which air is drawn for the combustion process, is assumed to be at 233 K (-40°C) and has a pressure of 1 bar. The unit cell design is first described followed by a parametric study to achieve the desired working conditions.

4-8-1 Design

Each unit cell of the CA μ CHX was designed to perform at a minimum, unit operations of combustion and heat exchange to the working fluid. To produce a high specific power within the device, an equivalence ratio of unity was considered. The large equivalence ratio also resulted in reduced pressure drop for the same thermal power generated when compared with lower equivalence ratio mixtures. In the initial design a combustion channel was surrounded on both sides by heat exchange channels, similar to Figure 14. Results from simulations (described in section 4-8-2) for such a unit cell design showed that the flow of the -73 °C (200 K) hydrogen gas

in the heat exchange channels reduced the temperature of the catalytic walls and prevented catalytic combustion. Therefore, there was need for a thermal buffer between the combustion and hydrogen channels, previous experience showed that the exhaust channels can provide the buffer needed. In addition, the recuperation section from the MH μ CHX was also added since the incoming gas would be at a much lower temperatures of $-40\text{ }^{\circ}\text{C}$ (233 K). The unit cell design in Figure 39 consists of a central combustor microchannel surrounded by two exhaust gas channels on either side. The heat exchange channels are on either side of the exhaust gas channel. The added length to the exhaust channels for recuperation was adjusted based on a constraint that the exhaust gas exit temperature remained greater than $100\text{ }^{\circ}\text{C}$ (373 K) - a requirement that was imposed in order to avoid condensation.

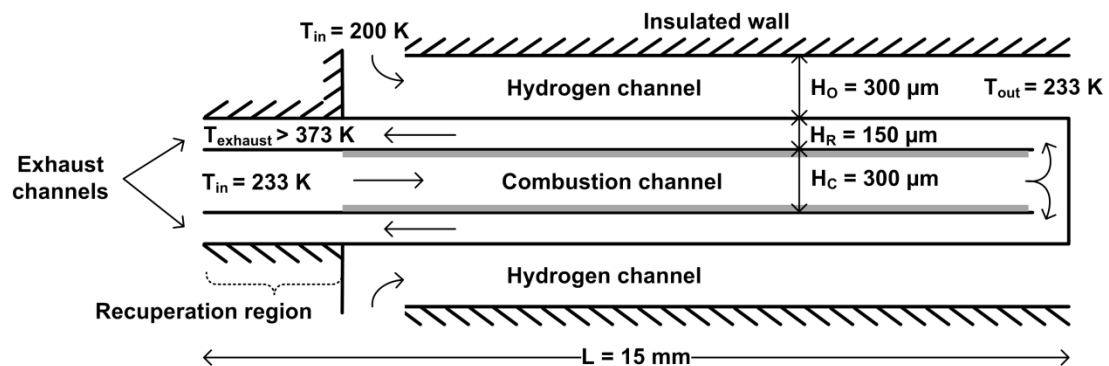


Figure 39: A schematic of a unit cell of the CA μ CHX with the catalytic beds shown as gray lines

The combustor and hydrogen channel heights are $300\text{ }\mu\text{m}$ each and exhaust channel height is $150\text{ }\mu\text{m}$. The width of all channels in the unit cell is assumed to be 2 mm while the length of the unit cell was kept at 15 mm , instead of 30 mm for the μ CHX design for the metal hydride system (Figure 16). Based on simulations, this length was found to provide sufficient area for heat exchange between the exhaust and cold gas channels while keeping the pressure drop low. All

outer walls were considered insulated and the inner walls of the combustor are partially covered with platinum catalyst. The location of the catalyst is shown by gray line in Figure 39.

Initially the catalyst beds were located on the walls of the combustion channels alone; however simulations showed that almost half of the catalyst length was not being efficiently utilized because of the low mixture temperature. Despite the thermal buffer provided by the exhaust gas channels, the cold hydrogen gas flow in the heat exchange channels tended to decrease the mixture temperature rapidly past the initial part of the catalyst bed. As a result, hydrogen conversion was 67.3 percent. The case is with the inlet hydrogen temperature, mass flow rate and pressure of 200 K, 2 g/s and 5 bar, respectively. Temperature contours of the unit cell are shown in Figure 40. The hot region at the starting point of the catalyst bed (Figure 39) can be seen. After that, the hot reacting flow transfers heat to the cold hydrogen stream reducing its temperature significantly. The second half of the combustion channel was so cold (<300 K) that almost no reaction occurs. The recuperation length, on the other hand, was enough to absorb the excess heat in the exhaust gas and increase the temperature of air/H₂ mixture to 458 K. This preheating played an important role in sustaining the reaction along with the thermal buffer provided by the exhaust channels.

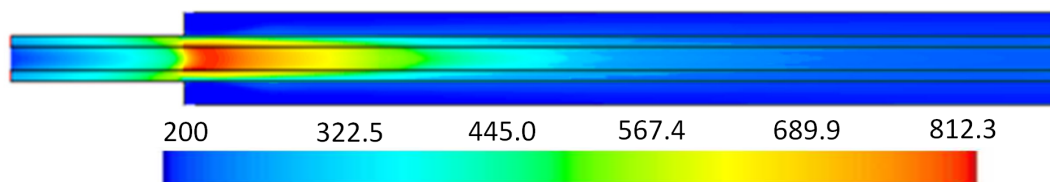


Figure 40: Temperature contours for the CA μ CHX unit cell (K), catalyst located in the combustion channel

Hydrogen mass fraction along the combustion channel is shown in Figure 41. It shows that hydrogen mass fraction almost remained constant at 0.00925 in the last 5 mm of the channel although catalyst existed in that length. The hydrogen conversion was 67.3 percent for this case.

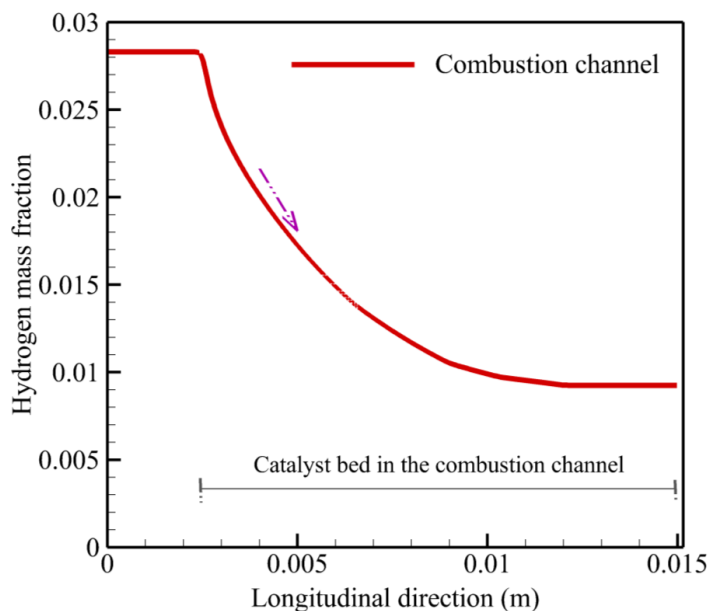


Figure 41: Hydrogen mass fraction along the length of the combustion channel

In order to obtain higher conversions while managing the amount of catalyst used, a novel catalyst bed arrangement was used. The basic premise of the new arrangement was that higher gas mixture and catalyst bed temperatures result in higher reaction rates and hence more complete hydrogen conversion. To achieve this larger catalyst temperature, the catalyst bed was redistributed such that two fifth of the catalyst bed was shifted from the end of the combustion channel and placed in the exhaust channels. The location of the catalyst within the exhaust channels coincided with the location of the catalyst in the combustion channel as shown in Figure 42. With this new arrangement of catalyst, hydrogen conversions of about 99% were achieved

with the 15 mm long channels and a total catalyst length of 12.5 mm distributed on each wall separating the combustor and exhaust channels.

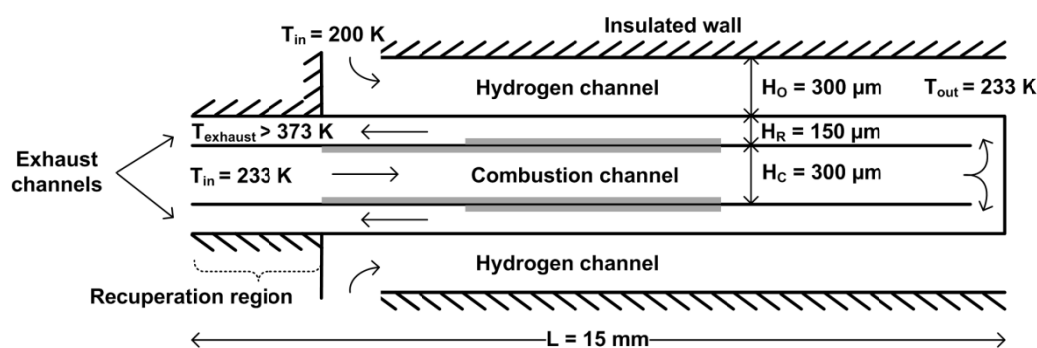


Figure 42: A schematic of a unit cell of the μ CHX for cryo-adsorbent systems with distributed catalyst with the catalyst beds shown as gray lines

A representative temperature contour plot within the unit cell for the same condition as Figure 40 is shown in Figure 43. The temperature contours indicate regions of high temperatures at the catalyst bed due to heterogeneous combustion. Fluid and surface temperatures reached a peak value near the first one-third length of the catalyst bed within the combustor and then decreased downstream due to the transfer of heat to the exhaust and heat exchange channels. For this condition, outlet hydrogen and exhaust gas temperatures were 235.7 K and 391.5 K, respectively.

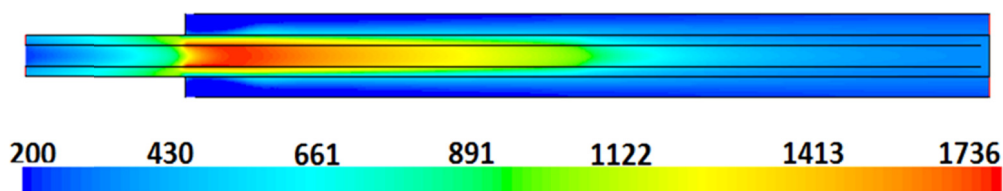


Figure 43: Temperature contours for the cryo-adsorbent μ CHX unit cell (K), segmented catalyst

Figure 44 illustrates the cross-sectional averaged hydrogen mass fraction distribution in the unit cell. The location of the catalyst beds in both the combustor and exhaust microchannels are represented in this plot for clarity. Hydrogen/air mixture enters the combustor with hydrogen mass fraction of 0.0283, corresponding with an equivalence ratio of unity. After going through the catalyst bed in the combustor channel, the mass fraction reduces to 0.0054 indicating that the hydrogen conversion is 81% within the combustor channel. The remaining hydrogen reacts in the catalyst bed in the exhaust channel such that the mixture exits the unit cell with less than 1% of the initial hydrogen content.

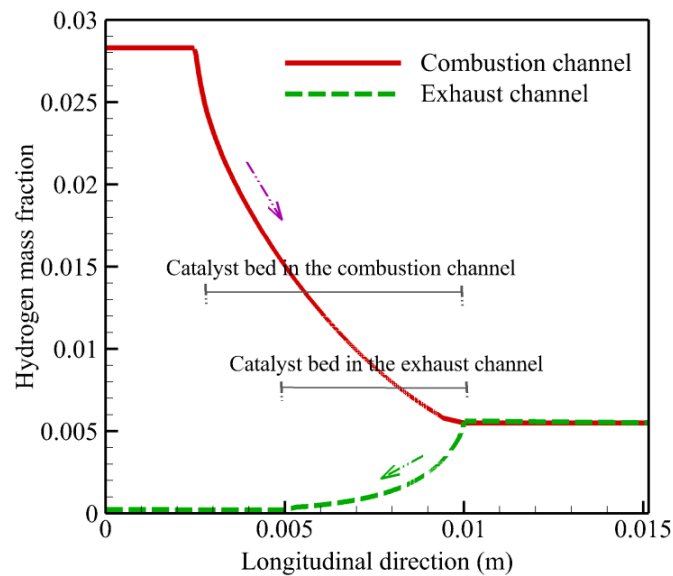


Figure 44: Hydrogen mass fraction along the length of the combustor and exhaust channels

4-8-2 Numerical simulation procedure

The same validated Fluent model as the MH μ CHX was used for the unit cell geometry indicated in Figure 42. The reactant gases entering the channel were modeled as comprised of a hydrogen

and dry air (approximated as a 21 percent by volume oxygen and 79 percent by volume nitrogen) mixture. The mass fraction of species at the inlet is defined by the equivalence ratio. The governing equations and boundary conditions were solved in FLUENT V14 in conjunction with Chemkin-CFD for the chemical reactions.

Based on the required mass flow rate of cold hydrogen in Table 5, the first step in a unit cell simulation was to determine the flow rate of cold hydrogen and flow rate of hydrogen in the combustion channels within each unit cell. Based on previous work with MH μ CHX, the initial inlet mixture velocity to the combustion channel was initially selected to be 4 m/s. The inlet velocity of the cold hydrogen stream in the HX channel was set arbitrarily to a value. The exit temperature of cold hydrogen stream was checked against the requirement in Table 5 (> 233 K). Simultaneously, the hydrogen conversion was verified to be in excess of 90 percent. If the exit temperature was found to be lower, the flow rate of cold hydrogen was lowered. If the hydrogen conversion was found to be lower, the inlet mixture velocity of the combustion gases was lowered. Once conditions that met both the cold hydrogen exit temperature as well as conversion were achieved, the fraction of hydrogen stream required for combustion to that being heated in the heat exchange channels was determined. Based on the ratio of the maximum mass flow rate of the cold gas in the μ CHX to the mass flow rate in each unit cell, a total number of 165 unit cells with the channel width of 2 mm was found to be sufficient to provide heat to 2 g/s of cold hydrogen. For lower mass flow rate limit of 0.5 g/s in Table 5, the same number of unit cells was retained, with a corresponding decrease in velocity of the cold hydrogen and combustion mixture gases. For example, at a pressure of 5 bar the flow rate of cold hydrogen gas through each of the 165 unit cells were 6.1 mg/s and 1.5 mg/s for a total flow rate of 2 g/s and 0.5 g/s, respectively.

4-8-3 Parametric variations

Limited parametric variation on the HX side was performed. In the unit cell simulations, based on the requirements stated in Table 5, three parameters were varied- the inlet pressure, mass flow rate of the cold hydrogen gas through the HC channels and also the heat exchange fluid. Table 12 summarizes the achieved conversions and unit cell efficiencies for the extremities in the range of the desired pressures and hydrogen mass flow rates presented in Table 5. It can be seen that the HX hydrogen exit temperature in all cases is in excess of 233K and that the conversions and efficiencies are in excess of 99% and 92%, respectively. Pressure drop values within the combustor and exhaust channels are also shown in Table 12. A larger cold hydrogen mass flow rate requires a proportionally larger hydrogen/air mixture flow rate, thereby increasing the pressure drop in the combustor-exhaust channels with increase in cold hydrogen mass flow rate. However, pressure drop is almost independent of the working fluid pressure because the mass flow rate of hydrogen is kept the same for both 5 bar and 20 bar. The slight increase in pressure drop with higher pressure is a result of the larger specific heat value at higher pressures. With the temperature difference between the inlet and exit fixed at 33 K, a larger C_p resulted in an increase in the amount of heat rate needed and hence a slightly larger flow rate of hydrogen-air mixture within the combustion channels.

Table 12: Simulation results for the desired pressure and hydrogen mass flow rate ranges shown in Table 5

\dot{m}_{H_2} (g/s)	P_{H_2} (bar)	T_{out,H_2} (K)	H ₂ conversion (in combustor) (%)	η (%)	ΔP (Pa)	Da	Pe
2	5	235.7	99.8	93.3	5736.3	3.80	0.206
	20	236.1	99.5	92.9	5833.9	3.80	0.206
0.5	5	237.7	99.8	92.4	991.6	14.24	0.055
	20	243.8	99.4	92.1	1014.4	14.24	0.055

One of the objectives of the work in this dissertation is to experimentally characterize a multi-unit cell CA μ CHX's performance. In the laboratory, for safety purposes, cold nitrogen gas is to be used in place of cold hydrogen gas as the heat transfer fluid. Since density and thermal properties of nitrogen are considerably different from those of hydrogen, simulations were performed using cold nitrogen gas on the same unit cell geometry (Figure 42).

There are two thermal resistances in the path for the requisite amount of heat to be transferred within the unit cell from the heat exchange wall (separating the exhaust and heat exchange channels) to the cold gas. The first one pertains to the convection resistance, $R_{\text{conv}} = 1/(h_{\text{coldgas}}A)$, while the second one is the resistance due to heating of the cold gas stream, $R_{\text{heat}} = 1/(\dot{m}C_p)$. For the range of hydrogen flow rates considered, the flow is laminar and hence the heat transfer coefficient, assuming fully developed flow, is constant at about 1120 W/m²-K. The R_{conv} and R_{heat} for cold hydrogen flow within each unit cell are therefore estimated at 35.7 K/W and 5,926 K/W respectively. The R_{heat} estimate is based on a working pressure of 5 bar and for a flow rate of 2 g/s. Since R_{heat} is the dominant thermal resistance in transferring heat to the cold gas, in order to preserve the same representative thermal conditions as cold hydrogen flow, it is clear that the R_{heat} between hydrogen and nitrogen flows has to be matched. Hence, the heat capacity rates ($1/R_{\text{heat}}$) between the cold hydrogen and cold nitrogen flows, as well as the temperature rise (see Table 5) were kept identical. This meant that, because of the high specific heat of hydrogen compared to nitrogen ($C_{p_{H_2}} = 13.02 \cdot C_{p_{N_2}}$), the nitrogen mass flow rate would be proportionally higher than hydrogen mass flow rate. This larger flow rate resulted in a R_{conv} of 35.0 K/W and a R_{heat} of 5,974 K/W for the cold nitrogen stream at a working pressure of 5 bar and flow rate of 26.1 g/s (~13 times the maximum cold hydrogen flow rate).

Table 13 shows the result of the simulations with nitrogen as the cold working fluid. The working pressure was fixed at 5 bar for these simulations. Nitrogen mass flow rate of 26.1 g/s and 6.57 g/s have the same heat capacity rate as 2 g/s and 0.5 g/s of hydrogen, respectively. The hydrogen conversion remains largely unaffected by changing the heat exchange fluid as long as the thermal resistances are matched. This result is to be expected since changing the heat exchange fluid only changes the boundary condition on the combustion process. When the heat capacity rates are matched, the temperature drop along the heat exchange channels would remain similar for both cold hydrogen and cold nitrogen cases, thereby causing little variation in the hydrogen conversion. It can also be seen that the unit cell efficiency remains unchanged between the two cases which is an indication that the convective resistances on the exhaust and cold gas channels are smaller than that of the thermal resistance along the cold gas channel ($1/\dot{m}C_p$). Table 13 shows that, similar to cold hydrogen flow, pressure drop in the combustor and exhaust channels are higher when the cold working fluid flow rate is higher.

Table 13: Simulation results for nitrogen as the working fluid for the cryo-adsorbent μ CHX

\dot{m}_{N_2} (g/s)	P_{N_2} (bar)	T_{out,N_2} (K)	H ₂ conversion (in combustor) (%)	η (%)	ΔP (Pa)	Da	Pe
26.1	5	233.6	99.9	93.1	5133.7	4.47	0.175
6.57	5	233.3	99.8	92.4	711.8	17.26	0.045

Simulations performed for the CA μ CHX have boundary conditions that positioned them in Region-I of the performance map presented in Figure 38. Therefore it was expected to have very high hydrogen conversions. The proposed equation (Eq. (46)) was tried with the results presented in Table 12 and Table 13, and the hydrogen conversions of the CA μ CHX were predicted within $\pm 10\%$. That extends the applicability range of the equation to colder boundary conditions. It

should be noted that when calculating the Peclet number, diffusion time was averaged between the combustion and exhaust channels since they have different channel heights.

5- DEVICE LEVEL DESIGN AND FABRICATION OF A MULTI-WATT μ CHX

In the following sections, design and fabrication of a μ CHX for the cryo-adsorbant systems are described. Unit cell proof of concept tests for MH μ CHX are presented in a thesis by David Haley [55].

The design involves use of several repeating unit cells that each performs three unit operations- combustion, recuperation, and heat exchange (Figure 16). Heterogeneous catalytic combustion occurs on the walls of microchannels in the presence of a platinum catalyst. μ CHX that is capable of producing and transferring about a 100 W to 200 W of thermal energy rate was designed and fabricated. The device consists of several stainless steel layers that are chemically etched to form the channels. The shims are designed to be diffusion bonded. A description of the fabrication process is presented in section 5-1. Section 5-2 presents the device level design while section 5-3 the details of the fabricated CA μ CHX . Platinum catalyst is deposited selectively within regions of the device to provide high conversion while minimizing the use of the catalyst.

5-1 Fabrication Steps

Fabrication of such a device involves several processes like machining, laser cutting, chemical etching, welding, diffusion bonding, and wet deposition. The method and limits of three of these processes are described here. The rest are described throughout this dissertation.

5-1-1 Microlamination

Over the past few decades, sheet lamination techniques have been used to fabricate a variety of complex geometric structures that were difficult to manufacture with conventional techniques. Each lamina is machined with a two-dimensional pattern so that when the laminae are bonded together they form a functional solid geometry. The microlamination procedures involve the forming, alignment and bonding of thin metal laminae [56]. A microlaminated device consists of several layers or shims with microstructures. The shims are usually made with interconnecting features that let the fluid flow through different shims. The shims are joined or bonded together to make a sealed setup. Different bonding methods can be used such as brazing, welding and diffusion bonding.

5-1-2 Chemical etching

Chemical etching is one of the most prevalent methods of creating features and is the method used in this dissertation. Chemical etching is the process of selective removal of a material by chemical action. The process can be used to produce small scale features in a short timeframe; it leaves no burrs or stresses. Chemical etching can be used to create features on shims that define the flowpaths of different fluids. For example in the case of this project, the removed (etched) parts construct the microchannels and the height of the channels is the etching depth. But it has its own limitations the form constraints in the design of a micro device (thermofluidic).

In the process, the part (shim) is partially covered with a mask with the to-be-etched area being exposed. The part then is submerged in a chemical bath while being connected to an electrical current. Different shim materials may need different solutions, for example oxalic acid can be

used to etch stainless steel. Density of the current (Amp/cm^2), the molarity of the solution and etching time are the three main factors in chemical etching.

Great Lakes Engineering, in Maple Grove, Minnesota performed chemical etching of the shims for this μCHX . The design requirements for chemically etched parts as identified by them are summarized in here. The best achievable tolerance is $\pm 0.010\%$ of the metal thickness. For example, if the shim thickness is $600\ \mu\text{m}$, the best tolerance is $\pm 6\ \mu\text{m}$.

When etching through the metal thickness, for every 0.001 etched down into the metal, there is a lateral etch of 0.00025 per hole side (a hole has two sides). The corners are also restricted by the thickness of the material. The standard rule is that the radius of the corner cannot be smaller than 60% of the shim thickness. For example, a $600\ \mu\text{m}$ stainless steel shim will have corners with $360\ \mu\text{m}$ radius. A comparison between a designed channel geometry and the etched channel is shown in Figure 45.

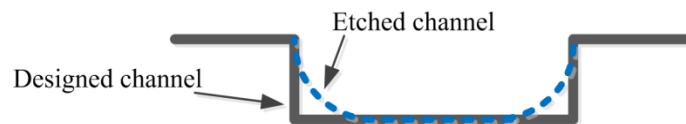


Figure 45: Designed channel versus etched channel

5-1-3 Diffusion bonding

Diffusion bonding is the process of joining two or more shims at very high pressures and temperatures. During the process, the atoms of two solid, metallic surfaces intermingle under pressure over time. No material is added in this technique and the joint exhibits both the strength and temperature resistance of the base metal.

The primary variables controlling diffusion bonding are pressure, temperature, surface finish and surface cleanliness. Typical contact pressures are 500 to 5,000 psi (34.4 bar – 344.7 bar) at temperatures of 60% or more of the melting temperature of the metal [57]. In this project, while experiments were performed by securing the shims with bolts, different bonding considerations were taken into account since an actual μ CHX would be diffusion bonded.

The restriction that diffusion bonding applies is that there should be enough contact between the two metals to provide the desired seal. In addition, pressure needs to be transferred from the top (where the pressure is exerted) to the bottom through all the walls that needs to be bonded. It means a bond between two surfaces is desired, the immediate top and bottom need to be either metal or a small gap. The size of the gap cannot be more than 7 times the thickness of the shim [58]. The schematic shown in Figure 46 describes this limitation. When pressure is exerted from top, the existence of fluid channel in the fluid shim does not let a uniform pressure distribution along the contact surface of shim #1 and shim #2. The wider is the channel; the worse is the pressure distribution. In order to have a sealed diffusion bonding at point (X), a to b ratio should not be higher than 7.

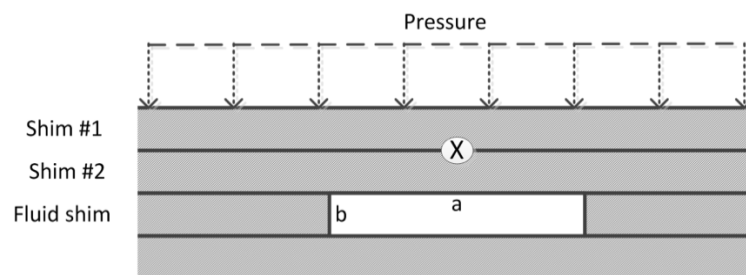


Figure 46: Schematic describing the diffusion bonding limitation

5-2 Device level Design and Fabrication

5-2-1 Layer design

The etching and bonding constraints were taken into account in the device level design presented herein. The device level design consists of the layer (shim) design as well as the headering that provides and removes fluid from multiple layers. 2D simulation results presented in Chapter 4 showed that 15 mm long channels with 300 μm height can provide over 99% hydrogen conversions and heat transfer to the cold working fluid. Furthermore, shim thickness of 600 μm was used to be etched 300 μm . Lower shim thicknesses could reduce the rigidity of the device and for the first generation; it was an endeavor to reduce the causes of failure. And thicker shims would increase the weight and fabrication costs. Since the simulations were carried out in 2D, the width of the channels remained unknown. As described in Section 5-1-3 *Diffusion bonding* the maximum width is limited by diffusion bonding requirement. With the channel height being 300 μm , the gap could not be higher than 2100 μm ($7 \times 300 \mu\text{m}$). Thus, 2 mm channel width was chosen. Knowing the height and width of the channel with the optimum velocity found from simulations, heat transferred to the cold nitrogen stream in each unit cell was found to be 5.42 W. In order to heat 26.1 g/s of nitrogen flow from 200 K to 233 K, a total of 165 unit cells would be required. However for the experiments performed here, only 16 unit cells were used.

Per the schematic in Figure 42, it is clear that a single unit cell would have to span 5 layers. The central layer would house the combustor microchannel, which would be surrounded by two exhaust gas layers and two heat exchange layers. Since the width of the microchannels within each unit cell is only 2 mm, several unit microchannels can be positioned alongside each other in

a single layer and the 5 layers can be stacked together to form blocks of unit cells. An example of the 5 layers comprising of unit cells is shown in Figure 47. The set of 8 unit cells have the overall dimensions of $24 \text{ mm} \times 73 \text{ mm} \times 3 \text{ mm}$. The flow direction of each of the streams is shown for one half of the unit cells. It can be seen that the H_2/air mixture and cold nitrogen streams flow in the same direction while the exhaust gases flow counter to the others. The positioning of the exhaust and inlet hydrogen-air mixture headers provided for preheating of the cold hydrogen-air mixture prior to the catalyst location in the combustor channel. Moreover, N_2 headers are located at the outer edges of the device so as to permit heat gain from the surroundings, and to mitigate the chances of thermal quenching in the combustion channel. The H_2/air mixture inlet is located well within the layers in order to increase the recuperation area. A second recuperation region is the headers wherein the reactant mixture and exhaust gas headers are located next to each other. Heat exchange also occurs between N_2 and exhaust headers. Twenty-one such blocks of layers could be stacked up with a top and a bottom header caps to form a 168 unit cell microscale combustor heat exchanger that could provide the desired heat (911 W) to the cold working fluid. The overall dimension of the layers, excluding the top and bottom caps would be $2.4 \text{ cm} \times 7.3 \text{ cm} \times 6.3 \text{ cm}$. Alternately, more unit cells could be located within each layer to reduce the height and increase the dimensions of each layer. For the experiments, two sets of these 8 unit cells were enough to produce and transfer 100 W to the HX fluid.

An example of the combustor channel shim with 8 unit cells of overall dimensions of $24 \text{ mm} \times 73 \text{ mm}$ is shown in Figure 48. Four channels are located on each side and combustion gas flows toward the center. Locations of different headers for the combustion gas mixture are also shown in Figure 48. Two holes are provided on diagonally opposite corners to permit alignment of layers during diffusion bonding.

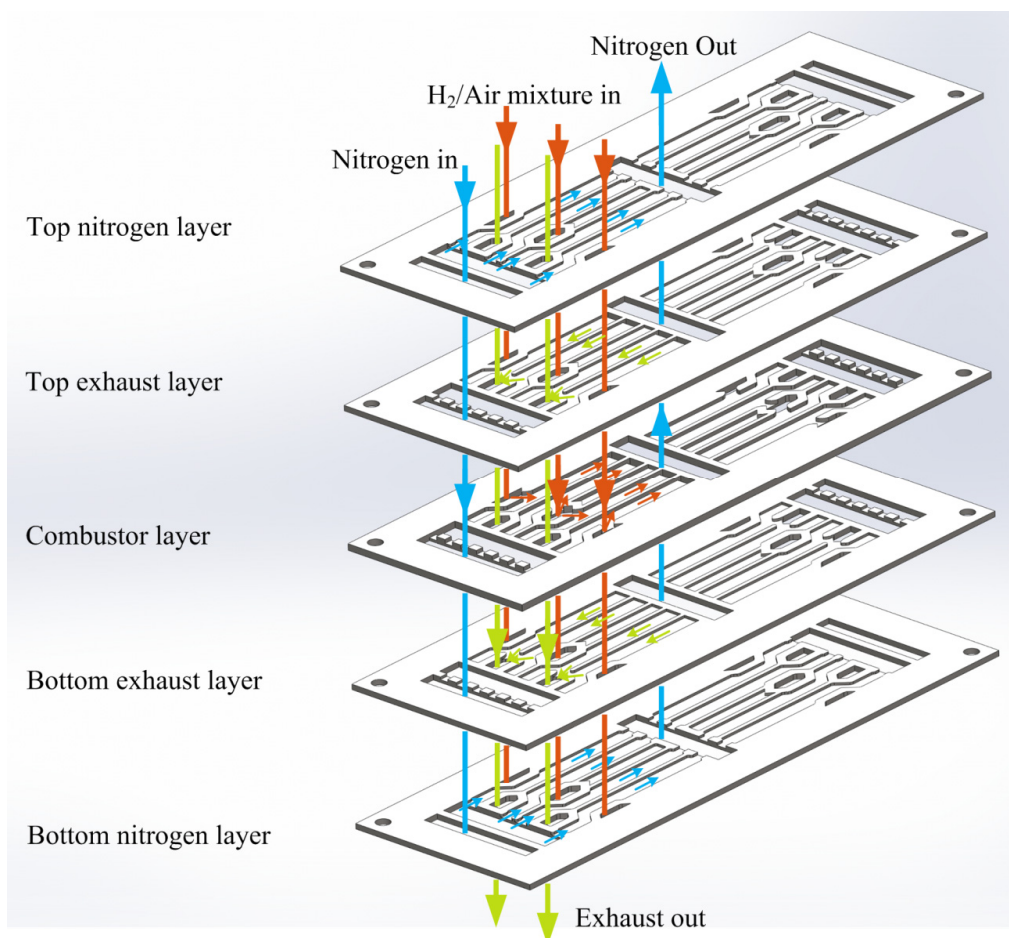


Figure 47: A set of 8 unit cells consisting 5 different layers

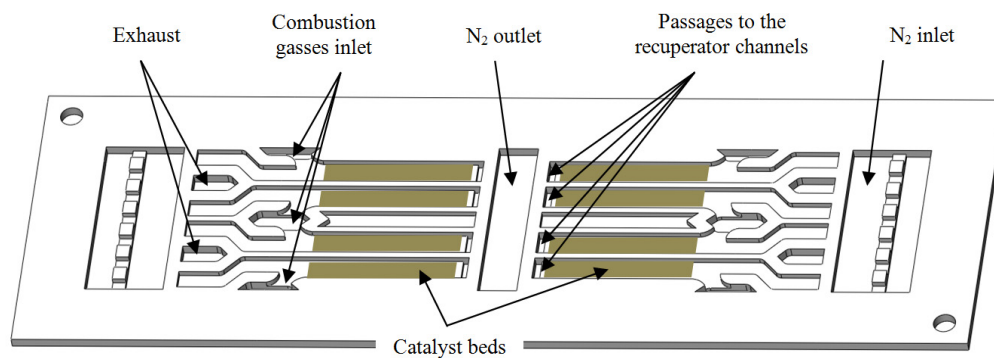


Figure 48: Combustor channel shim consisting of 8 channels

The dimensions of combustion layer are shown in Figure 49 as an example. The details of all layers can be found in Appendix B.

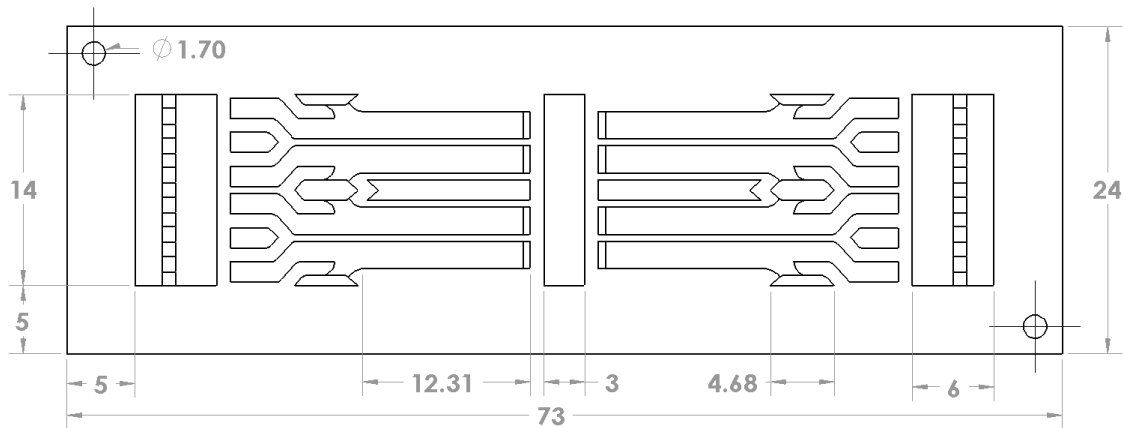


Figure 49: Dimensions of the combustion layer (numbers are in millimeters)

To ensure adequate material for bonding, walls that separated different fluids were thickened to 1 mm. These walls are around the inlets and outlets of the streams in each layer. In addition, to increase hermeticity, 5 mm of material was added around the main channels to ensure a leak-free device. Hexagonal and pentagonal inlets were chosen to facilitate flow distribution inside the layers. This design was adapted from a triangular headering systems described by Whyatt et al. [59] and Haley [55].

It should be noted the unit cells formed the combustion layer (along with the other 4 layers in Figure 47), are not exactly the same the unit cell design used in the computer simulations. Managing the three different fluid paths and their headering cause some change in the initial design on the unit cell. Each of the layers was designed in such a way that not only all etching and diffusion bonding criteria were met, but also a uniform flow distribution is achieved. Figure

50 shows the velocity contours of hydrogen/air flow through the combustion layer. No reaction or heat transfer was considered for these simulations since the flow distribution was the main concern. 3D simulations using Fluent was carried out with the inlet velocity of the fluids based on the requirements presented in Table 13.

Velocity contours of nitrogen flow are shown in Figure 51. Less than 0.8 % difference observed among the averaged velocities in each channel. Average velocities in each channel are summarized in Table 14. Note that the flow distribution within the exhaust channels will follow that of the combustor layer since the flow from each combustor channel goes into the corresponding exhaust channel.

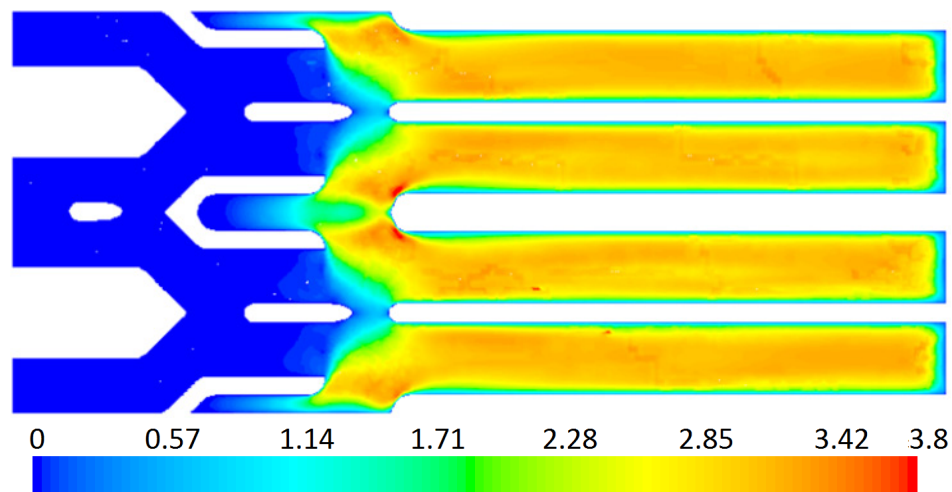


Figure 50: Streamwise velocity magnitude contours (m/s) for one half of the microchannels within the combustor layer shown in Figure 48

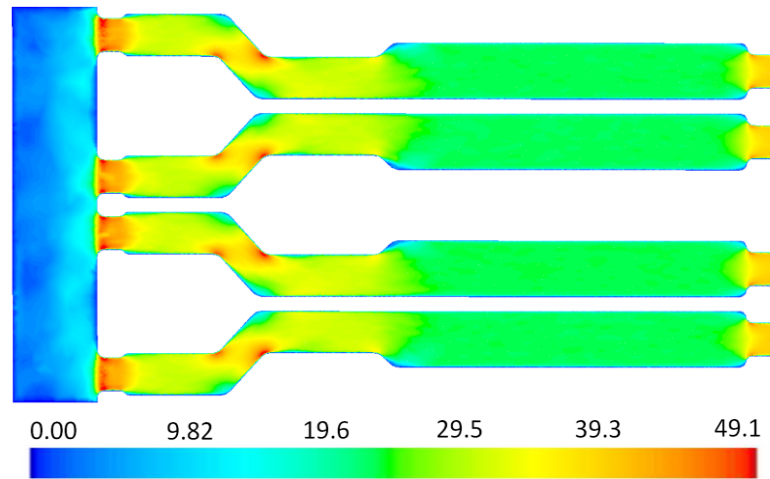


Figure 51: Streamwise velocity magnitude contours (m/s) for one half of the microchannels within the nitrogen layer shown in Figure 47

Table 14: Average velocity within each of the channels within a single layer

Layers	Average Velocities (m/s)			
	Channel 1	Channel 2	Channel 3	Channel 4
Combustor layer	2.55	2.56	2.57	2.56
Nitrogen layer	37.3	37.4	37.3	37.4

5-2-2 Design of the headers

The location of the inlet and exit manifolds to the device is shown in Figure 52 where a device consisting of several stacked layers of unit cells is shown. The headering system should be designed in such a way that uniform flow is permitted into each of the fluidic layers. The concept of the headering system described in US patent No. 7763217 [59] is used here for the hydrogen-air and exhaust gases. In the patent, the inventors used triangular shaped headers for their air/air

recuperator in a steam reforming device. In the present design, hexagonal inlets are used to provide better flow distribution and to reduce the size of the headering section.

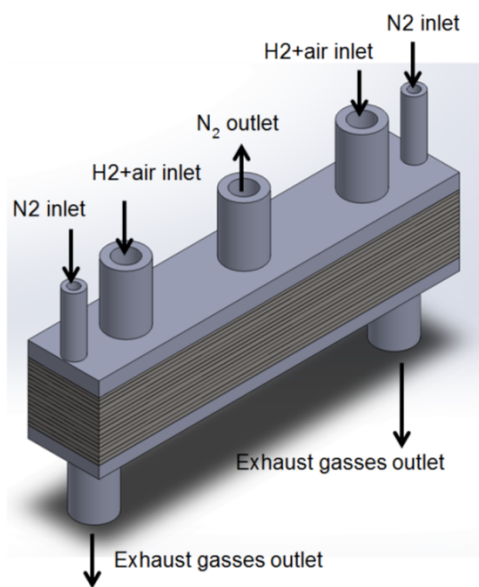


Figure 52: Schematic of the locations of the inlets and outlets

Several three-dimensional simulations of fluid flow were performed in ANSYS FLUENT in order to determine the proper headering design. The designs presented here represent iterative efforts aimed at obtaining uniform flow distribution amongst layers. In these simulations, 3 sets of 8 unit cell blocks such as that shown in Figure 47 are placed on top of each other to make a 24 unit cell μ CHX. The flow rate through each unit cell is kept identical to the largest flow rate in Table 13.

Four additional layers on top and three layers at the bottom of the stack were necessary to transition from circular tubing to the plenums that distribute flow amongst different layers. The main constraint in designing the headers lay in the transmission of force through the entire stack

when the pressure is exerted during diffusion bonding. Based on available research in literature [58], small unsupported gaps between walls of the channels in two different layers were found to be acceptable provided that the ratio on the span to the layer thickness was less than 7. The resulting design of the upper four layers of inlet headering is shown in Figure 53. The intricate micro-texturing was needed to satisfy the bonding criterion. Figure 54 shows the bottom three layers guiding the combustion products to the exhaust.

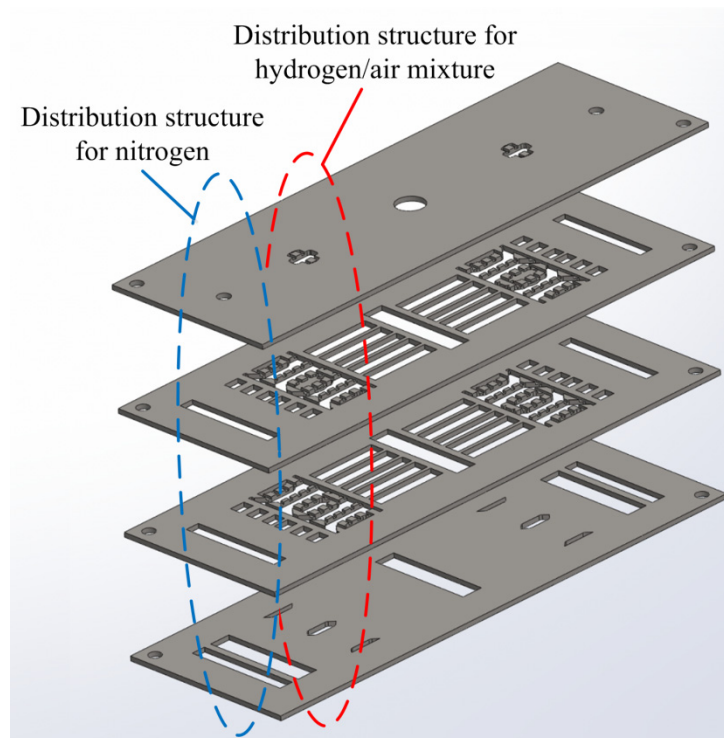


Figure 53: The top layers of H₂/air and nitrogen headers showing the transition from circular tubing to the respective plena

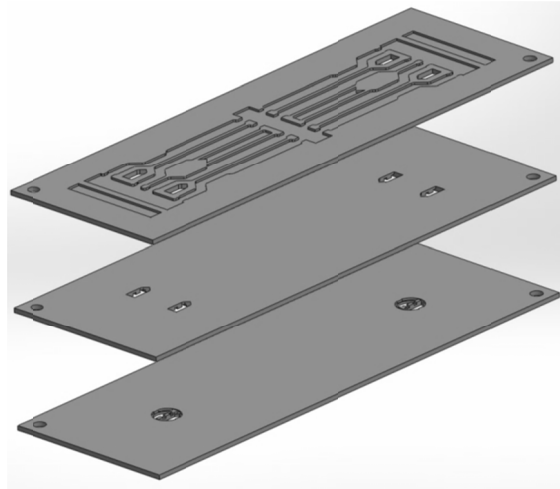


Figure 54: The bottom layers of the exhaust headers

Pressure contours for flow within the combustor headers and layers is shown in Figure 55. This figure shows the left half of the combustor layers with the inlet, the manifold and combustion channels (the exhaust channels are not shown for clarity). Table 15 shows the average velocity in the 12 channels. It can be seen that the flow is distributed uniformly between layers and maximum difference is less than 4 percent.

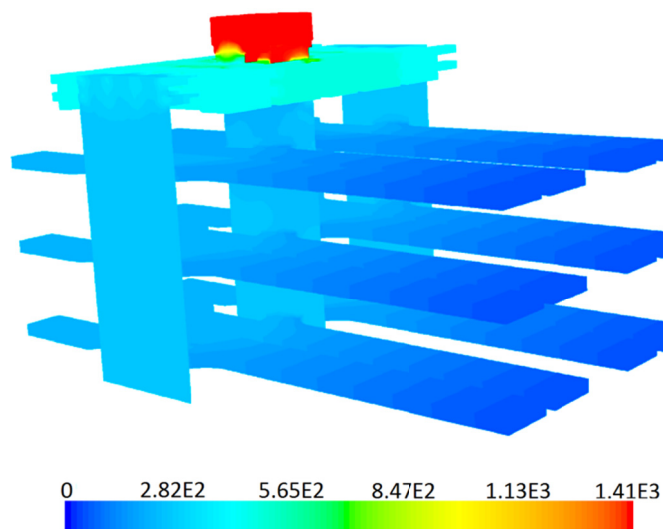


Figure 55: Pressure contours (Pa) of the combustible gases flow through the headers and layers

Table 15: Average velocity magnitude in combustor layers

Channel velocity (m/s)				
Layer 1	2.61	2.59	2.57	2.6
Layer 2	2.57	2.51	2.51	2.57
Layer 3	2.56	2.53	2.53	2.55

It should be noted that nitrogen has a much larger flow rate than combustion mixture flow, thereby making flow distribution uniform a much bigger challenge. Nitrogen first enters a rectangular outer plenum wherein because of the relatively high velocity of the flow, recirculation occurs. Figure 56 illustrates the recirculation in the outer plenum. Several small passages let nitrogen enter into a second (inner) the next resting plenum to which the nitrogen gas layers are connected.

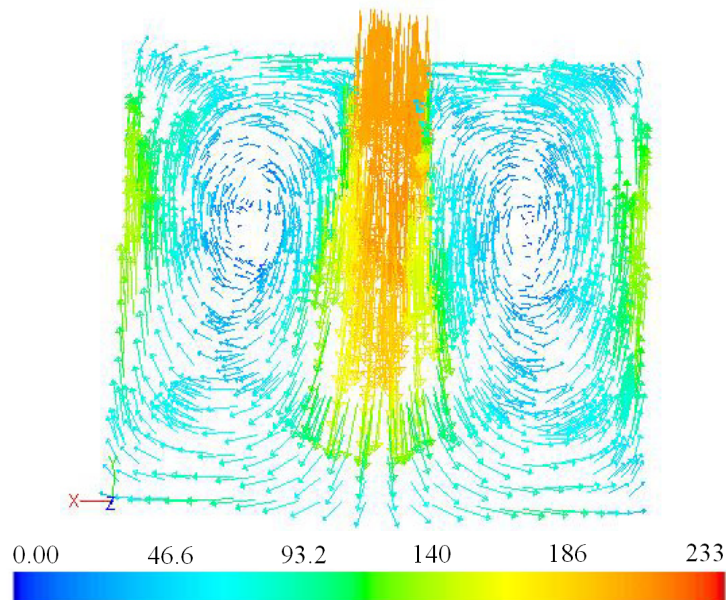
Figure 56: N₂ recirculation showed by velocity vectors in the first plenum (m/s)

Figure 57 shows the location of the first plenum and flow passages. The distances between each three rows of passages (Figure 57 (b)) are where the inlets of the nitrogen channels are. The passages are positioned such that all flow rests in the second plenum and no flow go directly into the nitrogen channels. It should be mentioned that this headering system was not an optimum one and was used to satisfy existing constraints.

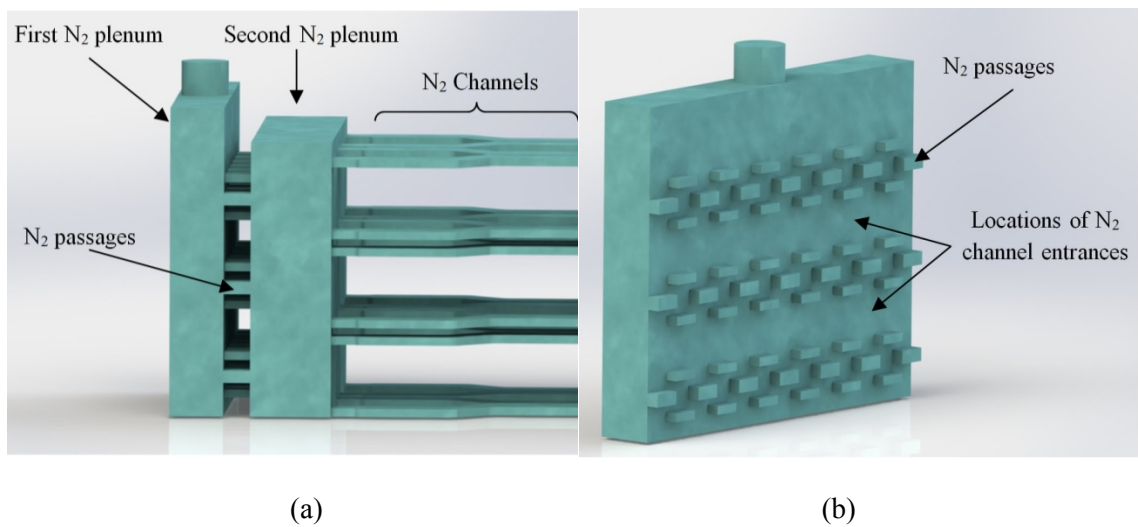


Figure 57: N₂ inlet headering system (a) First and second plenums, (b) First plenum and the location of the passages

Pressure contours of the nitrogen gas flow within the headers and the layers are shown in Figure 58. As with the combustion gas header, most of the pressure drop occurs in the header section. Average velocities in all channels in each layer are shown in Table 16. It can be seen that flow is distributed uniformly and maximum difference is less than 6%.

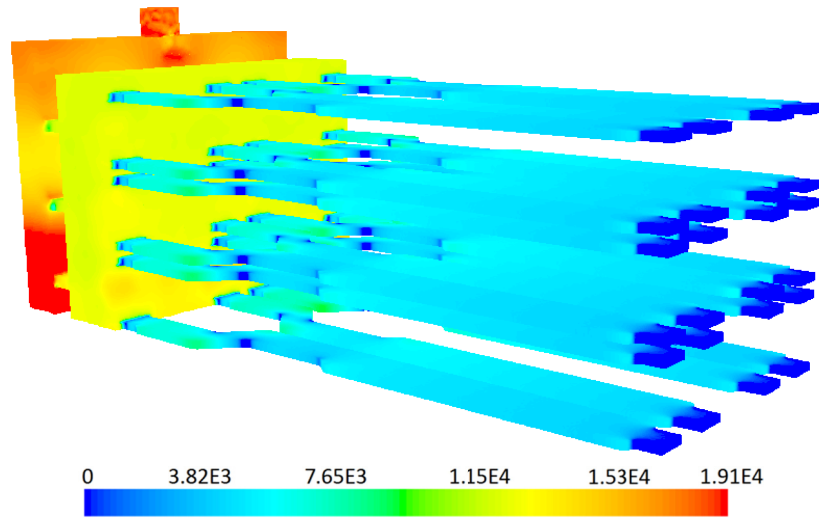


Figure 58: Pressure contours (Pa) of the nitrogen flow through the headers and layers

Table 16: Average velocity magnitude in nitrogen layers

	Layer 1	Layer 2	Layer 3	Layer 4	Layer 5	Layer 6
Velocity (m/s)	37.2	37.4	37.6	37.4	37.2	37.1
	37.1	37.4	37.8	39.4	37.4	37.2
	37.1	37.5	37.3	37.2	39.2	37.1
	37.2	37.5	37.6	37.1	37.3	37.3

The design presented for the nitrogen headering is an extreme case since the flow rates for nitrogen are 13 times that of the hydrogen, which will be the actual working fluid for the device. The thermo-fluidic design presented herein does not consider conjugate heat transfer effects, which could be significant especially when the thermal conductivity of the material is large.

5-2-3 Fabricated parts

The designs were sent to Great Lakes Engineering ® Company for fabrication via etching and laser cutting. Figure 59 shows different fabricated parts.

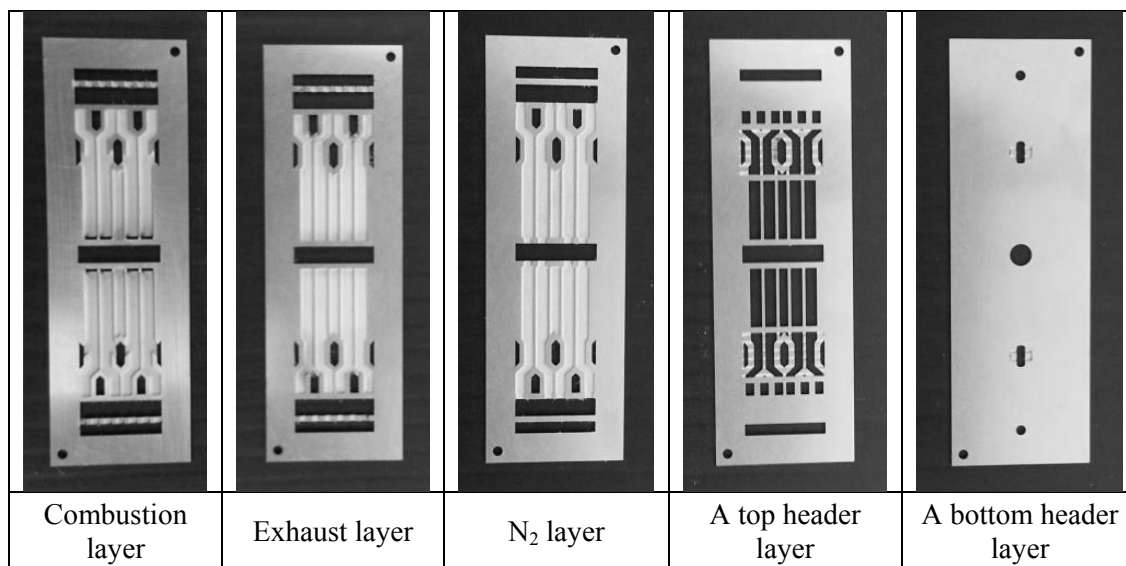


Figure 59: Sample fabricated layers for the CA μ CHX

After receiving these parts, the precision of the fabrication process was tested using ZeScope[®] optical profilometer to ensure that the parts had the same dimensions as requested. Optical profilometry is a method measuring the depth and width of features on the surface along with surface roughness. ZeScope profilometer (available for MBI¹ users) illuminates the surface with a white light and identifies the features on the surface by measuring the light reflections by the surface. The company's promise was to fabricate features within $\pm 15\%$ of the shim thickness. However, some of the layers that were received had dimensions significantly different from what was requested. Figure 60 shows a profilometer analysis for a combustion layer. The horizontal line in the figure shows where the profile (bottom of the figure) is plotted. It can be seen that not only was the depth of the channels greater than $400\ \mu\text{m}$, the tops of the walls were lower than the rest of the unetched section. It means that some material has been removed from the top of the

¹ Microproducts Breakthrough Institute (MBI), Corvallis, Oregon

walls. That gap (can be seen from the plot shown in Figure 60) would not make bonding possible. The thickness of the walls was designed to be 500 μm but the fabricated layer had wall with a thickness of 178 μm . The wall thickness is zoomed in and shown in Figure 60. Therefore, some of the layers had to be resent for fabrication. The next set of fabricated layers was within the promised precision.

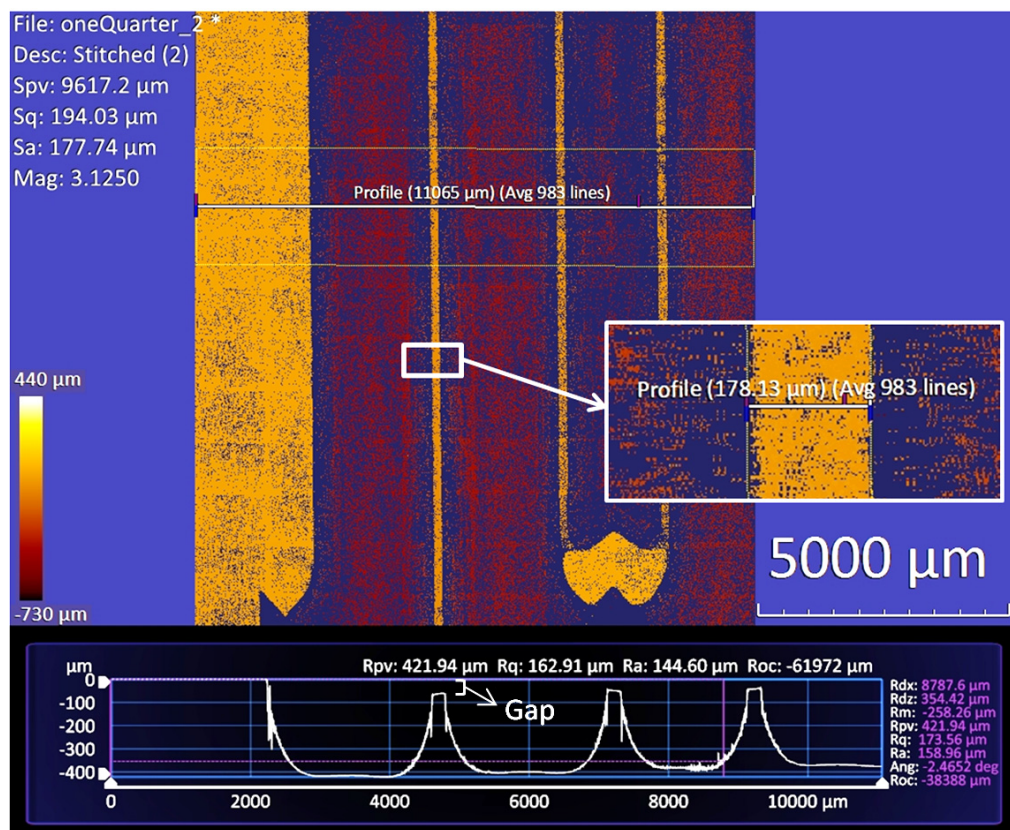


Figure 60: ZeScope analysis of a combustion layer with defects

Figure 61 shows profilometer measurement of one quarter of the combustor layer. Measurements were carried out for all layers and the fabricated parts had accuracies within the etching

limitations. The depth of the channels were in the range of 350 μm - 400 μm and the wall thickness was in the range of 400 μm - 500 μm .

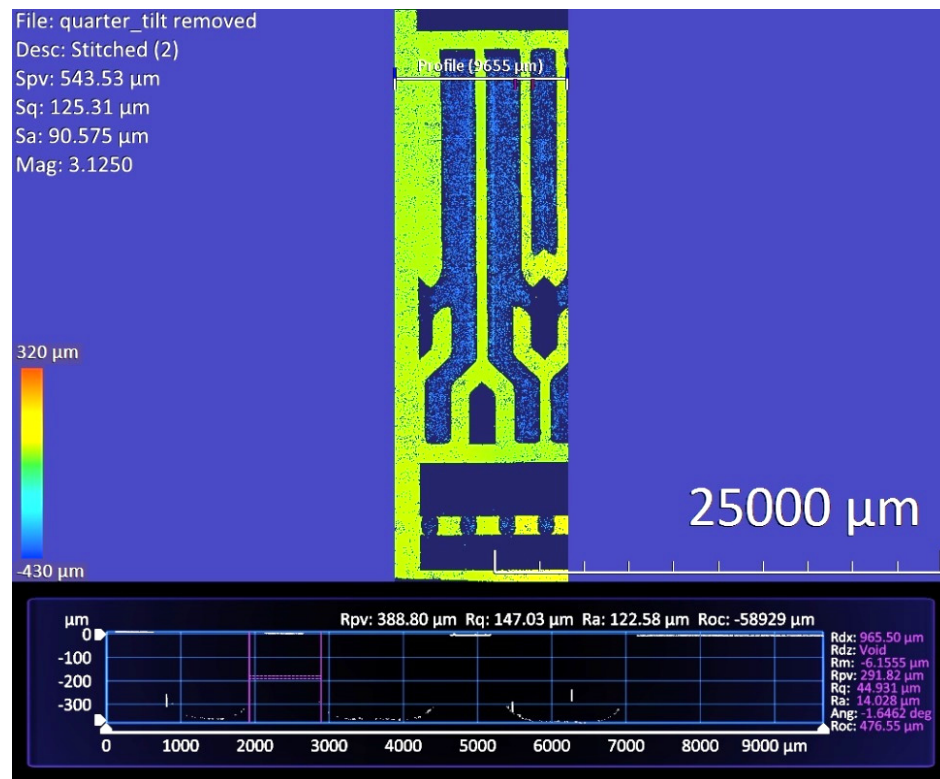


Figure 61: One quarter of the combustor layer

Figure 62 shows the nitrogen plenum section of the combustor layer. During the etching process, the cross sectional area of the pathways was reduced significantly and the edges were extended blocking some of the entrance region. The designed width of the pathways was 1 mm while that of the etched layer was less than 0.8 mm. Those could increase the pressure drop in the nitrogen headering section but since the pressure drop on the HX side was not an important factor for DOE, the experiments were carried out using these nitrogen layers.

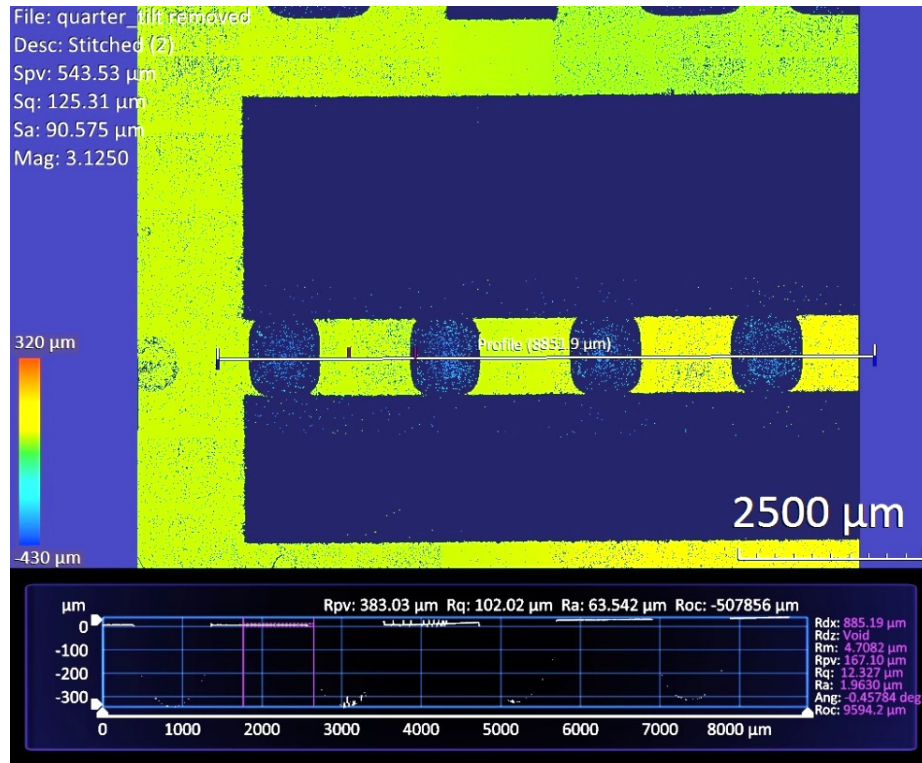


Figure 62: The entrance region (first and second plenum) of nitrogen on the combustor layer

6- EXPERIMENTAL FACILITY AND METHODS

Numerical simulation is a great tool to estimate what is going to happen, however there are several other factors that can affect the outcome of a phenomenon that may not be possible to take into account. Heat loss and flow leaks are one of them. The other important factor is catalyst properties and surface area. Therefore experimental testing is an inevitable effort to verify the predictions and optimizations made by computer simulations. A CA μ CHX was designed using CFD simulations to be fabricated and experimented. An existing experimental facility developed by Haley [55] for MH μ CHX proof of concept experiment was modified in order to conduct series of experiments on the CA μ CHX. Modifications included designing and fabricating a test section housing, as well as identifying and providing assembly equipment necessary for CA μ CHX compared to MH μ CHX.

6-1 Design Requirements

In order to be able to characterize the performance of the CA μ CHX, the facility needed to satisfy test section and test facility requirements.

a) Test section requirements:

- Two housing systems needed to be designed one for activation process and one for experiments.
- The activation housing system needs to be able to tolerate high temperatures (600 °C)

b) Test facility requirement:

- Very cold stream (-70 °C) to be provided at variable flow rates using liquid nitrogen
- The setup should be safe when dealing with hot test section and cold liquid nitrogen.

- Measurement uncertainties should be minimized
- No condensation of water should occur in the recuperator/exhaust pathways
- Heat loss needed to be minimized in all experiments

The experimental facility, which includes the test section and the flow loop, was designed and fabricated based on these requirements. Details of these and other requirements are presented in the following sections.

The results of the experiments would be used to characterize the performance of the CA μ CHX in terms of efficiency, hydrogen conversion and pressure drop. In order to calculate these performance indices the following measurements were needed:

- Inlet and outlet temperatures of Air/H₂ mixture/exhaust and N₂ flow
- Temperature of the body and surface of the CA μ CHX
- Flow rates of air, H₂ and N₂
- The exhaust gas composition
- Pressure drops on air/H₂ mixture and N₂ sides

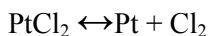
Thermo-fluid aspects that need to be verified with the experiments include

1. Determination of the operating condition that prevents condensation of water vapor inside the test section. The combustor is designed in such a way that -under appropriate working conditions- no condensation happens considering the fact that nitrogen flows at temperatures as low as 200 K.
2. Characterization of extraneous heat losses such as through insulation and natural convection. Heat losses in previous experiments [55] were more than 8% with a large uncertainty.
3. Characterize and calculate the performance based on performance indices.

6-2 Catalyst Preparation

6-2-1 Catalyst deposition

A platinum salt solution was wet deposited on the surface of the channel using the process followed by Stefanov et al. [60]. Chloroplatinic acid hexahydrate ($\text{H}_2\text{PtCl}_6 \cdot 6\text{H}_2\text{O}$) with purity higher than 95% was obtained from Sigma-Aldrich ®. The molecular weight of the compound is 517.90 g/mol and when the acid is heated, the following reaction steps occur and it decomposes to platinum chloride and then to elemental platinum [61].



A 0.007 M solution of the acid was made using deionized water. Then small needles of precisely known volumes of solution were deposited on the desired locations precisely. The amount of acid to be deposited on each channel was found by multiplying the surface area (cm^2) by the density (0.529 ml/cm^2). After each round of dripping the acid on the surface, the surface was left a side before drip depositing another layer. If required, a masking tape (Kapton ® polyimide tape) was used to cover the rest of the surface to avoid getting the platinum coat. RTV silicone rubber was used occasionally to stop the flow of the acid solution.

During different steps of catalyst preparation and after testing, Scanning Electron Microscope (SEM) was used to characterize the surface of the catalyst. Figure 63 shows two SEM images

captured at two different locations of a catalyst coated shim after wet deposition. Both of them have the same magnifications (500 x) and it can be seen that the surface may not get coated uniformly everywhere by wet deposition method.

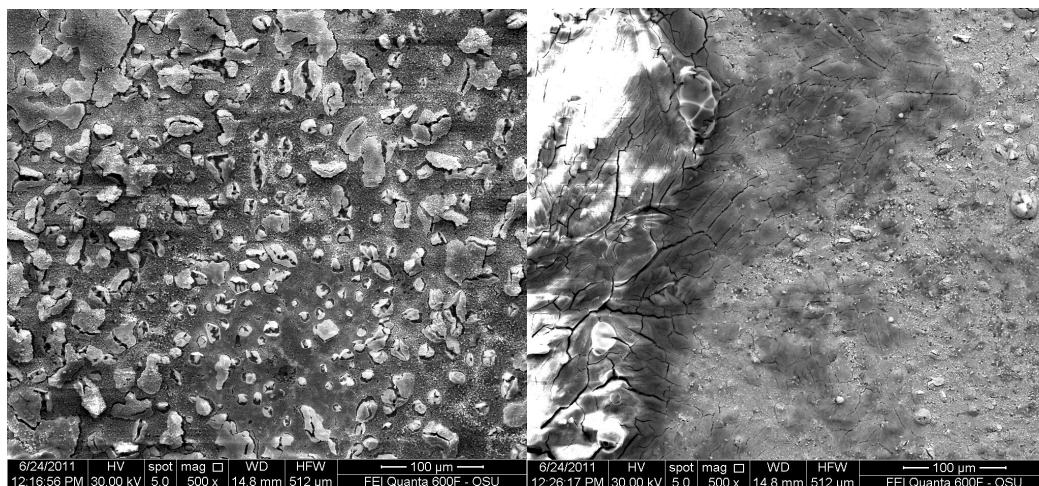


Figure 63: SEM pictures of deposited chloroplatinic acid at two different locations with the same magnification

When a very cold fluid is flowing close to the combustor and exhaust channels, the reaction rate decreases and condensation of water vapor in the channels is very probable. To avoid that, as described before, in the CA μ CHX catalyst beds are located on both sides of the combustor channel and one side of the exhaust channels. Figure 42 shows the location of catalyst beds with heavy gray lines.

Within each unit cell, both sides the walls separating combustor from exhaust channels should have catalyst deposited on them. For the shim (combustor layer) shown in Figure 64, catalyst deposition can be performed within the etched channels. The other side of this shim (the exhaust side), is a flat surface and deposition of the catalyst would add an extra thickness that would

reduce the channel height of the exhaust channels. Other than that, the catalyst deposition is done using wet deposition method that requires a rough surface for better attachment of the catalyst material to the surface. Therefore, the back side of combustor and top exhaust channels were selectively etched in the desired region of catalyst location enough to hold the catalyst. Once the back side was etched, catalyst was deposited.

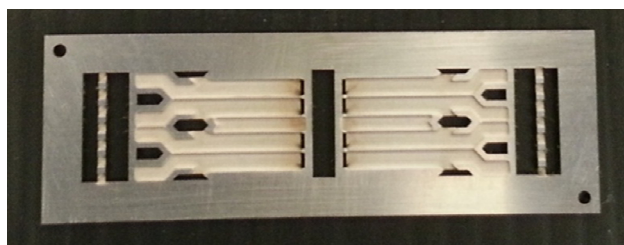


Figure 64: Top view of a combustor layer

Etching the back side of the shims: Etching was performed using 0.5 M oxalic acid solution. The desired regions to be etched were open for acid etching while the rest of the shim surface was masked with a Kapton[®] tape (Figure 65). The Kapton tape was laser cut expose the area to be etched precisely. One important factor to consider was is that the space between two channels to be at least 500 μm of clean surface to make sure that enough contact exists with the bottom layer walls for bonding. Uncertainties in the etching as well as the wet deposition steps were a concern therefore the mask was cut in such a way that the back side channels have smaller length and width compared to the actual channels. Based on the previous experience an etch depth of 30 μm was enough for the catalyst bed. A sample of the etched layer is shown in Figure 66. The etched channel dimensions are also shown in the picture. Note that the size of the etched channels (1.5 mm \times 10.5 mm) was smaller than the size of the combustion and exhaust channels (2 mm \times 12 mm)



Figure 65: The back of a combustor shim covered with mask for etching

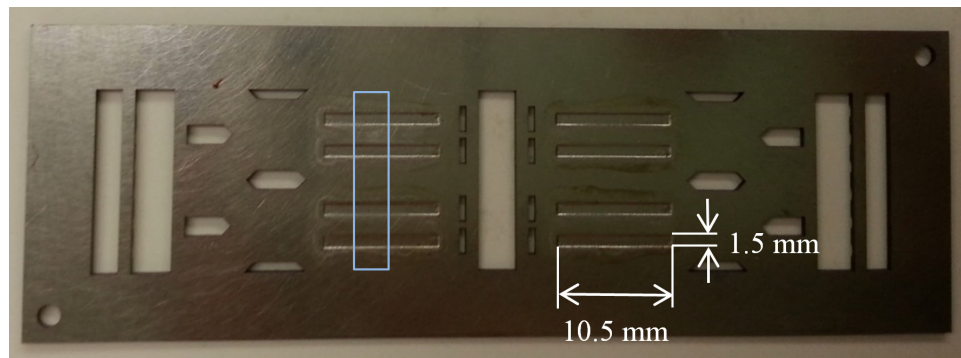


Figure 66: Etched channels on the back side of a channel

Figure 67 (a) shows a profilometry of the etched channels performed on the region marked with a rectangular in Figure 66. Figure 67 (b) shows the depth of the etched channels along the black line shown in Figure 67 (a). It can be seen that the depth of the etched area is about $35\ \mu\text{m}$. The top flat surface is the wall between the two channels and is $1500\ \mu\text{m}$ instead of $500\ \mu\text{m}$, thereby ensuring sufficient flat surface area for area.

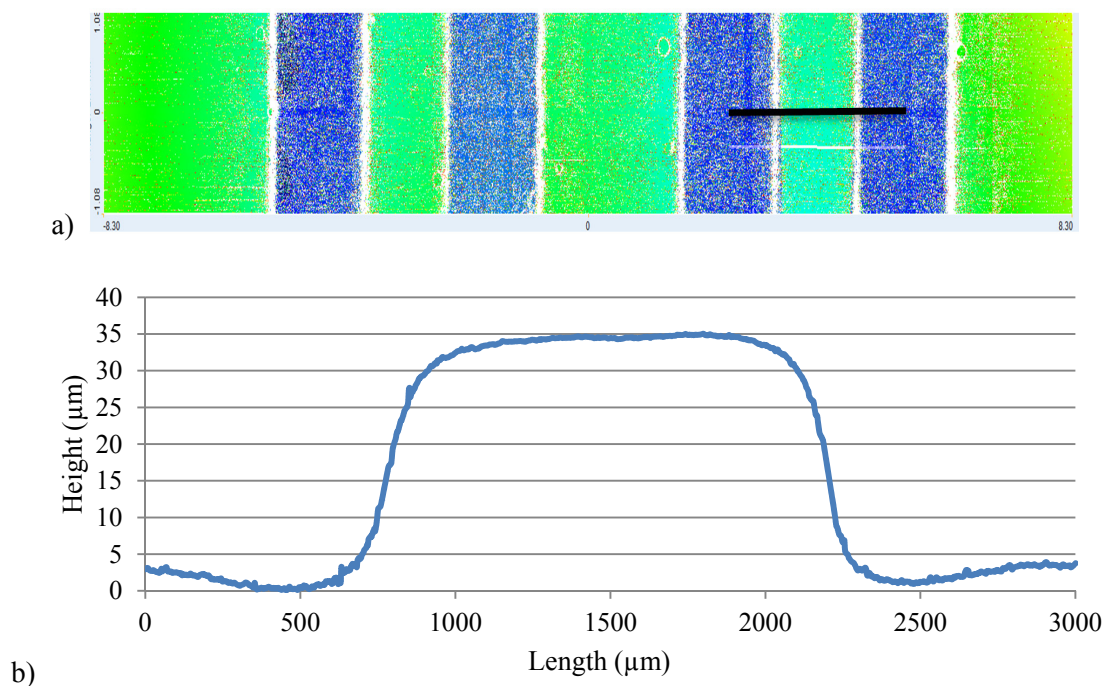


Figure 67: a) Profile of a section of the channels, b) Plot of the height of the area shown with a dark line

Catalyst deposition: After the back sides are etched, the shims were ready for catalyst deposition. Kapton tape masks were laser-cut again and were attached on top of the sides. 0.007 Molar solution of chloroplatinic acid hexahydrate were deposited with the density of 0.529 ml/cm^2 . Eight 1 ml syringes were used to deposit the desired amount of the catalyst solution onto each of the eight channels in each layer (Figure 68). After each deposition, the shim was put a side and then the next round of injection is done. After about 10 rounds, the syringes were empty and the desired amount was deposited. The required amount of the salt for each layer was 1 ml.

When the solution was evaporated, the mask was removed (Figure 69), and the back side of the shim was deposited with the catalyst shim.



Figure 68: Syringes used for catalyst deposition

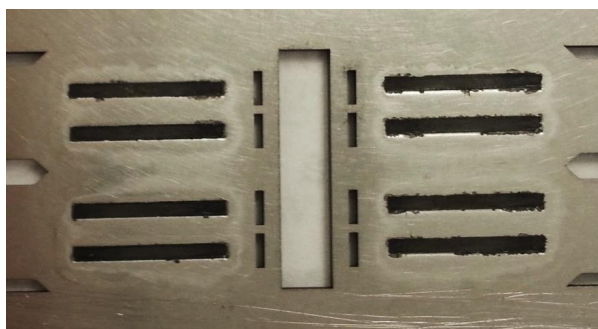


Figure 69: Catalyst deposited on back side of a shim

RTV silicone paste was used to retain the solution in the desired catalyst area. Figure 70 shows how the paste is positioned to stop the flow. After deposition, the mask and the paste can be removed easily.

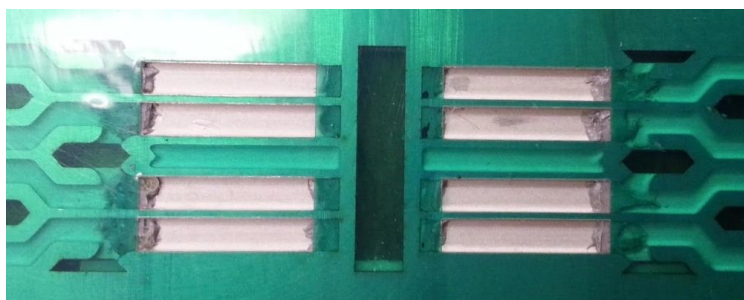


Figure 70: Use of mask and RTV to confine the catalyst area

6-2-2 Catalyst activation

Heating the chloroplatinic acid while an inert gas (N_2) is flowing over it leads to removal of water trapped in the compound (calcining), which is the first reaction shown in Eq. (47). And reduction (the second and third reactions in Eq. (47)) occurs with a 10:1 ratio flow of N_2 and H_2 . Based on available data in literature, common temperature range for calcining and reducing is 500 °C to 600 °C [36] [62] [47] [63]. Therefore, the activation test section was made completely out for stainless steel and aluminum. For calcining, nitrogen was introduced inside the combustor and exhaust channels while cartridge heaters were used to increase the temperature of the combustor to 600 °C and keep it constant at this temperature for 3 hours. Then, at the same temperature, a 10:1 volumetric mixture of nitrogen and hydrogen flowed inside the channels for 4 hours for the reduction step. After that process, the combustor was cooled down to room temperature with nitrogen flow within the channels. SEM pictures of the catalyst surface after the activation processes are shown in Figure 71. 20-30 μm cup-like regions were observed suggesting partial detachment of the coat (Figure 71 (a) and (b)), with more magnifications platinum submicron particles appear which participate in the reaction (Figure 71 (c) and (d)).

Thermofluidic characterization of the CA μCHX was the goal of the project and hence bonding was not performed. Layers were bolted together. When the layers were stacked on top of each other to create a 16 unit cell μCHX , a top and a bottom cap were necessary to hold them together and connect the μCHX to the inlet and outlet NPT fittings. PEEK was chosen as the material of the caps because of its low conductivity ($k = 0.25 \text{ W/m-K}$) that reduces heat losses. High temperature silicon rubber O-rings were chosen to prevent leaks from the inlet and exit tubing. PEEK parts are good for operating under a temperature of 300 °C; however, before running the

experiments the catalyst needed to be activated at temperatures of about 600 °C. Therefore a set of aluminum caps were designed to be used only for catalyst activation process. Two other aluminum parts are designed to hold four cartridge heaters that are used to heat up the μ CHX for activation process. Figure 72 shows an assembly view of the system with the heaters.

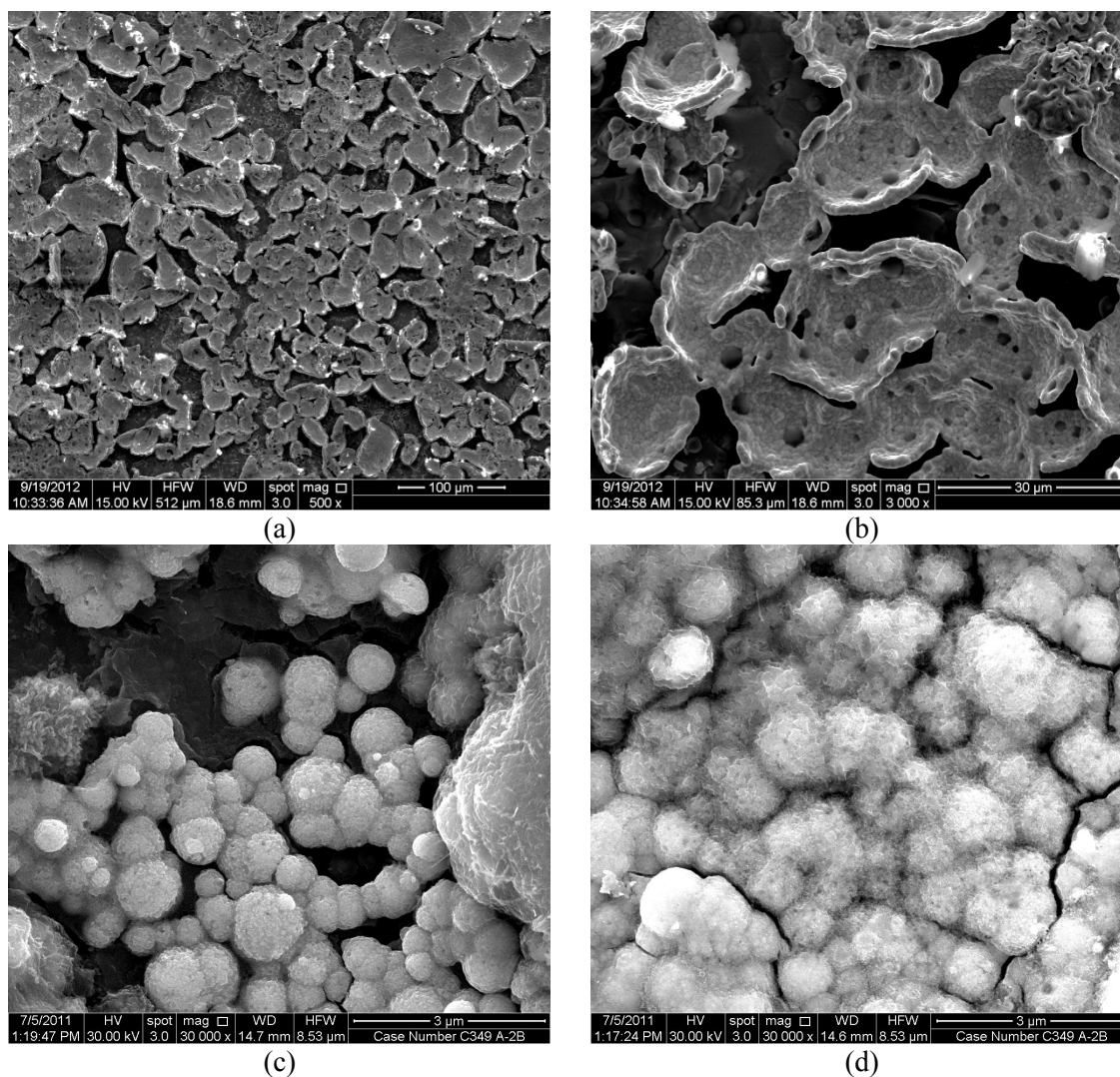


Figure 71: SEM pictures of a catalyst surface after activation processes , (a) 500 x magnification, (b) 3000 magnification, (c) and (d) 30000 magnification at two different locations

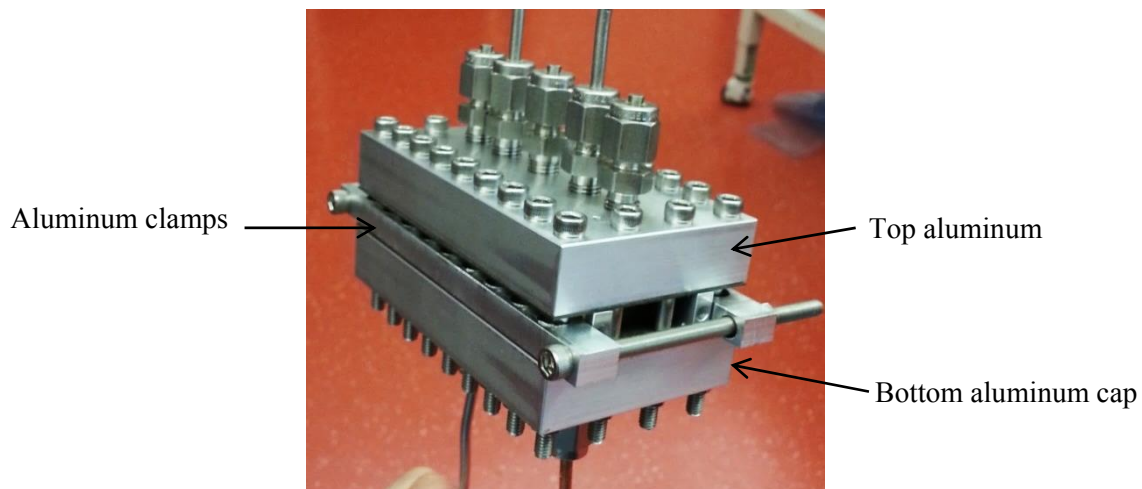


Figure 72: Final assembly of the device for activation process

Since O-rings cannot operate at those high temperatures, two gaskets were made from a high temperature Mica to surround and seal inlets and outlets. Then the combustor layers are put (Figure 73 (a)).

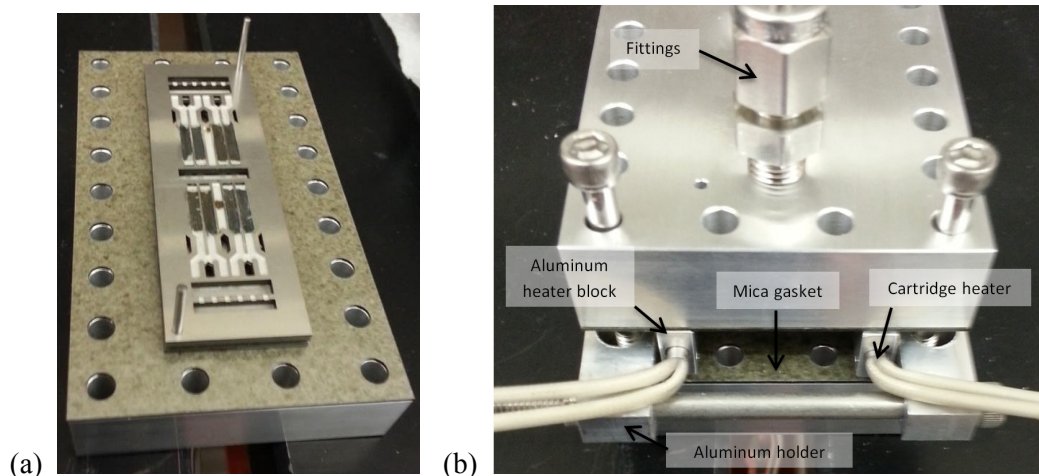


Figure 73: (a) Bottom aluminum block, the mica gasket and catalyst layers on the top (b) Detailed picture of the assembly

When all the μ CHX layers are put, the top gasket and then the top aluminum block are positioned. Two aluminum parts hold the heater blocks with cartridge heaters to make sure that a good contact exists between the heater blocks and the layers. The heat blocks are separated from the holders with a layer of Mica to reduce heat loss. Figure 73 (b) shows different parts of the assembly. The assembled device for activation process looks like Figure 72. To reduce the heat losses, the device is wrapped around with three layers of Pyrogel insulation.

6-2-3 Catalyst performance at high temperatures

As mentioned in section 5-1-3, diffusion bonding occurs at temperatures as high as 1000 °C. High temperatures tend to sinter catalyst and make agglomerates. Having catalyst agglomerates instead of particles reduces the available surface area for catalytic reaction and therefore reduces overall reactivity of a catalyst significantly. In order to avoid catalyst sintering, commonly the channels are coated with the platinum salt after diffusion bonding. The method is called wash-coating in which a catalyst solution flows inside the channels and covers the internal surface of the channels. In this method, all walls and even headers and plenum get the catalyst coating and selective coating of the catalyst is impossible. The other option is to cut the bonded layers in half and insert catalyst coated shims inside the channels and then join the cut section. This method cannot work for complicated geometries and small channels. Since the selective positioning of the catalyst was important, these methods would not be desired solutions. While not the focus of this dissertation, a preliminary effort was undertaken to investigate the effect of high temperatures on the catalyst surface and its reactivity. An ideal way of identifying catalyst reactivity is by measuring the number of active catalyst sites by physisorption methods like BET analysis. Since those tools were not available, SEM was used to check the catalyst surface visually and using EDX. SEM inspection was followed by testing the catalyst reactivity experimentally. Small coupons of

stainless steel were fabricated and covered with the chloroplatinic acid selectively (Figure 74 (a)). The coupon was then inserted in a test section made by Haley [55] for demonstrating the MH μ CHX unit cell performance (Figure 74 (b)). Upon activation, the reactivity of the coupon was tested by introducing a stream of air and hydrogen. Then, the coupon was taken out and put inside a hot vacuum press to go through the temperature cycle experienced in diffusion bonding.

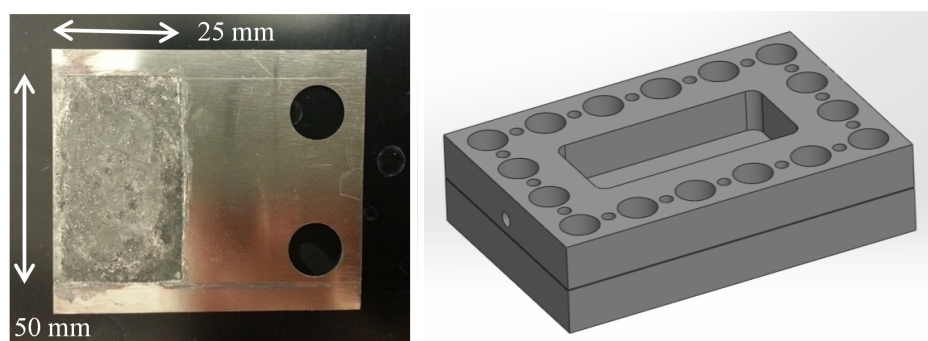


Figure 74: (a) Stainless steel shim coated by catalyst, (b) Test section for the catalyst activity

The cycle involves ramping up the coupon from room temperature to 850 °C at 5 °C/min. Note that at this stage the coupon was being bonded. Upon temperature cycling, the coupon was removed to obtain SEM pictures of the surface. Figure 75 compares the SEM pictures of catalyst surfaces prior to and after going through the diffusion bonding process. Figure 75 (a) and (c) show the catalyst surface. Figure 75 (b) and (d) shows a catalyst surface after the same process but at 1000 °C temperature. If compared by the SEM pictures for a catalyst surface without going through those high temperatures (Figure 71), it can be seen that the catalyst coating pieces have attached to each other and sintered. It is more obvious when compared at 5000 x and 15000 x magnifications. The submicron particles have made large agglomerates. The change is less for 850 °C than 1000 °C such that for the later, almost no submicron particles can be observed (Figure 75 (d)).

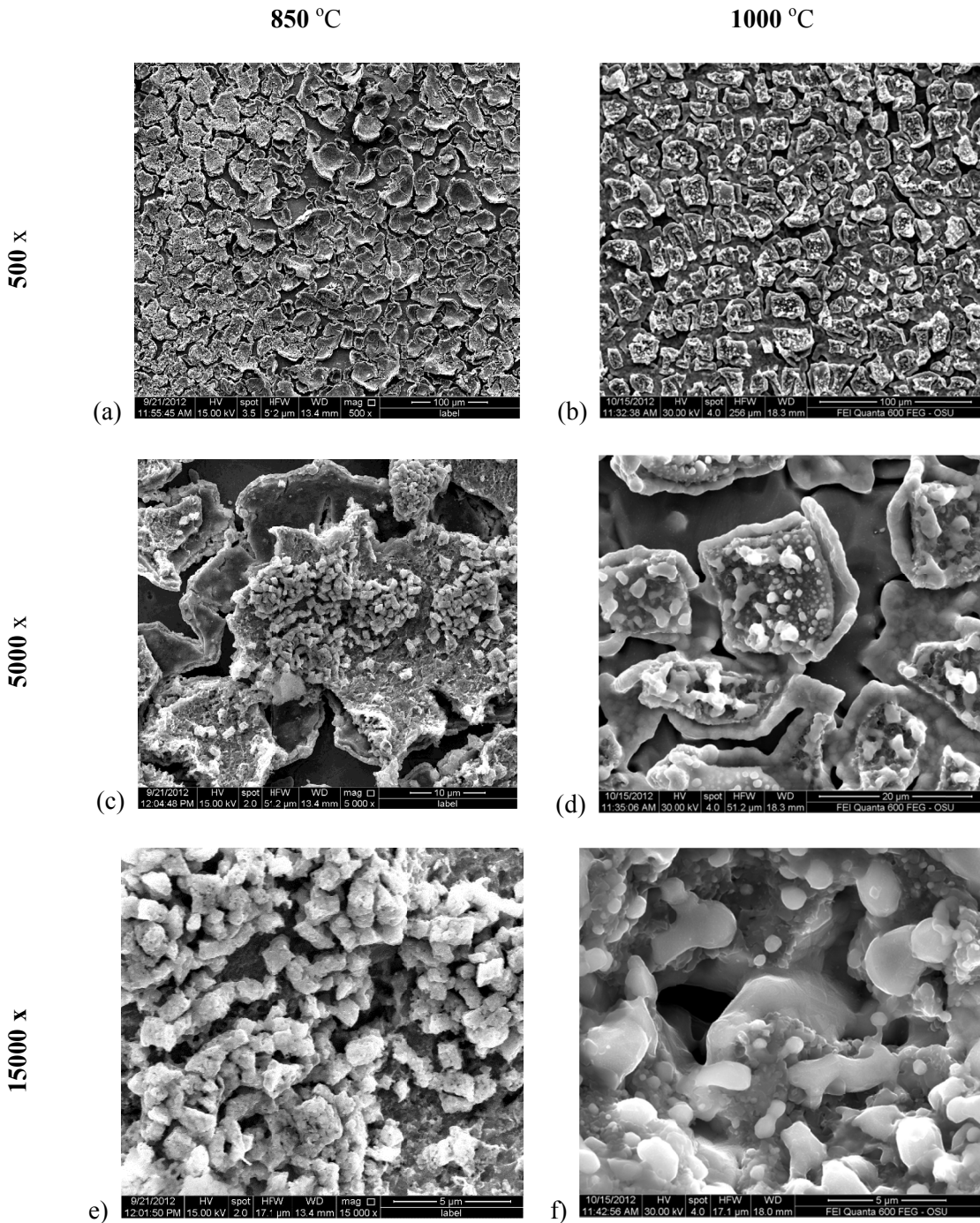


Figure 75: SEM pictures of a catalyst surface after diffusion bonding process , (a) under 850 °C, 500 x magnification, (b) under 1000 °C, 500 x magnification, (c) under 850 °C, 5000 x magnification, (d) under 1000 °C, 5000 x magnification, (e) under 850 °C, 15000 x magnification, (f) under 1000 °C, 15000 x magnification

To characterize the elemental composition of the surface, Energy Dispersive X-ray (EDX) spectroscopy was performed on each sample. EDX helps identify the elements present on a surface and their relative proportions (weight fraction for example). Figure 76 shows an EDX analysis for a catalyst surface that had gone through a 1000 °C process. The Y-axis shows the counts (number of X-rays received and processed by the detector) and the X-axis shows the energy level of those counts. Each energy level corresponds to an orbit of an atom. Table 17 summarizes different elements on the surface and their atomic and weight percentages. EDX showed that 48.9% of the weight of the materials on the surface is platinum. Although a significant portion of the surface is covered by platinum, the platinum coat is not very active for reaction because of sintering.

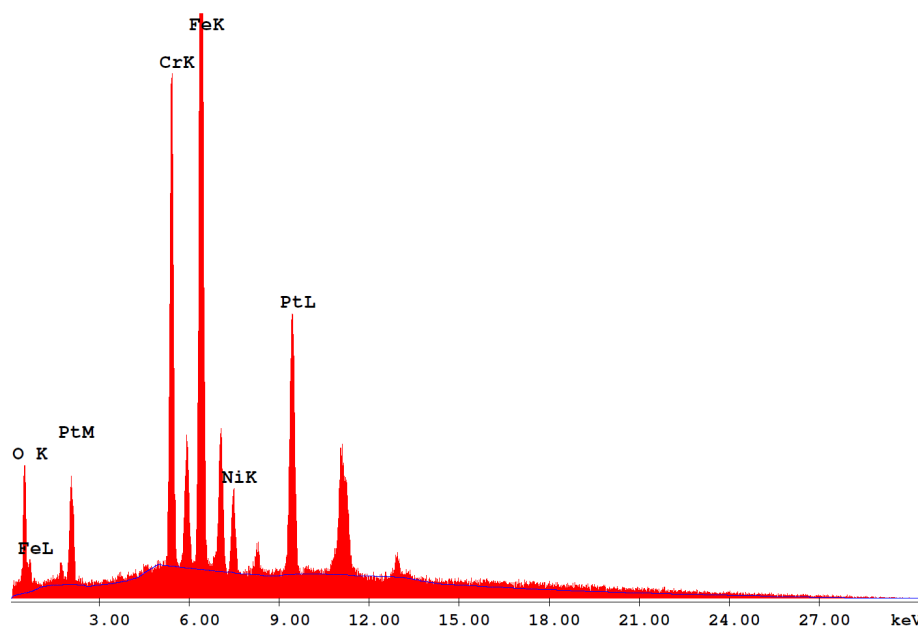


Figure 76: EDX analysis of a catalyst surface after going through a 1000 °C process

Uncoated stainless steel was also analyzed using EDX and results are shown in Table 17. The range of weight fractions of common 316 stainless steel (316 SS) material are also shown for reference. The EDX almost characterized the SS accurately. The EDX showed 5.6 % oxygen on the surface which could be because of a oxidation layer on the surface of the 316 SS.

Table 17: Elements and their weight and mass percentages

Element	Platinum coated 316 SS (measured using EDX)		316 SS (measured using EDX)	316 SS (composition range) [64]
	Weight %	Atomic %	Weight %	Weight %
O	7.04	29.5	5.58	-
Cr	12.05	15.53	15.42	16-18
Fe	28.7	34.44	66.66	62-69
Ni	3.27	3.73	9.92	10-14
Mo	-	-	1.54	2-3
Mn	-	-	-	2
Pt	48.93	16.8	-	-

Another way to visualize the EDX results is elemental mapping and is shown in Figure 77. The first picture shows an SEM image of the region (5000 x magnification) and the other five images show how different elements are distributed on the surface. The platinum coating can easily be seen in the SEM picture, the platinum map image verifies the existence of platinum. The top three atoms on the surface can also be shown in one picture for comparison (Figure 78). In this figure, iron is blue, platinum is green and oxygen is red.

Following the SEM and EDX characterization, the coupon was inserted in the test section again to test the reactivity of the catalyst by combusting air and hydrogen and later measuring the temperature of the test section. A series of experiments were carried out on the effect of high temperatures on a platinum catalyst surface using a test section shown in Figure 74.

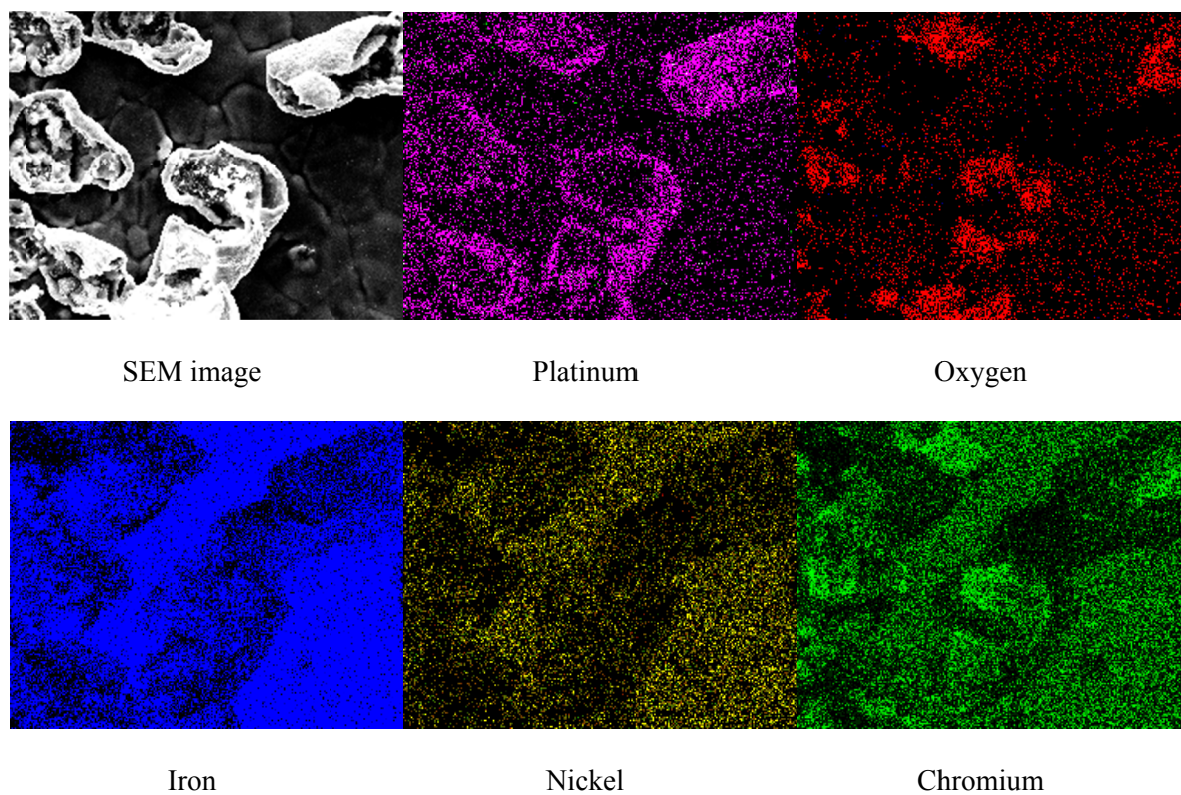


Figure 77: EDX elemental mapping for a 1000 °C catalyst surface (6400 x)

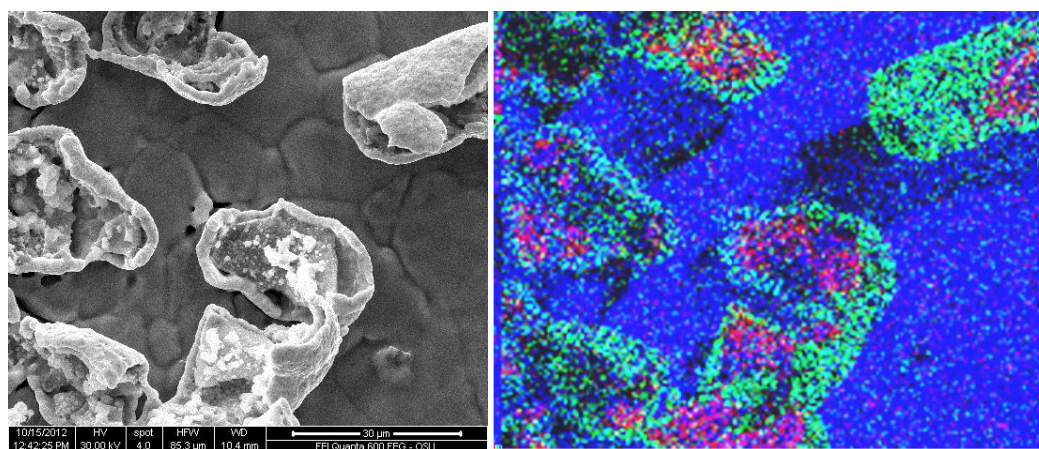


Figure 78: Elemental mapping of iron (blue), platinum (green) and oxygen (red) combined (Nickel and chromium are not shown in this map.)

The size of the vacuum hot press available at MBI limited the size of the coupon that could be heated to the desired temperatures. A shim that goes inside the hot press cannot have a diameter larger than 3 inches. With a small coupon, it is possible to only cover a small with the catalyst and therefore a low power would be generated by reaction. Because of the relatedly large size of the test section, the produced power was not enough to heat up the test section significantly. However, the increase in body temperature of the test section was enough to give meaningful results considering the uncertainties (0.51 °C). A thermocouple 5 mm under the catalyst surface was located and used to measure the temperature. Figure 79 compares the reaction rate of different catalysts by showing the catalyst surface temperature variation by time. In this plot, reaction rate of the 850 °C and 1000 °C temp cycled catalyst surfaces are compared with the reaction rate of an activated catalyst surface (without going through high temperatures). All three cases were preheated using cartridge heaters to a temperature of around 130 °C and the air/H₂ mixture was introduced to the channels. Black squares show the point that each catalyst surface reached a 2.5 °C increase in temperature because of the reaction. For the normal activated catalyst, it took 4.7 minutes to increase the temperature 2.5 degrees. For 850 °C catalyst it took 8 minutes and for 1000 °C catalyst it took 31.7 minutes. A huge difference between the reactivity of a catalyst after being sintered at 1000 °C compared to the other catalyst surfaces was observed. It should be noted that heat loss plays an important role here because of the test section was relatively large. More in depth experiments are needed to investigate the effect of temperature cycling on a catalyst.

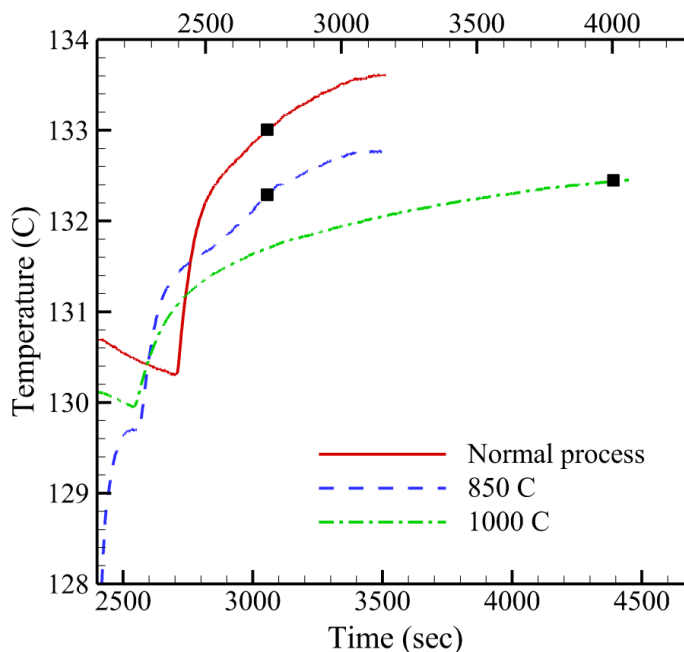


Figure 79: Temperature of the catalyst surface versus time for different processes catalysts (experimental results)

6-3 Experimental Test Section

After the activation process, the layers should be taken out and put in the test assembly. Since the layers are not bonded together, they will be held together by bolts. In order to prevent damage to PEEK caps, two aluminum caps will be put on top and bottom to distribute the pressure (Figure 80).

During the activation process, the device layers were bolted together and under pressure with the top and bottom aluminum headers to prevent leaks. The activation process took 7 hours and occurred at 600 °C. Figure 81 shows the μ CHX layers after going through the activation process.

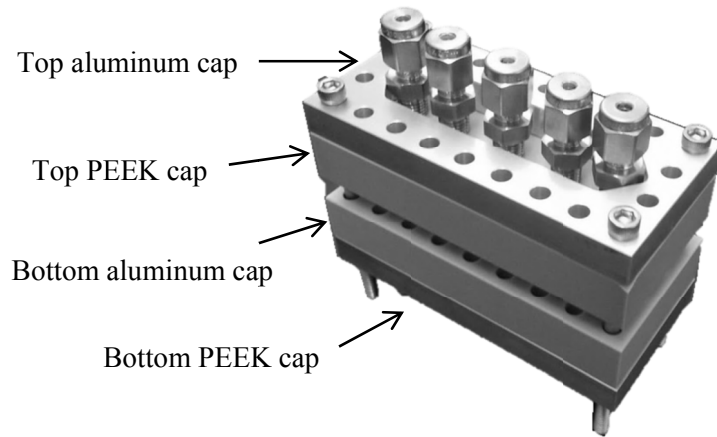


Figure 80: Assembly view of the test section without diffusion bonding to be bolted together

Being at high temperatures and under pressure for 7 hours simulated the diffusion bonding process and caused weak bonds between layers. This was an ideal occurrence for the next step which was testing of the device. Leak tests showed that in the test assembly, there was no need for exerting too much pressure to have a leak proof device, therefore the aluminum blocks (Figure 80) designed and fabricated to apply uniform pressure on the PEEK headers were removed to reduce the size and heat loss. PEEK caps are shown in Figure 82. The O-ring grooves can be seen from the bottom view picture. Parker silicone O-rings capable of operating from $-115\text{ }^{\circ}\text{C}$ to $204\text{ }^{\circ}\text{C}$ (158 K-477 K) were used.



Figure 81: μCHX layers after activation

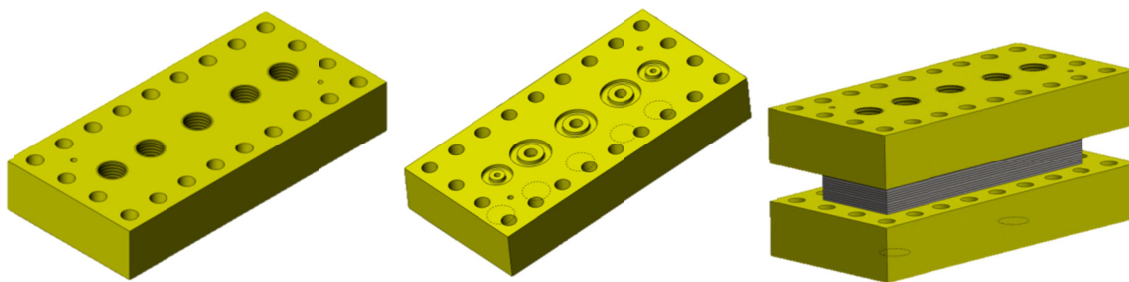


Figure 82: Top view of the top PEEK cap (left), bottom view of the top PEEK cap (middle), and assembly view of the test section (right)

Temperatures at four locations around the combustor are measured by T-type thermocouples shown in Figure 83a. One thermocouple was inserted in one of the alignment holes to get the inside temperature whereas other three were attached to three sides of the combustor (Figure 83b).

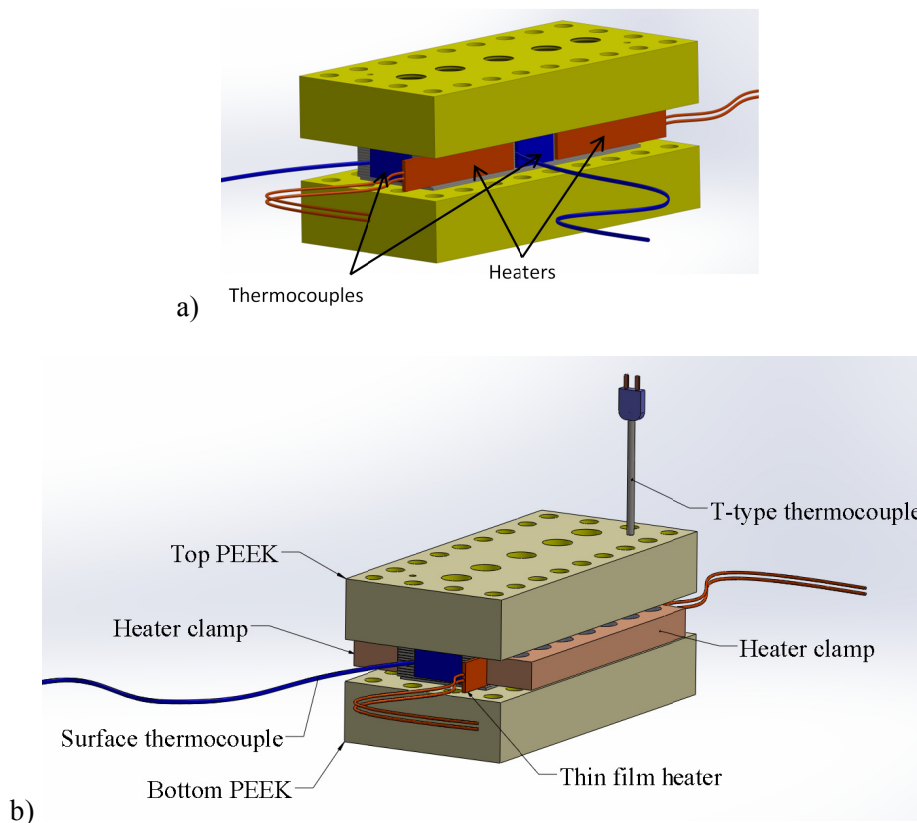


Figure 83: Detailed picture of the test section assembly

It was important to measure the temperatures on the short and long sides of the combustor since they have different positions relative to the catalyst coated region. Four 12 Ohm thin film heaters (Minco) were used to preheat the device to a temperature of around 120 °C to start the reaction. The final assembled test section can be seen in Figure 84. Polyetherimide plastic clamps were used to push the surface heaters in contact with the combustor layers. A copper thermal paste was also used between the heater and combustor body to reduce the contact resistance. Three way fittings divided the flow into two streams for air/H₂ mixture and nitrogen. Wherever possible, PFA tubings were used to reduce conduction heat losses. And at the end 5 layers of insulations were wrapped around the test section. The insulation had a thickness of 1 mm and a maximum use temperature of 650 °C. The thermal conductivity of the insulation varied by temperature and was 0.020 (W/m-K) at 0 °C and 0.023 (W/m-K) at 100 °C.

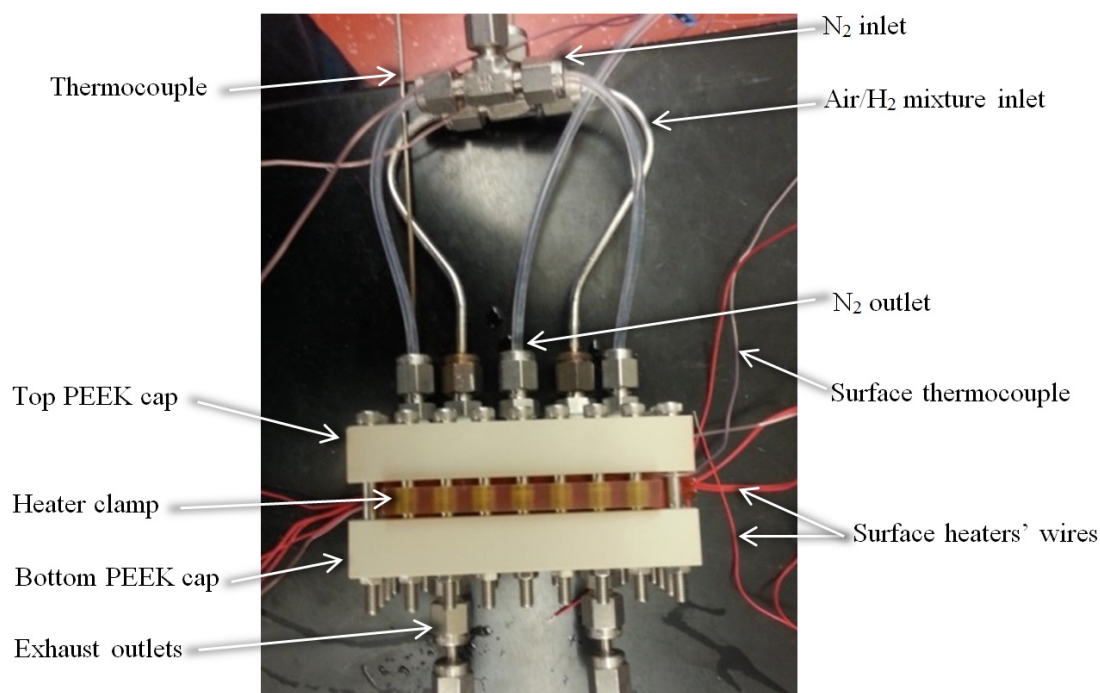


Figure 84: Final assembly of the test section

6-4 CA μ CHX Test Facility

The original test facility assembled by Haley [55] for a single unit cell MH μ CHX was modified for CA μ CHX testing. For completeness, the facility and the modifications are described here. A schematic of the test facility is shown in Figure 85. The test facility is located in the Hydrogen Storage lab at MBI. The instrumentation and equipment necessary was chosen such that the uncertainty is minimized in calculating the efficiency of the μ CHX. Table 18 summarizes the instruments and equipment used in the experiments.

Other required facilities were available in the lab and consisted of pressurized hydrogen and hydrogen delivery system, pressurized air and nitrogen and a supply of liquid nitrogen. Nitrogen gas was used as a heat exchanger fluid and also as a purging gas for hydrogen lines at the end of the experiments as part of the shutdown process. To regulate the flow rates of air and hydrogen, two mass flow controllers (MFC's) were used. Hydrogen MFC was normally closed while the air MFC was normally open to avoid combustion in case of a power outage. Downstream of both MFC's, two flashback arrestors with internal check valves were installed to prevent potential propagation of flame upstream. A normally closed solenoid valve was also installed on the hydrogen line as a safety feature.

Hydrogen and air got mixed in a T-junction before entering the combustor. The ratio of the flow rates of air and hydrogen was defined by the equivalence ratio (defined in section 4-2 Governing Equations). Hydrogen and air entered the μ CHX test section at room temperature and the exhaust products exited the μ CHX at temperatures typically higher than 100 °C. A cooling water stream was used to condense the water vapor existing in the exhaust before taking a GC sample.

Table 18: List of instrumentation and equipment for the facility shown in Fig. 13

Instrumentation/ Equipment	Manufacturer	Model	#	Range
H ₂ Mass Flow Controller	Advanced Energy	AERA Transformer	1	16 - 800 sccm
Air Mass Flow Controller	Advanced Energy	AERA Transformer	1	52 - 2600 sccm
H ₂ NC Solenoid Valve	ASCO	8262G2	1	
H ₂ Flame Arrestor	Concoa	532	1	50 psi
Air Flame Arrestor	Concoa	532	1	143 psi
Nitrogen Flowmeter	Brooks	SLA 5863	1	1 - 200 l/min
Desiccant Air Dryer	McMaster Carr	7793T1	2	130 F max
Cartridge Heaters	McMaster Carr	8376T24	4	30 W, 120 VAC, 778 °C max, 0.25 Amps Max
Surface heaters	Minco	HK5207R12.5L12A	4	12.5 Ohms, -200 °C to 200 °C, 3 Amps Max.
USB Data Acquisition Board	National Instruments	USB-6009	1	8 AI, 2 AO, 12-bit DIO, 1 Counter
CompactDAQ Thermocouple Module	National Instruments	USB-9213	1	16 Channel, 24-bit, Cold Junction
CompactDAQ Voltage Output Module	National Instruments	USB-9263	1	4 Channel, 16-bit
CompactDAQ Voltage Input Module	National Instruments	USB-9205	1	32 Channel, 16-bit
CompactDAQ Relay Module	National Instruments	USB-9481	1	4 Channel, SPST
Rotameter	Omega	FL-2044	1	10 - 100 lpm
Absolute Pressure Gauge	Omega	PX32B1	3	0 - 690 kPa [0-100 psia]
K-type Thermocouples	Omega	K-type (SLE)	12	0 - 1100 °C
T-type Thermocouples	Omega	T-type (SLE)	4	-200 to 350 °C
Pressure Regulator	Omega	PRG200-120	2	0 - 120 psig
H ₂ Pressure Regulator	Swagelok	PGI-63S-PG100-LAOX	1	0 - 100 psig
Gas Differential Pressure Gauge	Validyne	DP15 - 32	1	0 - 14 kPa [2.0 psi]
N ₂ Differential Pressure Gauge	Validyne	DP15 - 36	1	0 - 35 kPa [5.0 psi]

Inlet temperature and flow rate of the working fluid (nitrogen) was designed to be varied over a wide range of temperatures from room temperature to 200 K (-73 °C). Therefore a system for cooling nitrogen was added which consisted a liquid nitrogen dewar, a coiled tube and a valve. The dewar was filled with liquid nitrogen at atmospheric pressure ($T_{sat} = -196$ °C) and nitrogen

then flowed through the copper coil located inside the dewar and reached temperatures as low as -160 °C at its exit. The very cold stream of nitrogen then was mixed with room temperature nitrogen flowing through a bypass line to give the desired temperature. The flow rate of nitrogen was adjusted using two needle valves one upstream of the flow meter and a second one on the bypass line. When the flow rate was fixed to the desired value with the first needle valve, the temperature was adjusted by controlling the second needle valve.

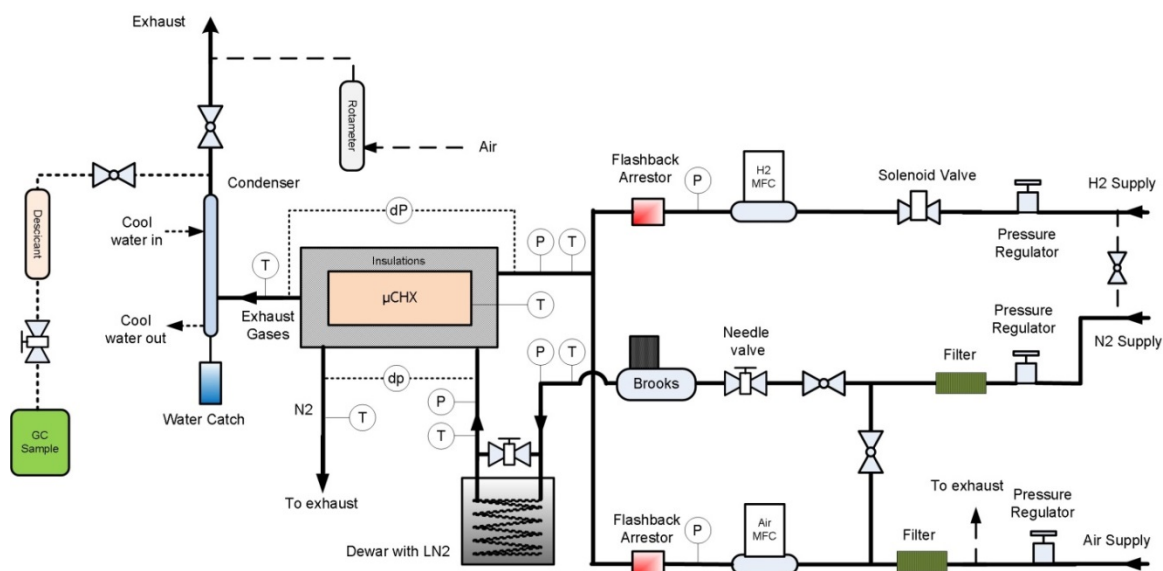


Figure 85: Test facility schematic

Two T-type thermocouples were inserted inside the dewar at different levels showed the extent of which the copper coil was submerged in liquid nitrogen (Figure 86).

Absolute pressures of air/H₂ mixture and nitrogen were measured at the inlet while differential pressures between the inlet and outlet of both streams were also measured. The temperatures of air/H₂ mixture and nitrogen were measured before and after the test section.

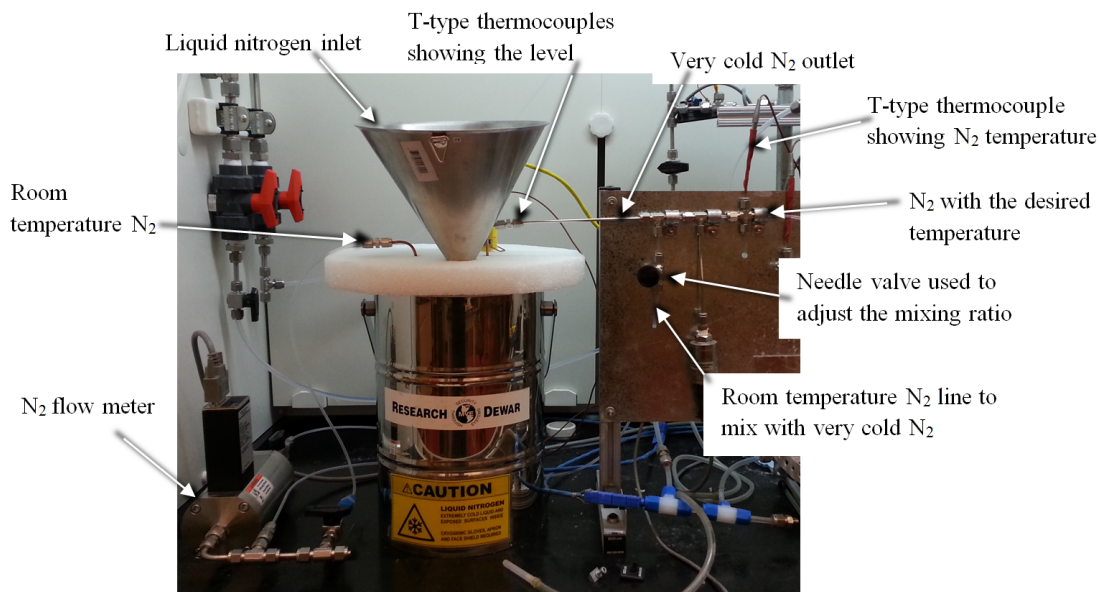


Figure 86: Nitrogen temperature and flow control system

Based on the previous experience [55], it was known that heat loss from the μ CHX test section can be a major player in the experimental results therefore several tactics were employed to reduce heat losses. Where possible, PFA tubings were used to connect external tubings to the inlets and outlets of the combustor to reduce heat loss by conduction. The thermal conductivity of PFA tubings ($k = 0.195 \text{ W/m-K}$) is much lower than the thermal conductivity of their stainless steel ($k = 15 \text{ W/m-K}$) counterparts. Initially, three layers of high temperature insulation (Pyrogel[®] XT, Aspen Aerogels, $k = 0.02 \text{ W/m-K}$) were put around the test section. Preliminary results showed more than 10% in heat loss depending on the input power. Therefore, two additional layers of insulation were added while also covering the connecting tubes. With those added, the heat loss reduced to less than 5% of the input power which was deemed acceptable. A gas chromatography system by Agilent Technologies (490 Micro GC[®]) was used to analyze the exhaust gas composition. One requirement of the GC was that there should be no moisture in the sample gas. Therefore, water vapor produced during the reaction of hydrogen and air was

removed in two steps. First, a condenser was placed in the exhaust stream following the test section wherein cold water was circulated within a tube in the shell and tube heat exchanger. The exhaust would flow in the shell of the condenser and the condensate was collected in a plastic bottle. Following the condenser, the exhaust stream was directed through two desiccant filters to further dry the air before being collected in sample bags. In some cases there might not be any reaction happening in the combustor while air/H₂ was flowing inside. One reason for that could be very low temperatures of the catalyst bed which could be caused by the cold working fluid. To avoid having hydrogen concentrations that could result in a combustible mixture in the exhaust and in the hood, the exhaust stream was diluted by a stream of air reducing the hydrogen to air ratio below the flammable range (4% - 75% by volume). Dilution flow rate was manually adjusted using a rotameter. The designed flow rates of the CA μ CHX are provided in Table 19 and the operating conditions are shown in Table 20. The pressure drops associated with turns and headers are not included.

Table 19: Design Flow Rates for μ CHX ($\phi=1$, max H₂ flow)

	Mass flow Rate (g/s)	Volumetric Flow Rate @STP (ml/min)
Air	0.027, 0.040	1,350-2,025
Hydrogen	7.57E-4, 1.14E-3	549-824
Nitrogen	2.53, 3.80	19,339-29,008

Table 20: Operating Parameters for μ CHX

H ₂ Chemical Power (W)	92.4-138.6
Nitrogen Inlet Temperature (K)	200
Nitrogen Desired Temperature at the Outlet (K)	233
μ CHX maximum body temperature (K)	473
ΔP Combustion Gases (bar)	<1
ΔP N ₂ (bar)	0.5 < ΔP < 3

Data acquisition: During the experiments, data were collected by a LabVIEW virtual instrument at the rate of 0.3 Hz. The LabVIEW program was also used to control different instruments and display graphs and results real time. The data acquisition system used is shown in Figure 87 schematically.

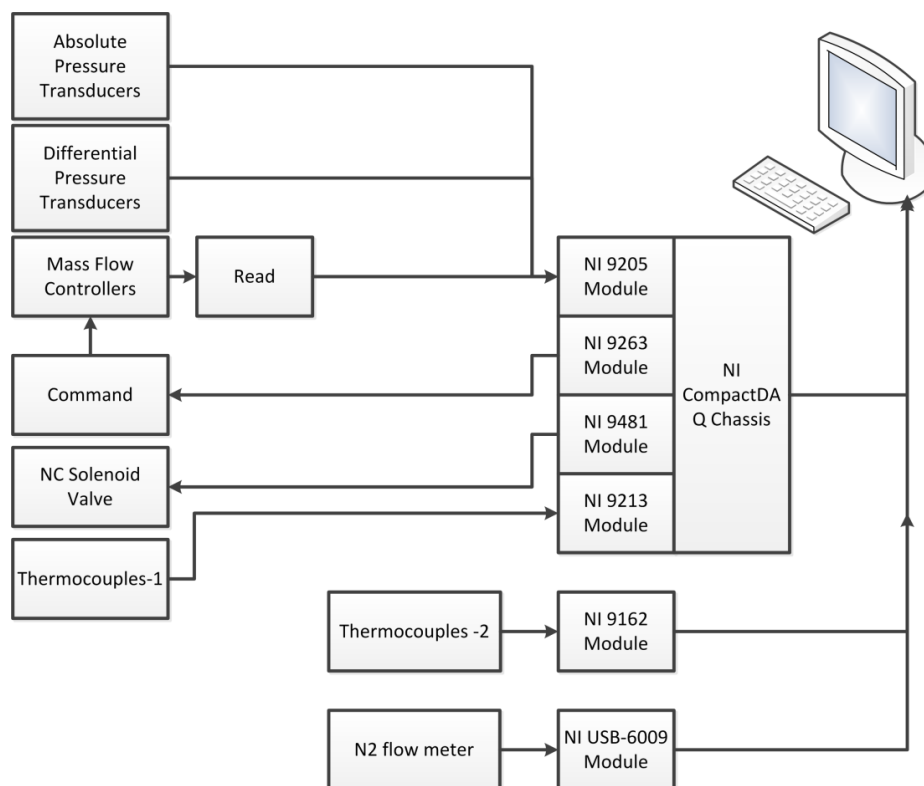


Figure 87: Data acquisition system used for the experiments

Table 21 summarizes the equipment used in DAQ system. National Instruments NI-9213 was used to read thermocouple inputs. A National Instruments USB-9162 was used to read other 4 thermocouples. To send signals to the MFC's, a National Instruments NI-9263 analog voltage output module was used. And a National Instruments NI-9205 analog voltage input module was used to acquire signals from MFC's and pressure transducers. And finally a National Instruments NI-9481 relay module was utilized to switch the hydrogen solenoid valve on and off.

Table 21: Data acquisition system components

DAQ Component	Manufacturer	Model	Range
USB Data Acquisition Board	National Instruments	USB-6009	8 AI, 2 AO, 12-bit DIO, 1 Counter
Hi-Speed USB Carrier	National Instruments	USB-9162	4-Ch, ± 80 mV, 24-Bit
CompactDAQ Thermocouple Module w/Cold Junction	National Instruments	USB-9213	16 Channel, 24-bit
CompactDAQ Voltage Output Module	National Instruments	USB-9263	4 Channel, 16-bit
CompactDAQ Voltage Input Module	National Instruments	USB-9205	32 Channel, 16-bit
CompactDAQ Relay Module	National Instruments	USB-9481	4 Channel, SPST

6-5 Experimental Procedures

The experimental procedures are summarized in this section consisting of four parts: start up, continuous operation, shutdown and emergency shutdown. Each procedure has several safety checks to be performed.

6-5-1 Start up procedure

Before starting an experiment, the experimental facility was checked according to the flowchart shown in Figure 88. Safety glasses were worn while working within the hood. If any modification has been done on the test section or in the plumbing, they were checked for leaks before starting the experiment. Power supplies for MFC's and pressure transducers were turned on. The desiccants were also checked and make sure that they were not in the loop (the valve was closed).

The desiccants were only in the loop when samples were taken from the exhaust gases. If the color of the desiccant's beads were blue instead of the normal yellow, they were replaced. Once the flow loop was inspected, the LabVIEW program was started. The program would start collecting data from the beginning. The data would not be saved until the save button was hit. All temperatures and pressure transducers readings were checked at this point to make sure that all are within the normal range.

With the system check completed, the experiment was started. After the air valve was opened, the rotameter in the exhaust line was adjusted to keep the exhaust gas composition below the flammable range for the worst case that all the introduced H_2 was unreacted. Preheating was necessary for the reaction to initiate. A body temperature of about $100\text{ }^\circ\text{C}$ was sufficient to start the reaction. The reaction was very slow at those temperatures; therefore in order to save time and reach a steady state sooner, the combustor was preheated to $120\text{ }^\circ\text{C}$ - $130\text{ }^\circ\text{C}$ before letting hydrogen flow within the combustor. At this point data saving was initiated in LabVIEW and the surface heaters were turned on and adjusted using a variable transformer. The power was slowly increased while a low flow rate of air (1000 sccm) was introduced. When the desired temperature ($130\text{ }^\circ\text{C}$) was reached, the heaters were turned off and unplugged. The air flow was increased to 2600 sccm and hydrogen valve was opened. After that hydrogen was let inside the combustor with an equivalence ratio of 0.05. The equivalence ratio was increased until a clear increase in the temperature was observed. Body temperature as well as other thermocouples around the combustor body was checked to remain below the maximum temperature ($250\text{ }^\circ\text{C}$). If the temperature reached $250\text{ }^\circ\text{C}$, hydrogen solenoid valve and heaters were automatically shut down and air flow rate was set to maximum to cool down the test section. Exhaust temperature were also check continuously to make sure that it remains higher than $100\text{ }^\circ\text{C}$ in order to prevent condensation inside.

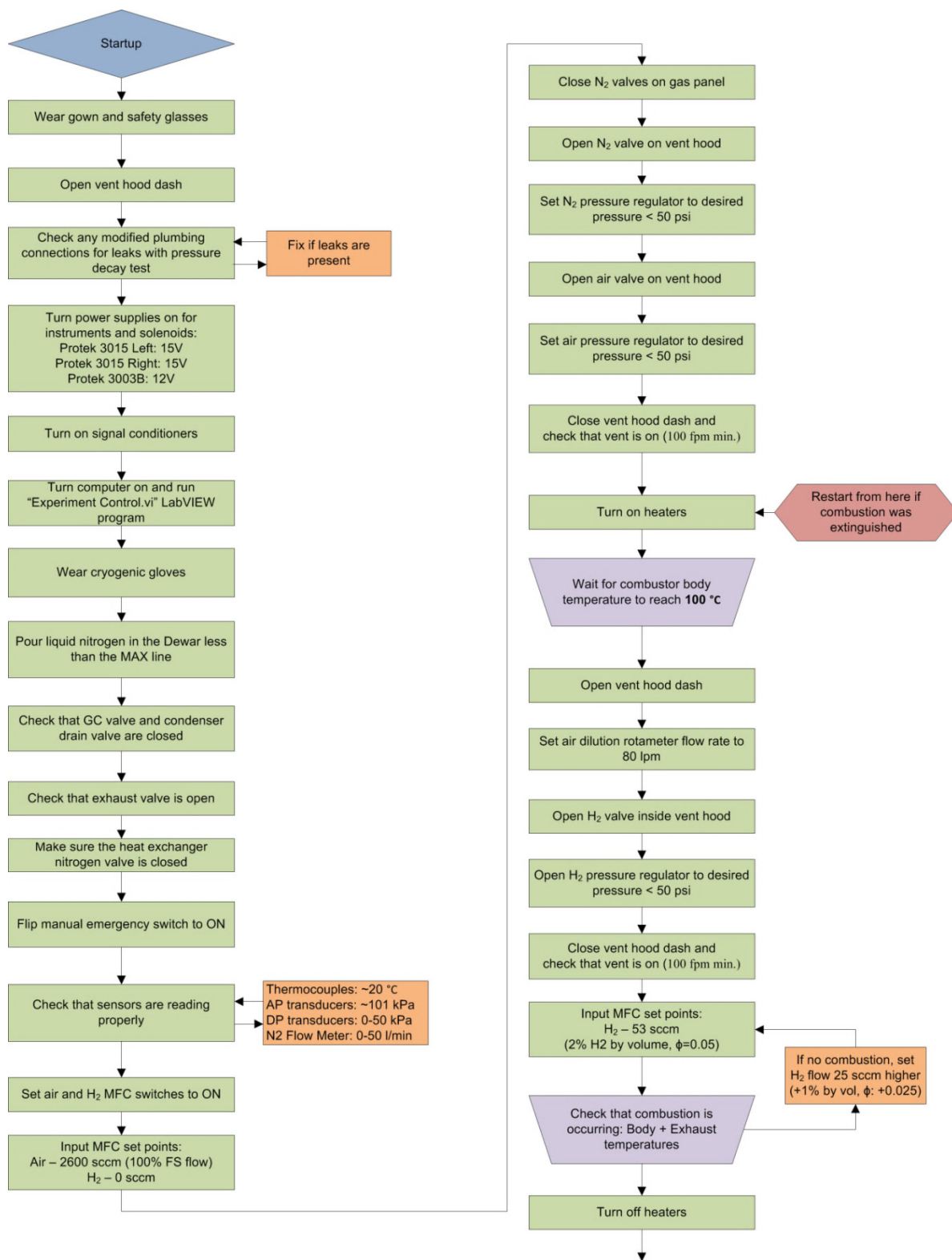


Figure 88: Test facility startup procedure

6-5-2 Continuous operation

With the combustion occurring in the combustor cold nitrogen was introduced into HX channels of the μ CHX (as the working fluid). The flow rate of nitrogen was adjusted by two needle valves and a flow meter. At first the desired nitrogen flow rate was flowed in the heat exchanger part of the μ CHX at room temperature. Then, liquid nitrogen was poured inside the dewar slowly, sudden change in temperature could block the flow since both stainless and copper tubings were used which have different thermal expansions.

Right after both thermocouples were submerged (showed a temperature lower than $-190\text{ }^{\circ}\text{C}$), no more liquid nitrogen was poured inside. Approximately $2/3^{\text{rd}}$ of the dewar were filled with liquid nitrogen which was enough for about 5 hours of testing. Cryogenic gloves, lab gown and masks were worn when handling liquid nitrogen. The temperature of the nitrogen stream could be changed by changing the mixing ratio of cold to room temperature nitrogen streams using the dewar bypass needle valve (Figure 86). The temperature of nitrogen going to the combustor was reduced in 5 degree intervals. After each time decreasing the temperature by $5\text{ }^{\circ}\text{C}$, it was made sure that the combustion was sustained and the exhaust temperature was remained higher than $100\text{ }^{\circ}\text{C}$. The flow chart presented in Figure 89 shows the steps were taken during continues operation. If at any point, the combustion was stopped or the exhaust temperature went below $100\text{ }^{\circ}\text{C}$, the nitrogen stream temperature was increased back to room temperature.

Steady state conditions at desired operating conditions of air/ H_2 and nitrogen flow rates and temperatures, were achieved in about 30 minutes – 2 hours. Steady state condition was defined as the state which the nitrogen outlet and combustor body temperature remain within $0.2\text{ }^{\circ}\text{C}$ for 15

minutes. Upon reading the steady state, a gas sample was collected for analysis in the Micro GC. Once the sample was collected, a difference flow rate of temperature was tested based on the experimental matrix or the shutdown procedure was initiated.

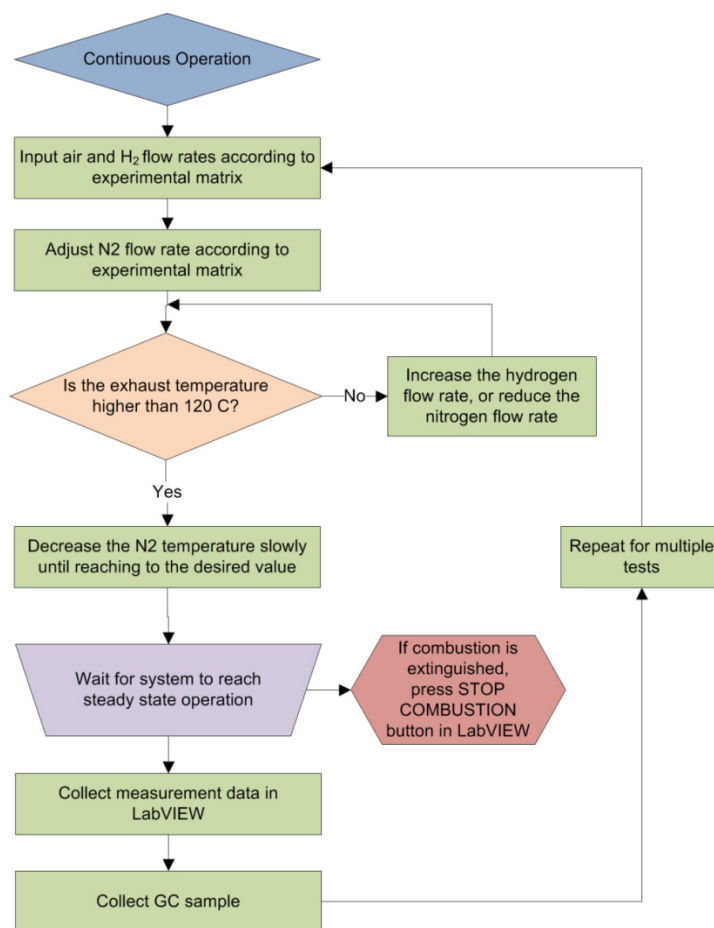


Figure 89: Continuous Operation Procedure

6-5-3 Shutdown procedure

A series of steps were followed in order to safely shutdown the system after all data and samples had been collected. A flow chart of the procedure is shown in Figure 90. First the cold stream of

nitrogen was stopped so that room temperature nitrogen would flow in the combustor. Then the vent hood dash was opened just enough to close the hydrogen main line (regulator). The hydrogen solenoid valve was remained open to empty the remaining hydrogen in the tubing through the exhaust line. Once the pressure on the hydrogen regulator dropped to less than 69 kPa (10 psi), the nitrogen valve on the hydrogen line was opened to purge the lines (Figure 85). Once the purge was completed and the temperatures dropped below 50 °C, the valves were closed and the LabVIEW program was stopped. Then all the power supplies were turned off and finally, the hydrogen valve in the outside cabinet was turned off.

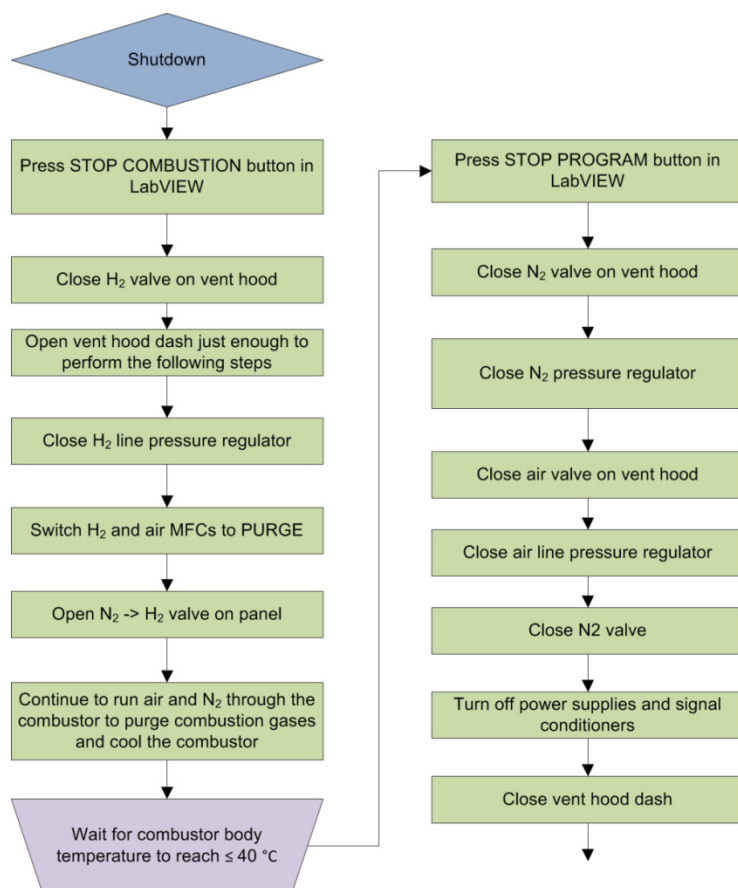


Figure 90: Shutdown Procedure

6-5-4 Emergency shutdown process

A flow chart was prepared describing the emergency shutdown procedure and is presented in Figure 91. An internal code was programmed in LabVIEW to stop the reaction and thus heat generation with one click. Hydrogen MFC was normally closed and air MFC was normally open therefore, in case of a power outage, air would flow inside the combustor without hydrogen and cool it down.

6-5-5 Hydrogen cabinet operation

Hydrogen supply to the lab was provided by two hydrogen tanks that were contained inside a safety cabinet located outside of the hydrogen storage lab. In the case when one of the cylinders was empty, the cabinet would automatically switch to the other cylinder with an alert to change the empty cylinder. Control of the cabinet was possible using a touch screen. If the delivery pressure of hydrogen was more than the defined value (80 psi), an alarm would go off requiring a pressure adjustment.

6-6 Safety Considerations

The facility has been designed for accuracy and safety. Figure 85 depicts the safety features built into the experimental facility. The major safety considerations are three items: (a) prevention of a flame from propagating upstream, (b) stoppage of the flow of hydrogen in the event of a leak or upstream flame propagation, and (c) prevention of liquid nitrogen to flow or splash anywhere outside the dewar. These safety features have been put in place through a consideration of the failure scenarios described in the next section.

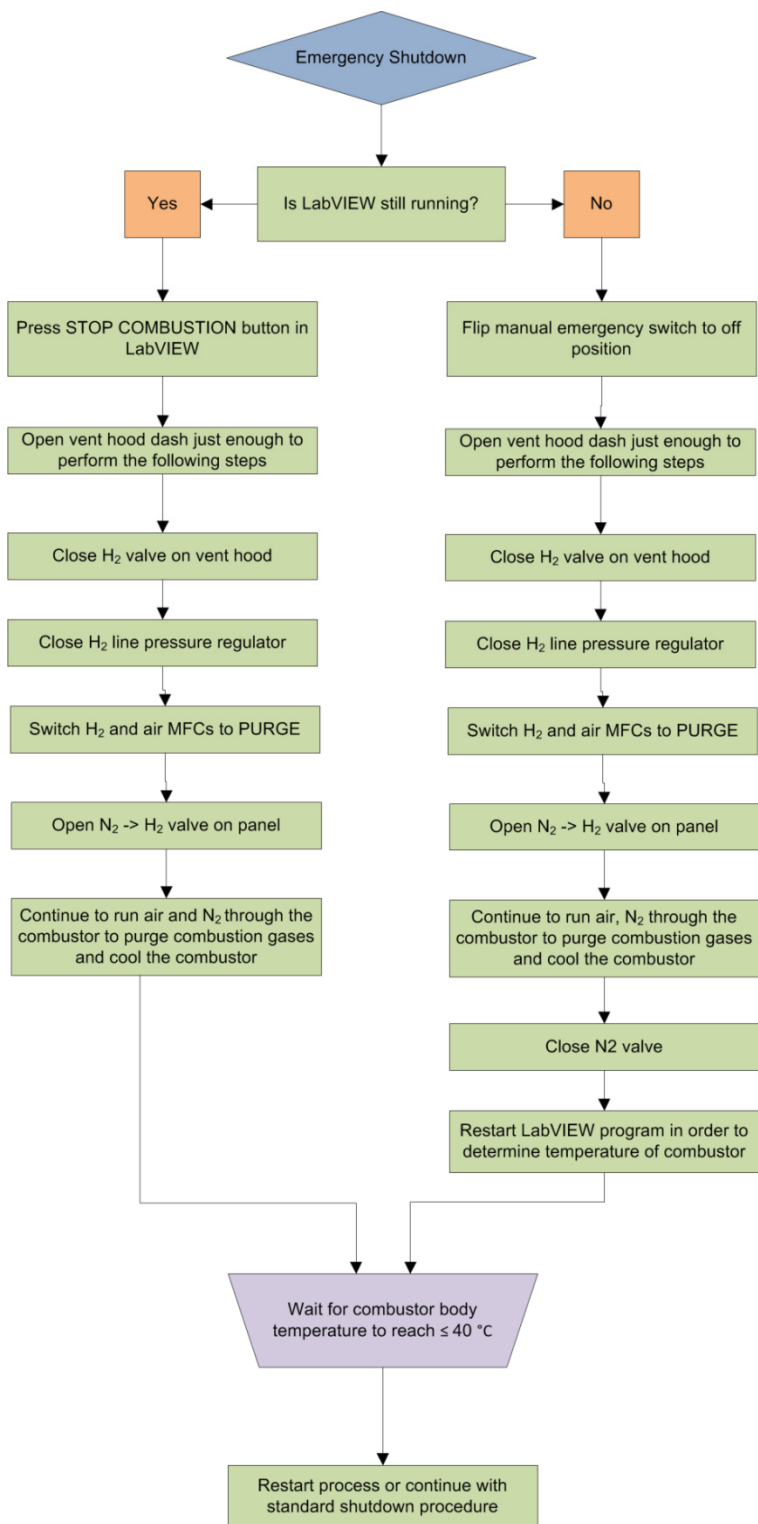


Figure 91: Emergency Shutdown Procedure

To address the first safety concern, flame arrestors are to be placed downstream of the mass flow controllers in the hydrogen and air lines. These are devices that prevent a flame or explosion from propagating upstream to the air or hydrogen sources. There is a sintered material in the arrestor that passively absorbs heat, stopping a flame from moving upstream. Also, there is an internal check valve that closes in the event of a flame or explosion, preventing the gas from flow back to the MFC. The valve is automatically reset by supplying flow in the correct direction. Additional check valves are located on the H₂ line, N₂ line and air line to prevent back flow of any gases to the gas supply lines or dilution system. This provides an additional level of safety redundancy.

To address the second safety concern, the H₂ MFC contains a normally-closed solenoid valve and a secondary normally-closed solenoid valve is located on the hydrogen line between the MFC and the pressure regulator. The air MFC contains a normally-open solenoid valve. The solenoid valves can be activated by one of four means: (a) an emergency switch within the LabVIEW program, or (b) a LabVIEW trigger set by the μ CHX body temperature sensor, or (c) a manual switch located near the vent hood, or (d) a loss of power. The safety system can be controlled through the DAQ system while retaining a manual emergency shutoff switch. The inside the Dewar is marked to show the maximum level of LN₂ to avoid splashing/spilling in case of small movements. Cryogenic gloves are worn whenever the operator is dealing with LN₂ Dewar or getting close to it.

Failure modes have been considered using a Failure Modes and Effects Analysis (FMEA). This process is a quantitative way to address failure risk for a product, system or process. The results of this analysis are tabulated in Table 22 and the corresponding legend is shown in Table 23.

Table 22: Failure Modes and Effects Analysis

Failure Mode	Effects	Severity Rating (S)	Cause(s)	Occurrence Rating (O)	Current Controls	Advance Detection Rating (D)	Risk Priority Number (RPN)
Flashback	Very high temperatures and fast upstream flame propagation.	9	Homogeneous combustion, low flow rates and high temperatures	2	Flashback arrestors are located before the MFCs. Extreme temperatures will trigger program to extinguish combustion.	10	180
Sustained Homogeneous Combustion in test section	Very high temperatures. May melt test section if sustained.	5	low flow rates and high temperatures	4	Extreme temperatures will trigger program to extinguish combustion.	2	40
Condensation/ice in the combustor	Blocks the flow, ruin the test section/ equipment	1	Low inlet N2 temperatures, high N2 flow rates. No combustion	5	Body and inlet and outlet temperatures of the streams are monitored. The experiment starts will very low N2 flow rate and higher temperatures.	4	20
Toppling of dewars	LN2 spill could cause potential burns to operator	4	Operator bumping against the table/dewar (table has wheels that if unlocked could result in tipping)	1	Fixtures for the dewar, operators will ensure that the dewar is fixed at all times; operators will wear safety equipment	10	40
Hydrogen Leak in Test Section	Fire risk	2	Improperly tightened test section. Improperly tightened fittings.	3	Entire flow loop is located within a vent hood. Test section tightened with torque wrench. CHX is pressure tested after every reassembly.	5	30
Hydrogen Leak in Flow Loop	Fire risk	2	Improperly tightened fittings.	2	The flow loop is located within a vent hood. An alarm goes off if vent hood fails. The H ₂ lines have been pressure tested to 50psi with no leakage.	5	20
Power Failure	Venthood, pump, computer and flow controllers turn off.	2	City power outage	1	H2 flow is stopped by NC solenoid and NC MFC. Air continues to flow through NO MFC.	10	20
Unreacted Hydrogen in Exhaust	Fire risk	1	Combustion not occurring	2	Entire flow loop is located within a vent hood. The exhaust gas is diluted below flammable levels if combustion were to stop.	1	2

Table 23: Failure Modes and Effects Analysis Legend

Severity Rating (S)	Meaning
1	Negligible Effect
2 to 3	Minor
4 to 6	Moderate
7 to 8	High
9 to 10	Very High (Results in unsafe operation)
Occurrence Rating (O)	Meaning
1	Negligible
2 to 3	Low (few failures)
4 to 6	Moderate (occasional failures)
7 to 8	High (repeated failures)
9 to 10	Very High (inevitable failure)
Advance Detection Rating (D)	Meaning
1	Negligible (certain detection)
2 to 3	Low risk (easily detected)
4 to 6	Moderate risk
7 to 8	High risk (unlikely detection)
9 to 10	Very high risk (almost undetectable)

The failure modes are ranked based on their risk priority number. This value is the product of the severity, occurrence and detection ratings. The risk priority number indicates the relative riskiness/importance of each failure mode. The failure modes are described in further detail following the FMEA table. Failure mode details are described in the following paragraphs.

Flashback: A flashback in the combustor or lines would result in very high temperatures and fast upstream flame propagation. To prevent flashbacks from damaging equipment, flashback arrestors are located before the MFCs. Flashback arrestors are standard components for welding systems; they have a sintered element that prevents upstream flame propagation and a check valve to prevent backflow. If a flashback is determined to have occurred, based on a high CHX

body temperature, the LabVIEW program will automatically shut off the H₂ flow. The severity of this failure is expected to be low (S=3) due to the flashback arrestors. The occurrence of this failure is expected to be moderately low (O=4) because the combustor has been designed to be intrinsically safe with channel sizes that should be too small for homogeneous combustion. Based on our current understanding of the system, flashbacks cannot be detected in advance (D=10). This results in a cumulative RPN of 120. While this is higher than preferred, it is acceptable because the severity of the failure is low.

Sustained Homogeneous Combustion in Test Section: Sustained homogeneous combustion (without flashback) in the test section would result in very high temperatures and may melt the test section. To prevent sustained homogeneous combustion, the LabVIEW program will automatically shut off the H₂ flow once a high CHX body temperature is exceeded. This limit will be 280°C, which is about 80% of the melting point of PEEK. The severity of this failure is high (S=9) because meltdown of the test section would be dangerous and damaging. The occurrence of this failure is expected to be moderately low (O=4) because the combustor has been designed to be intrinsically safe, as previously discussed. This failure will occur only if sustained and it will be easily detectable with the thermocouple attached to the body of the combustor (D=2). This results in a cumulative RPN of 72. While this is higher than preferred, it is acceptable because it should be easily detected and stopped before it can cause damage.

Condensation/ice in the combustor: When the heat produced in the combustor is not enough to maintain a minimum exhaust temperature of 100 °C, condensation (or worse freezing) of the water vapor content in the exhaust gases happens. The condensed water can block the channels and increase pressure drop. It can also ruin the test section after a while (S=4). This may occur at

low input chemical power, high nitrogen flow rates, or very low nitrogen temperatures. To avoid this all experiments will be started with room temperature nitrogen flow and while the body and exhaust temperatures are monitored carefully, the nitrogen temperature will be reduced to the desired temperature. When the temperatures are within the range, it is not likely to happen since the design was such a way to prevent that effect and simulations approved that (O=2). Detection of local condensation is impossible; however, if the exhaust temperature is high enough it will evaporate the local drops of water. Therefore, the exhaust and body temperatures are best ways to predict/detect condensation in the channels (D=7). This results in a cumulative RPN of 56. It is acceptable because it is not a severe incident and the experiment is monitored clearly. An alarm button is positioned in the LabVIEW program blinking when the inlet nitrogen temperature goes below 200 K or the exhaust gas temperature goes below 100 °C.

Toppling of the dewar: Stability of the dewars that contain LN2 is key to preventing spills and resultant freeze burns. The only way this can happen is if someone accidentally bumped the dewar (O=1), however the occurrence is unpredictable (D=10). The dewar and hoses will be fixed to a non-moving part inside the hood. A “MAX” sign will be marked inside the dewar showing the maximum level that the dewar should be filled. The level will be defined in a way that small movement will not cause any spill. Safety gear will be worn at all times by the operators during testing.

Hydrogen Leak in Test Section: The entire flow loop is located within a vent hood. Any leaks would rise, rapidly be diluted in the air and be ventilated through the hood (S=2). An audible alarm goes off if vent hood fails, alerting the operator to extinguish combustion. The risk of a leak is low (O=3) because the test section will be tightened with torque wrench and will be

pressure tested after every reassembly (D=5). The total RPN for this failure mode is 30, which is acceptable.

Hydrogen Leak in Flow Loop: The entire flow loop is located within a vent hood. Any leaks would rise, rapidly be diluted in the air and be ventilated through the hood (S=2). An audible alarm goes off if vent hood fails, alerting the operator to extinguish combustion. The risk of a leak is low (O=3) because the flow loop has been pressure tested to 50psi and will be retested after fitting adjustments (D=5). The total RPN for this failure mode is 20, which is acceptable.

Power Failure: When electrical power fails in the facility, the vent hood is shut off and so is the data acquisition program, active sensors, and flow controllers. Under such a situation, the flow of hydrogen is automatically turned off by the normally-closed solenoid valve while the air line is kept open in order to cool the apparatus (S=2). This is expected to be of very low occurrence (O=1) and it is impossible to detect in advance (D=10). The total RPN for this failure mode is 20, which is acceptable.

Unreacted Hydrogen in Exhaust: The entire flow loop is located within a vent hood. Any unreacted hydrogen will be diluted to less than 2% by volume in air (S=1). This is expected to happen regularly (O=10) as this will occur during start up and if combustion goes out during an experiment. It will also be readily detectable based on the readings of the thermocouples (D=5). The total RPN for this failure mode is 20, which is acceptable.

7- DATA ANALYSIS AND CALIBRATION

Methods of calibration and data analysis are described in this chapter. Gas leak as well as heat leak (loss) were two of the losses and are described here. Methods of instrument calibration are also presented and at the end sources of uncertainties are identified and uncertainty estimates provided.

7-1 Calibration

Calibration was performed for the thermocouples, pressure transducers and Micro GC. The factory calibrations were used for H₂ and air MFC's as well as N₂ flow meter. The mass flow controllers were calibrated by the manufacturer for full scale flow rates of 2600 sccm and 800 sccm for air and hydrogen, respectively. The calibration error was 1% of the setpoint for flow rates greater than 25% of the full scale flow rate. For flow rates between 2 – 25% of full scale, the error was 0.25% of full scale. The flow rate range used in the experiments was 500 sccm-2600 sccm for air and 0-600 sccm for hydrogen. The nitrogen flow meter was calibrated by the manufacturer to within $\pm 0.7\%$ of the measured flow rate if the rate is with 20% to 100% of full scale (200 l/min), and to within $\pm 0.2\%$ of full scale if the reading is below 20% of the full scale. Nitrogen flow rates used in the experiments were within 10-60 l/min.

7-1-1 Thermocouple calibration

Thermocouples were calibrated using a NIST-traceable RTD standard (with a bias error of ± 0.30 °C). A temperature-controlled chiller was used to perform a calibration of the T-type

thermocouples over the range -20 °C to 200 °C (Figure 92). Liquid nitrogen was used to calibrate the thermocouples at a single set point of -196 °C. Because of the large temperature interval (-200 °C to 200 °C), having all calibration data points on one plot did not give a good curve and the curve fit error was large. Therefore, the range was divided into two smaller intervals, -200 °C to 0 °C and from 0 °C to 200 °C. Curve fits for these two ranges are shown in Figure 93 for one of the thermocouples. For this thermocouple, the low range had an uncertainty of ± 0.319 °C and the higher range had an uncertainty of ± 0.363 °C. Thermocouple uncertainty was found using the following equation.

$$U_{TC} = \sqrt{\text{Random Error}_{TC}^2 + U_{NIST}^2 + \text{Curvefit Error}^2} \quad (48)$$

where

$$U_{NIST} = \sqrt{\text{Random Error}_{NIST}^2 + \text{Bias Error}_{NIST}^2} \quad (49)$$

A couple of K-type thermocouples were used for the activation process, which occurred at temperatures as high as 600 °C. The temperature readings during the activation process were not critical and the manufacturer accuracy (2.2 °C or 0.75%) was sufficient. Thermocouple calibration results are shown in Appendix C.

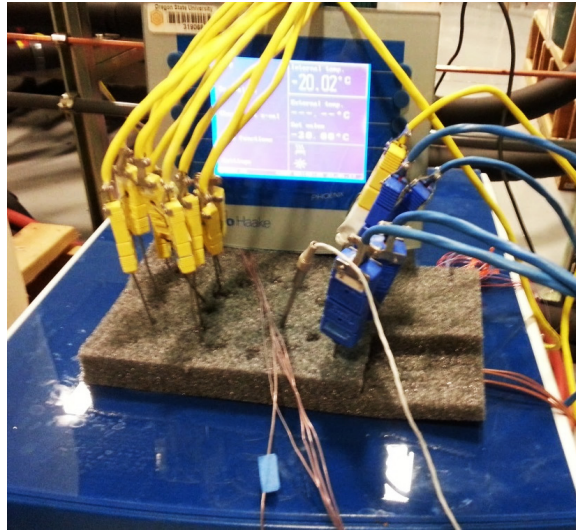


Figure 92: Chiller used to calibrate the thermocouples

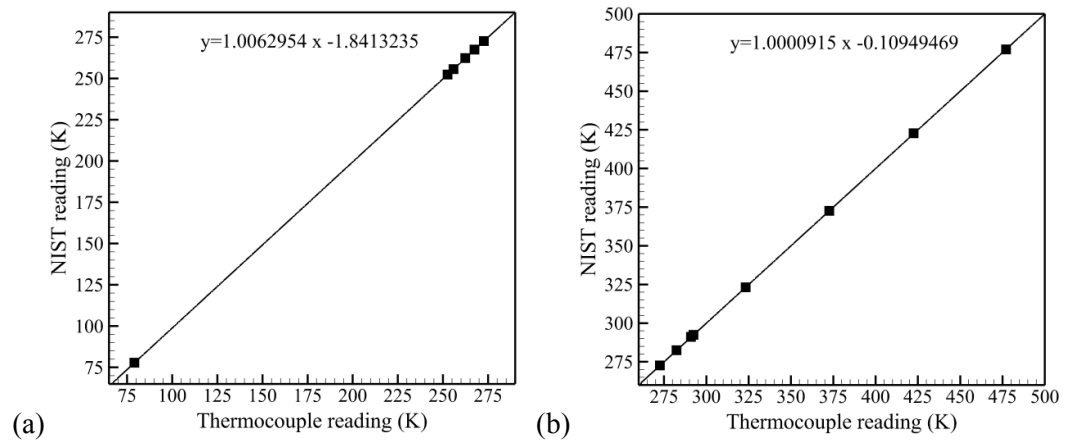


Figure 93: temperature calibration curves for thermocouple #1, (a) Below 0 °C, (b) above 0 °C K

7-1-2 Pressure transducers calibration

The Omega PX32 absolute pressure transducers were calibrated using a handheld Omega calibrator PCL-1B with a NIST-traceable absolute pressure module which was rated from 0 to 689.5 kPa and error of ± 0.345 kPa. The calibration was performed using compressed air while the

pressure transducer and calibrator were located in parallel and the pressure was controlled with an upstream regulator. The maximum calibration uncertainty for PX32 was 1.74 kPa. The uncertainty was found using the following equation.

$$U_{PT} = \sqrt{\text{Precision Error}_{PT}^2 + U_{NIST}^2 + \text{Curvefit Error}^2} \quad (50)$$

where PT stands for pressure transducer. The two differential pressure transducers were calibrated using the same Omega handheld calibrator but with different modules. The pressure transducer on the air/H₂ mixture side was calibrated by a differential module that was rated from 0 kPa to 49.8 kPa and with an error of ± 29.9 Pa. And the nitrogen side pressure transducer was calibrated using the absolute pressure module which was rated from 0 to 689.5 kPa and error of ± 0.345 kPa. A custom-built differential pressure calibration facility was used for the calibration. The nitrogen side pressure transducer uncertainty was ± 0.381 kPa (the corresponding calibration curve is shown in Figure 94) and the air/H₂ side had an uncertainty of ± 177 Pa.

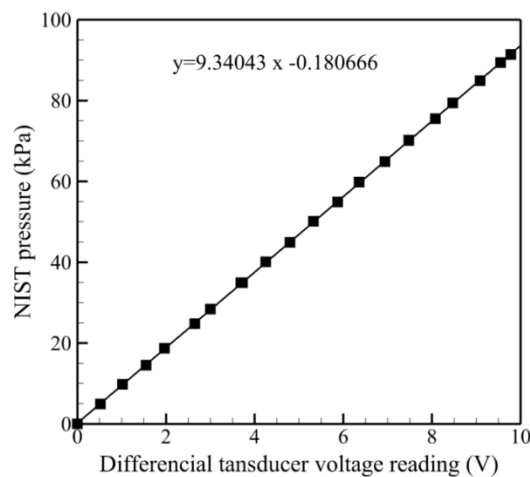


Figure 94: Differential pressure calibration for nitrogen side pressure transducer

7-1-3 Gas Chromatograph Calibration

The Micro GC was calibrated using two calibration samples with two different concentrations of hydrogen and nitrogen. The first one had a hydrogen volume fraction of 0.5 % and the other one had a hydrogen volume fraction of 30%. The GC plots and analysis from these two samples were used to fit a line through the data and calculated the volume and mass fraction of hydrogen in the exhaust.

Figure 95 shows the micro GC analysis plot for 0.5% volume hydrogen calibration gas. The peaks in the plot are signs of the existence of different gases. Each gas is identified by a retention time and in this plot, the 0.33 min retention time is for hydrogen and the 0.62 min retention time proves the existence of nitrogen in the mixture. The area under each peak is calculated by a software and can be used to measure the volume fractions of different gases in the mixture.

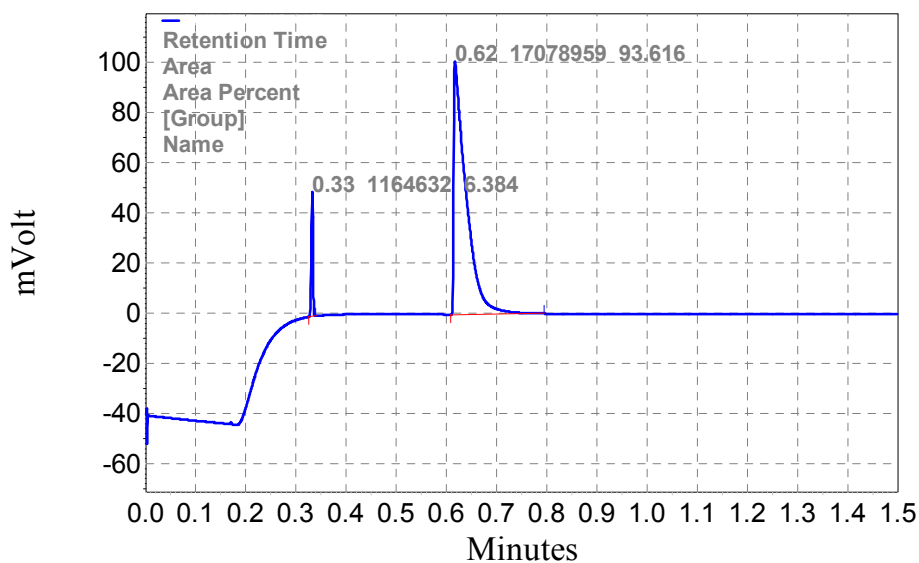


Figure 95: Micro GC composition analysis for a calibration gas mixture

7-2 Uncertainty Analysis

The precision uncertainty of the measured parameters was calculated by:

$$U_{Precision} = t_{95, N-1} \sigma_{\bar{X}} \quad (51)$$

where $t_{95, N-1}$ is the student t-test factor and $\sigma_{\bar{X}}$ is the standard deviation around the mean (\bar{X})

where X denotes a measured quantity. The student t-test factor was determined based on a 95% confidence interval and the numbers of degrees of freedom and N is the number of experimental data points collect. The overall uncertainty of the measured quantity was calculated as:

$$U_{\bar{X}} = \sqrt{U_{Precision}^2 + U_{Bias}^2} \quad (52)$$

where U_{Bias} is the bias error. When available, the calibration uncertainty was used as the bias error. Otherwise, the error reported by the manufacturer was used as the bias error. The uncertainty in the length of the catalyst coated part of the channels in the combustion channels could not be quantified because of the small variations in placement of the RTV paste (Figure 70). Therefore the uncertainty was estimated to be ± 0.5 mm. Table 24 summarizes the uncertainties in measured parameters used in calculating the efficiency of the μ CHX. These numbers are for an experiment with equivalence ratio of unity and residence time of 9.2 ms, and are shown as an example. Detailed example of uncertainty analysis is presented in Appendix C.

Table 24: Uncertainty of measured parameters for a sample experiment

Parameter	Bias Error	Precision Error	Total Uncertainty	Parameter Value	Percentage %
Pressure drop (Pa)	177	222	284	4162	6.82
N ₂ inlet temperature (C)	0.32	0.02	0.32	-69.86	0.46
N ₂ outlet temperature (C)	0.36	0.03	0.36	119.4	0.31
Hydrogen Flow rate (sccm)	2.64	6.12	6.67	660.5	1.01
Air flow rate (sccm)	6.28	15.7	16.9	1570.7	1.08
N ₂ flow rate (slpm)	0.17	0.34	0.38	24.62	1.55

The Kline-McClintock method was used for propagating the uncertainty of the calculated parameters. Table 25 summarizes the parameters and performance indices used throughout this and the next chapter.

Table 25: calculated parameters and indices and their equations

Index/Parameter	Equation
Efficiency (η)	$\eta = \frac{\dot{m}_{N_2} (h_{out} - h_{in})_{N_2}}{\dot{m}_{H_2} \Delta h_{reaction} / M_{H_2}}$
Equivalence ratio (ϕ)	$\phi = \frac{(H_2 / air)_{actual}}{(H_2 / air)_{st}}$
Hydrogen conversion	$H_2 \text{ Conversion} = \frac{Y_{H_2,in} - Y_{H_2,out}}{Y_{H_2,in}}$
Residence time (t_r)	$t_{r,global} = L / u_0$
Combustion time (t_c)	$t_{c,global} = \frac{C_{O_2,0}}{\dot{s}_{O_2,0}}$
Diffusion time (t_d)	$t_{d,global} = (H_c / 2)^2 / D_{O_2,0}$
Damkohler number (Da)	$Da = \frac{t_{r,global}}{t_{c,global}}$
Peclet number (Pe)	$Pe = \frac{t_{d,global}}{t_{r,global}}$

Table 26 shows the uncertainties of the calculated parameters using the above table.

Table 26: Uncertainty of calculated parameters for a sample experiment

Parameter	Total Uncertainty	Parameter Value	Percentage %
\dot{m}_{N_2} (kg/s)	7.39E-06	4.77E-04	1.55
\dot{Q}_{N_2} (W)	1.484	94.491	1.57
\dot{m}_{H_2} (kg/s)	9.19E-09	9.10E-07	1.01
\dot{Q}_{input} (W)	1.102	109.196	1.01
Efficiency (η)	0.009	0.865	1.01
Equivalence ratio (ϕ)	0.015	1	1.5
t_r (ms)	0.225	9.185	2.45
t_c (ms)	4E-7	1.2E-3	0.03
t_d (ms)	1.75E-6	1.26E-3	0.14

The uncertainties in calculation of hydrogen conversion came from the uncertainty in GC measurements and calibration. For each experiment, the exhaust gas sample was analyzed by the GC for three times. The repeatability of the analysis for each sample was then calculated (less than ± 0.5 %). The calibration gases also had an uncertainty of $\pm 2\%$ of the volume fractions. Therefore, the uncertainty in GC calculations can be found by

$$U_{GC} = \sqrt{U_{cal}^2 + U_{Repeatability}^2} \quad (53)$$

7-3 Leak Test

For results presented in this thesis, the multiple unit cell μ CHX was formed by bolting the layers together. Small scratches on the surface of the layers or uneven pressure distribution could cause leaks. Gas leaks can have several effects on the experimental results. They can be a cause of losing overall power as a part of heat losses and can also increase measured pressure drops.

Hydrogen gas leak might also cause fire hazard. In order to make sure that the leak is at a minimum, at the design stage, several bolts were evenly spaced to provide a uniform pressure on the layers. During the assembly, bolts were tightened to a specific torque. Then air was let inside the combustor until the pressure reached 2 bar. In this leak test all inlets and outlets were plugged except two of them: One where air came in and another that a pressure transducer was connected to one of the outlets of air. Once the pressure reached 2 bar, the air flow was turned off and the pressure decay was measured. Leak rate (g/s) could be calculated by the pressure decay with time and knowing the internal volume of the combustor. In the activation assembly, the bolts were tightened to 15 ft.lb with a leak rate of 58 Pa/s. For the actual tests, the leak rate was even lower because of the weak bonding between layers that occurred during the activation process. It was observed that tightening the bolt to 5 ft.lb was sufficient to give 24 Pa/s leak rate at 1.5 bar pressure. Figure 96 shows the pressure decay of air pressurized in the combustion/ exhaust channels. The volumetric leak rate is easy to calculate using the ideal gas law equation.

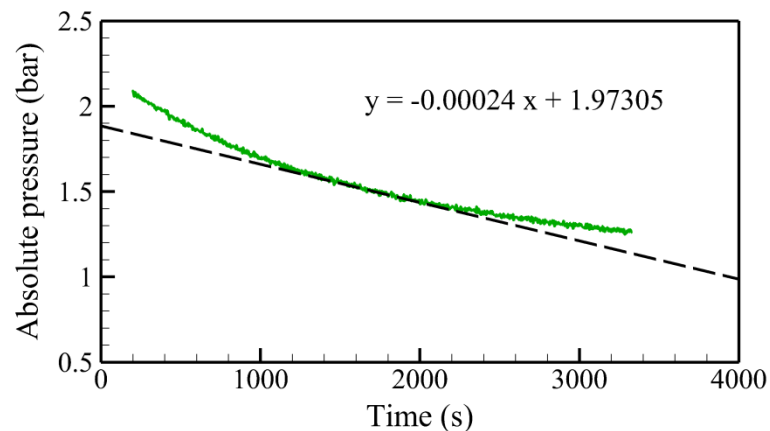


Figure 96: Pressure decay versus time and the rate at 1.5 bar

Based on ideal gas law:

$$PV = nRT \quad (54)$$

In this experiment, temperature and volume were constants. Therefore:

$$\frac{dP}{dt} V = \frac{dm}{dt} \cdot R_{air} \cdot T \quad (55)$$

And with the internal volume of the combustor being $1.773 \times 10^{-6} \text{ m}^3$, $T = 294.3 \text{ K}$ and $R_{air} = 287.00 \text{ J/(kg.K)}$, the leak rate was found to be $5.038 \times 10^{-7} \text{ g/s}$, or to 0.0107 sccm/s . A normal operating flow rate of air/H₂ mixture was 1000 sccm , therefore the leak rate was less than 0.0011% of the flow rate.

7-4 Heat Loss Calculations

Reduction and estimation of losses was one of the challenges of this project. The goal was to develop a μCHX that had an efficiency of more than 85% including heat losses. In the preliminary experiments, heat losses (including insulation and exhaust heat losses) were more than 12% of the chemical power input. Heat losses were not a major issue during activation process as long as the temperature of the device was kept at $600 \text{ }^\circ\text{C}$. It was started with three rounds of the Pyrogel XT[®] (Aspen Aerogels) high temperature insulations. After wrapping 5 rounds of insulations around the test section and also insulating the incoming and exiting metal tubing, the heat loss was reduced to less than 5% of the input power. As expected heat loss was a function of body temperature. Figure 97 shows the tests section with the insulations.

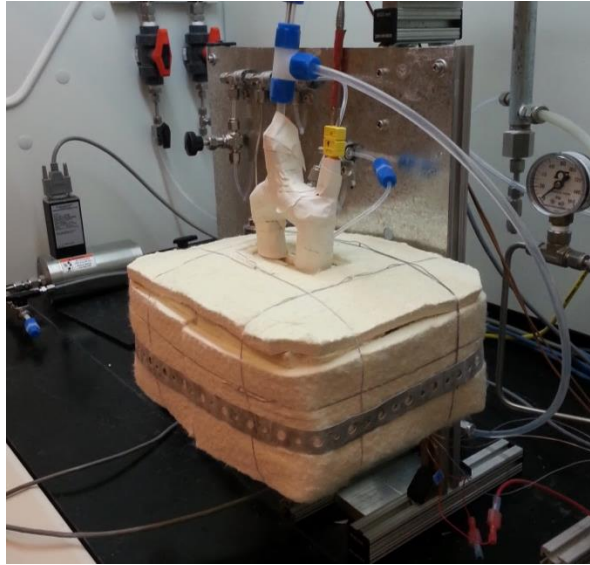


Figure 97: The test section covered by insulation

One way of estimating overall losses was to subtract the heat transferred to the nitrogen stream from the input power. The total lost (\dot{Q}_{Ltot}) included heat loss (\dot{Q}_L), chemical power lost because of uncompleted combustion (\dot{Q}_{CombL}) and also power lost by the gas leaks (\dot{Q}_{LeakL}). The last loss would be negligible since the leak rate was very small. The calculated \dot{Q}_{LeakL} was less than 10^{-4} W.

$$\dot{Q}_{Ltot} = \dot{Q}_{input, H_2} - \dot{Q}_{HX, N_2} \quad (56)$$

$$\dot{Q}_{Ltot} = \dot{Q}_L + \dot{Q}_{CombL} + \dot{Q}_{LeakL}$$

The power lost due to uncompleted combustion (\dot{Q}_{CombL}) could be calculated by measuring the hydrogen mass fraction in the exhaust gases using Micro GC. And as a result, heat loss (\dot{Q}_L) could be calculated using Eq.(56).

Q_L consists of two parts. Heat lost through the insulation and conduction and heat loss through the hot exhaust ($Q_{ExhaustL}$). Lower heating value (LHV) of hydrogen gas was used to calculate the input chemical power. The exhaust temperature is assumed to be 25 °C while water is still in vapor phase. Therefore the excess heat that the exhaust steam is carrying out of the system is one form of heat loss. The heat lost to the exhaust can be calculated by multiplying the heat capacity of the stream to the temperature difference between exhaust and 25 °C. This heat loss is relatively small (< 3 W) and was considered as part of the Q_L heat loss.

Another method was used to calculate heat loss. In this method, the combustor test section was heated up to a specific temperature with electric heaters. Then the heaters were turned off and the test section was let to cool down to room temperature. By measuring the temperature decay by time, heat loss could be calculated at any body temperature. Temperature decay plot presented in Figure 98 shows the body temperature of the test section decays at a rate of 0.00757 °C per second. Knowing that and the mass of the test section (layers, bolts, nuts, fittings and the PEEK parts), the heat loss was calculated to be 1.94 W at the body temperature of 100 °C.

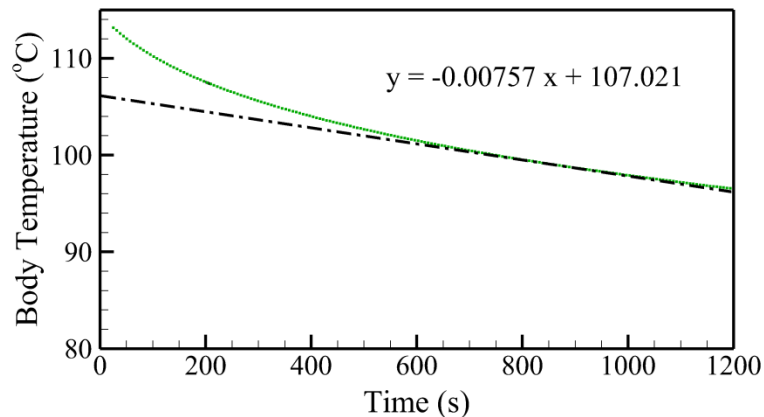


Figure 98: Temperature decay by time

8- EXPERIMENTAL RESULTS AND DISCUSSION

Nitrogen inlet temperature, equivalence ratio, body temperature among other parameters had significant effect on the overall efficiency and hydrogen conversion and their effects were studied. In chapter 4, a performance map was developed based on the simulation results. The map divided operating condition combinations into 4 different regions and for high hydrogen conversions and low pressure drop, Region-1 was suggested (Figure 38). The map was taken into consideration in the design of the fabricated μ CHX. The range of the experiments was also chosen such that the μ CHX operated in Region-1.

8-1 Experimental Matrix

Table 27 summarizes the experiments conducted on the μ CHX. The range of the varied parameters and the values of the fixed parameters are also shown. Since low temperature working fluid had the interest of DOE, most experiments were conducted at nitrogen temperatures around -70 °C. Initial tests were conducted at the room temperature nitrogen and a couple of experiments were run with nitrogen around -150 °C were also performed to test the capabilities of the μ CHX.

Table 27: Experimental matrix of the μ CHX experiments

Varied parameter	Equivalence ratio (ϕ)	Residence time (ms)	N ₂ inlet temperature (°C)	Body temperature (°C)
Equivalence ratio	0.2 to 1	9.85 (9.6 to 10.1)	-70.4 (-69.5 to -71.3)	186.15 (184.6 to 187.7)
Residence time	1	8.6 to 55.8	-16 (-13 to -19)	186.9 (185.9 to 187.9)
Residence time	1	20.9 to 61.6	23	187.4 (187.2 to 187.6)
N ₂ inlet temperature	1	8.6 to 61.6	-153 to -23	3.3 to 196.2
Body temperature	1	9.4 (8.6 to 10.2)	-70.15 (-69.2 to -71.1)	3.3 to 196.2

Operating conditions were chosen such that the performance map (Figure 38) is satisfied. Figure 99 shows the performance map with the experiments conditions plotted. The values of x -axis and y -axis are based on inlet conditions; therefore this plot does not show any of the experimental results. It can be seen that most of the experiments are at Region-1 which was desired. The marked area in the map was the location of desired operating conditions and the data points indicate actually achieved experimental conditions.

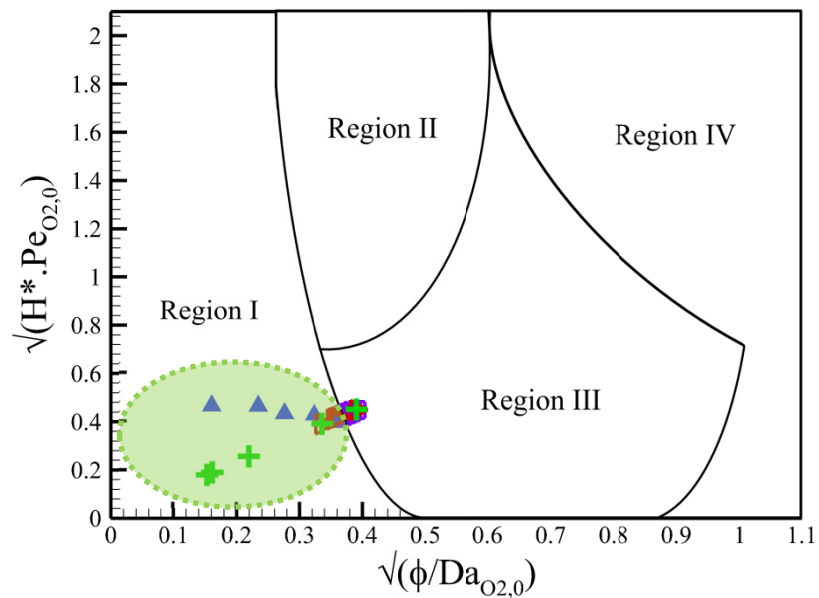


Figure 99: Experimental operating condition and the performance map

The limited resources (time and budget) did not make possible to change the catalyst bed length or channel heights. One parameter that was underestimated during the initial tests was the temperature of the body of the combustor. The body temperature had a significant effect on H_2 conversion. Hence a parametric variation on the effect of varying its value was also performed.

8-2 Repeatability of the Experiments

For repeatability estimate, one set of operating conditions were repeated three times on three different days. Two of these experiments were performed as the first experiments of the day, when the test section was cold. Another repetition was performed at the end of a day of experimentation when the test section was hot. The working conditions were the same as described in Table 24 and Table 26. The exact working conditions were very difficult to achieve but the conditions were kept the same as much as possible. The operating conditions are compared in Table 28. The first test was taken on April 1st, the next test was performed two days later on April 3rd and the last test was performed 8 days after. It should be noted that no experiments were performed from April 3rd to April 11th. The two experiments on April 1st and April 11th were conducted at the beginning of the day and the test of April 3rd was conducted at the end of the day. All operating conditions were within 2.2% of other experiments as shown in Table 28.

Table 28: Operating conditions and date of the experiments

Date	N ₂ temperature (°C)	N ₂ flow (slpm)	Air/H ₂ mixture flow rate (sccm)	Equivalence ratio (ϕ)	Residence time (ms)	Body temperature (°C)
1 April 2013	-69.9	24.6	2231.0	1	9.2	184.6
3 April 2013	-70.6	27.5	2276.4	1	9.0	185.7
11 April 2013	-70.1	25.0	2238.8	1	9.2	185.2

The results of the experiments are compared in Table 29 along with the date of the experiments. As it can be seen very good agreement was found between the tests for hydrogen conversion and

efficiency. The efficiencies were within the uncertainty of the experiments (0.865 ± 0.009).

Hydrogen conversion dropped slightly (1%) in the last experiment which was the main reason for the drop in efficiency. Pressure drop on the air/H₂ mixture side as well as nitrogen exit temperature seemed to have the highest variations. The higher pressure drop for the April 3rd test can be described by air/H₂ mixture and N₂ flow rates since it was higher than the other two experiments.

Table 29: Result comparison among three cases of the repeatability study

Date	Power in (W)	N ₂ exit temperature (°C)	H ₂ Conversion	Heat loss (W)	Efficiency (η)	ΔP air (Pa)	ΔP N ₂ (Pa)
1 April	109.2	119.4	0.904	4.48	0.865	4162.355	99555.2
3 April	114.0	102.6	0.907	4.61	0.866	4321.067	119223.6
11 April	109.4	111.9	0.898	4.41	0.858	4089.35	110236.6
Max difference	4.4%	15.9%	1.0%	4.5%	0.9%	5.6%	19.7%

8-3 Experimental Results

Hydrogen conversion is defined as the ratio of the amount of hydrogen reacted to that of input hydrogen,

$$H_2 \text{ Conversion} = \frac{Y_{H_2,in} - Y_{H_2,out}}{Y_{H_2,in}} \quad (57)$$

where Y_{H_2} is the mass fraction of hydrogen. Hydrogen mass fraction at the inlet is defined by equivalence ratio and adjusted by the mass flow controllers. At the outlet (exhaust), hydrogen mass fraction is calculated using the Micro GC.

Inlet and outlet temperatures, pressures and flow rates of the streams are measured using digital data acquisition. The gathered data is used to calculate the overall performance of the μ CHX and is defined as the ratio of the amount of heat transferred to nitrogen to the chemical energy of input hydrogen,

$$\eta = \frac{\dot{m}_{N_2} (h_{out} - h_{in})_{N_2}}{\dot{m}_{H_2} \Delta \bar{h}_{reaction} / M_{H_2}} \quad (58)$$

Heat losses are calculated by subtracting the heat transferred to nitrogen from the heat produced in the combustor by the reacted hydrogen.

$$Q_L = \frac{\dot{m}_{H_2} \Delta \bar{h}_{reaction} (H_2 \text{ Conversion})}{M_{H_2}} - \dot{m}_{N_2} (h_{out} - h_{in})_{N_2} \quad (59)$$

The temperature of the body of the device was measured at four different locations. To determine the body temperature, readings from two of the thermocouples located closest to the catalyst section of the μ CHX were averaged.

Varied parameters included the inlet temperature of cold nitrogen (150-273 K), mass flow rate of cold nitrogen, mass flow rate of the combustible gas mixture and equivalence ratio. The performance of the device was characterized using three parameters- pressure drop across the combustor and exhaust channels, hydrogen conversion, and efficiency index. The equivalence

ratio is defined as the ratio of the molar fuel-to-air ratio at the test conditions to that at stoichiometric conditions.

8-3-1 Effect of residence time

One of the important factors in hydrogen conversion is the residence time over the catalyst for reactions. Residence time is defined as the time a hydrogen molecule has to react before leaving the catalyst region which can be calculated by dividing the length of the catalyst bed to the mixture velocity. A mixture of air/H₂ flows over a catalyst bed in both combustion and exhaust channels. Therefore, the total residence time is calculated by adding the residence time of the mixture in the combustor channel and in the exhaust channel. Since there were 16 combustion channels, the average velocity in a combustion channel was found by dividing the mixture flow rate by 16 and by the cross section area. The etched channels did not have the shape of a perfect rectangular because of the etching limitations. Therefore the cross section area of the channels could not be calculated by simply multiplying channel width and height. Thus, the cross section area was calculated by analyzing the data from ZeScope profilometer. In the plot presented in Figure 100, the ZeScope data were extracted and plotted. It can be seen that the height of the channel is 377 μm instead of the desired 300 μm . In order to calculate the cross section of such channel, the curve in Figure 100 was integrated. The integrated area was 0.647 mm^2 compared to 0.6 mm^2 calculated by multiplying the height (300 μm) with the width (2 mm). It shows that the actual cross section area is about 8% higher. The same measurements were repeated for different combustion and exhaust channels and showed the same outcome since the same etching process was used for all shims.

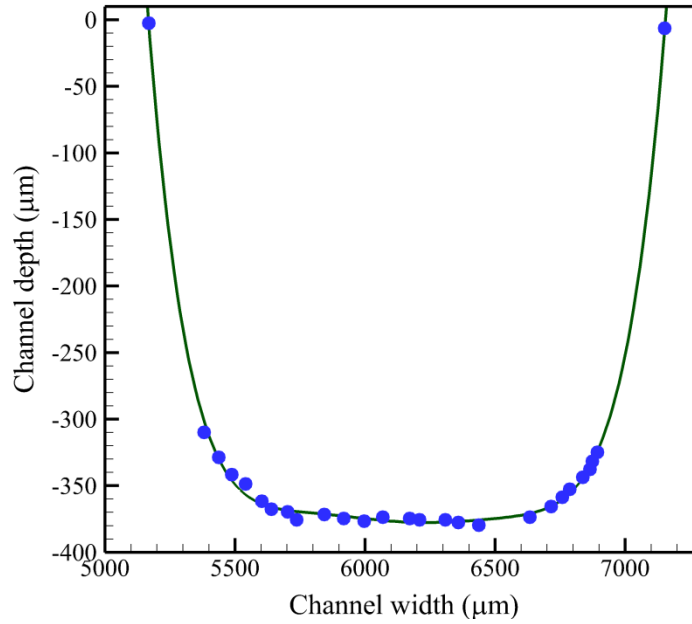


Figure 100: Cross section of a combustion channel

Figure 101 shows the effect of residence time on H_2 conversion and device efficiency. Table 30 summarizes the results of this plot. Equivalence ratio was kept constant at unity and inlet nitrogen stream temperature is kept constant at $-19\text{ }^\circ\text{C}$ for these experiments. Table 27 shows fixed parameters and their values for residence time variation experiment.

Table 30: Test conditions related to Figure 101

t_r (ms)	Input Power (W)	H_2 Conversion	η	Q_L (W)	r_{Q_L}
55.8	19.8	0.941	0.663	5.49	0.277
49.9	22.1	0.938	0.696	5.33	0.241
27.2	40.5	0.912	0.786	5.11	0.126
11.7	94.3	0.868	0.820	4.51	0.048
8.64	127.2	0.858	0.822	4.57	0.036

It can be seen that H_2 conversion increases by about 10% with increasing residence time from 8.6 – 55.8 ms. The same effect was observed by computer simulation results (Figure 31). However,

in the simulations, residence times higher than 8 ms led to almost complete conversions. It clearly shows that the catalyst surfaces in the experiments were not as active as an ideal catalyst surface.

The efficiency of the device drops from 82% to 66% with an increase in residence times. Since the total length of the catalyst and the equivalence ratio were fixed, in order to achieve different residence times the flow rate of hydrogen/air mixture had to be varied (see Eq. (33)). Different hydrogen/air flow rates results in different input power to the system (Table 30). When the power generated in a device is small, the effect of heat losses on the overall efficiency of the system can be significant. The body temperature was kept approximately the same between all experiments at about 186 °C and therefore there is not much difference between heat losses (in Watts, see Table 30). However, the ratio of the heat loss to total input power which is defined as,

$$r_{Q_L} = \frac{Q_L}{\dot{m}_{H_2} \Delta \bar{h}_{reaction} / M_{H_2}} \quad (60)$$

increased with an increase in residence time. Therefore, the heat loss ratio r_{Q_L} would be different for different cases and is shown in Figure 101. The higher is the heat loss ratio; the lower is the efficiency of the μ CHX.

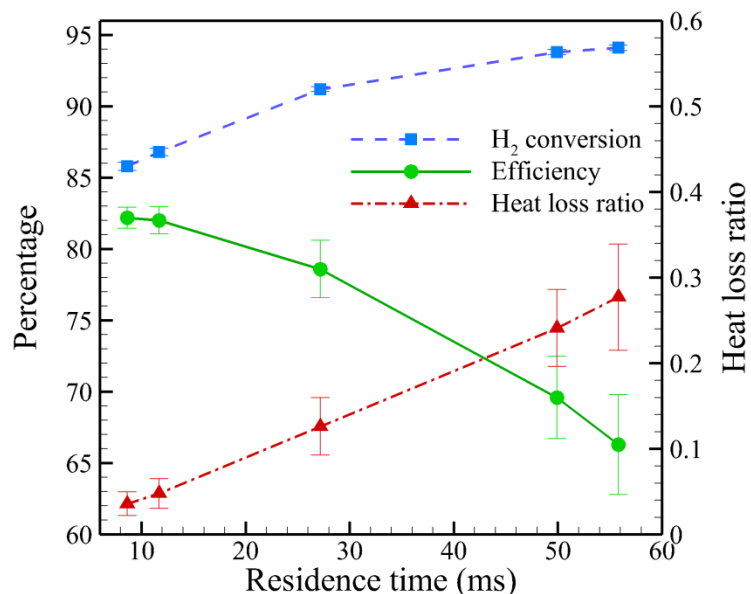


Figure 101: Variation of H₂ conversion, efficiency and heat loss ratio by residence time

Error bars indicate the uncertainty in the calculation of each of the data points. The uncertainty in hydrogen conversion was very small (0.3 %) which was because of the high precision of the GC. On the other hand, heat loss ratio had a large uncertainty of about 40%. The heat loss was calculated by subtracting two large numbers from each other (Eq. (59)). The uncertainty of efficiency varied from less than $\pm 1\%$ to over $\pm 5\%$ at higher residence times. Higher residence times correspond to lower input powers and therefore percentage error in η increased.

8-3-2 Effect of body temperature

The body temperature of the combustor is an important factor in conversion and device efficiency since higher body temperatures result in higher reaction rate and hence conversion (Eq. (20)). However, higher body temperatures would result in higher heat losses as well. The effect of an increase in body temperature on H₂ conversion is shown in Figure 102. The body temperature

was varied from 124 °C to 196 °C while keeping the residence time almost constant (varying from 8.94 ms to 10.2 ms) and equivalence ratio of unity. The body temperature was varied by increasing N₂ flow rate when the inlet nitrogen stream temperature was kept nearly constant in the range of -69.4 °C to -71.1 °C.

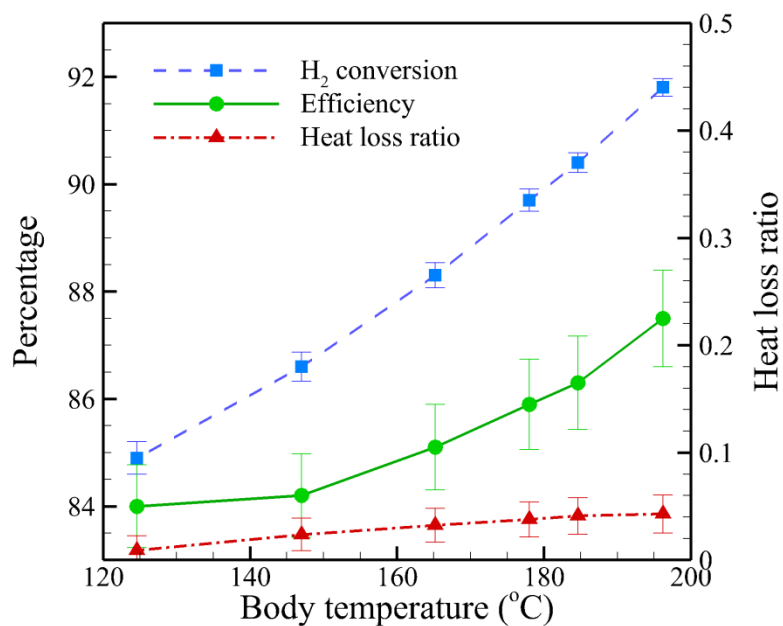


Figure 102: Variation of H₂ conversion, efficiency and heat loss ratio by body temperature

The heat loss values vary from 1.1 W for the body temperature of 124 °C to 4.6 W for the body temperature of 196 °C. Since the power input is high in these cases (120 W), although heat loss increases, the heat loss ratios are small numbers and have insignificant effect on the overall efficiency of the system. Therefore the efficiency also increases with increasing the body temperature.

Three lower body temperatures were also tested with the same residence times and inlet nitrogen temperatures. Figure 103 shows the performance indices at lower body temperatures. Also shown

for comparison the data point at $T_b = 124$ °C. The heat loss ratio changed from positive values at body temperatures higher than 34 °C to a negative value at the body temperature of 3.3 °C. That means in body temperature of 3.3 °C, the μ CHX was absorbing heat from the environment rather loosing heat. With a close look at Figure 103, it can be seen that efficiency of the device became more that hydrogen conversion which meant heat was being added to the system. It should be noted that for $T_b < 100$ °C, the exhaust temperature was less than 100 °C which means condensation was happening inside the μ CHX. Efficiency is still calculated based on lower heating value (LHV) of hydrogen combustion. If it were calculated based on higher heating value (HHV) of hydrogen combustion, the efficiency for 46 oC, 34 oC and 3.3 oC body temperatures would be 54.6%, 49.9% and 33.7%, respectively.

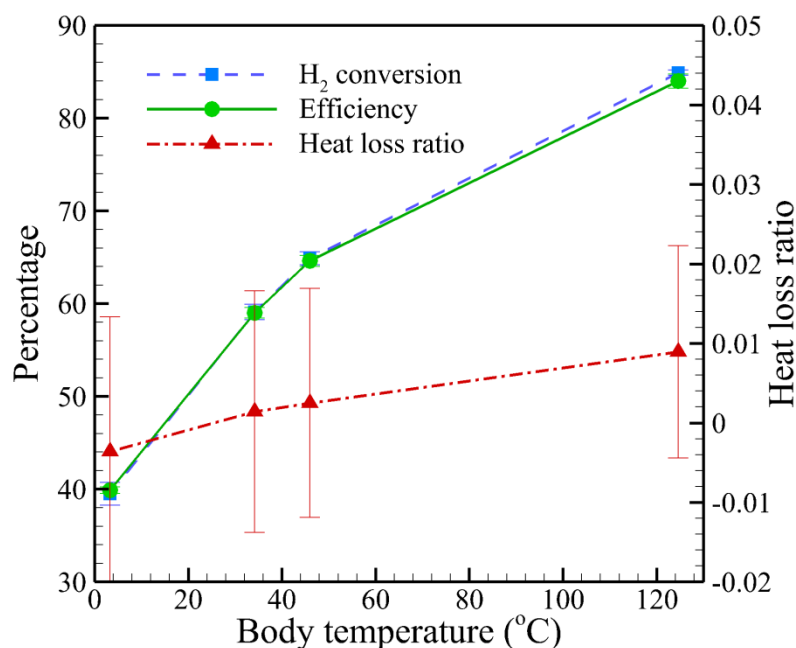


Figure 103: Variation of the performance indices at low body temperatures

When the body temperature drops, hydrogen conversion also drops significantly reaching 39.5% conversion at 3.3 °C. In this experiment, nitrogen gas exited the μ CHX at the temperature of -18.6 °C which meant that average temperature of nitrogen flowing through the heat exchanger layers was -44.7 °C. Previous experiments with a single channel combustor showed that a reaction could not be initiated at body temperatures lower than 100 °C and once started, the reaction extinguished/quenched² when the body temperature went below 30 °C. Having combustion when the body temperature is as low as 3 oC was hence attributed to the selective distribution of catalyst on both combustion and exhaust channels as identified by computer simulations.

The heat loss ratio trend in Figure 103 suggests that the heat loss would reach zero at body temperature of 25 °C while the temperature inside the hood was 20 °C. The body temperature was calculated by averaging the readings of two thermocouples attached to the short ends of the combustor where was closest to the catalyst (combustion) region (Thermocouples #1 and #2 in Figure 104). The other ends of the combustor had much lower temperatures because they were adjacent to the cold flow of nitrogen (Thermocouple #3). While the two side thermocouple readings averaged at 3.3 oC, the end thermocouple (#3) showed a temperature of -10.0 °C. So the ends were more than 13 degrees colder than the sides. For the body temperature of 34.2 °C (Figure 103), the ends temperatures were at 14.1 °C. Therefore, the μ CHX could absorb heat while the body temperature (averaged temperatures of thermocouples #1 and #2) was higher than room temperature.

² It should be noted that the starting and quenching temperature mentioned here are only related to the catalyst used in these experiments. Different catalysts with different deposition and activation methods may have different reactivity ranges.

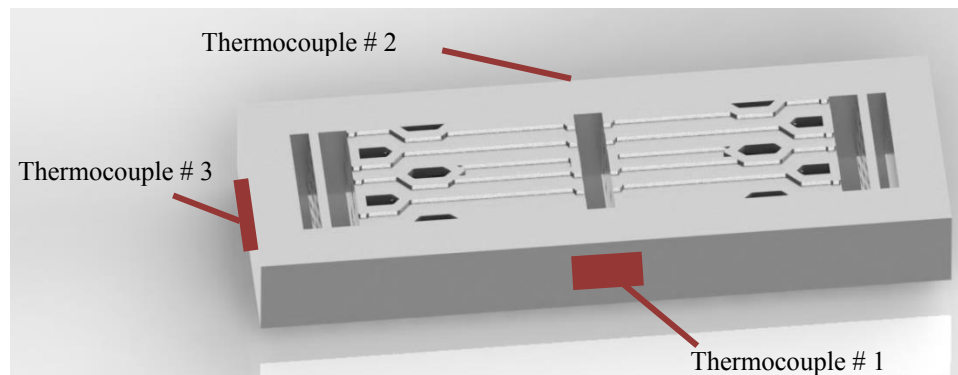


Figure 104: Location of thermocouples measuring the body temperatures

8-3-3 Effect of equivalence ratio

The effect of variation of equivalence ratio on the efficiency of the device was also investigated. Equivalence ratio was varied from 0.2 to 1 while residence time was kept approximately constant in the range of 9.6 ms to 10.1 ms. The body temperature was kept approximately constant in the range of 184.6 °C to 187.7 °C and the inlet nitrogen temperature were kept in the range of -69.5 °C to -71.3 °C. An increase of about 10% on hydrogen conversion as the equivalence ratio decreases from unity to 0.6. However, by decreasing the equivalence ratio, the efficiency increased at up to $\phi = 0.6$ but then decreased thereafter with further decrease in ϕ . The reason behind the drop of efficiency at lower equivalence ratio is the increase of heat loss ratio by a decrease in equivalence ratio from 0.6 to 0.2. To keep the residence time the same, the flow rates needed to be constant. When the flow rate is kept the same, lower equivalence ratio means lower mass flow rate hydrogen is incoming to the device and therefore input power is less. The input power varies from about 110 W (for $\phi=1$) to 29 W (for $\phi=0.2$). For the same body temperature of 186 °C, the heat loss is almost the same. Thus the heat loss ratio is higher at lower equivalence ratios.

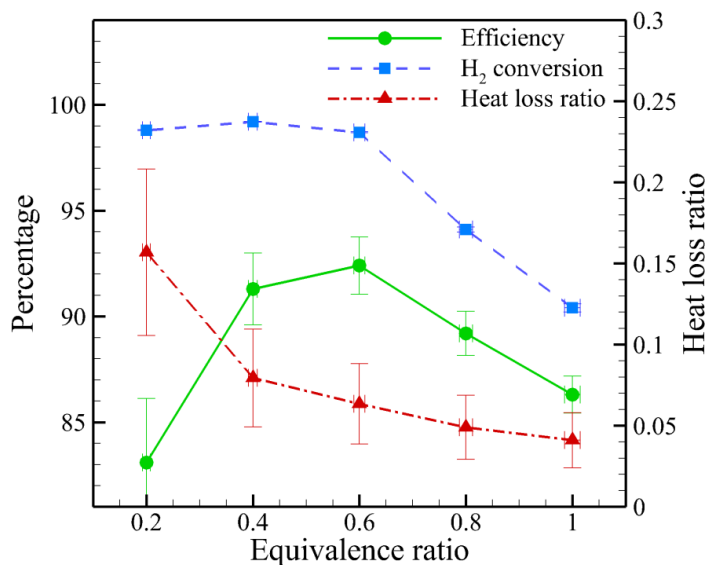


Figure 105: The effect of equivalence ratio on efficiency

It can be seen that the efficiency peaks at equivalence ratio of 0.6 with the value of 92.4%. This is the optimum operating conditions however, the input power is less (72 W) than equivalence ratio of one (109 W), therefore the size and weight of the system will be higher for the same power output. The size and weight comparison is shown in Table 31.

Table 31: Size and weight of a 1kW device for different equivalence ratios

Equivalence ratio	Efficiency (%)	Number of unit cells	Size (L)	Weight (g)
1	86.3	152	0.116	717.4
0.8	89.2	200	0.151	879.6
0.6	92.4	224	0.168	1035.6
0.4	91.3	288	0.214	1318.5

The SMART goal identified by DOE is to develop and demonstrate a 1 kW catalytic combustor heat exchanger having > 85% efficiency, having a dry mass less than 0.9 kg and volume less than 0.65 liters. Table 2 clearly shows that if the device operates at equivalence ratios of 0.8 or higher,

all goals were met while the size of the system is one quarter of the desired size. Although the desired power, size and weight were met, the desired outlet nitrogen temperature were much higher than the needed $-40\text{ }^{\circ}\text{C}$. The next section investigates the effect on inlet and outlet nitrogen temperatures.

8-3-4 Effect of N_2 inlet temperatures

The desired inlet and outlet temperatures for the nitrogen stream were $-70\text{ }^{\circ}\text{C}$ and $-40\text{ }^{\circ}\text{C}$, respectively. Nitrogen temperature is an important factor because it defines the temperature of the boundaries of the channels wherein combustion occurs. To study the effect of nitrogen inlet temperature on performance, it was varied from room temperature ($22.8\text{ }^{\circ}\text{C}$) to $-70\text{ }^{\circ}\text{C}$. The residence times and body temperature were kept within the range 9.7 ms to 11.7 ms and $184.6\text{ }^{\circ}\text{C}$ to $170\text{ }^{\circ}\text{C}$, respectively. The effect of inlet nitrogen temperature on performance of the μCHX is shown in Figure 106.

It can be seen that when the nitrogen inlet temperature was higher, hydrogen conversion and as a result, efficiency were lower. This trend is surprising given the fact that reaction rates are lower at lower temperatures. The body temperature was kept the same for all experiments but that does not necessarily mean that the temperature that the reaction was happening was the same. The body temperature was calculated by averaging the two temperatures measured on the sides of the combustor which were at least 7 mm far from the catalyst beds. So the body temperature cannot be a representative of the catalyst bed temperature, although that was the closest possible measure. What this plots suggests is that although the body temperatures were kept the same for

all these experiments, the catalyst bed temperature was higher for lower inlet nitrogen experiments.

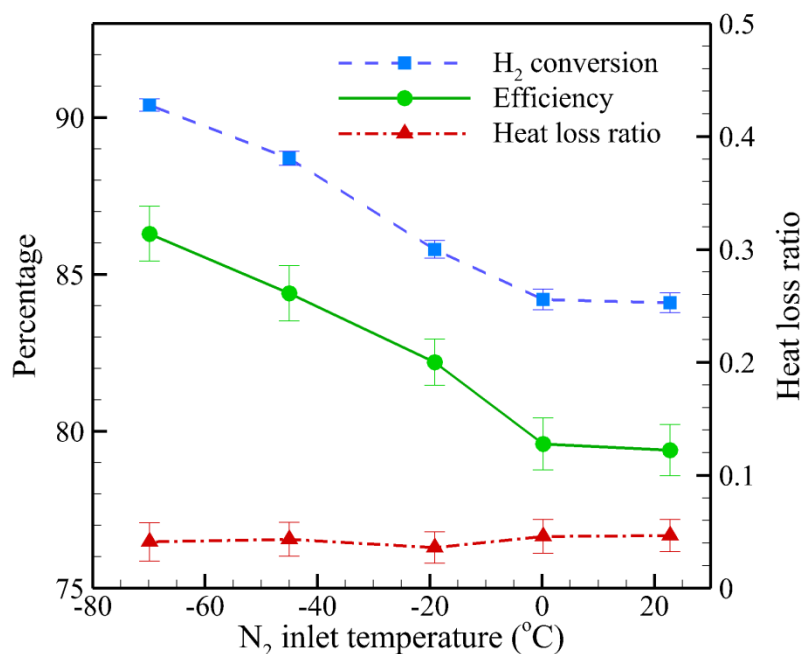


Figure 106: The effect on inlet nitrogen temperature on performance indices

When the nitrogen inlet temperature was lower, the two ends of the combustor (thermocouple #3 in Figure 104) could have temperatures more than 100 degrees lower than the sides temperatures. That means while heat generated closed to the sides of the combustor, it was transferred to the ends where the temperature was much lower. Figure 107 shows the heat transfer directions and temperature reading for the -70 °C inlet temperature case. When the temperature difference between the sides and ends are higher, the heat transfer via conduction through the stainless steel layers would be higher. And as a result, the internal temperature (catalyst bed temperature) is also higher.

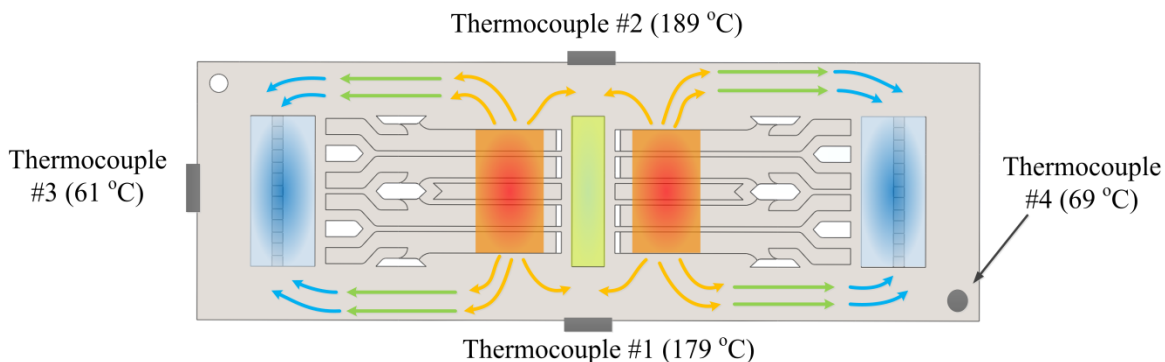


Figure 107: Heat pathways and location of thermocouples

And finally to see the capability of the combustor, the inlet temperature of nitrogen was reduced until the reaction is quenched. The combustion stopped when the inlet nitrogen temperature reached $-153\text{ }^{\circ}\text{C}$.

8-3-5 Pressure drops

Another factor for the performance of the device was pressure drop. For the specific application identified by DOE, pressure drop on the working fluid side was not an important issue. The device pressure drops on the nitrogen side were high and varied between 50 kPa (for 15 slpm) to 180 kPa (for 48 slpm). Pressure drops on air/H₂ mixture side, on the other hand, were much smaller and for the maximum flow rate was 20.1 kPa. High flow rates and complex headering system caused high pressure drops on nitrogen side.

8-3-6 Performance map

In chapter 4, a correlation was also developed using the results from computer simulations (Eq. (46)) to predict hydrogen conversions for the MH and CA μCHX unit cells. The same correlation

is used here to calculate hydrogen conversions with the operating conversions of the experiments (Eq. (46)). The comparison plot of correlation vs. experiment is shown in Figure 108 for the experimental data presented before. The legends identify the data points and the parameters that were varied. As can be seen, the correlation predicts the conversion within the promised precision ($\pm 10\%$) except for data points that were taken at lower body temperatures ($< 100\text{ }^\circ\text{C}$). Lower body temperatures reduced the reaction rate and hence hydrogen conversion. For these data points, the correlation over-predicted.

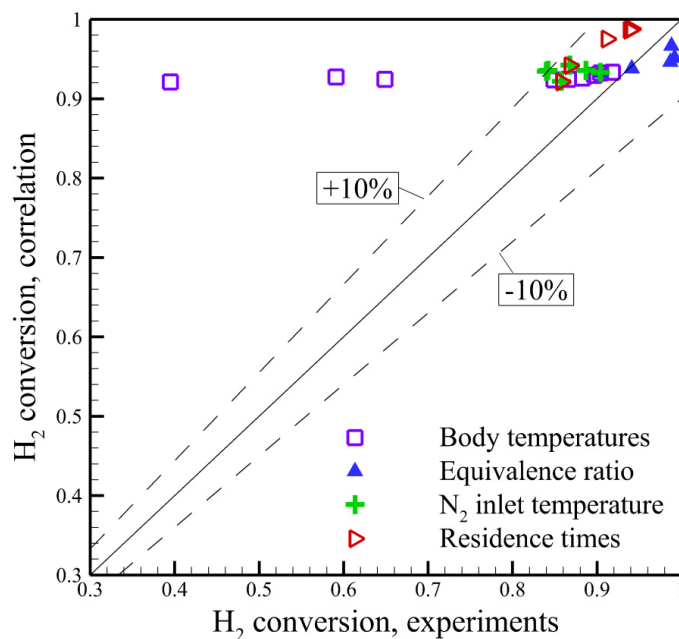


Figure 108: Comparison between the experimental and correlation values for hydrogen conversions

The body temperature was an important factor for the experiments therefore; it should be seen in the correlation. The equation can be modified by a term that carries the effect of body temperature. The term can be written as $(T_b/T_{\max})^\alpha$ where T_b is the body temperature and T_{\max} is a temperature that at that temperature maximum conversion was achieved. T_{\max} may be different

for different test conditions and catalysts. In these experiments, 200 oC was the temperature with the highest conversions. The experiments were mainly performed at 185 oC because operating at 200 oC for a long time could destroy the surface heaters and O-rings. And finally α is another experimental number and depends on the sensitivity of the catalyst to variations in temperature. In the experiments presented here $\alpha = 0.22$ was chosen. Therefore the modified correlation can be written as

$$\text{Con}_{H_2} = \left(1 - 0.45 \sqrt{\frac{\phi H^* \text{Pe}_{O_2,0}}{\text{Da}_{O_2,0}}} \right) \left(\frac{T_b}{T_{\max}} \right)^\alpha \quad (61)$$

where $T_{\max} = 200$ °C and $\alpha = 0.22$. The comparison plot is shown for Eq. (61) in Figure 109. It can be seen that all data points are within $\pm 10\%$ of the predicted value by the correlation.

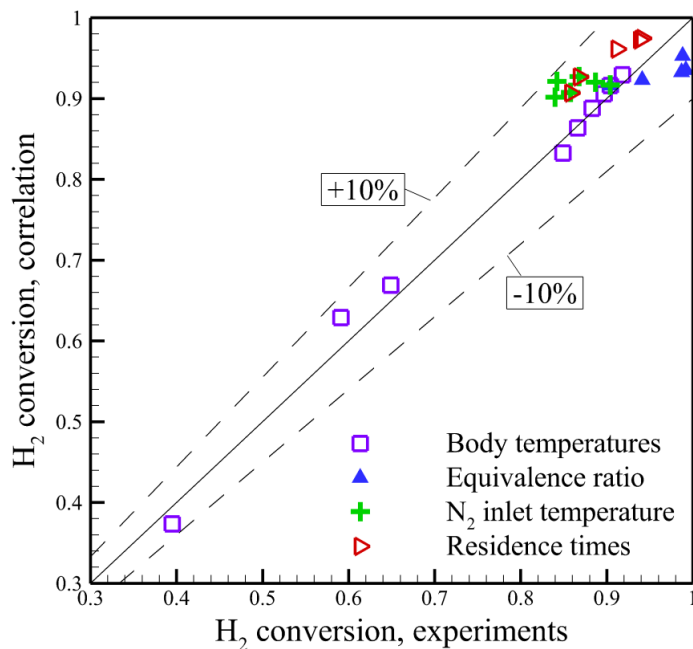


Figure 109: Comparison between the experimental and modified correlation (Eq. 61) values for hydrogen conversions

9- CONCLUSION AND FINAL REMARKS

A multi-unit cell microscale combustor and heat exchanger (μ CHX) was designed using CFD simulations and its performance was characterized via simulation and experiment. Computer simulations were carried up at the unit cell level and was used for the design of a 100 Watt μ CHX which was then fabricated and experimentally tested. The effects of different geometrical and fluidic parameters on the performance of the device were investigated.

9-1 Conclusions

Design of a novel microscale integrated combustor heat exchanger with recuperation (μ CHX) for the purposes of desorption of hydrogen was described. These specific μ CHXs were designed:

- One for a metal hydride storage system, heat exchange fluid: Oil, Inlet temperature: 160 °C and outlet temperature 180 °C.
- One for a cryo-adsorbent storage system, heat exchange fluid: hydrogen, inlet temperature -73 °C and outlet temperature -40 °C.

A detailed design for a compact combustor-heat exchanger with microchannels for a very cold working is presented. In hydrogen fuel cell cars with cryo-adsorbent storage, wherein heat needed to be supplied to the hydrogen gas under cold start conditions to raise its temperature from 200K to 233K. The design was performed in two stages, first at the unit cell and then at the device level.

The performance of a unit cell μ CHX was investigated using 2D numerical simulations with detailed surface reactions. The unit cell consisted of a combustor, two exhaust and two heat exchange fluid channels. The performance of the unit cell was characterized by use of the efficiency index, conversion and effectiveness. The effect of variation of different geometrical and thermo-fluidic parameters on the efficiency of the unit cell of MH and CA μ CHX was investigated.

For the MH μ CHX, the parameters investigated included catalyst surface length, catalyst location, gas and working fluid inlet velocity, working fluid inlet temperature, channel length and height, and equivalence ratio. The effect of these parameters was captured non-dimensionally using Damkohler and Peclet numbers. For the parameter space considered, a catalyst surface length of 15 mm presents a compromise between high efficiency and increased cost of the noble metal catalyst. It was found that higher hydrogen conversion resulted from higher residence time which meant that a longer catalyst bed and/or lower velocities increase the total efficiency. In addition, the simulation results showed that although hydrogen conversion decreased with increase in equivalence ratio, the efficiency did not change substantially due to the increase in effectiveness.

Dimensionless numbers were calculated based on the variable values at the inlet and were used to explain the effects of different geometrical and fluidic parameters. Damkohler number has the most effect on hydrogen conversion and efficiency; however, Peclet number is the dominant player where the reaction rate is limited by diffusion, for example in combustors with larger channel heights. A correlation was developed taking both Damkohler and Peclet numbers into account to predict the hydrogen conversion within the combustor. Based on the values of

efficiency and pressure drop, a performance map was developed as a design and operation guide for MH and CA μ CHX unit cells.

For the CA μ CHX, at the unit cell level a two-dimensional numerical model with detailed surface chemistry was used to generate a design with high thermal efficiency. A novel distributed catalyst arrangement was developed to prevent extinction of the reaction due to the cold heat transfer fluid. It was demonstrated that high hydrogen conversion (in excess of 99 percent) and unit cell efficiency (in excess of 90 percent) can be achieved for a range of operating conditions using this catalyst arrangement.

The second level of design described the layer and header design that would permit realization of such a multi-watt device by connecting several unit cells. At the device level, three dimensional simulations of fluid flow were performed to ensure uniformity in flow distribution while maintaining low device pressure drop. Fabrication constraints were also incorporated into the device level design and simulations. It was shown that the headering described in the dissertation can provide uniform flow distribution to the unit cells to within 6 percent.

A 100 W device consisting several layers (combustor, exhaust and heat exchange) and was fabricated using chemical etching. Activation and experiment test sections were designed and fabricated to experimentally investigate the performance of the μ CHX. The μ CHX consists of 16 unit cells providing heat to a cold nitrogen stream with an inlet temperature as low as -70 °C. Experimental results showed that hydrogen residence time and body temperature has significant effects on the overall efficiency of the device. The effects of equivalence ratio and inlet nitrogen temperatures were also investigated. Conversions as high as 99.2% and efficiencies as high as

92.4% were achieved. The correlation developed using computer simulations was used to predict the experimental data. A modified correlation was able to predict the experimental data on hydrogen conversion within $\pm 10\%$.

While the design of the μ CHX was motivated by hydrogen storage desorption, the concept can be used in applications where compact and high efficiency heat exchange is needed, such as distributed or off-grid space heating or compact water heaters.

9-2 Recommendation for Future Study

Uncertainties of most of the measured and calculated parameters were within an acceptable range ($\leq \pm 5\%$) except for heat loss. Identifying a way to calculate/measure heat loss other than the method used in the dissertation may reduce uncertainties. Controlling the inlet temperature of nitrogen was very difficult and time consuming. Adding a proportional valve to the test facility located after the LN2 dewar which can be controlled from the LabVIEW program can help the temperature adjustment and reduce the time required to each steady state.

For this dissertation, exhaust samples were gathered in sample bags and then analyzed within 10 minutes by connecting the bag to the GC intake. A part of the exhaust stream can be directly connected to the GC and exhaust composition can be tracked real time. Such a modification would enable having a transient data analysis from the start of the combustion process thereby. That helps to understand the preheating and ignition process.

Investigating different methods of joining the layers together instead of diffusion bonding can be very useful because of the sintering of the catalyst coat at high (>1000 °C) temperatures.

Different methods of catalyst coating may also reduce the sintering effects and should be identified. Some materials require lower temperatures for diffusion bonding and could be used without sintering the catalyst coat (if the bonding temperature is lower than 850 °C). Aluminum or other lower temperature materials can be used instead of stainless steel since the temperature of the device while testing never went higher than 200 °C. Materials like aluminum have much lower density and can reduce the weight of the device significantly.

The active catalyst area can be measured by chemisorption technique. Knowing the experiments active catalyst area, the factor B can be calculated and used to compare the experimental results and simulations.

Pressure drops on the nitrogen side was significant. Different designs may reduce the pressure drop by designing a different headering system.

The requirements of DOE for the cryo-adsorbent μ CHX were not completely met. They asked for an outlet temperature of -40 °C which was impossible with the current device. However, the hot nitrogen coming out of the CA μ CHX could be mixed with a cold nitrogen stream and result in the desired temperature.

BIBLIOGRAPHY

- [1] P. de Almeida and P. D. Silva, "The peak of oil production—Timings and market recognition," *Energy Policy*, vol. 37, no. 4, pp. 1267-1276, 2009.
- [2] R. Feely, S. Doney and S. Cooley, "Ocean Acidification: Present Conditions and Future Changes in a High-CO₂ World," *Oceanography*, vol. 22, no. 4, pp. 36-47, 2009.
- [3] Fernandez-Pello, "Micropower generation using combustion: issues and approaches," *Proceedings of the Combustion Institute*, pp. 883-899, 2002.
- [4] T. Q. Hua, R. K. Ahluwalia and J. K. Peng, "On-board and Off-board performance of hydrogen storage options for light-duty vehicles," *International Journal of Hydrogen Energy*, vol. 37, no. 3, pp. 2891-2910, 2012.
- [5] S. Satyapal, J. Petrovic, C. Read, G. Thomas and G. Ordaz, "The U.S. Department of Energy's National Hydrogen Storage Project: Progress towards meeting hydrogen-powered vehicle requirements," *Catalysis today*, vol. 120, no. 3-4, pp. 246-256, 2007.
- [6] G. Thomas and J. Keller, "Hydrogen Storage -Overview," May 2003. [Online]. Available: http://www1.eere.energy.gov/hydrogenandfuelcells/pdfs/bulk_hydrogen_stor_pres_sandia.pdf. [Accessed September 2013].
- [7] C. Loeb, "Enhancement and Modeling of Cryogenic Solid-State Hydrogen Storage Systems with a Novel Microchannel Thermal Management Device," PhD Thesis, Oregon State University, Corvallis, Oregon, May, 2013.
- [8] J. Zhang and T. S. Fisher, "A review of heat transfer issues in hydrogen storage technologies," *Journal of Heat Transfer*, vol. 127, pp. 1391-1399, 2005.
- [9] A. Zuttel, "Materials for hydrogen storage," *Materials Today*, vol. 6, no. 9, pp. 24-33, 2003.
- [10] J. Warnatz, U. Mass and R. W. Dibble, *Combustion, Physical and Chemical Fundamentals, Modeling and Simulation*, 4th edition, New York: Springer, 2006.
- [11] "GRI-3.0," Gas Research Institute, [Online]. Available: http://www.me.berkeley.edu/gri_mech. [Accessed 10 August 2013].
- [12] M. Aryafar and F. Zaera, "Kinetic study of the catalytic oxidation of alkanes over nickel, palladium, and platinum foils," *Catalysis letters*, vol. 48, pp. 173-183, 1997.

- [13] O. Deutschmann, R. Schmidt, F. Behrendt and J. Warnatz, "Numerical modeling of catalytic ignition," in *26th Symposium (international) on Combustion / The Combustion Institute*, 1996.
- [14] B. Hellsing, B. Kasemo and V. P. Zhdanov, "Kinetics of hydrogen-oxygen reaction on platinum," *Journal of Catalysis*, vol. 132, pp. 210-228, 1991.
- [15] J. Warnatz, M. D. Allendorf, R. J. Kee and M. E. Coltrin, "A model of elementary chemistry and fluid mechanics in the combustion of hydrogen on platinum surfaces," *Combustion and Flame*, vol. 96, pp. 393-406, 1994.
- [16] O. Deutschmann, F. Behrendt and J. Warnatz, "Modeling and simulation of heterogeneous oxidation of methane on a platinum foil," *Catalysis Today*, vol. 21, pp. 461-470, 1994.
- [17] E. Fridell, A. Rosen and B. Kasemo, "A laser-induced fluorescence study of OH desorption from Pt in H₂O/O₂ and H₂O/H₂ mixtures," *Langmuir*, vol. 10, pp. 699-708, 1994.
- [18] *Chemkin-CFD for Fluent User Manual*, Reaction Design, 2009.
- [19] M. K. Drost, C. Call, J. Cuta and R. Wegeng, "Microchannel combustor/evaporator thermal processes," *Microscale Thermophysical Engineering*, vol. 1, pp. 321-332, 1997.
- [20] P. D. Ronney, "Analysis of non-adiabatic heat-recirculating combustors," *Combustion and Flame*, vol. 135, pp. 421-439, 2003.
- [21] G. A. Boyarko, C. J. Sung and S. J. Schneider, "Catalyzed combustion of hydrogen-oxygen in platinum tubes for micro-propulsion applications," *Proceedings of the Combustion Institute*, vol. 30, pp. 2481-2488, 2005.
- [22] G. D. Stefanidis, N. S. Kaisare and D. G. Vlachos, "Modeling ignition in catalytic microreactors," *Chemical Engineering Technology*, vol. 31, no. 8, pp. 1170-1175, 2008.
- [23] G. B. Chen, C. P. Chen, C. Y. Wu and Y. C. Chao, "Effects of catalytic walls on hydrogen/air combustion inside a micro-tube," *Applied Catalysis A: General*, vol. 332, pp. 89-97, 2007.
- [24] N. S. Kaisare, G. D. Stefanidis and D. G. Vlachos, "Comparison of ignition strategies for catalytic microburners," *Proceedings of the Combustion Institute*, vol. 332, pp. 3027-3034, 2009.
- [25] J. Zhou, Y. Wang, W. Yang, J. Liu, Z. Wang and K. Cen, "Combustion of hydrogen-air in catalytic micro-combustors made of different material," *International Journal of Hydrogen*

- Energy*, vol. 34, pp. 3535-3545, 2009.
- [26] J. Mantzaras, R. Bombach and R. Schaeren, "Hetero-/homogeneous combustion of hydrogen/air mixtures over platinum at pressures up to 10 bar," *Proceedings of the Combustion Institute*, vol. 32, pp. 1937-1945, 2009.
- [27] S. Karagiannidis and J. Mantzaras, "Numerical investigation on the start-up of methane-fueled catalytic microreactors," *Combustion and Flame*, vol. 157, pp. 1400-1413, 2010.
- [28] C. Zhang, J. Zhang and J. Ma, "Hydrogen catalytic combustion over a Pt/Ce_{0.6}Zr_{0.4}O₂/MgAl₂O₄ mesoporous coating monolithic catalyst," *International Journal of Hydrogen Energy*, vol. 37, pp. 12941-12946, 2012.
- [29] A. D. Benedetto, V. D. Sarli and G. Russo, "A novel catalytic-homogeneous micro-combustor," *Catalysis Today*, vol. 147S, pp. S156-S161, 2009.
- [30] G. B. Chen, Y. C. Chao and C. P. Chen, "Enhancement of hydrogen reaction in a microchannel by catalyst segmentation," *International Journal of Hydrogen Energy*, vol. 33, pp. 2586-2595, 2008.
- [31] F. J. Weinberg, "Combustion temperatures: the future?," *Nature*, vol. 233, no. 5317, pp. 239-241, 1971.
- [32] S. A. Lloyd and F. J. Weinberg, "A burner for mixtures of very low heat content," *Nature*, vol. 251, no. 5470, pp. 47-49, 1974.
- [33] R. B. Peterson and J. A. Vanderhoff, "A catalytic combustor for microscale applications," *Combustion Science and Technology Communications*, vol. 1, pp. 10-13, 2000.
- [34] J. Ahn, C. Eastwood, L. Sitzki and P. D. Ronney, "Gas-phase and catalytic combustion in heat-recirculating burners," *Proceedings of the Combustion Institute*, vol. 30, pp. 2463-2472, 2005.
- [35] C. H. Kuo and P. D. Ronney, "Numerical modeling of non-adiabatic heat-recirculating combustors," *Proceedings of the combustion Institute*, vol. 31, pp. 3277-3284, 2007.
- [36] M. T. Janicke, H. Kestenbaum, U. Hagedorf, F. Schuth, M. Fichtner and K. Schubert, "The controlled oxidation of hydrogen from an explosive mixture of gases using a microstructured reactor/heat exchanger and Pt/Al₂O₃ catalyst," *Journal of Catalysis*, vol. 191, no. 2, pp. 282-293, 2000.
- [37] S. Ryi, J. Park, S. Choi, S. Cho and S. Kim, "Novel micro fuel processor for PEMFCs with heat generation by catalytic combustion," *Chemical Engineering Journal*, vol. 113, no. 1,

- pp. 47-53, 2005.
- [38] T. A. Johnson and M. P. Kanouff, "Development of a hydrogen catalytic heater for heating metal hydride hydrogen storage systems," *International Journal of Hydrogen Energy*, vol. 37, pp. 2304-2319, 2012.
- [39] Y. Fan and L. Luo, "Recent applications of advances in microchannel heat exchangers and multi-scale design optimization," *Heat Transfer Engineering*, vol. 29, no. 5, pp. 461-474, 2008.
- [40] M. G. Khan and A. Fartaj, "A review on microchannel heat exchangers and potential applications," *International Journal of Energy Research*, vol. 35, pp. 553-582, 2011.
- [41] K. R. Hwang, C. B. Lee, S. W. Lee, S. K. Ryi and J. S. Park, "Novel micro-channel methane reformer assisted combustion reaction for hydrogen production," *International Journal of Hydrogen Energy*, vol. 36, pp. 473-481, 2011.
- [42] M. S. Mettler, G. D. Stefanidis and D. G. Vlachos, "Enhancing stability in parallel plate microreactor stacks for syngas production," *Chemical Engineering Science*, vol. 66, pp. 1051-1059, 2011.
- [43] A. Y. Tonkovicha, S. Perrya, Y. Wang, D. Qiu, T. LaPlantea and W. A. Rogers, "Microchannel process technology for compact methane steam reforming," *Chemical Engineering Science*, vol. 59, pp. 4819-4824, 2004.
- [44] J. Thormanna, P. Pfeifer and U. Kunz, "Dynamic performance of hexadecane steam reforming in a microstructured reactor," *Chemical Engineering Journal*, vol. 191, pp. 410-415, 2012.
- [45] N. T. Stetson, "DOE Hydrogen Program Annual Merit Review Proceedings 2011," [Online]. Available: http://www.hydrogen.energy.gov/annual_review11_plenary.html. [Accessed August 2013].
- [46] "Paratherm-MR thermal properties," Paratherm, [Online]. Available: <http://www.paratherm.com/Paratherm-MR/index.asp>. [Accessed Dec 2011].
- [47] D. G. Norton, E. D. Wetzel and D. G. Vlachos, "Thermal Management in Catalytic Microreactors," *Industrial and Engineering Chemistry Research*, vol. 45, no. 1, pp. 76-84, 2006.
- [48] D. Haley and V. Narayanan, "Performance characterization of a microscale hydrogen combustor recuperator and oil heat exchanger," in *IMECE 2011, Proceedings of the ASME 2011 International Mechanical Engineering Congress and Exposition*, Denver, Colorado,

USA, 2011.

- [49] C. Appel, J. Mantzaras, R. Schaeren, R. BomBach, A. Inauen, B. Kaepperli, B. Hemmerling and A. Stampanoni, "An experimental and numerical investigation of homogeneous ignition in catalytically stabilized combustion of hydrogen/air mixtures over platinum," *Combustion and Flame*, vol. 128, pp. 340-368, 2002.
- [50] J. Warnatz, R. W. Dibble and U. Mass, *Combustion, physical and chemical fundamentals, modeling and simulation*, New York: Springer-Verlag, 1996.
- [51] M. Forsth, "Sensitivity analysis of the reaction mechanism for gas-phase chemistry of H₂-O₂ mixtures induced by a hot Pt surface," *Combustion and Flame*, vol. 130, pp. 241-260, 2002.
- [52] A. Schneider, *Experimental and numerical investigation of the catalytic partial oxidation of methane to synthesis gas for power generation applications*, PhD thesis, ETH Zurich, 2007.
- [53] J. Braun, T. Hauber, H. Tobben and P. Zacke, "Influence of Physical and Chemical Parameters on the Conversion Rate of a Catalytic Converter: A Numerical Simulation Study," SAE Technical Paper, 2000.
- [54] R. Schwiedernoch, S. Tischer, C. Correa and O. Deutschmann, "Experimental and numerical study on the transient behavior of partial oxidation of methane in a catalytic monolith," *Chemical Engineering Science*, vol. 58, pp. 633-642, 2003.
- [55] D. Haley, *Performance Characterization of an Integrated Microscale Hydrogen Combustor Recuperator and Oil Heat Exchanger*, Corvallis, OR.: Master's Thesis, Oregon State University, June 2011.
- [56] B. K. Paul and T. Terhaar, "Comparison of two passive microvalve designs for microlamination architectures," *Journal of Micromechanics and Microengineering*, vol. 10, pp. 15-20, 2000.
- [57] T. W. Eagar, "Processes of Joining Materials," MIT, [Online]. Available: <http://www-old.me.gatech.edu/jonathan.colton/me4210/joiningchapter.html>. [Accessed August 2013].
- [58] B. K. Paul, P. Kwon and R. Subramanian, "Understanding limits on fin aspect ratios in counterflow microchannel arrays produced by diffusion bonding," *Journal of Manufacturing Science and Engineering*, vol. 128, pp. 977-983, 2006.
- [59] G. A. Whyatt, C. M. Fischer and J. M. Davis, "Rapid start fuel reforming systems and techniques". USA Patent 7763217, 2010.

- [60] P. Stefanov, D. Stoychev, I. Valov, A. Kakanakova-Georgieva and T. Marinova, "Electrochemical deposition of thin zirconia films on stainless steel 316 L," *Materials Chemistry and Physics*, vol. 62, no. 2, pp. 222-225, 2000.
- [61] A. E. Schweizer and G. T. Kerr, "Thermal decomposition of hexachloroplatinic acid," *Inorganic Chemistry*, vol. 17, no. 8, pp. 2326-2327, 1978.
- [62] W. Choi, S. Kwon and H. Dong Shin, "Combustion characteristics of hydrogen-air premixed gas in a sub-millimeter scale catalytic combustor," *International Journal of Hydrogen energy*, vol. 33, no. 9, pp. 2400-2408, 2008.
- [63] A. M. Karim, J. A. Federici and D. G. Vlachos, "Portable power production from methanol in an integrated thermoelectric/microreactor system," *Journal of Power Sources*, vol. 179, no. 1, pp. 113-120, 2008.
- [64] "Stainless steel specification and composition chart," Engineers Edge, [Online]. Available: http://www.engineersedge.com/stainless_steel.htm. [Accessed 1 Sept. 2013].
- [65] O. Deutchmann, L. I. Maier, U. Riedel, A. H. Stroemman and R. W. Dibble, "Hydrogen assisted catalytic combustion of methane on platinum," *Catalysis Today*, vol. 59, pp. 141-150, 2000.
- [66] V. Seshadri and N. S. Kaisare, "Simulation of hydrogen and hydrogen-assisted propane ignition in pt catalyzed microchannel," *Combustion and Flame*, vol. 157, no. 11, pp. 2051-2062, 2010.
- [67] S. J. Kline and F. A. McClintock, "Describing Uncertainties in Single-Sample Experiments," *Mechanical Engineering*, vol. 75, pp. 3-8, 1953.

APPENDICES

APPENDIX A. PARATHERM MR PROPERTIES

Physical Properties

Chemical Name	Linear Alkene
Appearance	Water White Liquid
Odor	Slight Odor
Maximum Recommended Film Temperature	600°F/316°C
Maximum rec'd operating temp – fired heaters	550°F/288°C
Maximum rec'd operating temp – all others	580°F/304°C
Minimum operating temperature 20 cPs (20 mPa-s)	38°F/3°C)
Minimum start-up temp 300 cPs (300 mPa-s)	-37°F/-38°C
Viscosity @ 60°F/15.5°C sSt (mm ² /sec)	13
Density @ 60°F/15.5°C lb/gal (kg/m ³)	6.7 (804)
Flash Point Pensky-Martens Closed Cup (D93)	>300°F/149°C
Boiling Point (14.7 psia/101 kPa)	>650°F/343°C
Vapor Pressure @ max operating temp psia (kPa)	8.4 (61)
% Volume expansion over rec'd operating temp per 100°F (°C)	4.4 (7.9)
Average Molecular Weight	300
Heat of Combustion (approximate) BTU/lb (kJ/kg)	20,000 (46,300)
Heat of Vaporization (approximate) BTU/lb (kJ/kg)	115 (266)

APPENDIX B. MH μ CHX LAYERS

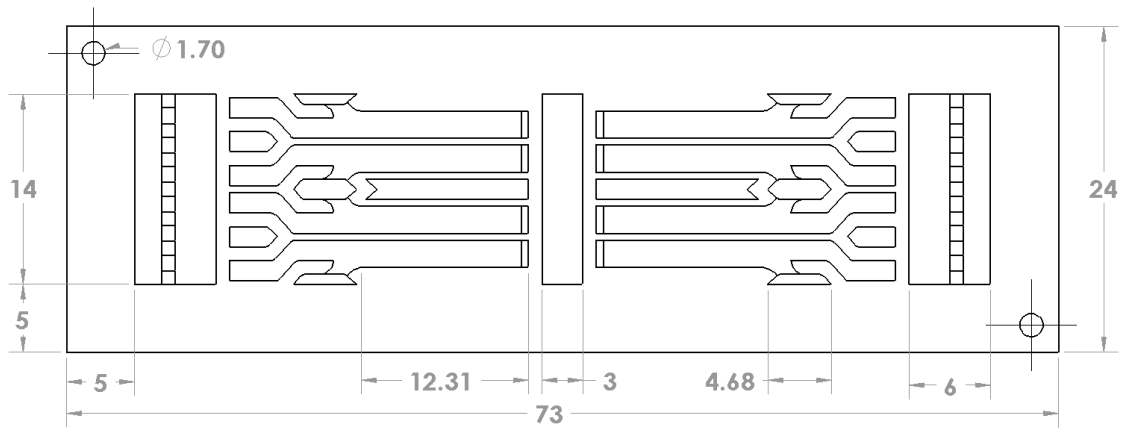
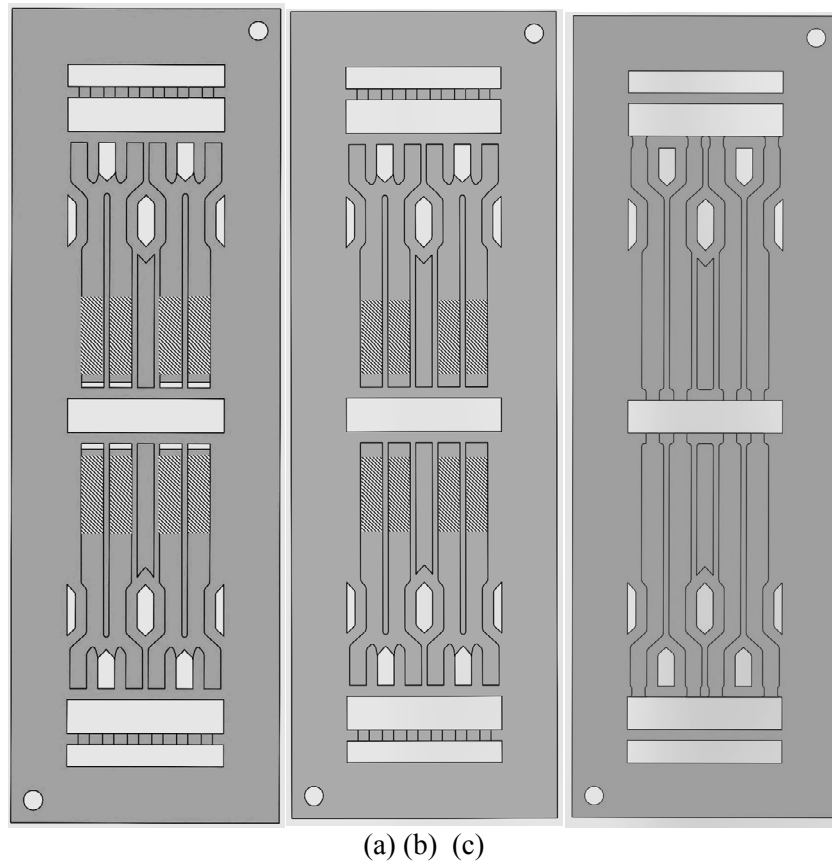


Figure B-1. Combustor layer design (dimensions are in mm)



(a) (b) (c)

Figure B-2 (a) Top exhaust layer, (b) Bottom exhaust layer, (c) Heat exchange layer

APPENDIX C: SAMPLE UNCERTAINTY CALCULATIONS

Table C-1: Uncertainty calculations for measured parameters

	Bias Error	Precision Error	Total Uncertainty	Parameter Value	Percentage %
Pressure drop (Pa)	177.00	222.148	284.040	4162.350	6.82
N2 inlet temperature (C)	0.32	0.020	0.320	-69.863	0.46
N2 outlet temperature (C)	0.36	0.031	0.364	119.412	0.31
Outlet gas Temperature (C)	0.36	0.060	0.365	54.040	0.68
Hydrogen Flow rate (sccm)	2.64	6.119	6.665	660.499	1.01
Air flow rate (sccm)	6.28	15.739	16.947	1570.705	1.08
N2 flow rate (slpm)	1.72E-01	3.40E-01	3.81E-01	2.46E+01	1.55
Catalyst length (mm)	1.00E-02	5.00E-01	0.500	22.500	2.22
Channel height (um)	1.00E-02	0.00E+00	1.00E-02	3.77E+02	0.00

Table C-2: Uncertainty propagation in calculated parameters

	Total Uncertainty	Parameter Value	Percentage %
m dot _N2	7.39E-06	4.77E-04	1.55E+00
Q dot N2	1.484087787	94.49076238	1.570616798
m dot _H2 (kg/s)	9E-9	9.10388E-07	1.009034791
Q dot input	1.10	109.1964834	1.009034791
EFFICIENCY	0.01	0.865327889	1.009137301
Flow rate air (m3/s)	2.82448E-07	2.61784E-05	1.078936074
flow rate H2 (m3/s)	1.11078E-07	1.10083E-05	1.009034791
m dot air (kg/s)	3.4035E-07	3.1545E-05	1.078936074
m dot total	3.49536E-07	3.24554E-05	1.076975311
DT exhaust	0.509116882	100	0.509116882
Q lost to exhaust	0.039010422	3.274747717	1.191249689
V comb	0.038020694	3.592812087	1.058243329
V recup	0.019010347	1.796406043	1.058243329

Table C-2 (Continued)

L comb	0.0005	0.012	4.166666667
L recup	0.0001	0.01	1
T res comb	0.143585095	3.340002124	4.298952204
T res recup	0.081049627	5.845003717	1.386648006
T res total	0.224634722	9.18500584	2.445667714
H2 exhaust mass fraction	0.0019296	0.096	2.01
Q combL	0.235765407	10.4828624	2.249055626
Q L	1.863365867	4.222858577	44.12569904
r Q L	0.017068801	0.038672111	44.13723448
H2 conversion	0.0019296	0.904	0.213451327
Equivalence	0.014784521	1.000816813	1.477245498

APPENDIX D: CHEMKIN REACTION MECHANISM CODE

Reaction mechanism from: Deutschman et al., 26th Symp. (Intl.) on Combustion, 1996

```

SITE/PT_SURFACE/ SDEN/2.7063E-09/
PT(S) H(S) H2O(S) OH(S) O(S)
END
BULK/PT_BULK/
PT(B)
END
!
THERMO ALL
300.0 1000.0 3000.0
O(S) 92491O 1PT 1 I 300.00 3000.00 1000.00 1
0.19454180E+01 0.91761647E-03-0.11226719E-06-0.99099624E-10 0.24307699E-13 2
-0.14005187E+05-0.11531663E+02-0.94986904E+00 0.74042305E-02-0.10451424E-05 3
-0.61120420E-08 0.33787992E-11-0.13209912E+05 0.36137905E+01 4
O2(S) 92491O 2PT 1 I 300.00 3000.00 1000.00 1
0.35989249E+01 0.20437732E-02-0.23878221E-06-0.22041054E-09 0.53299430E-13 2
-0.41095444E+04-0.21604582E+02-0.20174649E+01 0.14146218E-01-0.16376665E-05 3
-0.11264421E-07 0.60101386E-11-0.25084473E+04 0.79811935E+01 4
H(S) 92491H 1PT 1 I 300.00 3000.00 1000.00 1
0.10696996E+01 0.15432230E-02-0.15500922E-06-0.16573165E-09 0.38359347E-13 2
-0.50546128E+04-0.71555238E+01-0.13029877E+01 0.54173199E-02 0.31277972E-06 3
-0.32328533E-08 0.11362820E-11-0.42277075E+04 0.58743238E+01 4
H2(S) 92491H 2PT 1 I 300.00 3000.00 1000.00 1
0.15330955E+01 0.34586885E-02-0.32622225E-06-0.36824219E-09 0.83855205E-13 2
-0.36401533E+04-0.10822206E+02-0.21517782E+01 0.87039210E-02 0.11154106E-05 3
-0.42477102E-08 0.96133203E-12-0.22640681E+04 0.97397461E+01 4
H2O(S) 92491O 1H 2PT 1 I 300.00 3000.00 1000.00 1
0.25803051E+01 0.49570827E-02-0.46894056E-06-0.52633137E-09 0.11998322E-12 2
-0.38302234E+05-0.17406322E+02-0.27651553E+01 0.13315115E-01 0.10127695E-05 3
-0.71820083E-08 0.22813776E-11-0.36398055E+05 0.12098145E+02 4
OH(S) 92491O 1H 1PT 1 I 300.00 3000.00 1000.00 1
0.18249973E+01 0.32501565E-02-0.31197541E-06-0.34603206E-09 0.79171472E-13 2
-0.26685492E+05-0.12280891E+02-0.20340881E+01 0.93662683E-02 0.66275214E-06 3
-0.52074887E-08 0.17088735E-11-0.25319949E+05 0.89863186E+01 4
PT(S) PT 1 S 300.0 3000.0 1000.0 1
0.00000000E+00 0.00000000E+00 0.00000000E+00 0.00000000E+00 0.00000000E+00 2
0.00000000E+00 0.00000000E+00 0.00000000E+00 0.00000000E+00 0.00000000E+00 3
0.00000000E+00 0.00000000E+00 0.00000000E+00 0.00000000E+00 4
PT(B) PT 1 S 300.0 3000.0 1000.0 1
0.00000000E+00 0.00000000E+00 0.00000000E+00 0.00000000E+00 0.00000000E+00 2
0.00000000E+00 0.00000000E+00 0.00000000E+00 0.00000000E+00 0.00000000E+00 3
0.00000000E+00 0.00000000E+00 0.00000000E+00 0.00000000E+00 4
END
!
!!*****!
!!***** H2-O2 Surface Reaction on Pt *****!
!!***** Mechanism from DUECHMANN, *****!
!!*****!
REACTIONS KJOULES/MOLE
H2 + 2PT(S) => 2H(S) 0.046 0.0 0.0 !
STICK FORD/PT(S) 1.0/

```

```

2H(S) => H2 + 2PT(S)      3.70E+21  0.00  67.4  !
COV/H(S) 0 0 -6 /
O2 + 2PT(S) => 2O(S)      21 -1.0  0.00
STICK
2O(S) => O2 + 2PT(S)      3.7E+21  0.00  213.2
COV/O(S) 0 0 -60 /
H2O + PT(S) => H2O(S)     0.75  0.0  0.0
STICK
H2O(S) => H2O + PT(S)     1E+13  0.00  40.3
OH + PT(S) => OH(S)       1  0.0  0.0
STICK
OH(S) => OH + PT(S)       1E+13  0.00  192.8
H(S) + O(S) = OH(S) + PT(S) 3.70E+21  0.00  11.5
H(S) + OH(S) = H2O(S) + PT(S) 3.70E+21  0.00  17.4
OH(S) + OH(S) = H2O(S) + O(S) 3.70E+21  0.00  48.2

H + PT(S) => H(S)         1.0  0  0
STICK
O + PT(S) => O(S)         1.0  0  0
STICK
!.....!
END

```